Velocities and Structures in the Orion Molecular Cloud

Maiken Gustafsson

Department of Physics and Astronomy
University of Aarhus, Denmark

PhD thesis

August 2006

This thesis is submitted to the Faculty of Science at the University of Aarhus, Denmark, in order to fulfil the requirements for obtaining the PhD degree in Astronomy.
The studies have been carried out under the supervision of Prof. David Field at the Department of Physics and Astronomy, Aarhus University from August 2002 to August 2006.

This work was funded by the Faculty of Science, University of Aarhus, the Instrument center for Danish Astrophysics (IDA) and the Aarhus Center for Atomic Physics (ACAP).

Per aspera ad astra

Contents

Acknowledgements

First of all, I would like to thank my advisor, David Field, without whom this work could not have been done. Especially I want to thank him for always pushing me in new directions. I also have to thank him for trying to teach me proper English (all the bad words I got from him), the numerous discussions on anything related to this Universe and for always having an insult ready on any time of the day. I also want to thank both David and Jean-Louis Lemaire for making the observation trips to Hawaii and Chile truly memorable. Markus Hartung has been an invaluable help with the NACO-FP observations and data reduction.
I should also thank the people who have been very patient and helped me with numerous computer problems. Especially Nykola Jones for trying to make Windows make sence and Michael Weidinger for showing me all the smart tricks in Linux.
I'm also indepted to Majken, Lars, Brian, Michael and Henrik who have always been up for a coffee break and who made sure that I always got plenty of the vital vitamins contained in coffee and cake.
My deepest gratitude goes to my wonderful husband, Jacob, who has always been a great support. Without his never dwindling love and strong belief in me I would have been a nervous wreck by now. I guess I should also thank my parents, Hanne and Uffe. Somehow they are kind of responsible for getting me where I am today. I'm forever grateful for the consolation in desperate times and who knows, maybe I will write that book some time. I would also like to thank my parents and parents-in-law for the patience and help during these last couple of months.
Finally, but not least, I would like to acknowledge the financial support for this work from ACAP, the Aarhus Center for Atomic Physics and IDA, Instrument center for Danish Astrophysics, the latter funded by FNU.

List of Publications

Refereed publications:

[I] **M. Gustafsson**, L.E. Kristensen, Y. Clénet, D. Field, J.L. Lemaire, G. Pineau des Forêts, D. Rouan, E. Le Coarer,
New insight into shocks and star formation in Orion: First light with GriF
A&A, 411, 437 (2003) **(Chapter 4)**

[II] L.E. Kristensen, **M. Gustafsson**, D. Field, G. Callejo, J.L. Lemaire, L. Vannier, G. Pineau des Forêts,
H_2 excitation imaging of the Orion Molecular Cloud,
A&A, 412, 727 (2003)

[III] F. Lacombe, E. Gendron, D. Rouan, Y. Clénet, D. Field, J.L. Lemaire, **M. Gustafsson**, A.M. Lagrange, D. Mouillet, G. Rousset, T. Fusco, L. Rousset-Rouviere, B. Servan, C. Marlot, P. Feautrier,
VLT/NACO infrared adaptive optics images of small scale structures in OMC1,
A&A, 417, L5 (2004) **(Chapter 8)**

[IV] **M. Gustafsson**, D. Field, J.L. Lemaire, F.P. Pijpers,
Probing Turbulence with Infrared Observations in OMC1,
A&A, 445, 601 (2006) **(Chapters 5 and 6)**

[V] H.D. Nissen, **M. Gustafsson**, J.L. Lemaire, Y. Clénet, D. Rouan, D. Field,
Observations of spatial and velocity structure in the Orion Molecular Cloud,
to appear in A&A (2006): astro-ph/0511226

[VI] **M. Gustafsson**, A. Brandenburg, J.L. Lemaire, D. Field
The nature of turbulence in OMC1 at the star forming scale: observations and simulations
A&A, 454, 815 (2006) **(Chapter 7)**

[VII] **M. Gustafsson**, J.L. Lemaire, D. Field,
A Method for the Detection of Structure
A&A in press (2006): astro-ph/0606150 **(Chapter 8)**

Other publications:

[I] **M. Gustafsson**, L.E. Kristensen, Y. Clénet, D. Field, J.L. Lemaire, G. Pineau des Forêts, D. Rouan, E. Le Coarer,
Shocks and Star Formation in Orion: First Light with GriF,
Proceedings of the ESO workshop on Science with adaptive optics, 229 (2004)

[II] **M. Gustafsson**, F. Lacombe, E. Gendron, D. Rouan, Y. Clénet, D. Field, J.L. Lemaire, A.-M. Lagrange, D. Mouillet, G. Rousset, B. Servan, C. Marlot,
Imaging in Orion: NAOS-CONICA Adaptive Optics on the ESO-VLT,
Proceedings of the ESO workshop on Science with adaptive optics, 232 (2004)

[III] J. Sollerman, J. Andersson, **M. Gustafsson**, P. Jakobsson, G. Oye, F. Patat,
Supernovae 2003gk and 2003gl,
IAU Circ., 8164, 3 (2003)

Abstract

In order to get a better understanding of the mechanisms of star formation in molecular clouds it is necessary to describe in detail the physical conditions of highly active star forming regions. Using high resolution data of shock and photon excited H_2 we have characterized the gas motions and the morphology in the OMC1 region of the Orion Molecular Cloud in the highest possible detail.

Results in this thesis are mainly based on IR Fabry-Perot interferometric observations in conjunction with adaptive optics of rovibrationally excited H_2 emission in the K-band S(1) v=1-0 line at 2.121μm. The data refer to the dynamical characteristics of warm perturbed gas. Data consist of spatially resolved images with a measured velocity for each resolution limited region in the image.

We show graphic images of interstellar shocks in OMC1, displaying a level of detail which has not previously been attained. Observed structures suggest that some shocks are not associated with the large scale outflow seen in the region but are created by local, internal shocks associated with low mass star formation in the clumps of gas.

Using the radial velocity data we present a statistical analysis of the velocity structure in OMC1 at scales ranging from 70 AU to $3{\cdot}10^4$ AU. This analysis includes autocorrelation functions, the size-line width relation, probability distribution functions (PDFs) of radial velocities and structure functions. Deviations from power law behaviour of structure functions below 2000 AU are attributed to outflows associated with low mass star formation within OMC1. The scaling of the higher order structure functions with order deviates from the standard scaling for supersonic turbulence. 170 individual H_2 emitting clumps have been analysed with sizes between 500 and 2200 AU. These show considerable diversity with regard to PDFs and structure functions displaying a variety of shapes of the PDF and different values of the scaling exponent within a restricted spatial region.

We compare the statistical results from the observations of OMC1 to two-dimensional projections of simulations of supersonic hydrodynamic turbulence. Based on this comparison we explain the unusual scaling of structure

function observed in OMC1 as a selection effect of preferentially observing the shocked part of the gas. Deviations of the structure functions in OMC1 from power laws cannot be reproduced in simulations and remains an outstanding issue.

Three different methods for detection of preferred scale sizes in the medium are described. One of the methods, the structure function method, is developed for this work and appears to more sensitive to the presence of characteristic scales than other methods. The density structure in OMC1 exhibits mean characteristic sizes of 100, 550, 1000, 1900 and 3000 AU. A set of larger clumps in OMC1 may be gravitationally unstable.

Chapter 1

Introduction

We live in a very dynamical universe where new generations of stars are born, go through their main-sequence life and die out in an ever continuous circle. About 4.5 billion years ago our own Sun and planetary system were born in a manner that we can only guess was similar to the star formation processes we observe today in other regions in the Milky Way. In order to get a better understanding of how the Sun, the Earth and ultimately human beings were created and formed, we need to understand how stars and planets are formed, how common a planetary system is and how and where bio-molecules can be created. These are big questions which are far from settled, but observations and theoretical studies focusing on many different aspects have got us far down the road.

Stars form in gravitationally collapsing gas clouds. However, the regulating processes causing the collapse depend on the physical conditions in the cloud. Therefore we need detailed observations and analysis of the conditions in star-forming regions as well as regions without active star formation in order to determine the dominating processes. Traditionally, observations have been carried out in the radio regime focusing on the structure of clouds and cores in clouds. However, with the advent of adaptive optics high resolution imaging in the infrared has opened up a window to the very inner region around protostars.

In this thesis we focus on the conditions in the region surrounding BN-KL in the Orion Molecular Cloud 1 (OMC1). OMC1 is the closest site of active massive star formation making it an ideal testbed for probing the processes associated with star formation. The distance to Orion used throughout this thesis is 460 pc following Bally et al. (2000). We use radial velocity data obtained in a 1'×1' region with high spatial resolution to characterize the structure of the H_2 outflows seen in this region. The spatial resolution of the velocity data is an order of magnitude higher than similar previously published data of OMC1.

In Sect. 1.1 we give an introduction to theories of star formation. We will see that two opposing schools of thought exist. One favours a long-lived quasi-static evolution of molecular clouds, while the other favours a dynamical picture where clouds are transient phenomena and star formation happens rapidly. About the only thing the two models agree on is that all stars are formed in molecular clouds. Turbulence has an outstanding role in either model and in Sect. 1.2 we give an overview of how turbulence may be characterized and how it is related to the interstellar medium. In Sect. 1.4 a short review of the nature of OMC1 is presented and in Sect. 1.5 excitation mechanisms of the NIR emission which we observe is discussed.
In Chapter 2 we describe the three sets of observations of OMC1 used here. In Chapter 3 we discuss the observed continuum emission and present 4 new compact IR sources. In Chapter 4 we show that the detailed velocity and brightness data represent very graphic views of interstellar shocks and that the direction of these shocks are disordered with respect to the general outflow direction. In Chapter 5 we analyse the velocity field in OMC1 using standard statistical techniques from turbulence theory. Features similar to those of the cold turbulent gas at (sub)parsec scales are recovered at these smaller scales in the highly excited part of the gas which we observe. However important deviations from self-similarity are found. In Chapter 6 the analysis is extended to small individual clumps of emission showing large variations of the probability distribution function and the structure function within the region. In Chapter 7 we compare the statistical analysis of Chapter 5 with a set of hydrodynamic simulations. The comparison shows that those parts of the simulations which can be associated with shocks generally display the same behaviour as observed for the velocity field in OMC1. However, the deviations from self-similarity observed in OMC1 is not recovered. In Chapter 8 we use several techniques to confirm that the gas in OMC1 is not self-similar and contains characteristic scales between 100 and 3000 AU. In Chapter 9 we summarize and outline the major conclusions of this work.

1.1 Star formation

1.1.1 Molecular Clouds

All star formation in our Galaxy occurs in molecular clouds (MCs) behind large amounts of extinction from dust. Interstellar clouds were first discovered in the eighteenth century by Herschel (1785). Wolf (1923) found that the opaque material in these dark clouds consists of dust. In the 1970s it was realized, mainly through the discovery of cold interstellar CO (Wilson et al. 1970), that the clouds consist primarily of molecular hydrogen mixed with

small amounts of dust and more complex molecules.

Molecular clouds range from giant molecular clouds with masses of $10^5 - 10^6 M_\odot$ and number densities of 1-5$\times 10^2 cm^{-3}$ to molecular clouds (MCs) with masses of $10^2 - 10^4 M_\odot$ and number densities of $10^2 - 10^4 cm^{-3}$ (Mac Low & Klessen 2004). Denser structures (n $\sim 10^4 - 10^6 cm^{-3}$) within MCs are called clumps or cores. MCs exhibit supersonic line widths, which are interpreted as evidence of supersonic turbulence (Zuckerman & Evans 1974). Larson (1981) established a relation between the size and the observed line width of clouds, $\Delta v \propto R^\alpha$, where $\alpha \sim 0.2 - 0.7$ (Goodman et al. 1998). This relation agrees with a turbulent flow in which the energy spectrum, $E \propto k^{-n}$ and $k \sim R^{-1}$, has a negative slope of $n = 2\alpha + 1$ (Kolmogorov 1941, and see Sect. 1.2). Here the velocity difference between two regions increases when the distance increases.

Molecular clouds have masses far exceeding the Jeans mass (Jeans 1928; Evans 1999). That is, the thermal energy is less than the gravitational energy and the clouds should be collapsing in a free-fall time. The free-fall time, $t_{ff} = (G\rho)^{-1/2}$, is just the characteristic time it would take a body to collapse under its own gravity. This would, however, lead to a highly exaggerated star formation rate compared to the observed rate of $3 M_\odot year^{-1}$ in the Galaxy (Scalo 1986). In order to settle this contradiction turbulent motions and magnetic energy within the clouds have been interpreted as acting as support mechanisms against gravitational collapse resulting in long-lived MCs. Supersonic turbulence should, however, decay in a crossing time of the driving scale (Goldreich & Kwan 1974). The crossing time is defined as $t_c \sim l/\sigma_v$ where l is the size of the cloud and σ_v the velocity dispersion (e.g Stone et al. 1998). This assumption has been confirmed from numerical simulations (Mac Low et al. 1998; Stone et al. 1998; Padoan & Nordlund 1999). Thus the turbulence has to be replenished in order to provide the necessary support in this picture. It has been suggested that energy injection from massive protostars in the form of supernovae explosions, massive outflows and stellar winds can maintain the turbulence (Norman & Silk 1980; McKee 1989; Matzner 2002). However, Mac Low & Klessen (2004) argue that outflows from massive stars may dominate the driving locally but not globally. Other suggested energy sources include galactic rotation and galactic gravity (but see Mac Low & Klessen 2004).

In contrast to the quasi-static evolutionary model outlined above recent work suggests that MCs are transient, dynamical evolving, high density features produced by compressive motions in the diffuse ISM (Ballesteros-Paredes et al. 2006). At the largest scale, density waves in the spiral arms of the Galaxy may form giant molecular clouds while MCs at smaller scales might be formed from supersonic flows caused by supernovae. Large scale compressions

also seem capable of producing the internal turbulence observed in MCs (Ballesteros-Paredes et al. 2006, and references therein). In this picture the supersonic turbulence creates large density enhancements. Some of these are gravitationally unstable and collapse to form stars, some dissolve again. The lifetimes of clouds and cores within clouds are comparable to the free-fall time (Ballesteros-Paredes et al. 1999a, 2003; Hartmann 2003), but the star formation efficiency is low since collapse on the global scale is prevented (Ballesteros-Paredes et al. 2006).
These two views represent the extremes of models of star formation. In the first model, the cloud evolves in a slow, quasi-static manner. The cloud gradually becomes more centrally condensed, either through ambipolar diffusion (Shu et al. 1987; Mouschovias 1991) or dissipation of the turbulence (Myers 1998) or a combination. At some stage collapse sets in and fragmentation of the cloud into smaller cores is likely (Shu et al. 1987). In the other model the MCs are not in quasi-static equilibrium but highly dynamic and the timescale of star formation is short.

1.1.2 Properties of dense cores

Dense cores within molecular clouds are the actual sites of star formation. Dense cores are generally defined, as the name suggests, as regions in a molecular cloud which are over-dense compared to the surroundings. Dense cores come in two species, starless and protostellar. A starless core contain no evidence of hosting a protostar, while protostellar cores harbours either a Class 0 or Class I object (see Sect. 1.1.5). A starless core which is gravitationally bound is often called prestellar (Ward-Thompson et al. 2006).

Density fields

Low mass dense cores in molecular clouds are found to have radial column density profiles resembling those of Bonnor-Ebert spheres (Alves et al. 2001; Lada et al. 2006). A Bonnor-Ebert sphere is an isothermal ball of gas in which the internal pressure balances self-gravity and external surface pressure (Lada et al. 2006). The shape of the density profile of the Bonnor-Ebert sphere is characterized by a single parameter, ξ_{max}, and each solution corresponds to a truncation of the infinite isothermal sphere at a different radius. The higher the value of ξ_{max} the more centrally concentrated the cloud is (Lada et al. 2006). Bonnor (1956) and Ebert (1955) showed that the gas cloud is in a state of unstable equilibrium when $\xi_{max} > 6.5$. A number of starless cores have been examined (see the recent review by Lada et al. 2006) which display values of ξ_{max} on both sides of and close to the critical value. Lada et al. (2006) argue that these cores are relatively stable and the thermal pressure

provides significant support against gravity. Thus the cores should be long-lived.
The apparent stability of cores is in contrast to the dynamical model where cores are formed by supersonic compressions and their lifetimes are of the order of a few free-fall times (Nakamura & Li 2005; Vázquez-Semadeni et al. 2005). However using non-magnetic numerical simulations Ballesteros-Paredes et al. (2003) showed that Bonnor-Ebert like column density profiles may be found in rapidly-evolving cores produced by supersonic turbulent compression. Thus Bonnor-Ebert spheres may appear in transient objects and do not necessarily imply a long-lived, quasi-static state.

Core lifetimes

The lifetimes of cores in different evolutionary states can be estimated observationally by counting the number of cores in each state. The timescale of cores surviving against collapse is usually extrapolated from the typical lifetimes of Class I or II sources (Sect. 1.1.5, Ward-Thompson et al. 2006). Observational results were recently collected in Ward-Thompson et al. (2006) who showed that all of the observed timescales of cores are longer than the free-fall time by a factor of 2-5 in the density range of $10^4 - 10^5 \mathrm{cm}^{-3}$, that is, longer than implied in the turbulent model. The timescales are, however, too short for the cores to be supported by large magnetic fields, as discussed below. Ward-Thompson et al. (2006) suggest that models lying between the quasi-static picture and the model of transient, turbulence dominated cores are more appropriate, that is, models with some level of turbulent support and some level of support from magnetic fields.

Magnetic fields

The influence of magnetic fields is very important for distinguishing between different models. In models where the cloud is supported by magnetic fields we talk about magnetically critical clouds or cores. A critical core is defined as one in which the magnetic energy density exactly balances the gravitational potential energy (e.g. Ward-Thompson et al. 2006). If the magnetic field is too weak to provide support against gravity, the core is super-critical and collapse occurs on the free-fall time in the limit. If the field is stronger than necessary for support the core is sub-critical.
The magnetic field is only coupled to the ions in the gas, which means that neutral matter can be driven through the field by gravity. Eventually the density in the core will increase enough to turn a sub-critical core into a super-critical and collapse will proceed (e.g. Shu et al. 1987; Ward-Thompson et al. 2006). The timescale, τ_{AD}, for this process, known as ambipolar diffusion, is

proportional to the ionisation fraction. For highly sub-critical clouds τ_{AD} is roughly ten times the free-fall time (Nakano 1998).
The magnetic fields have been studied in five, isolated prestellar cores (for comparison see Ward-Thompson et al. 2006) showing that turbulence and magnetic fields provide an equal amount of energy for the support against collapse and thus play an equal role in the evolution of cores. However, the observational determination of the relative importance depends on the assumed geometry of the clouds. Numerical simulations suggest that the role of the magnetic field depends on whether the turbulence is being driven or is decaying. Vázquez-Semadeni et al. (2005) found low star formation efficiencies, $\leq 5\%$, in super-critical clouds in driven simulations while Nakamura & Li (2005) showed that such low efficiencies are only found in magnetically sub-critical clouds in simulations of decaying turbulence.

Velocity fields

Molecular line profiles can be used as tracers of kinematics inside cores. For a recent review see Di Francesco et al. (2006). Internal velocity gradients of 1-2 $\mathrm{kms^{-1}pc^{-1}}$ have been observed and interpreted both in terms of rotation and more complex motions (e.g. Barranco & Goodman 1998; Caselli et al. 2002). Furthermore, line profiles have been used to detect inward motions in cores (e.g. Lee et al. 1999, 2004). Some data show infall motions over an extended region (Tafalla et al. 1998) which is inconsistent with "inside-out" collapse (Shu et al. 1987).
Low mass dense cores typically have trans- or subsonic non-thermal line widths, that is, low levels of turbulence (Jijina et al. 1999). This is consistent with the turbulent model and a consequence of the size-line width relation (see Sect. 1.1.1). The relation $\Delta v \propto R^{\alpha}$ with $\alpha \sim 0.5$ implies that velocity differences across regions smaller than 0.05pc are subsonic (Ballesteros-Paredes et al. 2006). Goodman et al. (1998), however, found nearly constant line widths at scales less than 0.1 pc in some cores contradicting the size-line width relation.

Mass distribution

Recently it has been found that the distribution of core masses, the core mass function (CMF), is very similar to the stellar initial mass function (IMF) (Testi & Sargent 1998; Motte et al. 1998). This suggests that the IMF is a direct consequence of the CMF which is again determined directly by the fragmentation of turbulent clouds. Simulations of turbulence have also found that the IMF is directly related to the distribution of self-gravitating clumps generated by turbulent interactions (Padoan & Nordlund 2002).

The theory of identifying the CMF with the IMF assumes that there is a 1-1 mapping of cores to stars. That is, that the final mass of the star is proportional to the mass of the core. This is however not certain. Simulations for example show that cores generally produce more than one star and that the CMF may change with time as cores merge with each other (Ballesteros-Paredes et al. 2006, and references therein). Thus the relation of the IMF to the CMF is not settled yet.

1.1.3 Isolated versus clustered star formation

The evolution of a cloud core depends on its environment. Winds and outflows from young stars may have a profound impact on the surrounding medium. The model of triggered star formation by Elmegreen & Lada (1977) suggests that shock and ionisation fronts from young stars can compress the surrounding gas and initiate collapse (see also Fig.1 in Lada 1987). Evidence of such sequential star formation is for example seen in the ρ Oph MC (Loren 1989). The outflows may however also have a disruptive effect on their immediate surroundings, dispersing the core very quickly and preventing further star formation (Briceno et al. 2006). Numerical studies indicate that the outcome of a shock impacting on a core mainly depends on the type of shock (C-type or J-type, see Sect. 1.3.1) and the velocity. Shocks with velocities of 15-45kms^{-1} can induce collapse while shocks travelling faster than 50kms^{-1} tend to destroy the cores (see the review of Briceno et al. 2006).

The majority of stars in the Galaxy are formed in OB associations, which are clusters of stars around blue luminous O or B stars (Briceno et al. 2006). Star formation in such dense clusters may also be influenced by dynamical interactions of stars. Close encounters can truncate or disrupt the accretion disk (see Sect. 1.1.5) and thereby change the final mass of the protostar and influence the protostars ability to create a planetary system (Ballesteros-Paredes et al. 2006, and references therein). Close encounters or stellar mergers may also trigger outflow events as suggested for outflows in Orion (Tan 2004; Bally & Zinnecker 2005).

Dense cores in clusters are observed to have higher masses and column densities than isolated cores (Jijina et al. 1999). Prestellar cores in clusters (in ρ Oph and Serpens cores) have densities of $10^6 - 10^7$cm^{-3} and are more compact with diameters of 0.02-0.03 pc (e.g. Motte et al. 1998; Testi & Sargent 1998; Johnstone et al. 2000) compared to isolated cores which have $n = 10^5$cm^{-3} and $D = 0.1$ pc in Taurus (Onishi et al. 2002). This could imply a different formation mechanism for cores in isolated and clustered regions, with the latter formed by fragmentation of higher-mass, more turbulent cores (Ward-Thompson et al. 2006).

1.1.4 Observational properties of Class 0

The prestellar cores and at least some of the starless cores are expected to evolve into Class 0 objects (André et al. 1993) and subsequently Class I protostars. Class 0 objects are invisible in the near-infrared and are mainly distinguished from prestellar cores by indirect evidence of a central young stellar object. Such evidence can be the detection of a compact centimeter radio continuum source, a collimated CO outflow or an internal heating source (André et al. 1993). Class 0 protostars display a more centrally condensed density profile than the prestellar cores (Motte & André 2001). The luminosity of these young sources is associated with the accretion luminosity created by material falling onto the central object (Shu et al. 1987). Class 0 sources are defined by a high ratio of sub-millimeter ($\lambda > 350\mu$m) to bolometric luminosity, suggesting that the mass of the envelope exceeds the central stellar mass (André et al. 1993). Thus they are likely to be very young protostars in which a hydrostatic core has formed but not yet accumulated the majority of its final mass (André et al. 2000). Models show that the mass infall rate peaks during the Class 0 stage and is generally a varying function of time (e.g. Henriksen et al. 1997; Schmeja & Klessen 2004). The mass infall rate of an isolated Class 0 object in Taurus (IRAM 04191) has been estimated to $\dot{M} \sim 3 \times 10^{-6}\,\mathrm{M}_\odot\,\mathrm{yr}^{-1}$ (Belloche et al. 2002). In clustered regions higher infall rates are found in Class 0 protostars, $\dot{M} \sim 10^{-4} - 10^{-5}\,\mathrm{M}_\odot\,\mathrm{yr}^{-1}$ (e.g. Ceccarelli et al. 2000; Di Francesco et al. 2001). The spectral energy distribution is described by a modified single-temperature blackbody with a bolometric temperature of T<70 K (Ciardi et al. 2003, see Fig. 1.1). Direct evidence of gravitational infall has been reported for several Class 0 object (see André et al. 2000).

1.1.5 Evolution towards ZAMS

The early phases of star formation are difficult to observe because the protostar is buried in the gas of its parental core. Based on the observed differences in the spectral energy distributions (SEDs, see Fig. 1.1) at near/mid-infrared wavelengths a theoretical evolution sequence (Class 0 $\rightarrow$ Class I$\rightarrow$ Class II $\rightarrow$ Class III) has been proposed for isolated young stars. Class 0 stars described above are cloud cores just beginning their collapse. Stars in Class I to III are distinguished based on the slope of the SEDs between 2.2μm and 10-25μm, $\alpha_{IR} = d\log(\lambda F_\lambda)/d\log(\lambda)$ (Lada 1987). Class I stars have $\alpha_{IR} > 0$. They are embedded in the circumstellar envelope of infalling material. The central protostar is surrounded by an accretion disk on which the infalling gas accumulates before being channeled onto the star. Class II stars are characterized by $-1.5 < \alpha_{IR} < 0$. They are nearly fully assembled stars undergoing

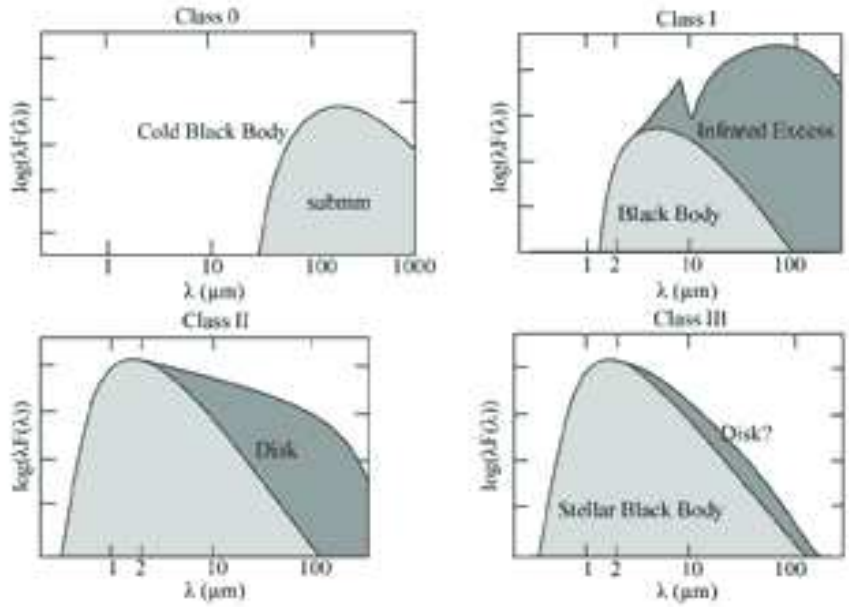

Figure 1.1: Sketch of the evolution of the spectral energy distribution in Class 0 to Class III protostars (Lada 1987).

pure disk accretion. Class III stars ($\alpha_{IR} < -1.5$) have stopped the accretion but have not yet reached the zero-age main-sequence (ZAMS) (White et al. 2006). Class II and III are also known as T-Tauri stars.
It is believed that the main part of the final stellar mass is accreted during the Class 0 and I stages. During the accretion process material is expelled in a bipolar jet/outflow. The outflow is very powerful during the Class 0 stage, while Class I objects tend to have much less powerful outflows (André et al. 2000).

1.1.6 Molecular outflows

Outflows from protostars can accelerate entrained gas and thereby create a molecular outflow. Molecular outflows have been observed from stars with a wide mass-range, from low mass protostars to early B-stars (see the review by Arce et al. 2006, and references therein). There is strong evidence for protostellar jets being powered by accretion disks with an outflow rate of $\sim 10\%$ of the infall rate (Königl & Pudritz 2000). Magnetic field may help to launch and collimate the outflow (see Pudritz et al. 2006). From low mass stars the outflows typically extend over 0.1-1 pc with velocities of 10-100kms^{-1} and outflow mass flux of $\sim 10^{-6}$M$_{\odot}$yr^{-1}. Observations suggest

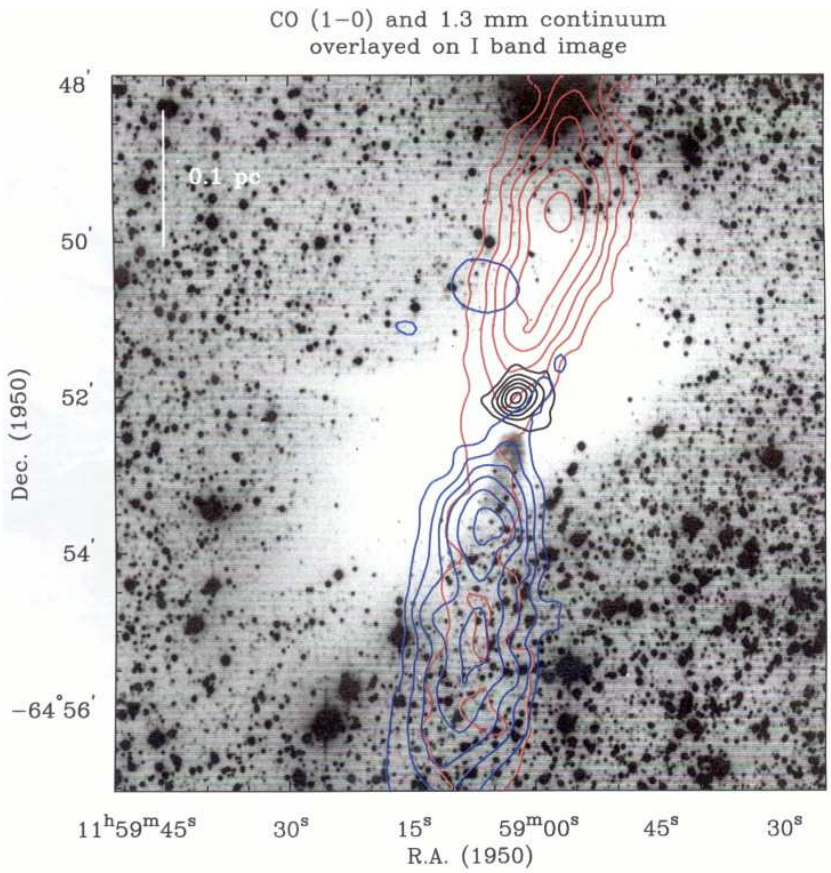

Figure 1.2: CO outflow from BHR71. The blue contours represent the blue outflow lobe, the red contours the red outflow lobe, and the black contours the 1.3 mm continuum emission. From Bourke et al. (1997).

that the ejection is episodic in young outflows. This could be explained by variations in the accretion rate resulting in variations of the outflow velocity (Arce et al. 2006). The degree of collimation of the outflow decreases as the source evolves (Lee et al. 2002). Young outflows are highly collimated while older outflows display larger opening angles pointing towards a wind-driven outflow.

Outflows from B-stars have mass outflow rates of $10^{-5} - 10^{-3} M_{\odot} yr^{-1}$. Both collimated and poorly collimated outflows are observed. O stars generate powerful winds with opening angles of about 90° within 50 AU of the star. An example is radio source I in OMC1 observed from SiO masers to have a wide-angle bipolar outflow emerging from an edge-on disk (Greenhill et al. 2004b). This outflow is also described in Sect. 1.4. The resulting molecular outflow from O-stars can have even larger opening angles (Arce et al. 2006, and references therein). As for low mass sources the poorly collimated flows

are seen in more evolved sources. An example of a highly collimated outflow from BHR71 is shown in Fig. 1.2. The driving source of this outflow is classified as a Class 0 object (Bourke et al. 1997).

Models of molecular outflows

Models of molecular outflow formation can be divided into four groups (Cabrit et al. 1997): (i) wind-driven shells where a wide-angle wind blows into the ambient material and forms a shell of swept-up material. (ii) jet-driven bow shocks in which a highly collimated jet propagates into the surrounding medium and produces an outflow shell around the jet. (iii) jet-driven turbulent flows in which Kelvin-Helmholtz instabilities along the boundary of the jet and ambient material lead to the formation of a turbulent layer through which the surrounding gas is entrained. Eventually the whole flow becomes turbulent. (iv) infalling gas deflected away from the star. According to Cabrit et al. (1997) the most promising models are those of wind-driven shells and jet-driven bow shocks. However, while the models of jet-driven bow shocks can reproduce the observed features of collimated outflows, they have difficulty reproducing the poorly collimated outflows. Wind-driven shells can explain large opening angles but fail to reproduce discrete bow shock features. Thus a model which combines both jets and winds may be the solution (Arce et al. 2006).

Impact on the surrounding environment

Outflows inject momentum and energy into the surrounding molecular cloud at distances ranging from a few AU up to tens of parsecs from the source. Young outflows have a strong impact on the circumstellar envelope, within 10^4 AU of the source, entraining the gas along the outflow axis (Arce & Sargent 2005). The wide-angle outflows observed in Class I sources may clear out the envelope and constrain the infalling gas to a limited region outside the outflow lobes (Velusamy & Langer 1998; Arce & Sargent 2004). Thus outflows have a profound influence on the accretion and subsequently the final mass of the protostar.

At larger distances outflows may also influence the parental core, that is, the dense gas within 0.1 to 0.3 pc of the protostar. Outflows has been proposed to be a major source of the turbulence in cores (Zhang et al. 2005). The kinetic energy of outflows are comparable to the gravitational binding energy of the core, suggesting that outflows may disperse the entire cloud (Tafalla & Myers 1997). However, winds impacting on dense clumps may trigger collapse and accelerate star formation, as discussed in Sect. 1.1.3.

Outflows from groups or clusters of stars interact with a substantial part

of their parent molecular cloud and may be an important source of energy for driving of the turbulence inside clouds (Mac Low & Klessen 2004), as described in Sect. 1.1.1.

1.2 Turbulence

Even if controversy still remains about how exactly turbulence influences the star formation process it is clear that turbulence is very important. In Chapters 5 to 7 we will study the effects of turbulent motions in the star forming region OMC1 and thus a brief overview of the concepts of turbulence and especially interstellar turbulence is given here. The literature is very large, but comprehensive reviews can be found in Elmegreen & Scalo (2004) and Mac Low & Klessen (2004). Furthermore, Davidson (2004) provide a very good and intelligible textbook on the subject of turbulence.
The theory of the interstellar medium being dominated by turbulent motions was already formulated by von Weizsäcker (1951). He stated that the interstellar gas is moving in a turbulent and compressible manner abiding by the laws of hydrodynamics and that there is a hierarchy of clouds. Large clouds consist of a number of smaller clouds, which again consists of a number of even smaller clouds and so on. This self-similarity of structures is in fact observed in molecular clouds (e.g. Fig.2 in Falgarone et al. 1992).

1.2.1 General concepts

The motion of gasses or fluids are dictated by external forces acting on the fluid particles and changes in the pressure forces and viscous forces. The Navier-Stokes equations give a dynamical statement of the balance of these forces. The general form of the Navier-Stokes equations are (Davidson 2004):

$$\frac{\partial \rho}{\partial t} + \nabla \cdot (\rho \boldsymbol{u}) = 0 \tag{1.1}$$

$$\frac{\partial \boldsymbol{u}}{\partial t} + (\boldsymbol{u} \cdot \nabla)\boldsymbol{u} = -\frac{1}{\rho}\nabla P + \boldsymbol{F} + \frac{1}{\rho}\nabla \cdot \sigma \tag{1.2}$$

where $\rho, \boldsymbol{u}, P, \boldsymbol{F}$ are the mass density, velocity, pressure and force per unit mass, respectively, and σ is the shear stress tensor related to the viscosity. Eq. (1.1) expresses conservation of mass and Eq. (1.2) is the equation of conservation of momentum. In the latter the first term on the left is the ordinary time derivative in a fixed reference frame and the second term is the advection term, that is, the changes in velocity brought about by the moving fluid. The force term may for example involve gravity and magnetic fields. Coupled with the Maxwell equations the Navier-Stokes equation can

be used to describe magnetohydrodynamics (MHD). In incompressible fluids the density is constant. However, a gas is compressed when the velocity is larger than the velocity of sound, v_s, (von Weizsäcker 1951), that is, if the Mach number, $Ma = u/v_s > 1$. The Navier-Stokes equations can only be solved analytically for very simple situations, therefore theories of hydrodynamics and turbulence often use simple pictures, statistical tools and empirical relations found from experiments.

Turbulence is nonlinear motion resulting in the excitation of an extreme range of correlated scales (Elmegreen & Scalo 2004). Turbulence arises because the nonlinear advection term in Eq. (1.2) distort the velocity field by stretching, folding and dilating fluid elements (Elmegreen & Scalo 2004). The solutions to the Navier-Stokes equations are turbulent if the Reynolds number is larger than a critical value, which is in the order of ~ 1000 (von Weizsäcker 1951). The Reynolds number

$$Re = \frac{ul}{\nu} \tag{1.3}$$

is the ratio of inertial forces to viscous forces (Davidson 2004). Here u and l are the mean velocity and characteristic length scale of the flow, respectively, and ν is the kinematic viscosity. If the Reynolds number is large, the kinematic viscosity is low.

In his pioneering work Kolmogorov (1941) formulated a theory of incompressible turbulence based on dimensional arguments. His results capture the general behaviour of turbulence well, although corrections have been made subsequently. He assumed, that the turbulence is driven on a large scale, l, and forms eddies at that scale. An eddy is a partial volume of the fluid having a common motion for an interval of time (von Weizsäcker 1951). These eddies interact to form slightly smaller eddies, transferring some of their energy to the smaller scales. The smaller eddies form even smaller eddies and so on, until the energy has cascaded down to the dissipation scale, η. At this scale and only at this scale, the energy is dissipated as heat by means of the viscosity. The energy passed down in this energy cascade is $\dot{e} \sim u^3/l$. In order to maintain a steady state, equal amounts of energy must be transferred trough all eddie sizes, that is $\dot{e}$ must be independent of scale. Thus $u \propto l^{1/3}$ and $E \propto k^{-5/3}$, $k = l^{-1}$ (Davidson 2004). We emphasize that this model is non-dissipative between the driving scale, l, and the dissipation scale, η. The range $\eta < r < l$ is called the inertial range. In the inertial range the terms of the Navier-Stokes equation related to viscosity and forcing have little effect. The dynamical range of eddies from the largest scale, l to the smallest, η, scales with the Reynolds number, $l/\eta \sim Re^{3/4}$ (Davidson 2004).

1.2.2 Interstellar turbulence

Interstellar turbulence is rather more complicated than incompressible turbulence. It is highly compressible with Mach numbers up to as high as 50 in cold molecular clouds (Mac Low & Klessen 2004) and have energy injection at many scales from e.g. galactic rotation, supernovae explosion and protostellar outflows as mentioned earlier (Elmegreen & Scalo 2004). Furthermore, in supersonic turbulence energy may dissipate in shocks, which can transmit energy between widely separated scales (Mac Low & Klessen 2004). Therefore the concept of a direct non-dissipative cascade of energy from large scales to small scales is absent. It is not known how energy flows between scales in interstellar turbulence and in principle it could cascade in either direction (Elmegreen & Scalo 2004). Introducing a magnetic field gives a preferred direction of forces. MHD simulations show that the energy cascade is diminished in the direction parallel to the field (Müller et al. 2003). With all this in mind, we emphasize that an energy cascade from larger to smaller scales is usually assumed. This seems to be confirmed by observations of molecular clouds in which the energy spectrum has a power law shape resembling that of Kolmogorov, $E(k) \propto k^{-n}$, as described above.

1.2.3 Characterization of interstellar turbulence from observations

The turbulent velocity field fluctuates randomly in time and space and even though the Navier-Stokes equation is deterministic the velocity field is unpredictable. However the statistical properties of a turbulent flow are uniquely determined by the boundary conditions and the initial conditions (Davidson 2004) and can be used to make comparisons between observations, experiments and simulations. Using two-point statistics involving points separated by a specific lag (spatial vector or distance) observations of interstellar turbulence have been characterized by structure functions (Scalo 1984; Falgarone & Phillips 1990; Miesch & Bally 1994; Ossenkopf & Mac Low 2002; Padoan et al. 2003), autocorrelations (Scalo 1984; Kleiner & Dickman 1987; Spicker & Feitzinger 1988; Miesch & Bally 1994), power spectra (Stutzki et al. 1998; Plume et al. 2000) and Δ-variance (Stutzki et al. 1998; Bensch et al. 2001; Ossenkopf & Mac Low 2002). One-point probability distribution functions of centroid velocities that give no spatial information have also been used (Miesch & Scalo 1995; Miesch et al. 1999; Ossenkopf & Mac Low 2002). Furthermore, profiles of molecular emission lines have been used as estimates of the velocity probability distribution (e.g. Falgarone et al. 1992; Pety & Falgarone 2003).

The density of neutral gas seems to be correlated over a range of scales

from sub-parsec to hundreds of parsec. The energy spectra, $E(k) \propto k^n$, have power-law slopes of -1.8 to -2.3 (see Elmegreen & Scalo 2004, and references therein). Structure functions, $< |\Delta v|^2 > \propto r^\beta$, and the associated size-line width relation, $\Delta v \propto r^\alpha$, (Larson 1981) generally show power law behaviour, but there is significant variation in the exponents between regions (see Elmegreen & Scalo 2004, and references therein). Such regional variations are difficult to explain in the context of conventional turbulence and should be investigated. Structure functions and the probability distribution function of velocities will be used in this thesis to characterize the velocity field in OMC1. Observational, numerical and experimental results based on these functions will be more properly described in the relevant sections (Sects. 5.3 and 5.4)

1.2.4 Self-similar structure or characteristic scales?

The self-similarity of structures associated with the observed power law shape of the energy spectra and structure functions, as described above, must break down at smaller scales when self-gravity and star formation become important. As described earlier, turbulence creates local clumps of dense gas and this process may give rise to large density contrasts (e.g. Padoan & Nordlund 2002). Star formation takes place locally in the densest clumps (Elmegreen & Scalo 2004; Ballesteros-Paredes et al. 2006). The predominantly turbulent era, characterised by lack of preferred scale, is then expected to end when gravitation becomes dominant in clumps. At this stage, certain scales may be over-populated or under-populated relative to the model of a simple Kolmogorov-type cascade (Kolmogorov 1941; Frisch 1995). Hence, the density and velocity fields will contain characteristic scales. The range of scales, at which clumps become gravitationally bound and turbulence looses its kinematically dominating effect, is important for both theories of star formation and of turbulence.

The energy being injected into clouds from different sources acting on different scales will also impose characteristic scales on the medium. These scales may be associated with sources, mentioned above, such as supernovae explosions injecting energy at the cloud size, outflows from massive stars acting at the tens of thousands of AU scale or outflows from low mass protostars at scales of a few thousand AU (Mac Low & Klessen 2004; Elmegreen & Scalo 2004). In order to understand the evolution of molecular clouds it is essential to identify the presence of these energy injection processes and the scales at which they occur.

In Chapter 8 we use three different methods to show that the structure of OMC1 is not self-similar and to determine the sizes of the characteristic scales. One of the methods, the structure function technique, was devel-

oped specifically for this thesis and show great improvement in sensitivity compared to existing methods.

1.2.5 Simulations of interstellar turbulence

Observational methods only obtain line-of-sight motions in 2-dimensional maps, projected in the plane of the sky. Thus numerical simulations solving the hydrodynamical or MHD equations provide the only means to observe interstellar turbulence in action and to obtain the 3-dimensional density and velocity structure. However, the results from simulations depend crucially on the physical processes included, how the forcing, if any, is implemented, the initial conditions and the spatial resolution. Thus care should be taken both when comparing simulations to other simulations and when comparing simulations with observations. Nevertheless, our understanding of turbulence has gained significantly from simulations in the last decade or two (see references in Elmegreen & Scalo 2004). Some of the results have already been mention in Sect. 1.1.

The dynamical range of turbulence scales, as seen above, with the Reynolds number, $l/\eta \sim Re^{3/4}$. In order to resolve a turbulent flow properly simulations need as least as many grid points as l/η in each dimension (Frisch 1995). Thus with todays computer power simulations are limited to much lower Reynolds numbers than found in molecular clouds ($\sim 10^5 - 10^7$ Miesch et al. 1999; Elmegreen & Scalo 2004).

Using simulations it has been found that supersonic turbulence decays in a crossing time, l/σ_v, regardless of magnetic fields (Mac Low et al. 1998; Stone et al. 1998). Furthermore simulations have shown clouds to be transient entities (Ballesteros-Paredes et al. 1999b) that form stars rapidly (Elmegreen 2000). The details of shock dissipation seem to depend on whether the turbulence is decaying or being driven. Smith et al. (2000a,b) found that the energy dissipates in a large number of weak shocks at low Mach numbers in simulations of decaying turbulence, while the dissipation occurs in a small range of fast shocks in simulations where the turbulence is driven by energy injections. Simulations with and without self-gravity show that turbulence can suppress global collapse of a cloud by transferring the turbulent energy to motions of substructures at smaller scales. Local collapse will occur in the densest of these substructures (Nordlund & Padoan 2003; Bate et al. 2003; Bonnell et al. 2003).

Both simulations and observations suffer from limitations. The observations do not yield the 3D structure and the simulations do not include all the relevant physics. Only by a close interplay between both theory and observations can we hope to uncover the mechanisms of interstellar turbulence. This approach is exactly what is used in this thesis. First we derive the statistical

properties of the velocity field in OMC1 (Chapter 5) and then test if this can be reproduced by a set of hydrodynamical simulations (Chapter 7).

1.3 The H_2 molecule

The observations presented in this thesis are all of rovibrationally excited molecular hydrogen. Therefore we give a brief description of the molecule and its excitation mechanisms.
The H_2 molecule is the most abundant molecule in the Universe and in molecular clouds. It can be rotationally and vibrationally excited, but since H_2 is a homonuclear molecule it has no permanent dipole moment and spontaneous emission occurs through weak quadrupolar transitions. The purely rotational transitions ($\Delta J = \pm 2$, $\Delta v = 0$) are extremely weak and because H_2 is a light molecule the rotational constant is large. Even the lowest rotational transitions are therefore very energetic (located in the MIR) and cannot be collisionally excited at the cold temperatures ($\sim$ 10K) of molecular clouds. Pure rotationally excited H_2 is used as a tracer of the warm interstellar medium (e.g. Falgarone et al. 2005). Cold hydrogen is rarely detected directly.
The rovibrational levels of H_2 may be populated (see below) by collisions in dense gas heated by shocks (e.g. Gautier et al. 1976; Kwan 1977), by ultraviolet radiation (Black & van Dishoeck 1987; Sternberg & Dalgarno 1989; Störzer & Hollenbach 1999) and in the H_2 formation process (Black & Dalgarno 1976; Black & van Dishoeck 1987; Hornekær et al. 2003; Amiaud et al. 2006, and A. Baurichter, private comm.). The selection rule for quadrupolar rovibronic transitions is:

$$\Delta J = \begin{cases} -2 & \text{S-branch} \\ 0 & \text{Q-branch} \\ 2 & \text{O-branch} \end{cases}$$

where J denotes the rotational quantum number. There is no selection rule on the vibrational quantum number. Rovibrational transitions are located in the infrared part of the spectrum. Lifetimes are typically in the order of $10^6 - 10^7$s (Wolniewicz et al. 1998) which is long compared to molecules with dipole transitions. However since H_2 is over abundant by a factor of 10^4 compared to other molecules, H_2 emission is relatively bright. A transition is denoted by first writing the vibrational transition and then the relevant branch and the lower level of the rotational transition. The observations reported in this thesis are mainly based on the transition $v = 1 - 0$ S(1), i.e. from J=3, v=1 to J=1, v=0.

1.3.1 Near-Infrared Excitation mechanisms

Shocks

Shocks are, as mentioned above, one of the primary excitation mechanisms of H_2. A shock can be expressed as a "hydrostatic surprise" or more properly defined as "the propagation of an irreversible, pressure driven disturbance at a supersonic speed" (Draine 1980). At molecular cloud temperatures ($\sim$ 10 K) the velocity of sound is typically less than 1kms^{-1} and supersonic flows are readily observed. In the absence of a magnetic field neutral and charged particles behave as a single fluid and because the shock is moving at a supersonic velocity the gas in the pre-shock zone cannot receive information of the shock-front (Draine 1980). Thus the density, temperature, pressure and velocity will change very abruptly across the shock-front. This change may be treated as a discontinuity on the scale of the mean free path of the particles, which is of the order of 10^{-4} AU, and the shock is called a jump-type shock (J-type). The shock heats the gas and thus excites the molecules. As the post-shock gas cools by radiation the pressure remains constant and the density increases.
Introducing a magnetic field perpendicular to the direction of the shock front will, however, separate the neutral and charged particles so the gas becomes a multi-fluid medium (Draine 1980). The charged particles couple to the magnetic field, gyrating around the field lines. The neutral particles do not feel the magnetic field directly, but only through collisions with charged particles. A mechanical signal can now propagate at either the sound speed or at the Alfven velocity (Alfven 1950)

$$v_A = \sqrt{\frac{B^2}{\mu\rho}}$$

where B is the magnetic field strength, μ the mean molecular weight and ρ the density of either the neutral, the ions or the electrons. Since the ionisation fraction typically is very low the Alfven velocity of the ions can be much faster than the shock velocity. Thus information of the shock can propagate through the agency of the ions faster than the shock itself. The ions do not undergo any discontinuity since they are heated, compressed and accelerated before the arrival of the shock (Draine 1980). The signal is communicated to the neutrals through collisions with the charged particles. Consequently the neutral fluid is accelerated before the shock arrives and undergoes a velocity jump of a smaller amplitude. Such shocks are called J-shocks with magnetic precursor. If the magnetic field exceeds a critical value, which can only be derived analytically in adiabatic shocks, the discontinuity vanishes and the shock is continuous (C-type) (Draine 1980).

After the passage of the shock the medium cools down again through mainly H_2 emission. The cooling time is longer in a C-shock than a J-shock and the cooling time in a C-shock increases with the magnetic field strength. The cooling length, that is, the distance traveled by the shock wave in the cooling time, increases similarly with the magnetic field. C-shocks and J-shocks can be distinguished by comparison of temperatures and brightness of for example H_2 emission lines with numerical shock models (e.g. Draine et al. 1983; Pineau des Forêts et al. 1988; Wilgenbus et al. 2000; Flower et al. 2003). For shock velocities higher than 25-80kms^{-1}, depending on the density, H_2 will dissociate due to the temperature increase (Le Bourlot et al. 2002).
Shocks are evidently very important in molecular clouds. In regions dominated by supersonic turbulence most of the turbulent energy is dissipated in shocks (Elmegreen & Scalo 2004). Furthermore shocks can be generated by supernova explosions, stellar winds and by jets and outflows from young stars (Mac Low & Klessen 2004). The rapid heating and compression of the region involved trigger different processes that do not occur in the unperturbed gas. Processes such as molecular dissociation, endothermic reactions and dust grain disruption (Flower et al. 1996) alter the chemical composition of the shocked gas relative to the unperturbed gas (see Arce et al. 2006).

Photodissociation regions

Radiation fields around stars may be strong enough to dissociate molecules and ionize atomic hydrogen, producing H II regions. This is generally the case for O and B stars in which the effective temperatures exceed 10^4K. As the H_2 molecules closest to the star dissociate they form a zone of H atoms (Hollenbach & Tielens 1999). These atoms will be ionized if the radiation exceeds 13.6 eV. Thus PDRs are often overlaid by layers of H and H II. In high density regions self-shielding of H_2 become important and the H/H_2 transition zone can be sharp (Hollenbach & Tielens 1997). The photodissociation region (PDR) will eat its way into the molecular cloud. The expansion of the H II region stops when the number of ionizing photons is balanced by the number of recombinations, that is, at the Strömgren radius. In a PDR H_2 is electronically excited and decay to the ground state by fluorescence while populating the rovibrationally excited states (Black & Dalgarno 1976; Black & van Dishoeck 1987). This is a simplified picture focusing on H_2. In a real cloud the PDR will be layered with zones of other ionized and neutral atoms, such as C and C^+ and zones where molecules such as CO are dissociated (Hollenbach & Tielens 1999). The radiation field, G_0, is measured in units of the average interstellar flux between 6 eV $< h\nu <$ 13.6 eV of $1.6 \times 10^{-6}\,\mathrm{Wm}^{-2}$ (Habing 1968). The incident far-ultraviolet flux can range

from $G_0 = 1.7$ to $G_0 > 10^6$ near an O-star (Hollenbach & Tielens 1999).

1.4 Orion

The Orion giant molecular cloud is the closest region with ongoing massive star formation. Due to its proximity (460 pc) and brightness it is the most studied region on the sky and offers unique possibilities for studying star formation in detail. With hundreds of papers on Orion surfacing each year it is by no means possible to give credit to all. Here I will give a brief overview of the morphology of Orion, which will be focused on the BN-KL nebula in the OMC1 region.

A large proportion of all molecules discovered in space are present in Orion (van Dishoeck & Blake 1998) and many of them were discovered here (e.g. Jefferts et al. 1970; Wilson et al. 1970), including larger organic molecules (e.g. White et al. 2003). Large scale mapping of rotational transitions in CO show that the complex consists of two clouds, the Orion A and B clouds, which are connected by a bridge of low-level emission (Maddalena et al. 1986, see also Fig. 1.3). The two clouds cover about 50 deg^2 on the sky in total and the mass contained in each is $\sim 10^5\,M_\odot$ (Maddalena et al. 1986). The molecular cloud complex was reviewed in Genzel & Stutzki (1989).

OMC1 is a region with prominent molecular emission near the Orion Nebula in the Orion A cloud (see Fig. 1.3). The whole A cloud has a clumpy or filamentary structure. Bally et al. (1987) identified over 100 condensations with typical length scales of 0.8 to 1.5 pc and masses of tens to hundreds of $M_\odot$. The OMC1 region is one of these filaments. The molecular ridge in OMC1 consists of individual clumps with sizes of $\sim$0.05 pc and densities of $> 10^5\,cm^{-3}$ (Ziurys et al. 1981; Mundy et al. 1986).

The Orion Nebula (M42) is an HII region excited by the Trapezium stars. Clustered around the Trapezium stars are lower mass members of the Orion Nebula Cluster (ONC). ONC consists of about 3500 stars (Hillenbrand & Hartmann 1998) with ages of less than a few times 10^6yr (Herbig & Terndrup 1986). The central density in the ONC is $\sim 2 \times 10^4\,stars\,pc^{-3}$, which is about twice as dense as other clusters (Hillenbrand & Hartmann 1998). Blaauw (1964) suggested that ONC is the youngest site in a sequence of star formation in the Orion OB1 associations.

ONC is located in front of the molecular cloud. The O and B stars of the Trapezium (especially θ^1 Ori C) create a compact HII region around them and it is believed that the ionisation front eats its way into the molecular cloud (Zuckerman 1973) as described in Sect. 1.3.1. The radiation field of θ^1 Ori C is $G_0 = 2 - 3 \times 10^5$ (Störzer & Hollenbach 1999). Wen & O'Dell (1995) created a 3-dimensional model of the ionisation front, see Fig. 1.4.

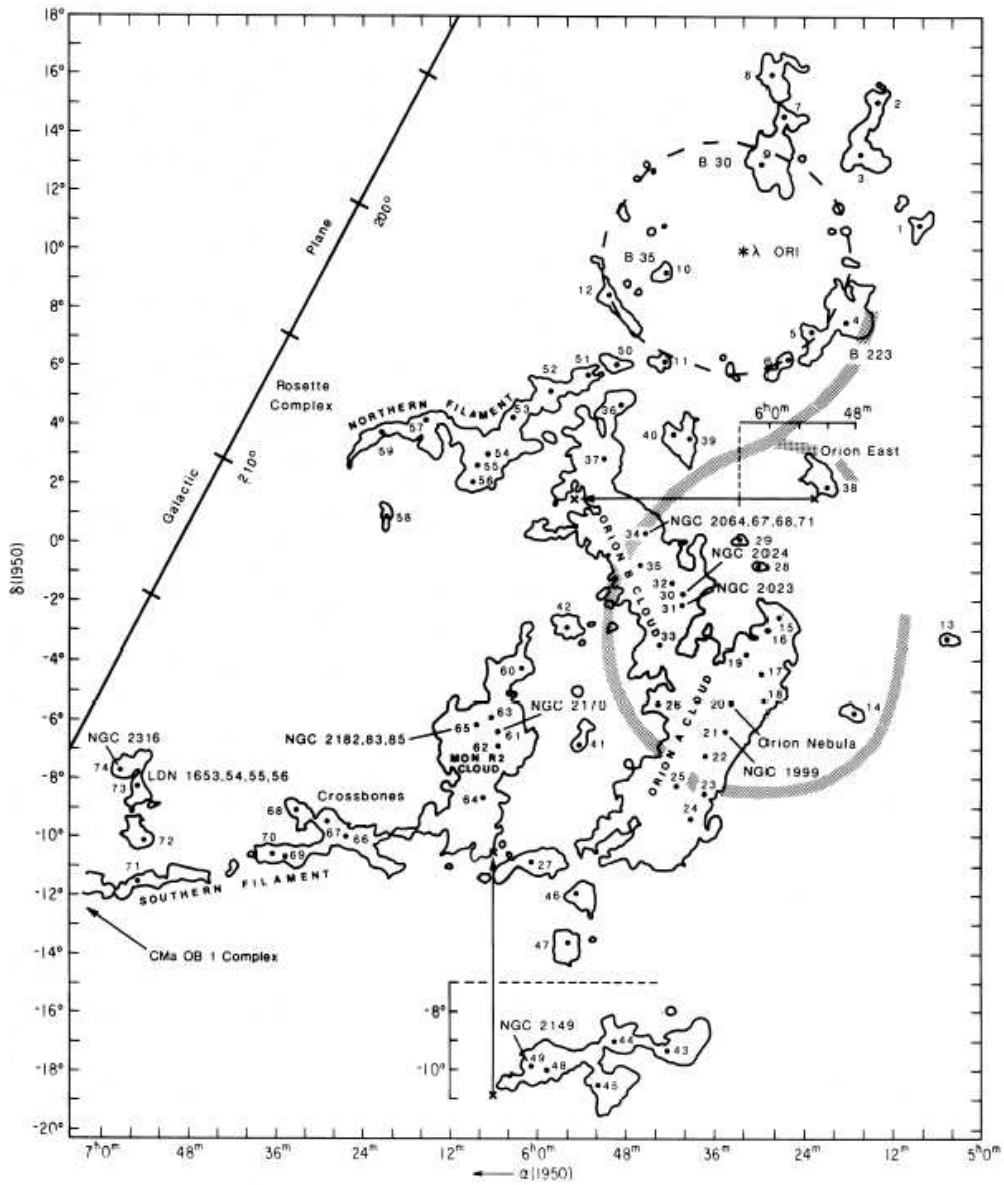

Figure 1.3: Schematic diagram of the large scale distribution of molecular clouds in Orion. From Maddalena et al. (1986).

θ^1 Ori C lies about 0.2 pc in front of the molecular cloud and the BN-KL infrared nebula is located near the surface of the cloud (Zuckerman 1973; Wen & O'Dell 1995). The Orion Nebula is reviewed in O'Dell (2001).
Bright ionisation fronts surrounding circumstellar disks (proplyds) (e.g. O'Dell et al. 1993; Bally et al. 2000) and circumstellar disks in silhouette (McCaughrean & O'Dell 1996; Bally et al. 2000) have been observed around many young stars in the ONC. Microjets extending 500 to 3000 AU with width of 20 to

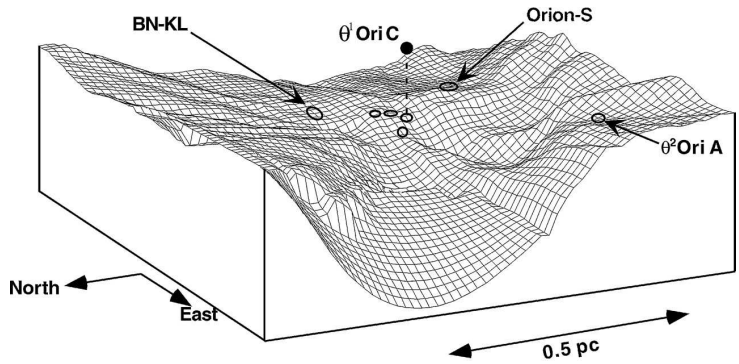

Figure 1.4: 3-dimensional model of the surface of OMC1 and the PDR from θ^1 Ori C. From O'Dell (2001).

200 AU are detected around a number of low mass sources in the cluster (Bally et al. 2000).

1.4.1 The BN-KL region

The Becklin-Neugebauer object (BN), at the heart of OMC1, is located approximately 45″(0.1 pc) north of the Trapezium stars. It was first discovered by Becklin & Neugebauer (1967) and has since been observed at all wavelengths, ranging from radio to X-rays (e.g. Churchwell et al. 1987; Wright et al. 1996; Garmire et al. 2000; Doi et al. 2002; Grosso et al. 2005). Brα emission, which implies a central star with effective temperature $> 10^4$ K, was first detected by Grasdalen (1976). BN has been identified as a B3 star, with L= 2500 $L_\odot$, deeply embedded in the molecular cloud behind material of visual extinction, A_V = 17mag (Gezari et al. 1998). The Kleinman-Low infrared nebula (Kleinmann & Low 1967) is located south of BN and has been found, from increasingly higher resolution studies, to consists of an increasing number of different sources, see below (e.g. Rieke et al. 1973; Gezari et al. 1998; Greenhill et al. 2004a; Shuping et al. 2004). A high resolution image of the infrared emission is shown in Fig. 1.5. The entire infrared nebula system is often referred to as the BN-KL nebula.
The Orion hot core is a warm (T> 220 K), dense (n$\sim 5 \times 10^7$ cm^{-3}) (Morris et al. 1980) cloud in the SE region of the KL-nebula (Fig. 1.5). It was first observed in ammonia emission by Morris et al. (1980). Extending from the hot core in the NE-SW direction is the dense ridge which is associated with a low velocity outflow of $\sim$ 18kms^{-1} (Genzel et al. 1981; Wright & Plambeck 1983; Wright et al. 1996). An massive outflow of high velocity and shocked gas extends to the NW and SE of BN (see below, Beckwith et al. 1983; Genzel & Stutzki 1989)

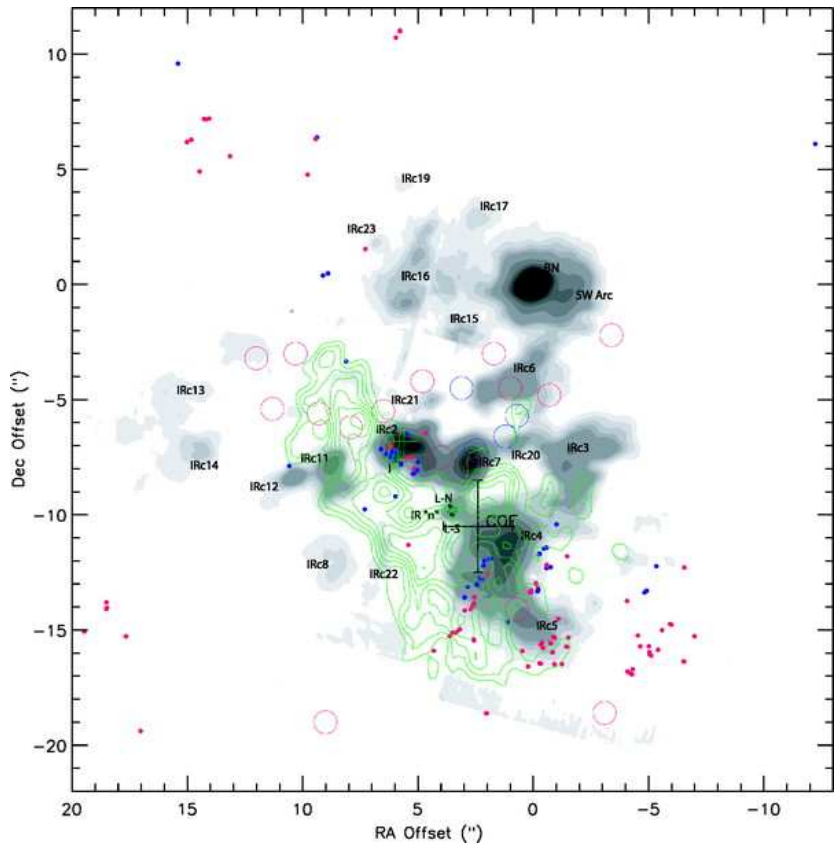

Figure 1.5: Map of 12μm emission in the BN-KL region (grey scale, Shuping et al. 2004) overlaid with NH_3 emission tracing the hot core (green contours, Wilson et al. 2000), H_2O masers (filled circles, Genzel et al. 1981; Gaume et al. 1998) and OH maser clusters (open circles, Johnston et al. 1989). From Shuping et al. (2004)

.

What is powering BN-KL?

The structure of the infrared emission in BN-KL is most probably determined by a few self-luminous high mass sources embedded in a very clumpy environment. There is an on-going debate on how many massive stars are present and which are powering the IR luminosity and the outflows. Possible origins of the high velocity outflow in the NW-SE direction is described in the next subsection.

The strong radio continuum from source I, see Fig. 1.5, (Churchwell et al. 1987; Menten & Reid 1995) indicates that it is very luminous, $L = 5 \times 10^3 - 10^4 L_\odot$ (Menten & Reid 1995; Beuther et al. 2004), however an IR counterpart has not been detected at wavelengths as long as 22μm (Greenhill et al. 2004a). This suggests that the emission is blocked in the Orion hot core by dust with

an optical depth of more than 300 at 22μm (Greenhill et al. 2004a). SiO masers and H_2O "shell" masers (Gaume et al. 1998) are centered on source I (Menten & Reid 1995; Gaume et al. 1998; Greenhill et al. 2004b) tracing a wide-angle bipolar outflow (Greenhill et al. 2004b). SiO maser emission show evidence of a disk around source I in the NW-SE direction (Greenhill et al. 2004b). Nissen et al. (2006) found a H_2 outflow with velocity of $\sim 18\text{kms}^{-1}$ in the NE-SW direction believed to be the IR counterpart of the outflow from source I.
IR source n (Fig. 1.5) is another candidate for powering the BN/KL region. A circumstellar disk with rotation axis oriented NE-SW has been identified in MIR emission (Shuping et al. 2004; Greenhill et al. 2004a). OH and a complex of H_2O masers trace a cavity produced by outflows (Johnston et al. 1989; Shuping et al. 2004) with center of expansion near source n (Menten & Reid 1995). A bipolar outflow from source n in the NE-SW direction perpendicular to the disk could be responsible for these masers (Shuping et al. 2004). Thus, the low velocity outflow mentioned above could originate in either source I or source n. However, the luminosity of source n might be relatively low, $L \sim 2000 L_\odot$ (Greenhill et al. 2004a), compared to source I.

IRc2 north of source I is also believed to be a powerful source. It is seen to consist of five compact sources at 3.8μm and MIR wavelengths (Dougados et al. 1993; Shuping et al. 2004; Greenhill et al. 2004a). If all five knots (A-E) are embedded protostars the total IR luminosity for IRc2, $L = 1000 \pm 500 L_\odot$, implies that the masses would be in the $3-8 M_\odot$ range (Shuping et al. 2004). This requires an unusually high density.
In all events it is not clear which source dominate the IR luminosity or which powers the outflows observed in the region.

The H_2 outflow

Gautier et al. (1976) discovered H_2 emission in the BN-KL nebula and Beckwith et al. (1978) resolved the H_2 emission around BN into two main peaks; Peak 1 north of BN and Peak 2 south-east of BN. The H_2 emission is mainly produced by shocks (see Sect. 1.5.1) and traces an outflow from one of the high mass sources in the BN-IRc2 complex (Fig. 1.6).
Fast moving HH objects in Peak 1 were first discovered by Axon & Taylor (1984) in the optical. Proper motion studies conducted with the Hubble telescope show that these HH objects move with velocities of several hundred kms^{-1} (Lee & Burton 2000; Rosado et al. 2001; Doi et al. 2002). Allen & Burton (1993) associated the HH-objects with H_2 streamers or "fingers", closely resembling bowshocks. [FeII] emission associated with dissociative shocks is found at the tip of almost all fingers. Allen & Burton (1993) refer

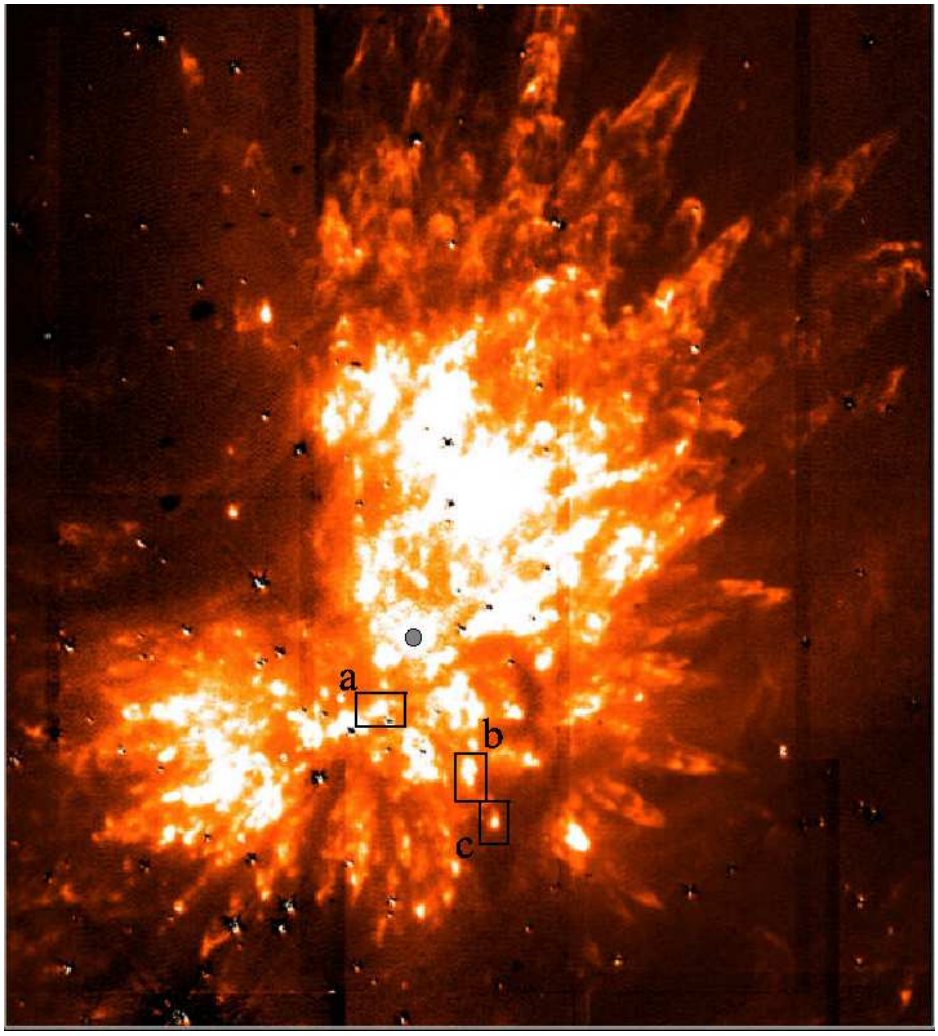

Figure 1.6: The H_2 outflow taken with the Subaru telescope. Emission regions shown in close-up in Fig. 1.7 are marked with boxes and the position of BN is indicated by a filled circle.

to these knots of [FeII] emission as "bullets" and propose a formation scenario where dense clumps of material were ejected in an explosive event 1000 years ago. They traced the origin of the explosion to within 5″of BN and IRc2. Schultz et al. (1999) found that fingers in the central region around BN-IRc2 are not tipped by [FeII] emission. This may indicate that only the most distant bullets travel fast enough to dissociate H_2 at the tip. Fingers to the south-east and south-west have also been found (Schild et al. 1997; McCaughrean & Mac Low 1997; Stolovy et al. 1998).

Observations of the radial velocity structure of the outflow with Fabry-Perot interferometers have shown the gas in Peak 2 to be $\sim$ 10kms^{-1} more red-

shifted than the gas in Peak 1 (Sugai et al. 1995; Chrysostomou et al. 1997; Salas et al. 1999). In Chapter 2 we present Fabry-Perot data with higher spatial resolution than these previous observations. These data enable us to study the motions in the outflow in much more detail.
IR observations with increasing spatial resolution have shown the H_2 outflow to be highly structured and clumpy (Stolovy et al. 1998; Vannier et al. 2001; Lacombe et al. 2004). The detection of bright H_2 emission is, however, strongly affected by the local dust opacity. The H_2 emission in OMC1 originates from within the star forming molecular cloud (Rosenthal et al. 2000) and may be strongly obscured. Features which are apparently weak may in reality be bright, but buried within a few hundred AU of dense material with number density (n_H+2n_{H_2}) as high as $10^6 - 10^7$ cm^{-3} (Rosenthal et al. 2000; Vannier et al. 2001). Thus we are likely preferentially to observe material emerging from the obscuring screen of dense gas, that is, blueshifted from the ambient gas, rather than redshifted.
As an alternative to the explosion model of Allen & Burton (1993), Stone et al. (1995) proposed that the bullets were caused by instabilities in a shell of material swept-up by a spherical stellar wind. In this model instabilities form when the wind accelerates and result in fragmentation of the shell into smaller knots. The bipolar appearance of the outflow may be explained by blocking of the spherical wind by the hot core of dense gas that runs NE-SW in the region around IRc2, as desribed above (Genzel & Stutzki 1989; McCaughrean & Mac Low 1997).
The proper motion of the BN object (0.0181 yr^{-1} toward position angle (P.A.) $= -37.7°$ Plambeck et al. 1995; Tan 2004) suggests that BN was ejected from the Trapezium cluster 4000 years ago and made a close passage of source I approximately 500 years ago (Tan 2004). This could have triggered the explosive event causing the H_2 outflow (Tan 2004). Bally & Zinnecker (2005) suggest that the outflow is the result of a stellar merger that took place 1000 years ago.

1.4.2 The magnetic field in OMC1

The magnetic field strength in OMC1 was estimated from OH-masers to be $\sim$ 3 mG (Norris 1984). Crutcher et al. (1999) estimated the line of sight component from Zeeman splitting of CN and found a value of 0.36mG. The measured values are not consistent, but Crutcher et al. (1999) measure only the line of sight component and thus underestimate the true value. Furthermore the value obtained from masers may likely be local to the masing regions. Measurements of polarized scattered light can be used to infer the direction of the magnetic field. Elongated interstellar dust grains are aligned with their short axis parallel to the magnetic field. The grains absorb and

emit light whose electric vector is parallel to the long axis. Thus emitted light is polarized perpendicular to the magnetic field while the transmitted light in absorption features is polarized parallel to the field (Simpson et al. 2006). Houde et al. (2004) and Schleuning (1998), at 350 and 100μm, respectively, show that the magnetic field is generally oriented NW-SE with P.A.$\sim$ 120°. Higher resolution maps at 2μm show that the magnetic field changes direction to $\sim$ 140° in the region south and east of IRc2 (Simpson et al. 2006). Polarization measurements also show the dust distribution in OMC1 as described in Sect. 1.5.2 (Aitken et al. 1985; Bailey et al. 1998; Chrysostomou et al. 2000; Simpson et al. 2006).

1.5 Origin of NIR emission in OMC1

The excitation mechanism of the H_2 emission observed has an important bearing on the conclusions drawn in this thesis. Here we discuss the origin of the H_2 and continuum emission in the region observed, that is, a 1'×1' field centered on BN, see Figs. 1.6 and 2.1.

1.5.1 H_2 emission

H_2 emission in OMC1 arises from heating in J-type and C-type (magnetic) shocks (e.g. Draine et al. 1983; Pineau des Forêts et al. 1988; Smith & Brand 1990; Kaufman & Neufeld 1996b,a; Timmermann 1998; Wilgenbus et al. 2000; Vannier et al. 2001; Le Bourlot et al. 2002; Kristensen et al. 2003) and from photon excitation in photodissociation regions (PDRs) (e.g. Black & Dalgarno 1976; Black & van Dishoeck 1987; Sternberg & Dalgarno 1989; Störzer & Hollenbach 1999).
Shocks in the region observed arise from one or more large-scale outflows, thought to originate from the BN-IRc2 region as mentioned above (O'Dell 2001; Doi et al. 2002, 2004; O'Dell & Doi 2003, and references therein). As will be discussed in Chapter 4, shocks in the zone observed may, however, also arise from local outflows associated with protostars buried within emitting clumps of gas (Nissen et al. 2006) or from supersonic turbulence. Turbulent motions may arise in the outflows or originate from an energy cascade initiated at much larger scales.
Dense clumps in OMC1 may be bathed in PDRs from the Trapezium stars, to the south of BN, of which the dominant contributor is θ^1Ori C (Sect. 1.4). The BN object, which is a young and massive B-star (Sect. 1.4.1), may also provide a source for PDR excitation. Furthermore, the young, deeply buried massive stars, such as source I, source n and IRc2 (Sect. 1.4.1), located in the region (Menten & Reid 1995; Doeleman et al. 1999; Greenhill et al. 2004a,b;

Shuping et al. 2004) may possess a UV field even higher than the standard value for Orion. However the resulting H_2 emission from these dense regions would be highly obscured from our view. Detailed models of H_2 emission have been devised, for example in Störzer & Hollenbach (1999), for UV fields of the intensity of that of θ^1Ori C falling upon dense gas. These models show that the maximum contribution to emission brightness in the H_2 v=1-0 S(1) line from PDRs including advection does not exceed a few times 10^{-6} W m^{-2}sr^{-1}, given a line-of-sight normal to the PDR. The PDR contribution is therefore no more than 10-15% of the maximum emission observed here of $\sim 3.0 \times 10^{-5}$W m^{-2}sr^{-1} (see Sect. 2.4). This remains true even when effects of high density, advection and photoevaporation (Lemaire et al. 1999; Henney & O'Dell 1999) are included.

The relative importance of PDR and shock excitation in the strongest H_2 emitting regions has been discussed in detail in Kristensen et al. (2003) using detailed models of shocks and PDRs. The conclusion is that in the subset of clumps studied in that work, which are those to the south-east of BN, C-type shocks are the major contributor to H_2 excitation. However, towards the fringes of bright clumps, J-type shock and PDR excitation by θ^1Ori C take the place of C-type shock excitation, with shock and PDR excitation contributing roughly equally. Thus the conclusion is that the major contributor to H_2 emission is shock-excitation and that the brightness due to photoexcitation contribute a minor, though non-negligible part.

In all cases of very bright emission, the post-shock densities are high, exceeding several times 10^7 to $>10^8$cm^{-3} (Kristensen et al. 2003). In such regions, the scale of both hot shocked zones and of PDRs is very small, of a few AU or less, and the cooling times to 10K are less than a few years. Thus the effect of numerous, individually unresolved shocks are observed in Orion. Excited gas rapidly accumulates into cold compressed zones and excited H_2 is the very rapid progenitor of cold dense gas. Thus the structure of excited H_2, provides a measure of the structure of cold H_2 clumps, where the latter is the gas from which stars will ultimately form. In Chapter 8 we will also see that the cold gas is distributed in clumps of the same size as the H_2 clumps.

In other regions, which are presumably less dense, the correspondingly larger shock structure appears to be clearly resolved in H_2 emission. This is illustrated by data in Fig. 1.7 which are details from the VLT/NACO data presented in Sect. 2.2. These shocks are located south of BN as indicated in Fig. 1.6. Numerous objects in these figures resemble bow shocks. The emission may also in part be due to complex density structure associated with PDR excitation. At all events high spatial resolution data allow us to specify the width of the filamentary regions containing excited gas. For example in Fig. 1.7a and c, widths of some filaments appear marginally resolved. If

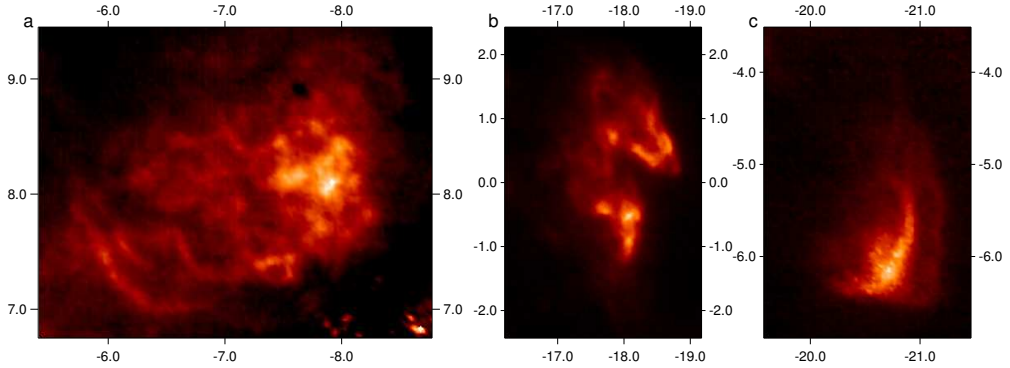

Figure 1.7: Details of H_2 v=1-0 S(1) line emission from VLT/NACO, see Fig. 2.5. Axis are labelled in arcseconds relative to TCC0016. The locations relative to BN are indicated in Fig. 1.6.

these scales of $\sim$ 40-50 AU are shock widths, these data provide important constraints on shock models (Le Bourlot et al. 2002; Wilgenbus et al. 2000), in which parameters of density, magnetic field and shock speed determine the shock width (Kristensen et al. 2006). If the features are PDRs, the widths of structures are again valuable parameters, providing a good indicator of the gas density (Sternberg & Dalgarno 1989; Lemaire et al. 1996; Kristensen et al. 2003).

1.5.2 Continuum emission

The origin of extended NIR continuum emission in the OMC1 region, is most likely reflected light from dust which is evident from polarization measurements (e.g. Aitken et al. 1985; Bailey et al. 1998; Chrysostomou et al. 2000; Simpson et al. 2006). Regions with extended continuum emission are either externally illuminated condensations or self-luminous protostars. In this connection, there is little H_2 emission where strong continuum emission is observed, as for example a comparison of Figs. 3.1 and 2.16 will reveal (or see Fig. 3 in Stolovy et al. 1998). Thus little mechanical energy is being injected into these zones.
Chrysostomou et al. (2000) find high values of polarization, both circular and linearly, in regions associated with continuum emission at 2μm. The high circular polarization arises from scattering off oblate dust grains composed of silicates or organic material. According to Chrysostomou et al. (2000) the illuminating source of the bright continuum region north of Peak 2 (see Figs. 2.6 and 3.1) is likely to be located close to IRc2 or radio source I.

Using linearly polarized light Simpson et al. (2006) also investigated the

origin of the nebulosity around the BN-IRc2 complex (Fig. 1.5). They showed that BN is the illuminating source for most of the diffuse emission to its north. They also found that IRc2-B and IRc2-D are most likely deeply embedded, self-luminous sources while IRc3 could be illuminated from IRc2-A. IRc4 and IRc5 could both be illuminated from a star near radio source I. IRc7 most likely contains an embedded source. They find is no evidence of a single object being the dominating illumination source in OMC1.
In Chapter 3 we present the continuum emission in OMC1 at 2μm observed with adaptive optics at the VLT yielding very high spatial resolution.

Chapter 2

Observations and data reduction

Three sets of observations of vibrationally excited H_2 in OMC1 are used in this thesis. In November 2002 the region was observed using the ESO-VLT with NACO (Fig. 2.1 presents a finding chart), an association of the NAOS adaptive optics system and the CONICA infrared array camera. This was part of the First Light campaign with NACO and the main part of the data reduction was performed by Daniel Rouan and Jean-Louis Lemaire. In December 2000 the CFHT was used and the instrument GriF (Clénet et al. 2002) which combines the PUEO adaptive optics with Fabry-Perot interferometry (FP) to spectro-image the H_2 $v = 1 - 0$ S(1) emission line (Fig. 2.2). Spectro-imaging was again performed using the VLT/NACO-FP (Hartung et al. 2004) in December 2004 (Fig. 2.3) in which I took part. Here we obtained data for three H_2 lines, namely $v = 1 - 0$ S(1), $v = 1 - 0$ S(0) and $v = 2 - 1$ S(1).
Since all three data sets involve Adaptive Optics (AO) Sect. 2.1 has been devoted to the basic principles of AO, followed by the VLT/NACO data in Sect. 2.2. Fabry-Perot Interferometer will be described in Section 2.3. I have chosen to make a detailed description of the data reduction techniques for FP data since these are anything but trivial to reduce and because FPs in general are not widely used by the astronomical community. The CFHT/GriF data and reduction is described in Sect. 2.4 followed by the VLT/NACO-FP in Sect. 2.5.

2.1 Adaptive optics

Under ideal circumstances, the resolution of an optical system is limited by the diffraction of light waves. The diffraction limit (in radians) of a telescope is given by $\alpha = 1.22\frac{\lambda}{D}$, where λ is the wavelength of the light and D the diameter of the mirror. Thus observations in the NIR K-band

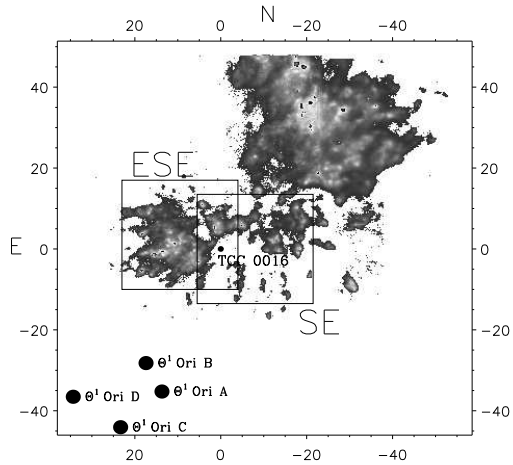

Figure 2.1: Finding chart for the VLT/NACO observations (Sect. 2.2) Nov 2002 relative to the Trapezium stars. The two observed fields, designated ESE and SE, are indicated as boxes on top of an image recorded in H_2 v=1-0 S(1) line emission. Coordinates are arcseconds relative to TCC0016 ($05^h35^m14^s.91$, -05°22'39".31 (J2000)).

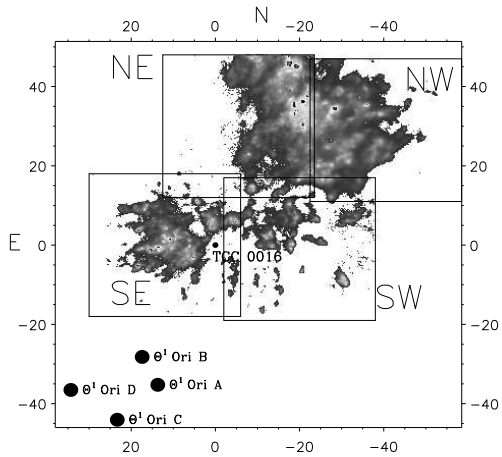

Figure 2.2: Same as Fig. 2.1 but for the CFHT/GriF observations Dec. 2000 (Sect. 2.4). The four observed fields are designated NE, NW, SE and SW.

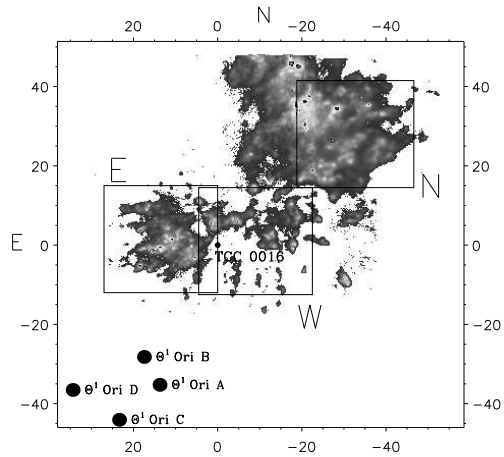

Figure 2.3: Same as Fig. 2.1 but for the VLT/NACO-FP observations Dec. 2004 (Sect. 2.5). The three observed fields are designated E, W and N.

with wavelengths of $\sim 2.1\mu$m with the VLT ($D = 8.2$m) have a diffraction limited resolution of $0\farcs06$. In practice, however, the resolution of Earth based observations is limited by the seeing of the atmosphere, which even in the best conditions is seldom better than $0\farcs3$.

An Adaptive Optics system compensates for the atmospheric turbulence by measuring the shape of the distorted wavefronts and applying an opposite cancelling distortion using adaptive optical elements. In Fig. 2.4 a schematic overview of an adaptive optics system is shown. A nearby reference point source is used to probe the shape of the wavefronts. This may be a bright star or a "laser guide star" created by exciting sodium atoms in the upper part of the Earth's mesosphere with a laser. The light from the reference source is analysed by a wavefront sensor and the result is sent to actuators. These actuators change the shape of the deformable mirror (Fig. 2.4) in order to provide the deformation necessary to yield a uniform wavefront. In order to correct continuously for the wavefront changes in the atmosphere this process takes place in a "closed-loop" with sampling frequencies of hundreds of Hertz. In this way the science target can be observed at high spatial resolution for a long period of time. However, to obtain good results an AO system should generally not be kept in closed-loop for more than one hour. In that time interval the conditions in the atmosphere will have changed significantly and the AO system should be relocked.

Good correction can only be made over a region in the sky which extends over the scale of a turbulent cell. This region is called the isoplanatic patch and is dependent on wavelength, $\theta \sim \lambda^{6/5}$ (Coulman 1985; Beckers 1993). It is typically $\sim 20''$ in the infrared. Thus AO systems without artificial laser guide stars are limited to regions where bright stars that are suitable as reference stars are found very close by. At the time of our observations no laser guide stars were available at either VLT or CFHT, but useful reference stars are present in OMC1. Different natural reference stars were used in the observations in order to minimize the distance from reference star to the field of view. The reference stars used will be specified in connection with the observations.

The efficiency of the AO system can be quantified by the Strehl ratio, which is given by the ratio of the measured maximum intensity in the point spread function (PSF) to the theoretical maximum for a telescope with no aberrations. The higher the Strehl ratio the higher is the resolution. The resolution is generally expressed as the Full Width at Half Maximum (FWHM) of the PSF.

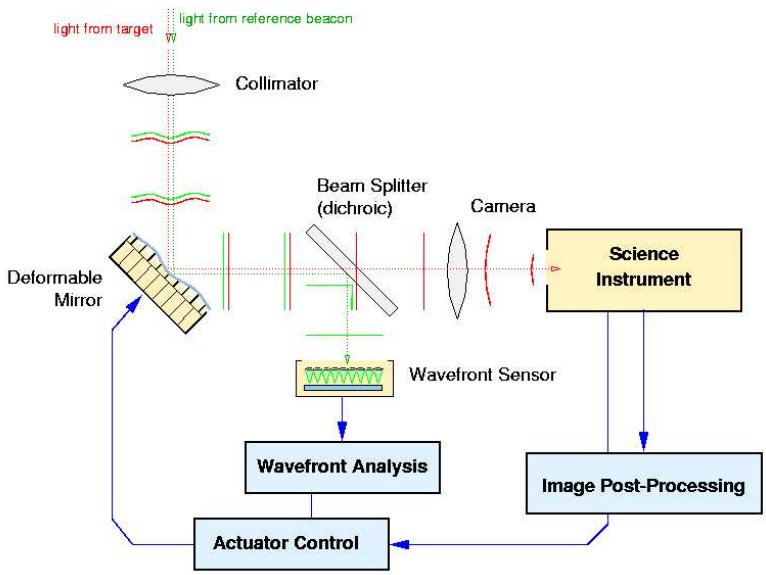

Figure 2.4: Schematic overview of an adaptive optics system. Adapted from http://cfao.ucolick.org/

2.2 VLT/NACO First light 2002

Observations of OMC1 were performed with the VLT UT4 during guaranteed NACO time on the 21st of November 2002, for about 4.5 hours in total. I did not take part in these observations nor the data reduction. However I was heavily involved in data analysis (Sect. 8.1). The seeing was variable during this night ranging from 0.″65 to 1.″13. Two regions have been observed located south-east (SE frame) and east-south-east (ESE frame) from BN and IRc2, with the star TCC0016 common to both frames (Figs. 2.1 and 2.5). The IR wavefront sensor was used for the SE frame using BN (m_K~8) as the adaptive optics reference star. The average seeing was ~0.″85 and the resulting resolution as measured by the FWHM of the PSF on several stars in the SE field was ~0.″08. The ESE frame was recorded using the visible wavefront sensor locked on the star TCC016 (m_V~14). The lower luminosity of the star, combined with an average seeing of ~1.″03, led to a measured FWHM of the PSF of ~0.″12. The Strehl ratio was clearly highest in the SE frame, compared to the ESE frame, indicating that the AO system was able to give nearly full correction to the diffraction limit of ~0.″06. Using camera mode S27, the field of view was 28"×28" and the pixel scale was 0.″027, a size sufficient to satisfy the Nyquist sampling criterion (Nyquist 1928). 0.″027 corresponds to 12 AU at the distance of Orion.

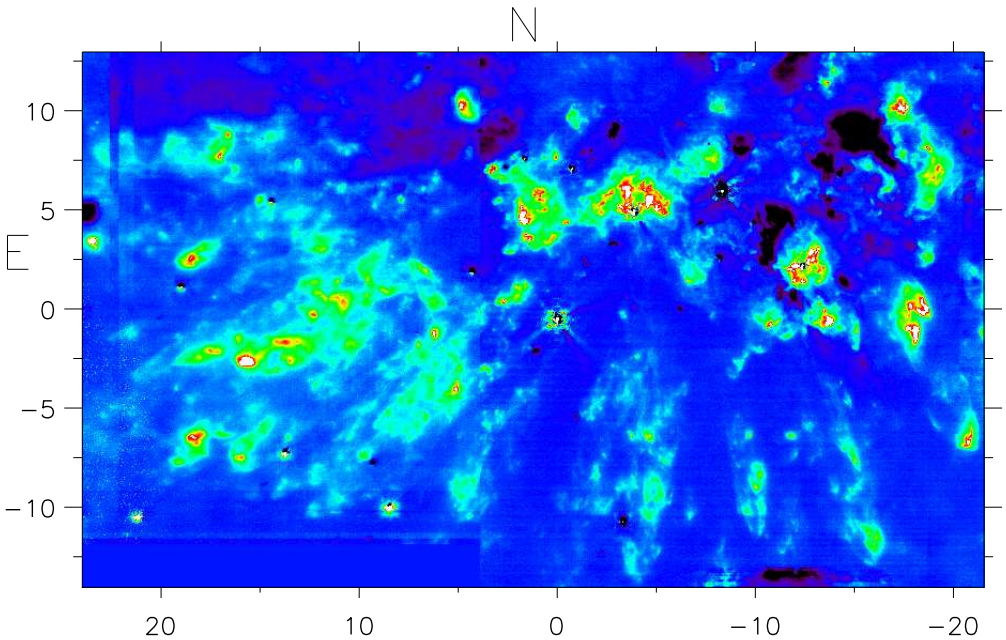

Figure 2.5: H_2 emission in the v=1-0 S(1) line with continuum emission subtracted from VLT/NACO. Coordinates are in arcseconds and relative to TCC0016.

Several filters were used: NB212 at 2.121±0.011μm, which contains the H_2 S(1) v=1-0 line at 2.12μm(Bragg et al. 1982), IB224 at 2.24±0.03μm and IB227 at 2.27±0.03μm. Within the NB212 filter the v=3-2 S(4) (2.127μm) and the v=8-6 O(4) (2.121μm) lines may be found. These contaminating lines are, however, found to be weak in both shocks and PDRs (Black & van Dishoeck 1987) and are ignored. The IB224 filter includes the H_2 v=1-0 S(0) line at 2.223μm and the H_2 v=2-1 S(1) line at 2.247μm (Bragg et al. 1982), as well as weak [FeII] lines at 2.218 and 2.242μm. The IB227 filter includes the H_2 v=2-1 S(1), v=9-7 O(3) (2.253μm), v=3-2 S(2) (2.286μm) lines and the [FeII] line at 2.242μm. The v=9-7 O(3) and v=3-2 S(2) lines are weak compared to the v=2-1 S(1) line in both shocks and PDRs.
Images were recorded including random jitter for ease of data reduction. That is, at each exposure the telescope moves according to a random pattern in a $6'' \times 6''$ box. Cross-correlation was used to recenter the images to a precision of ∼0.15 pixel. For the ESE frame, an empty background sky has been recorded for the purpose of sky subtraction. For the other less crowded SE frame, the background sky has been created by performing a median filtering of the set of 32 randomly jittered individual frames. The total exposure time on object for each filter was 800 seconds for the SE frame and 1500 seconds

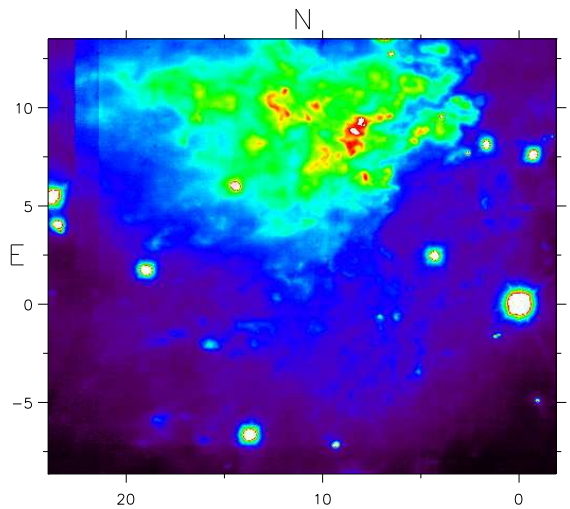

Figure 2.6: Continuum emission at 2.27 ± 0.03μm in the ESE field from VLT/NACO. Coordinates are in arcseconds and relative to TCC0016.

for the ESE frame, with exposures of 10 seconds for each data acquisition.

To obtain an image in the H_2 v=1-0 S(1) line, the data in the IB224 continuum image was subtracted from the NB212 image after division of the latter by a factor of 2.5 as derived from measuring fluxes of a number of stars in both filters. The resulting image is shown in Fig. 2.5 where the ESE and SE frames have been combined. The contribution of v=1-0 S(0) and v=2-1 S(1) in IB224, known to be small in OMC1 from spectroscopy (G. Callejo, private communication), was ignored in image processing. By subtraction of the image in the IB227 filter from that in the IB224, using a conversion factor obtained as before, it was possible to obtain an image in H_2 S(0) v=1-0. This image includes the very weak [FeII] line at 2.218μm. The image in v=1-0 S(0) shows essentially the same structure as that in Fig. 2.5, but is 4 to 5 times weaker.

Strong continuum emission is seen for example in the northern part of the ESE region and is shown in Fig. 2.6, which displays emission in the IB227 filter. Data in Fig. 2.6 also include weak emission from v=2-1 S(1) and [FeII]. Continuum emission is also seen at this position in the data of (Aitken et al. 1985; Schultz et al. 1999; Chrysostomou et al. 2000, and see Sect. 1.5.2).

The data in Figs. 2.5 and 2.6 will in the following be referred to as the VLT/NACO data and will be analysed with respect to characteristic sizes of structures in Sect. 8.1.

2.3 Fabry-Perot Interferometry

The theory of Fabry-Perot (FP) interferometers is based on multiple reflections at planar surfaces and was first described by Fabry & Perot (1901). The instrument consists of two plane, parallel, highly reflecting surfaces separated by some distance d. The distance between the two plates can be accurately adjusted. The outer uncoated sides of the plates are often made to have a wedge shape in order to avoid interference patterns from reflections off these sides. Of the two FPs used here GriF at CFHT have wedge shaped plates, while NACO-FP at VLT is constructed with plane parallel outer sides. The design of the latter introduces some additional challenges in the data reduction (see Sect. 2.5.2). The theory of Fabry-Perot interferometers is described briefly here. A more detailed examination can be found in Born & Wolf (1999) and Hecht (1998).
The theoretical intensity transmitted by the interferometer is given by the Airy function:

$$\frac{I_t}{I_i} = \frac{1}{1 + F\sin^2(\delta/2)} \tag{2.1}$$

where I_t and I_i denote the intensities of the transmitted and incoming beams, respectively. F is defined as

$$F = \frac{4R}{(1-R)^2} \tag{2.2}$$

with R being the reflectivity of the plates. The phase shift δ is:

$$\delta = \frac{4\pi n d \cos\theta}{\lambda} \tag{2.3}$$

Here n is the refractive index, d the plate separation, θ the inclination angle to the optical axis and λ the wavelength. Note that when $\delta \ll 1$, Eq. (2.1) reduces to a lorentzian function. That is, the generic instrumental profile of a FP at a specific inclination and varying plate separation is a lorentzian. However, if the wings of the profile are noisy a gaussian profile may also fit.

The condition for constructive interference is that the optical distance between the two plates must equal an integral number of half wavelengths. That is

$$nd\cos\theta = m\lambda/2 \tag{2.4}$$

It is seen from Eq. (2.1) that maxima of transmitted intensity occur when the order of interference m

$$m = \frac{\delta}{2\pi} = \frac{2nd\cos\theta}{\lambda} \tag{2.5}$$

has integral values and minima when m has half-integral values. Evidently fringes of equal inclination in the focal plane, that is at constant θ, are formed if the source is (nearly) monochromatic. Maximum intensity is found at constant θ corresponding to integral values of m. The focal plane is parallel to the plates and the fringes are circles with a common centre at the focal point for normally transmitted light. Generally the field of view of astronomical FPs include only a limited range of inclination angles and thus include only interference from one order for a given plate separation and wavelength.

If the plate separation d is kept constant for a polychromatic light source the two variables are θ and λ. It is seen that when θ varies constructive interference (or maximum light transmittance) occur at different wavelengths. The transmitted wavelength is a function of position on the detector which has a parabolic shape centered on the focal point. This means that for observing light with a specific wavelength, that is, a spectral line, over the whole field of view it is necessary to take a number of exposures with different plate separation (Fig. 2.7a and b). In a (x, y, d) data cube a narrow emission line will trace a parabolic surface of constant m and λ (Fig. 2.7c). When observing light with a large range of wavelengths a narrow band filter is normally used to avoid interference from orders corresponding to other wavelengths. Each exposure in a complete scan will here be referred to as a channel map. All channel maps of a scan constitute the data cube.

The reflective finesse, f, is defined as the ratio of fringe separation and halfwidth of the fringes. The finesse is given by

$$f = \frac{\pi\sqrt{F}}{2} \tag{2.6}$$

In practice the surfaces of the plates are not perfectly plane and this gives rise to a "defect finesse" f_d. When $R \to 1$ the finesse approaches the limit f_d. This means that due to imperfection in the plates there is an upper limit of fringe sharpness which cannot be exceeded even if the reflectivity of the coatings is increased. The finesse of GriF is measured to be 104 and for NACO-FP it is 26. The resolution limit or bandpass of a FP is given by

$$\delta\lambda = \frac{\lambda^2}{f2nd} \tag{2.7}$$

and the resolving power is $\lambda/\delta\lambda$. The bandpass of GriF is $\delta\lambda = 1.014$nm giving a spectral resolution of $\lambda/\delta\lambda = 2030$. For NACO-FP the values are $\delta\lambda = 2$nm and $\lambda/\delta\lambda = 1100$.

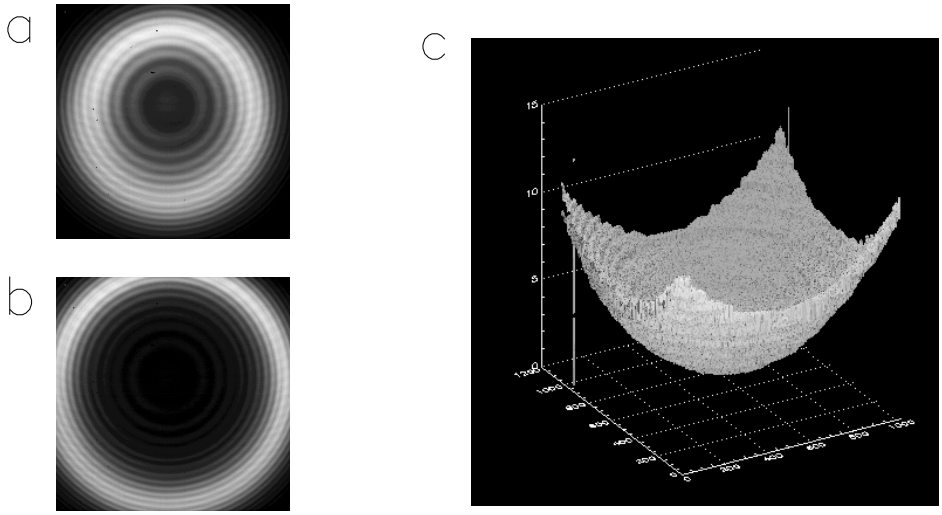

Figure 2.7: Examples from VLT/NACO-FP of output from a Fabry-Perot interferometer illuminated with a monochromatic Ar lamp. **a)** and **b)** show images taken at different plate separation, d. The intensity indicate the spatial position where the FP transmits the Ar line at 2.099μm for the associated d. It is evident that a number of images at different plate separation are needed in order to observe the line in the full field of view. **c)** shows the position of the Ar calibration line in a data cube constructed of 14 images with different values of d. The cube is 1024 $\times$ 1024 $\times$ 14. The third axis indicates increasing plate separation. The calibration line traces a parabolic surface of constant λ.

2.3.1 Standard data reduction for FPs

Basic data reduction for FP observations in combination with infrared array detectors involves (i) dark and bias subtraction, (ii) flatfielding, (iii) bad pixel correction, (iv) recentering of data cube, (v) sky and continuum subtraction, (vi) wavelength calibration and (vii) phasemap correction.

Darks can be obtained as daytime/twilight calibrations of the detector. Flatfields should be obtained using the same settings of the FP as for the science cube as the sensitivity of the pixels may vary with wavelength. By this means a flatfield cube is built and the flatfield corrected cube is constructed by dividing the two cubes plane by plane. If the FP instrument is placed at the Cassegrain focus (GriF) the flexure of the telescope may also affect the sensitivity of the detector and flatfields should be taken at the same telescope position as for the science scan using a white light lamp. For instruments located in the Nasmyth focus (NACO-FP) this is irrelevant and flatfields can be taken as daytime calibrations. Bad pixels are replaced us-

ing the IDL routine "sigma_filter" from the IDL Astronomy User's Library (http://idlastro.gsfc.nasa.gov).
Spatial drifts of the telescope and differential diffraction of the atmosphere are responsible for shifting the position of the stars on the detector between each channel map of the scan. Thus it is necessary to re-align the cube and bring the stars to the same spatial position on the detector.
Science spectra are affected by the sky background emission and the telluric absorption features. The infrared sky spectrum contains a large amount of emission lines, specifically OH Meinel band emission (Meinel 1950; Rousselot et al. 2000), that are superposed on the science data. These sky lines can be removed by obtaining a scan of the sky with the same characteristics as the science scan. The sky spectrum can also be extracted from the science cube from spatial regions with no emission in the line studied. Note that if the scanned wavelength domain is not influenced by sky emission lines the sky background can be obtained from a channel map in the far wing of the science line. This channel map also contains the continuum emission of the region. Note also that if spatial drifts during the scan are insignificant, then re-alignment is superfluous and dark, sky and continuum subtraction can be performed all at once by subtracting a channel map from the wing. This is the case in the CFHT/GriF data (Sect. 2.4) but not in the VLT/NACO-FP data (Sect. 2.5). Telluric absorption features can be corrected by observing a source with a flat featureless spectrum, such as an A0 star. None of the H_2 emission lines observed here are polluted by atmospheric absorption (Livingston & Wallace 1991) and no such calibration spectrum has been observed here.

2.3.2 Wavelength calibration

The transmitted wavelength of a FP should be calibrated before and after each scan to account for small offsets caused by drifts of the piezo stack controller. The plate separation of the FP at NACO is controlled with z values given in "Fabry-Perot Control Units" (FCU) and a conversion function to wavelengths must be known. GriF at CFHT is controlled in a similar way. For ease of references we will use the terminology from NACO-FP (Hartung et al. 2004) here. In the following we will also use z to represent the plate separation. The conversion between z values and wavelengths, which is very stable, is carefully measured and implemented in the controlling software. However, small drifts may occur during the observations and these should be measured to assure high precision in the wavelengths. A calibrated Argon line (at 2.062μm or 2.099μm) is scanned for this purpose. The emission profile in the zero phaseshift point (the focal point) is constructed as a function of z and a gaussian or lorentzian fit is applied to locate the z value for which the

emission peaks. The difference between the measured and expected z value is a direct measure of any drift.
The scan of the Argon calibration line is also used to construct the "phase map" which describes the wavelength variation for the whole field of view. From the Ar scan we can derive a map that indicates for each pixel the difference between the z value at which the emission is maximum and the expected z value at which the maximum should have occured had there been no (x, y) dependence of wavelength. The z value is found by fitting a lorentzian or a gaussian to the emission profile for each pixel. The difference in z can be directly transformed into a difference in transmitted wavelength and this gives the phase map. Thus the transmitted wavelength in a given pixel for a given value of z is found by converting z to wavelength and subtracting the phase map value of this pixel.
After these steps we can find the brightness and the radial velocity in each spatial pixel by fitting a gaussian or lorentzian to the profile of the scanned emission line. The radial velocity is derived from the peak position of the profile in wavelength and the brightness from the peak amplitude. Further information on data reduction techniques can be found in Clénet et al. (2002) and Hartung et al. (2004).

2.4 CFHT/GriF 2000

2.4.1 Observations

OMC1 was observed using the CFHT equipped with GriF on the night of December 5th 2000 and these data constitute the First Light observations with GriF. The data were taken before I joined the group and therefore I was not involved in the actual observations, but I did perform the data reduction. As mentioned earlier the GriF instrument, described in detail in Clénet et al. (2002), is a combination of the PUEO AO system on the CFHT and interferometric spectral scanning. The interferometer is a Queensgate ET50WF Fabry-Perot, with a measured spectral resolution of $\lambda/\delta\lambda = 2030$, that is $\sim$ 150kms^{-1} in the NIR K-band. The FP is operated at room temperature. GriF is placed at the Cassegrain focus. The detector has a field of view of $36'' \times 36''$ and a pixel scale of $0\farcs035$.
Observations were performed in the NIR K-band where the strongest H_2 emission line in Orion, v=1-0 S(1) was scanned with the FP. This line has a rest wavelength of 2.1212544 μm in standard air (Bragg et al. 1982; Black & van Dishoeck 1987, and see Table 2.1). The observed region of OMC1 consists of four overlapping fields with the entire region centered approximately 15″N and 15″W of TCC0016 ($05^h35^m14\fs91$, -05°22'$39\farcs31$ (J2000)), which we use

Line	Wavelength/μm	
	standard air	vacuum
v=1-0 S(1)	2.1212544	2.121833
v=1-0 S(0)	2.2226833	2.223290
v=2-1 S(1)	2.2471	2.2477

Table 2.1: Wavelengths of H_2 lines in standard air and vacuum (Bragg et al. 1982; Black & van Dishoeck 1987).

as a positional reference throughout (Figs. 2.2 and 2.8). The centre position corresponds roughly to the position of the Becklin-Neugebauer object (BN) which lies about 50″N and 30″W of the Trapezium cluster. We designate these four fields as SE, NE, SW, NW (see Fig. 2.2).
Various AO reference stars were used to ensure a minimum distance between field and reference star (see Sect. 2.1). TCC0016 ($m_V \sim 14$) was used in the SE and SW field, Parenago 1838 ($m_V \sim 15.2$) in NE and Parenago 1819 ($m_V \sim 14.4$) in NW. The FWHM of the PSFs of the stars in the region have been measured to yield a spatial resolution of 0.″15. This near diffraction[1] limited spatial resolution was maintained throughout all observations.
Observations proceeded by setting the Fabry-Perot to a nominal wavelength far in the wings of the H_2 emission line and for each region progressively scanning through the H_2 line, using step sizes varying between 4.4x$10^{-4}\mu$m and 4.6x$10^{-4}\mu$m, that is, ~ 65 kms^{-1}. This step size allows a correct Nyquist sampling of the instrumental profile. The nominal wavelength corresponds to the transmitted wavelength at the centre of the interference fringes (see Sect. 2.3). To prevent the superposition of different FP orders during scanning, an H_2 v=1-0 S(1) interference filter with a central wavelength of 2.1222 μm and bandwidth of 0.02 μm was inserted between the FP and the detector. The four fields were scanned with a different number of steps in nominal wavelengths (8-12) and thereby in different wavelength ranges. The number of steps and step sizes were decided during the observations by the observing astronomers to make sure that the full data set could be obtained in one night. The nominal wavelengths for the four fields are listed in Table 2.2. For each region and each wavelength, a single exposure of 400s was performed, yielding a 2D image, that is a channel map. For each region the 2D channel maps are stacked in a data cube with nominal wavelength as the third dimension.

Calibration of GriF (Clénet et al. 2002) was performed before and after each complete scan of the H_2 line. Calibration covers (i) wavelength calibration by scanning through the 2.06163 μm Ar line using a Ar lamp, with a step-size of 4.21x10^{-4} μm and (ii) flat-fielding to account for different sensitivities

[1] CFHT is a 3.6m telescope with a diffraction limit of 0.″147 at 2.1μm.

Region SE	Region SW	Region NE	Region NW
2.1194	2.1186	2.1186	2.1186
2.120467	2.119036	2.119036	2.119036
2.121	2.1194	2.119473	2.119473
2.121457	2.119857	2.119909	2.119909
2.121533	2.120314	2.120345	2.120345
2.121914	2.120771	2.120782	2.120782
2.122371	2.121229	2.121218	2.121218
2.1226	2.121686	2.121655	2.121655
2.122829	2.122143		2.122091
2.123186	2.1226		2.122527
2.123743			
2.1242			

Table 2.2: The nominal wavelengths used for the scan of the H_2 v=1-0 S(1) line for the four fields observed with CFHT/GriF. All numbers are in μm.

of each pixel of the detector, using a halogen lamp white light source at the same set of wavelengths as used in the observations and at the same telescope position.

2.4.2 Data reduction

The spatial drift between channel maps in each scan is found to be very small. In each field the intra-pixel positions of the stars have been measured using 2D gaussian fits and the shifts are estimated to be less than 2 pixels in the x- and y-directions respectively. As this is less than the spatial resolution of ~ 4 pixels no re-alignment of the cubes has been performed.
The sky background and the continuum emission are obtained from data in the far wings of the H_2 line. In OMC1, the sky background is small compared with signals in the H_2 v=1-0 S(1) emission line and problems such as temporal variability of background do not arise. Sky lines from the OH Meinel bands, are not troublesome in the wavelength region of interest here. The closest skyline is found at 2.12324μm (in vacuum) well outside the spectral resolution of GriF ($\sim$ 1nm) and is very weak. No skylines are apparent in our spectra. The four raw data cubes are flatfielded, channel maps from the far wing of the line are subtracted to correct for dark, bias, sky and continuum and bad pixels are replaced using the SIGMA_FILTER IDL procedure from ASTROLIB[2].
All images have been smoothed by a moving average of 3 by 3 pixels to

[2]http://idlastro.gsfc.nasa.gov/

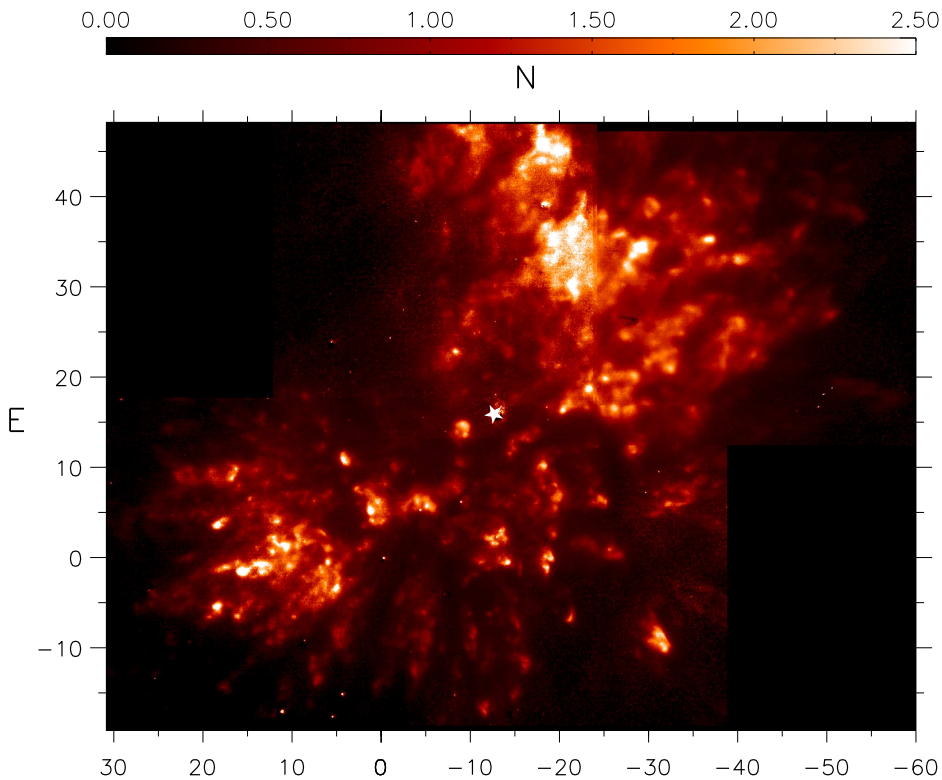

Figure 2.8: Peak emission in the H_2 v=1-0 S(1) emission line covering the observed field in OMC1 with CFHT/GriF. (0,0) marks the position of TCC0016 and the star marks BN. The colourbar represents counts per second per pixel.

improve S/N. Hereafter the effective resolution is 0.″18. Values of brightness in each pixel are taken as the peak emission associated with a lorentzian or gaussian fit to the emission line (see below). The brightness of the observed region is shown in Fig. 2.8.

No standard star was observed and therefore no direct conversion from count rates to brightness is possible. Conversion of count rates to absolute values of surface brightness can be obtained by comparison with calibrated data in Vannier et al. (2001) taken at a similar resolution. Thus the count rate of 3.43 counts per second per pixel, at the peak of emission to the SE of TCC0016, corresponds to a velocity integrated brightness of 3.0±0.15 x 10^{-5}Wm^{-2}sr^{-1}. This conversion may be applied to all regions with the caution that systematic errors may arise through the differing conditions of airmass and of the atmosphere prevailing at the times of observation. For this reason, brightness is recorded in terms of count rate throughout.

2.4.3 Radial velocities

Radial velocities are found by choosing a specific position on the sky and taking a cut through the cube made up of the channel maps. This yields a set of count rates as a function of nominal wavelength constituting a line profile. Nominal wavelengths are transformed into transmitted wavelengths in the spatial pixel in question by subtracting the phase map value, as described in Sect. 2.3.2, and a lorentzian is fitted to the profile (Clénet et al. 2002). The position of the peak in emission then gives the radial velocity and the value of the peak emission gives the brightness. The lorentzian form was chosen because it represents the instrumental profile of the Fabry-Perot, but as noted earlier a gaussian profile will often fit just as well when the wings are dominated by noise. We note that the instrument profile is highly symmetric (Clénet et al. 2002) and thus a choice for example of a centroid rather than the peak of a lorentzian is immaterial to an estimation of the velocity.

Uncertainty on velocity

Performing these operations pixel by pixel for the full field of view results in very accurate fits for the brighter regions. Including statistical error in the count rates, but assuming negligible error on the wavelengths, relative peak wavelengths may be found in bright local zones to 2 to 3 parts per $10^6(3\sigma)$, that is, to better than $\pm 1\mathrm{kms}^{-1}$ (see below). The quality of the fit decreases with decreasing brightness. High precision on the wavelengths require that the FP is stable and the transmitted wavelength remains fixed during an exposure, which is the case here. An example of high precision lorentzian fits in a bright region is shown in Fig. 2.9. The figure shows the peaks of normalized lorentzians fitted to channel map data, making a cut in the plane of the sky moving south to north through bright emission between two positions 15.″9 E, 2.″0 S to 15.″9 E, 1.″5 S relative to TCC0016 (Fig. 2.8). Peak positions march monotonically in velocity to progressively more red-shifted values, ranging here over ~ 10 kms^{-1}. Progressing further north, we find that the velocity smoothly turns back upon itself from the maximum red-shift shown in Fig. 2.9. This behaviour is omitted for clarity. The relative velocities of widely separated high brightness regions within any frame should in principle be as well-determined as local relative velocities, through application of the phase map.

The accuracy of determination of the central wavelength depends on brightness. This dependency has been estimated by performing a large number of fits for a range of pixel brightness. For a chosen pixel the value in each channel map is taken from the 3 by 3 smoothed maps (Sect. 2.4.2). The total photon number, S, is found by multiplying the count rate by the gain of the

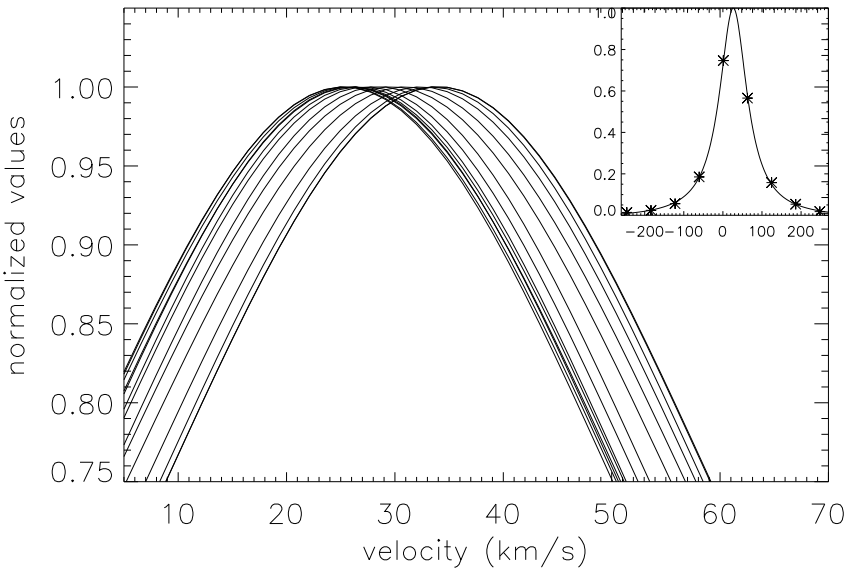

Figure 2.9: A set of normalized lorentzian curves, zooming in on the peak, obtained by fitting to sets of count rates in the S(1) v=1-0 H_2 line, averaged over 3x3 pixels, for 9 velocity channels in the SE region. These results correspond to 14 steps, each of 1 pixel (0.″035), moving from south to north (left to right) over an angular range of 0.″5, in a brightly emitting region starting at position 15.″9 E, 2.″0 S relative to TCC0016, the (0,0) position in Fig. 2.8. The insert shows a typical fit obtained to a set of normalized count rates vs velocity in kms^{-1}. Taken from Gustafsson et al. (2003)

detector (Gain = 3.6 e^-/ADU for GriF). From photon statistics the noise in each channel is given by noise = $\sqrt{S + n_{pix}(sky + D + R^2)}$ (Howell 2000) where D is the dark current, R is the readout noise and n_{pix} is the number of pixels used for the signal S. For GriF $D = 0.15e^-/s$, that is 60e^- for 400 s exposure. R is 20 e^-/pixel. The sky value is estimated from an average over a large region in a channel far in the wing of the H_2 line and is typically $22e^-/s$.

A lorentzian is then fitted to the emission profile and the noise estimates in each point of the profile are used as weights in the fit. The 1σ uncertainty in the peak position of the fitted lorentzian is used as the 1σ uncertainty in the radial velocity. The relation between brightness and error in velocity is shown in Fig. 2.10. The empirical correspondence between brightness and error in velocity can be expressed in a functional form as:

$$\sigma = -9.37 + 3.05\exp(-I * 6.93) + 10.11\exp(-I * 0.026) \qquad (2.8)$$

where σ is the standard deviation of the radial velocity in $\mathrm{kms}^{-1}$and I is the brightness in counts $\cdot$ pixel$^{-1} \cdot s^{-1}$ for the peak emission associated with the

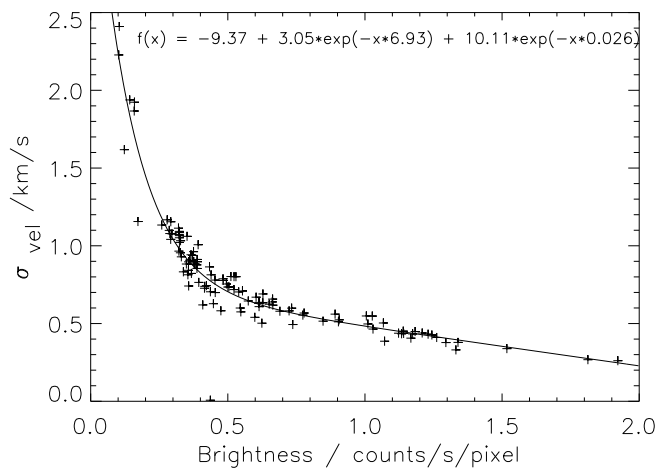

Figure 2.10: Relation between peak brightness, I, and uncertainty in velocity, σ_{vel}. I and corresponding σ_{vel} are found from lorentzian profile fitting. The solid line indicates a fit to the experimental points (Eq. (2.8)).

lorentzian fit. In any statistical analysis (see Chapters 5 and 6) all pixels with brightness below 0.05 counts $\cdot$ pixel$^{-1} \cdot s^{-1}$, that is 2% of the maximum brightness, have been excluded. Thus the largest uncertainty, σ, in the radial velocity that may be encountered in our data is 2.9 kms^{-1}. The functional form of Eq. (2.8) with the two exponentials is chosen simply to match the shape outlined by the data points in Fig. 2.10. There is no theoretical basis for choosing this form. The parameters of Eq. (2.8) are determined by a fit.

Possible caveats in velocity determination

When amalgamating the four fields into a single data cube, inconsistencies were found in velocities of overlapping regions. This was resolved by introducing wavelength shifts in the SW (+14kms^{-1}) and NE (-33kms^{-1}) regions to bring all fields to the same wavelength values. The inconsistency in velocity could be due to spectral drifts or jumps within some or all of the scans. As mentioned in Sect. 2.3.1 the conversion between FCU and wavelength of the FP is calibrated before and after each scan. However temperature variations, telescope flexures and mechanical instabilities may cause this conversion to change during a scan. This means that we may be observing wavelengths different from the wavelengths that we seek to observe. Here we analyse the effect of a potential drift and test if the presence of a linear drift can be detected in the data.

In the following we distinguish between the true observed wavelengths, f, and

the instrumental wavelengths, λ, that we seek to observe. The FP should be stable enough to stay fixed with a certain plate separation during an exposure (400 seconds), but when we adjust the plate separation between exposures some instability may cause different wavelengths to be transmitted than those requested. This does not change the random error associated with the fitted velocities as estimated above but has a bearing on the systematic errors.

It is clear that if the true observed wavelengths, f, are different from the instrumental wavelengths, λ, the derived velocities would be affected. Depending on the differences, values of velocities could be shifted enough to explain the inconsistencies of $\sim 14-33\mathrm{kms}^{-1}$ found above. Whereas potential drifts or spectral jumps limit the accuracy of the absolute calibration the relative velocities are less affected. Unfortunately we do not have access to information on if and how the wavelength calibration changes during a scan. The spectral offset can occur as a linear drift during the scan, as a jump between two exposures or any combination of the two and detailed knowledge of the pattern would essentially require wavelength calibration before each exposure. This has not been performed due to time limitations. However, even if the drift pattern is not known we can estimate the effects in a "worst case scenario".
Assume that the drift is linear in wavelength through the cube, such that $\mathrm{f}_i = a+b\lambda_i$. The wavelength of the first exposure in the scan, λ_0, is calibrated correctly and the total drift during the scan can be evaluated through a calibration after the last exposure giving an offset value δ for the wavelength of the last exposure, λ_f. Thus $\mathrm{f}_f = \lambda_f + \delta$. The linear relation can be expressed as

$$\mathrm{f}_i = -\frac{\delta}{\lambda_f - \lambda_0}\lambda_0 + (1 + \frac{\delta}{\lambda_f - \lambda_0})\lambda_i \tag{2.9}$$

Assume for the sake of argument that the offset is 10% of the scanned wavelength interval and $\lambda_0 = 2.119$ (see Table 2.2), then a = -0.2119 and b = 1.1. This means that an emission line at f=2.12125μm would be measured at λ = 2.121045μm, that is at Δv= -29/kms. Thus an offset of 10% can explain the velocity offsets seen in the observations. The relative velocities are f_1-f_2 = $b(\lambda_1 - \lambda_2)$ which means that in the case outlined above measured velocity differences between any two pixels could be systematically in error by 10%.
Spatial wavelength variation has been neglected above. Because the transmitted wavelength depends on (x, y) position we have f(x, y)=f_{00}-ph(x, y) where f_{00} is the true wavelength in the focal point and ph(x, y) is the value of the phase map in the (x, y) position. We measure $\lambda(x, y) = \lambda_{00}$-ph$(x, y)$. Then

$$\mathrm{f}(x, y) = a - \mathrm{ph}(x, y) + b\lambda_{00} = a + (b-1)\mathrm{ph}(x, y) + b\lambda(x, y) \tag{2.10}$$

where a and b are the same as above. True velocity differences are found as:

$$\mathrm{f}(x_1, y_1) - \mathrm{f}(x_2, y_2) = (b-1)(\mathrm{ph}(x_1, y_1) - \mathrm{ph}(x_2, y_2)) + b(\lambda(x_1, y_1) - \lambda(x_2, y_2)) \tag{2.11}$$

Thus, in addition to the scaling of the measured velocity difference there is an offset which is spatially dependent. If the curvature of the phase map is large compared to the wavelength difference between to adjacent channel maps the latter could greatly influence the relative velocities of points with a large spatial separation. In the case of GriF the curvature across the field-of-view is comparable to the steps in wavelength that was used, $\sim 65\mathrm{kms}^{-1}$(Sect. 2.4.1), and the spatial dependent offset is small.

Note that under a linear transformation in wavelength a lorentzian line shape remain lorentzian. However the width scales with the slope of the linear relation. The instrumental profile of GriF is a lorentzian with a width of w=$150\mathrm{kms}^{-1}$. If there is a linear drift the width of the measured profile is w/b. This can be used to infer if linear drifts have occurred or not and to deduce the value of b directly. However, analysis of the measured line widths do not yield a consistent picture. We measure line widths that are both smaller and larger than the instrumental line width of $150\mathrm{kms}^{-1}$. Therefore we cannot deduce a value of b and we ignore the possible influence of a linear drift and guess that the spectral offset has occurred as a sudden jump. This must, however, have occurred in the start of a scan since no distortion of the lorentzian profile is detected. Thus we amalgamate the four regions by simply adding a wavelength shift as described above.

In this connection, observations of a restricted part of the full field comprising two $36''\times36''$fields to the SE and NW were performed in January 2003. I took part in these observations and carried out the main part of the data reduction. Due to bad weather the quality of these data was rather poor compared to the 2000 data presented here and no further analysis of the 2003 data has been attempted. However detailed comparisons have been made of the velocity fields in the 2000 data and in the 2003 data showing very good agreement. Average velocities have been estimated within regions of about 50×50 pixels ($1\farcs75\times1\farcs75$) separated by up to $60''$, the full size of the image. We find that velocity differences in the 2000 data and the 2003 data agree to better than $\pm1\mathrm{kms}^{-1}$. Since these results were obtained using independent calibration data, they provide a clear indication that systematic errors in velocity differences between remote regions from drifts are not present. Neglecting the systematic errors, the uncertainties on the derived radial velocities are dominated by the random errors of Eq. (2.8).

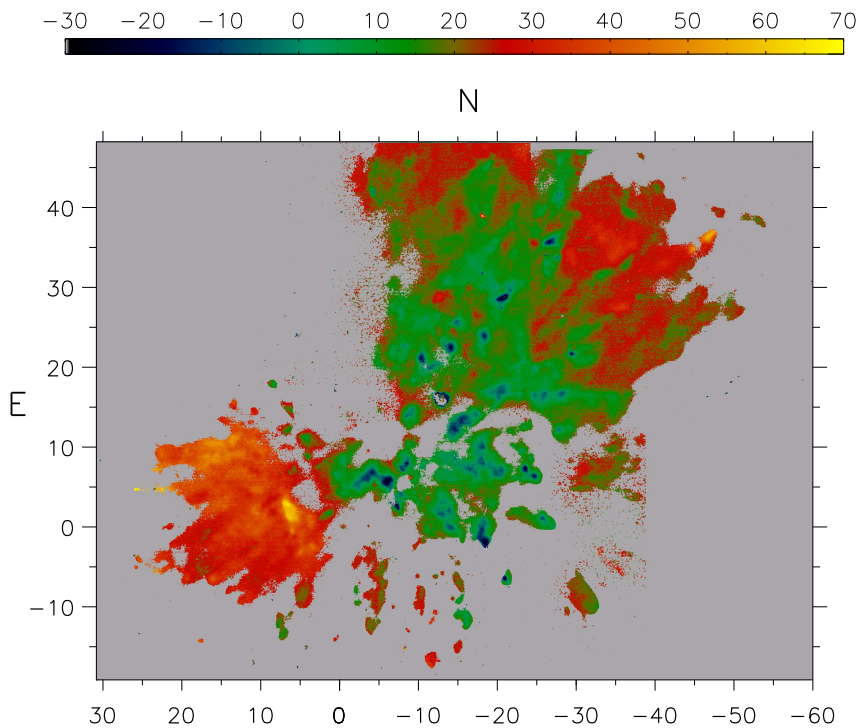

Figure 2.11: Radial velocities in OMC1 as measured with CFHT/GriF, see text. Velocities are given in kms^{-1} and values are indicated in the colourbar.

Final velocity map

After the velocity shifts of +14kms^{-1} and -33kms^{-1} was introduced we still found a large discrepancy between the mean velocity of our data and those quoted by others (Chrysostomou et al. (1997), Salas et al. (1999), O'Dell (2001)). It was later found that this was due to an error in the instrumental software, and therefore we can only determine relative velocities between the regions measured, not the local standard of rest velocities, that is, v$_{lsr}$. For consistency with other data for Orion, we have chosen to assign to the mean velocity of all our observations a value of 12±6 kms^{-1}, in the local standard of rest as provided through data in Chrysostomou et al. (1997); Salas et al. (1999) and O'Dell (2001). This has been achieved by adding 68kms^{-1} to all velocities. There is no significance to be attached to this value. All values of velocity quoted or shown in figures are v$_{lsr}$ as derived on this basis. Since we are essentially concerned only with the relative velocities of regions within OMC1, the uncertainty in the value of v_{lsr} is not material to the discussion. The resulting radial velocity map is shown in Fig. 2.11.

In the treatment of the data described above, all regions are rejected for which no peak can be found in the data for a cut through the velocity channels. If a double peak (say) is encountered, which is the case in only 2% of the profiles, then we record a fit only to the stronger of the two peaks. This procedure rejects relatively weakly emitting fast moving objects superimposed on slower brighter objects. This is however a rare occurrence and we are aware of only two such cases: (i) the emission feature around position 24.″2W 6.″5N of TCC0016, whose velocity profile, taken from Chrysostomou et al. (1997) and shown in Stolovy et al. (1998), has a strong low velocity component and a weak high velocity component differing by 80kms^{-1}. Emission at this position is indeed observed in the high velocity channel map centered around a nominal wavelength of 2.119909μm. (ii) at -19.″7E 16.″2N where we observe the object HH208 at a radial velocity of -19kms^{-1}. HH208 has however been identified as a bullet, on the basis of associated FeII emission, with a radial velocity between -120 and -180kms^{-1}(Axon & Taylor 1984; O'Dell et al. 1997b).
These data, including both the brightness map and velocity map (Figs. 2.8 and 2.11), will be referred to as the CFHT/GriF data. The main part of analysis presented in this thesis is based on these data. In Chapter 4 we analyse the spatial and velocity structure of 19 distinct emitting regions and in Chapters 5 and 6 we use the velocity information of these data to perform a statistical analysis of the turbulent motions. In Chapter 8 we use the CFHT/GriF data to detect characteristic scale sizes of emission in OMC1.

2.5 VLT/NACO-FP 2004

Additional observations of OMC1 were obtained with the VLT/NACO-FP on the nights of December 3rd-5th 2004, by Jean-Louis Lemaire and myself. During this run three H_2 lines, namely the v=1-0 S(1) line, the v=1-0 S(0) line and the v=2-1 S(1) line, were scanned in three regions, see Fig. 2.3. The v=1-0 S(1) line was however not scanned in region E. The NACO-FP is a cryogenic Queensgate Fabry-Perot mounted in the collimated beam of the near-infrared camera CONICA which is fed by the NAOS AO system (Hartung et al. 2004). The CONICA camera including the FP is positioned in a vacuum chamber cooled by liquid nitrogen. The vacuum wavelengths of the H_2 lines can be found in Table 2.1 (Bragg et al. 1982). The FP has a finesse of 26 and a spectral resolution of $\sim$ 1000, that is 2 nm or 300kms^{-1} in the region of interest. The S27 camera of CONICA, which was used, has a field of view of 28″$\times$ 28″ and a pixel scale of 27.15 mas.
The visible wavefront sensor was used in all observations. In the N field Parenago 1819 ($m_V \sim 14.4$) was used as AO reference star. TCC0016 ($m_V \sim$

14) was used in the E field and Parenago 1839 ($m_V \sim 14.6$) in the W field.

Scans of the three H_2 lines were performed from a wavelength in the far blue wing of the profile to a wavelength in the far red wing. The transmitted wavelength of NACO-FP is a strong function of the distance from the focal point, that is, the phasemap is strongly curved, see Fig. 2.7, with a difference of about 8 nm from the focal point to the edge of the detector. Thus the scan should start 3 to 4 nm to the blue of the centre wavelength and extend to 7 to 9 nm to the red to cover the whole line profile in the whole field of view. The number of channel maps in each scan was 15-18. For the v=1-0 S(1) line an exposure time of 120 seconds in each channel map was used (Table 2.3). The v=1-0 S(0) and v=2-1 S(1) lines are approximately 4 and 9 times weaker than the v=1-0 S(1) line, respectively, and therefore longer exposure times are necessary to keep the S/N ratio reasonably high. As mentioned before the AO system should not be kept in closed-loop observations for more than one hour. This limits the possible exposure times since a full scan should be performed without re-locking the AO. Otherwise the FP should be re-calibrated. Exposure times of 120 and 240 seconds were used and several scans of the two weak lines were obtained to increase the S/N ratio. The total exposure time was 480s for both lines in the N and W fields. Due to time restrictions the total exposure time was 120s in the E field (Table 2.3). Wavelength calibration of the FP was done before each scan by scanning the Ar line at 2.0992μm using the S54 camera. The S54 camera was used because a scan can be made faster with this camera than the S27. Phase maps for the S27 camera were constructed from scans of the Ar line using the S27 camera on the first and third night. Since NACO-FP is located at the Nasmyth focus, telescope flexures do not influence the instrument and phase maps remain largely invariant in time. Darks and flatfields were obtained during daytime calibrations for the same reason.

2.5.1 Reduction of VLT/NACO-FP data

The spatial drift during a scan was calculated in each data cube by fitting a two-dimensional gaussian profile to the stellar emission in the field. The peak position of the gaussian, which is found with subpixel accuracy, is taken to be the stellar position. In this manner the positions of four stars have been found in each channel map of every data cube. The maximum drifts in x- and y-direction between the channel maps of the scan are listed in Table 2.3 for all scans. For half of the data cubes we find that the drift is less than 3 pixels when measured as the total length of the drift in both the x- and y-direction. The drift of 3 pixels is comparable to the diffraction limited resolution of the telescope (2.4 pixels), which was in fact never achieved in

Region	Line	scan nr	exp. time /s	spatial drift /pixel x-direc.	y-direc.	FWHM (arcsec)	wavelength range (nm)	spectral drift[a] (nm)
N	v=1-0 S(1)		120	2	0	0.27	9.74	0.04
	v=1-0 S(0)	1	240	2	2	0.18	10.47	-0.22
	v=1-0 S(0)	2	240	3	2	0.18	15.31	-0.13
	v=2-1 S(1)	1	240	4	2	0.24	10.60	–
	v=2-1 S(1)	2	240	3	1	0.15	15.42	-0.16
W	v=1-0 S(1)		120	1	1	0.17	13.25	0.20
	v=1-0 S(0)	1	120	3	1	0.14	15.31	0.13
	v=1-0 S(0)	2	120	3	1	0.13	15.31	0.32
	v=1-0 S(0)	3	120	2	0	0.12	15.31	-0.04
	v=1-0 S(0)	4	120	2	0	0.10	15.47	-0.28
	v=2-1 S(1)	1	120	2	0	0.12	15.26	0.01
	v=2-1 S(1)	2	120	2	2	0.17	15.26	-0.11
	v=2-1 S(1)	3	120	4	1	0.23	15.26	-0.27
	v=2-1 S(1)	4	120	5	6	0.12	15.42	-0.32
E	v=1-0 S(0)		120	4	2	0.15	15.47	-0.18
	v=2-1 S(1)		120	2	1	0.13-0.24	6.91	0.0

Table 2.3: Parameters for the 16 scans performed with VLT/NACO-FP: exposure time for each channel map, spatial drifts measured from position of stars, average FWHM of the PSFs from stars, wavelength interval of scan, estimated spectral drift during scan.
[a]: minus signs indicate that the spectral drift has truncated the wavelength range. Positive values indicate expansion.

these observations. In the other half of the scans the drift is generally between 3 and 6 pixels, but may be as large as 8 pixels. The data cubes should be re-aligned if the drifts are larger than the spatial resolution.

The spatial resolution in each channel map has been estimated by the FWHM of the stars within the field in question. In Fig. 2.12 the measured FWHM of stars in a scan of the W region in the v=2-1 S(1) line are displayed. The top panel of the figure shows the FWHM of the ten stars within the region for all 17 channel maps of the scan. The FWHM of each star is connected by a line. It is seen that the FWHM varies from channel map to channel map and that the relative size of the FWHM of the stars also varies. As an example look at the two stars marked with the red and green lines. In some channel maps the FWHM of the red star is greater than the FWHM of the green star. In other channel maps the FWHM of the green surpasses that of the red star. Thus there are no clear indications that the isoplanatism cause differential resolution throughout the field of view. If this was the case the stars located far from the AO reference star would be expected to yield continuously larger values of the FWHM than the stars closer to the reference star. This does not seem to be the case. The bottom panel in Fig. 2.12 shows the average FWHM of the stars plotted as function of the distance to the reference star Parenago 1839. Again there is no dependence of the FWHM on the distance.

We estimate the spatial resolution in each channel map by the average of the FWHM of all the stars in the field. The average FWHM as a function of channel map is shown in Fig. 2.12(centre panel). The spatial resolution varies throughout a scan since the AO has not been able to maintain the same correction for all channel maps. Since the peak emission and radial velocity is found from fits that involve all channel maps, the final spatial resolution cannot be expected to be better than some average value of the FWHM within a scan and may not be better than the largest value in some regions. For reference we quote the largest value of the FWHM obtained in a channel map. In the data shown in Fig. 2.12 this corresponds to a spatial resolution of $0\farcs12$ about twice the diffraction limited resolution of VLT. In Table 2.3 the estimated resolutions of all 16 scans carried out are listed. In the E field, where the AO reference star is located outside the field of view, there is some evidence of differential resolution. This is most clearly evident in the scan of the v=2-1 S(1) line and therefore the resolution of this scan is listed as a range of resolutions.

Although the spatial drift in most cubes is smaller than the resolution we choose to treat all data cubes similarly and re-align all cubes. Thus the channel maps are initially dark subtracted and flat-fielded. The same flat-field is used for all channel maps irrespective of the wavelength in contrast to the reduction performed on the CFHT/GriF data in Sect. 2.4 where a

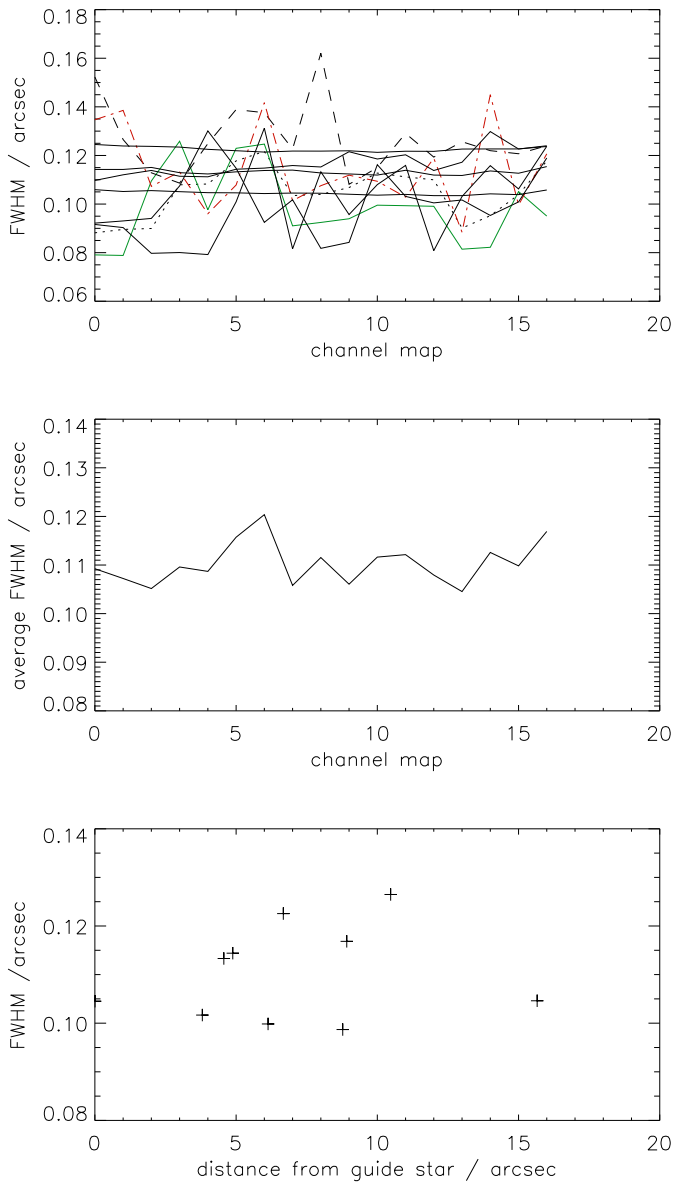

Figure 2.12: Measured FWHM of stars in the W region from a scan of the v=2-1 S(1) line. **Top:** FWHM of ten stars in the field measured in each of the 17 channel maps. **Centre:** Average FWHM of the ten stars above. **Bottom:** Average FWHM of the stars as a function of displacement from the reference star Parenago 1839. The FWHM is averaged over all channel maps.

specific flat-field was obtained for each channel map. This procedure is chosen because the wavelength dependency of the sensitivity of the pixels is very small within a scan. Bad pixels in the channel maps are replaced using the SIGMA_FILTER procedure. The data cubes are re-aligned at the subpixel level by expanding each channel map 10 times in (x, y) and then shifting them so that the stars are at the same spatial position. Afterwards the channel maps are shrunk to the original size. Finally the continuum emission found in the first channel map of the scan is subtracted.

2.5.2 Methods specific for NACO-FP

The conversion between plate separation, z (in FCU) and wavelength is given by (Hartung et al. 2004):

$$z = \frac{1}{B}(m\lambda + 2\delta(\lambda) - A) + C \tag{2.12}$$

The values of $A, B, \delta(\lambda)$ are very stable and the precise values can by found in Hartung et al. (2004). The constant C reflects the offsets caused by drifts and should be measured frequently during observations. Before each science scan an Ar line was measured for the purpose of wavelength calibration (see Sect. 2.3.2). From this scan the constant C can be determined and Eq. (2.12) used to transform plate separation in z-values into wavelength.
Prior to the determination of velocities the phase map has to be calculated from the Ar line scan. The phase varies as a parabolic function over the field of view (Sect. 2.3), however the calculated phase map shows a substructure, that is, small wiggles superposed on the parabolic shape (Fig. 2.13). This substructure is due to interference from reflections off the outer sides of the FP and is a result of the plane parallel design. The substructure is also seen in Fig. 2.7a,b where intensity wiggles are clearly visible in the transmission rings. Note that the plate separation is typically 40μm while the thickness of the etalon plates themselves is roughly 1cm. It is evident from Eq. (2.5), $m = \frac{\delta}{2\pi} = \frac{2nd\cos\theta}{\lambda}$, that the difference in inclination angle between adjacent orders for a monochromatic source is much smaller for the interference pattern arising from within the plates than from the cavity. Furthermore the reflectivity of the outer sides of the plates is very low. Thus the effect is seen as a substructure on the main interference pattern with small intensity variations.
It is also evident from Eq. (2.5) that the wavelength difference corresponding to a displacement of one order ($\Delta\delta = 2\pi$) is given by $\Delta\lambda \sim \frac{\lambda^2}{2nd\cos\theta}$. This is called the free spectral range and has a value of $\sim$ 2nm for the etalon plates. If the light source is polychromatic and the wavelength distribution

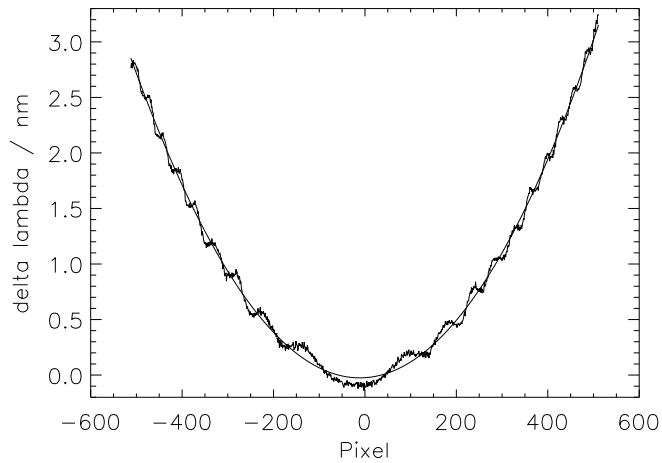

Figure 2.13: Phase map from VLT/NACO-FP, horizontal cut. Substructures arising from reflections off the outer sides of the plates are seen superimposed on the parabolic shape. The smooth parabolic phase map (smooth line) is found from a polynomial surface fit.

is broader than the free spectral range, different orders from different wavelengths will mix and the interference pattern smear out. That is, if the width of the emission line approaches the free spectral range the wiggles smear out. Thus wiggles should not be present for lines broader than ~ 1 Å and in general astronomical data should not be affected by this phenomenon since the intensity variations are small and lines often are broad.

The phase map corresponding to the interference from the cavity is extracted by making a polynomial surface fit to the phase map, with wiggles. The result is shown in Fig. 2.13 as the parabolic curve.

Using the relation between z-value and wavelength and the phase map the radial velocities can be found for each scan by fitting lorentzians to the spectral profiles as described for the CFHT/GriF data. However it is found that when velocities are deduced from different observations of the same region and H_2 line, for example from the four scans of the v=2-1 S(1) line in the W region (Fig. 2.3), the results are different and velocities differ by as much as 25kms^{-1}. This is most likely due to spectral drift of the interferometer during scans. The effect of drifts can be estimated by the C-constant (Eq. (2.12)) which was found from calibration scans before each science scan. If drifts occur, the C-value changes and it might be more appropriate for the last channel map to use the C-value found using the calibration scan performed after completion of the scientific scan. In Table 2.3 the total spectral drift

has been estimated as the difference in wavelength of the last channel map calculated using C-values calibrated before and after the scan.
Assuming that the drift occurs linearly during the scan we can recalculate the wavelengths corresponding to each channel map and the radial velocities. It is now found that the velocities derived from different scans is found to agree within a few kms^{-1}.
In order to increase the signal to noise of the weaker lines (1-0 S(0) and 2-1 S(1)) the 2 to 4 scans we have obtained of the same line in the same region were added. In order to be able to add the scans it is necessary to transform the xyz-cubes, with planes of constant z-value where the transmitted wavelength depends on xy-position, into $xy\lambda$-cubes with planes of constant transmitted wavelength. This is done by cubic-spline interpolation and using the phase map. When all xyz-cubes have been transformed into $xy\lambda$-cubes with the same λ-values the brightness can be added plane by plane. Hereafter the radial velocity and the total brightness are found from lorentzian or gaussian fits as in the case of the CFHT/GriF data. Images of the brightness and the radial velocity maps can be found in Figs. 2.14-2.19.
The spatial resolution of the VLT/NACO data, especially of the v=1-0 S(0) and the v=2-1 S(1) line (Table 2.3), is higher than for the CFHT/GriF data and the brightness maps show considerable more detail. The two data sets are compared in Fig. 2.20, showing details of a bowshock located (-21″, -6″) relative to TCC0016 and assumingly moving towards the south-east. The H_2 emission is seen to be broken up and "spotty" in the VLT/NACO-FP data, whereas the CFHT/GriF data look more uniformly emitting. The velocities derived from both data sets peak behind the maximum emission.
Images of the continuum emission are extracted from channel maps far out in the wing, that is, generally the first channel map of a scan. In Chapter 3 we consider the continuum and show the first detection of IRc2-C and 4 compact sources at 2μm.

2.5.3 Wiggles in the velocity maps

By close inspection, concentric rings can be seen in the velocity maps, especially in that of v=1-0 S(1) in Fig. 2.15. The centre of the rings coincide with the centre of the wiggles seen in the phase map and we conclude that the rings originate from the same effect, that is, reflections from the outer sides of the plates of the interferometer. There exists two possibilities as to why this occurs. One possibility is that the H_2 lines observed are narrower than 1 Å $\sim 14\mathrm{kms}^{-1}$. If that is the case the extra fringes can come from the H_2 line emission itself. The second possibility is that they come from OH Meinel lines, which are usually very narrow. If skylines exist closer to the H_2 lines than the spectral resolution of the FP they can be mixed together.

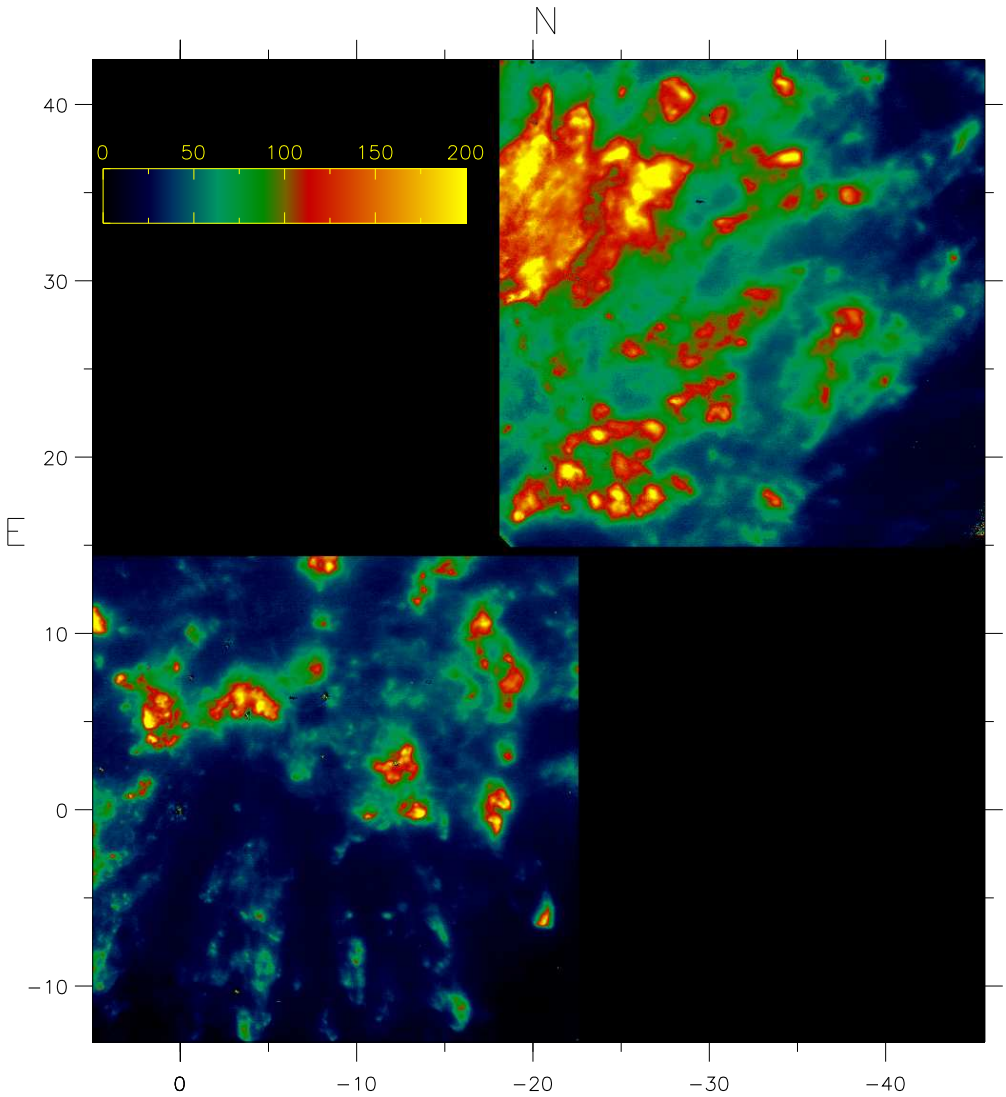

Figure 2.14: Brightness map of the v=1-0 S(1) H_2 line from VLT/NACO-FP. The colourbar indicates count rates per 120s.

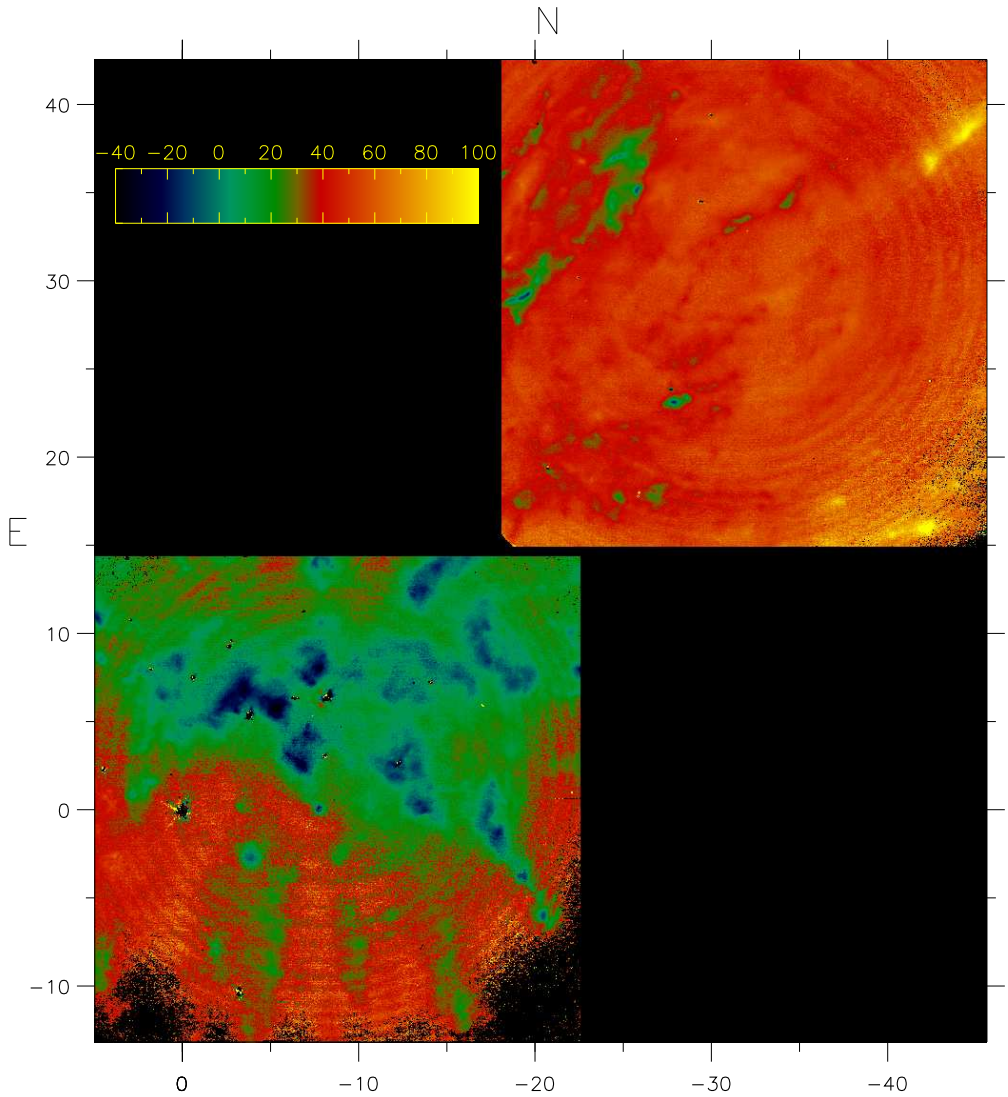

Figure 2.15: Velocity map from the v=1-0 S(1) H_2 line from VLT/NACO-FP. The colourbar indicates radial velocity in kms^{-1}.

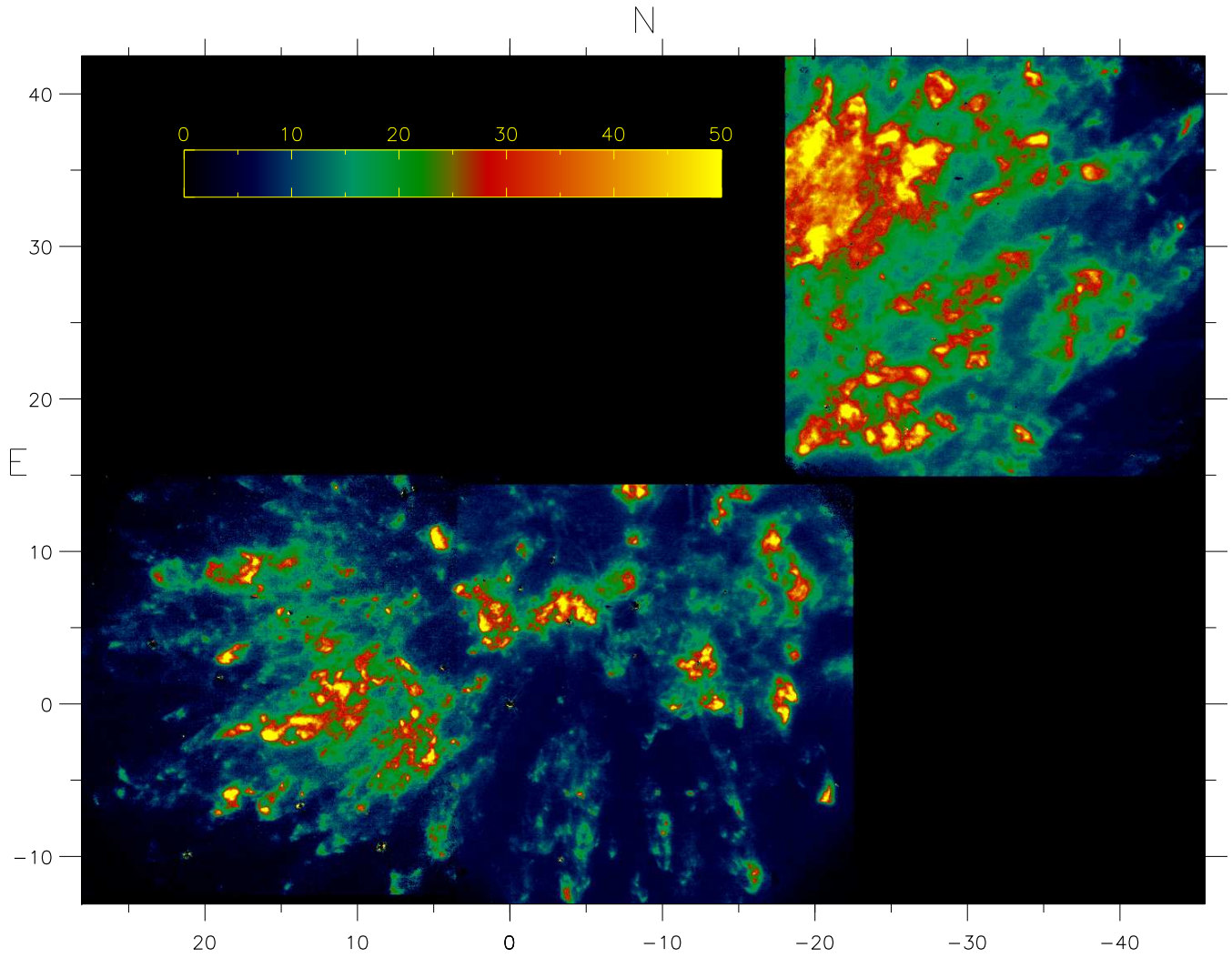

Figure 2.16: Brightness map of the v=1-0 S(0) H_2 line from VLT/NACO-FP. The colourbar indicates count rates per 120s.

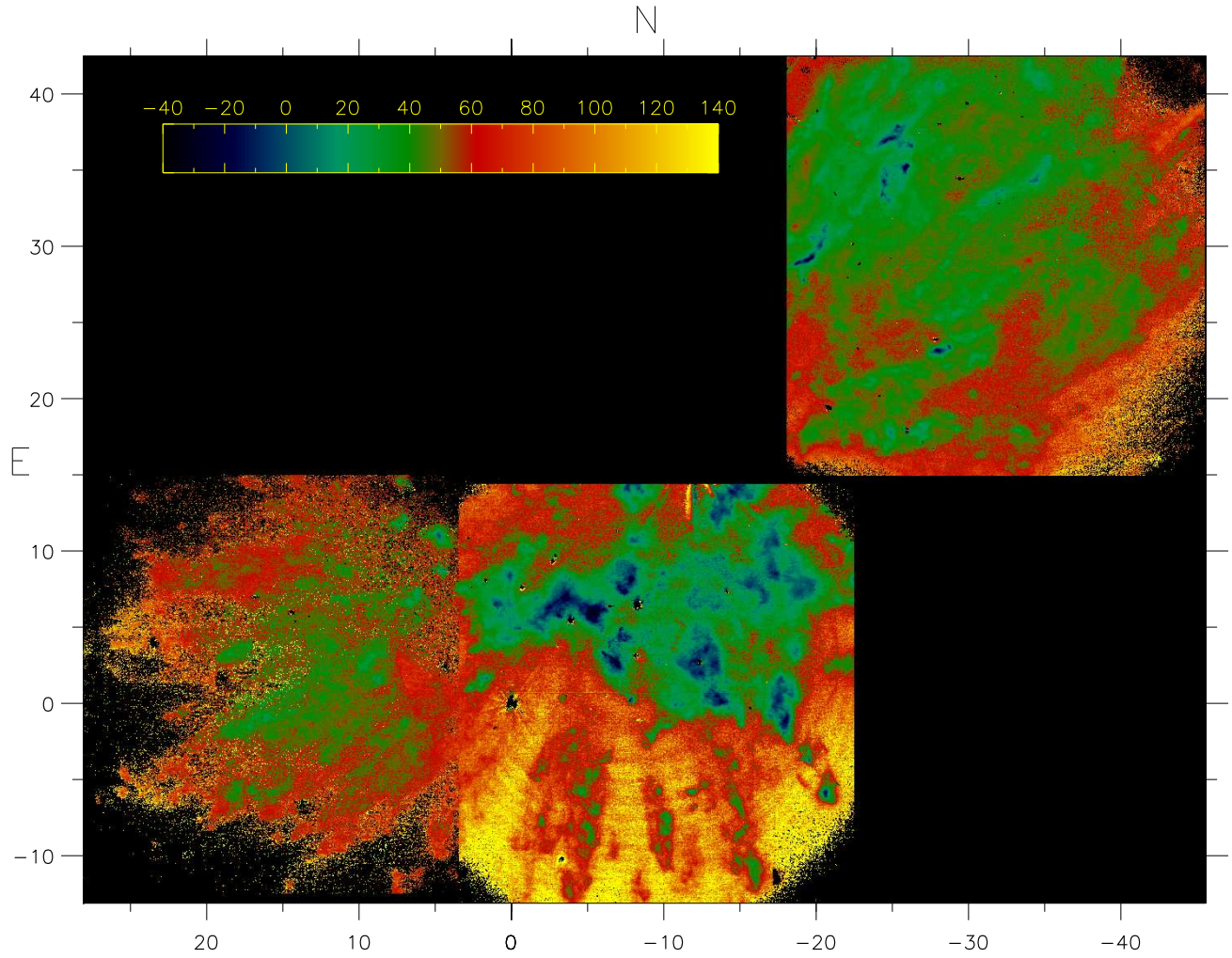

Figure 2.17: Velocity map from the v=1-0 S(0) H_2 line from VLT/NACO-FP. The colourbar indicates radial velocity in kms^{-1}.

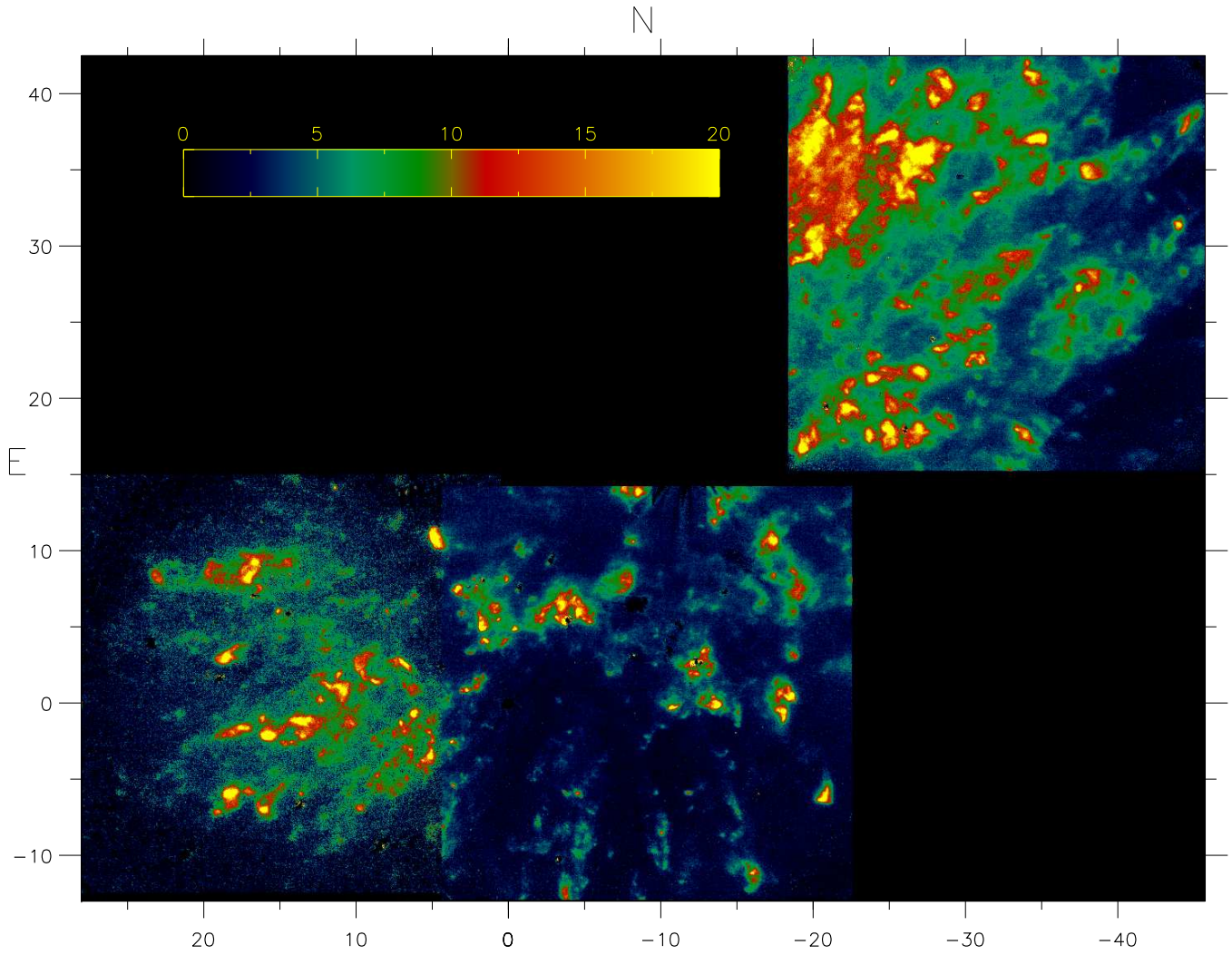

Figure 2.18: Brightness map of the v=2-1 S(1) H_2 line from VLT/NACO-FP. The colourbar indicates count rates per 120s.

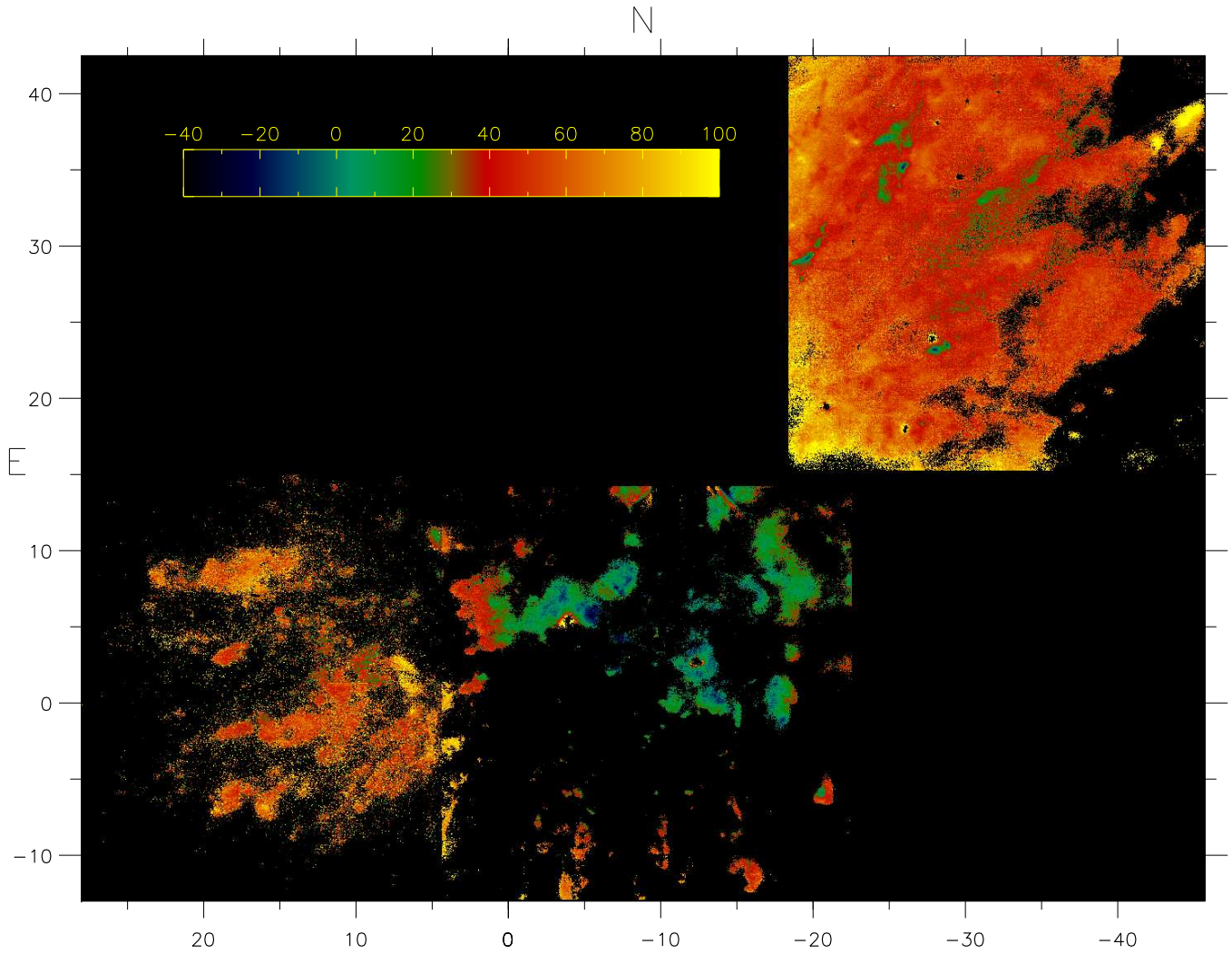

Figure 2.19: Velocity map from the v=2-1 S(1) H_2 line from VLT/NACO-FP. The colourbar indicates radial velocity in kms^{-1}.

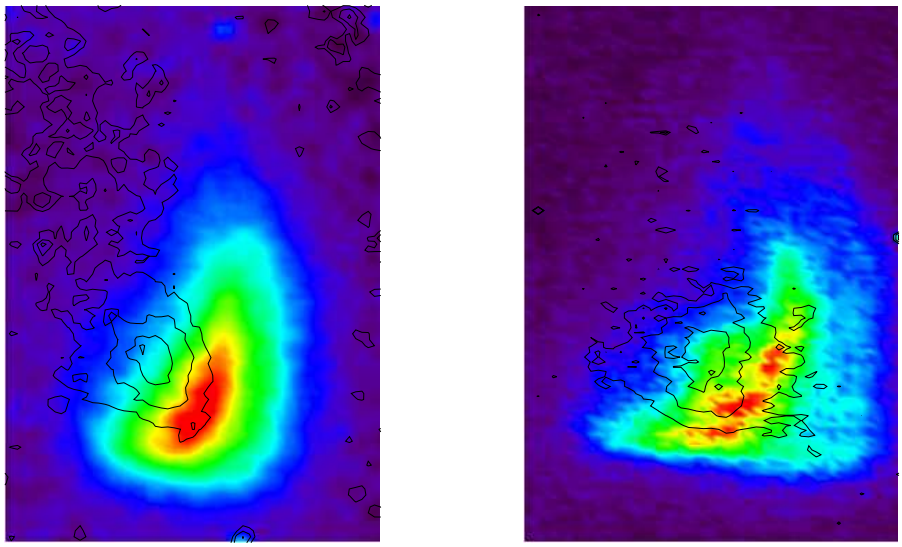

Figure 2.20: Details of bowshock at (-21″, -6″) relative to TCC0016, see Fig. 2.16. **Left:** CFHT/GriF brightness data with contours of velocity. **Right:** VLT/NACO-FP brightness data of the H_2 v=1-0 S(0) line with contours of velocity.

Skylines from OH do exist close to the H_2 lines, compared to the spectral resolution and curvature of NACO-FP, and in some scans emission from such skylines (with wiggles) can be seen in the field of view clearly separated from the H_2 emission. However, for all three H_2 lines observed, there is a OH line only $\sim$ 2nm away, which corresponds to the resolution of the FP. Unfortunately we were not aware of the problem at the time of observations and therefore we did not spend time on sky observations. Furthermore weak extended H_2 emission is present everywhere in OMC1 and it is not possible to find empty regions from which to extract sky spectra. Thus it is impossible directly to remove the contributions from skylines and this also excludes any possibility of determining whether the wiggles are caused by the H_2 lines or skylines. The intensity variations from the wiggles in the H_2 emitting regions are too small to be detected directly in the channel maps, but are apparently strong enough to show in the velocities.

With a great deal of help from Markus Hartung, ESO, we tried to remove the wiggles by various methods, but with little success. For completeness these different attempts will be described briefly here. In principle it is possible to simulate the response of the FP to a monochromatic light source, taking reflections from all surfaces into account. This requires detailed knowledge of the reflectivity of all surfaces, the width of the etalon plates, the plate

separation and the focal length of the camera. Except for the reflectivity of the cavity sides and the plate separation these are all poorly determined parameters. Further complications might arise if the plates are not completely parallel. Using an IDL-programme from Markus Hartung to simulate the response, we tried to fine tune the missing parameters by comparing the simulated output to the calibration scan of the Ar line. In that scan the only light source is a very narrow Ar line. This seemed like the perfect test case. However it turned out to be impossible to find a set of parameters which allowed the simulated response to match the real data for all plate separations used in the Ar scan. This could be due to small changes in the parallelism of the plates, which cannot be measured.

We also tried to Fourier transform the individual channel maps. The idea was that since the wiggles appear in an almost fixed pattern they should only contribute to a specific range of frequencies. If those frequencies are removed, the wiggles should be gone. Note that removing certain frequencies is really a filtering or smoothing of the image. Again the result was not satisfactory. In order fully to remove the wiggles a large range of frequencies were removed, which decreased the spatial resolution substantially.

In conclusion we did not succeed in removing the wiggles in the velocity map. It is not clear whether they arise from the H_2 lines or from mixing OH skylines or a combination. Skylines do however not appear to be very strong, a few counts at the most compared to hundreds of counts in the v=1-0 S(1) line. Thus I think it is most likely the H_2 lines that are narrow enough to cause the problems. This question will however not be settled without new observations. Wiggles are very clear in the velocity maps derived from the v=1-0 S(1) line. Wiggles are weak but present in the v=1-0 S(0) line, but the velocity maps derived from the v=2-1 S(1) data do not seem to be afflicted by wiggles. However before we find the cause of the wiggles all velocity maps should be regarded with some caution. It is probably safe to trust relative velocities in small local regions, but not relative velocities from distant regions. The wiggles could affect the brightness maps as well. However, as mentioned above, the wiggles in the channel maps are very faint and seem to have little impact on the brightness.

Due to the wiggles in the velocity maps these VLT/NACO-FP data can unfortunately not be used in a full scale statistical analysis as the CFHT/GriF data. The velocity data combined with brightness data will, however, be shown in a few detailed regions in Chapter 4 in order to illustrate interesting velocity features. Where presented the VLT/NACO-FP data show more detail than the CFHT/GriF data of poorer spatial resolution, as seen in Fig. 2.20. The brightness data, which are unaffected by wiggles, are used in Chapter 8 to confirm the characteristic scale sizes detected in the

CFHT/GriF.

2.6 The lesson to be learned when using FPs

Fabry-Perot interferometers are very powerful instruments and when they are combined with adaptive optics systems, as here, the output data can be quite extraordinary. Using the full field of view to observe extended objects, as we have done, is challenging but the extra effort to obtain good phase maps is well rewarded by data containing both brightness and velocity information.

That being said, there are some aspects to contemplate further. It has been seen above in both data from CFHT/GriF and VLT/NACO-FP that spectral drifts can be significant during a scan. If precise velocity determination is one of the primary goals the wavelength of the FP should be calibrated more frequently than in the present data.
Sky emission lines can interfere, especially in low resolution interferometers. Sky should always be observed at the same wavelengths that are used in the science scans. FP observations with AO are very time consuming and it might be tempting to cut down on calibrations and sky observations. However it is worth spending the extra time as it may very well be the extra calibrations that validates your data.
Based on the experience from CFHT/GriF and VLT/NACO-FP the optimal observing sequence would be: - wavelength calibration using Ar lamp. - One exposure of target - move to sky and repeat exposure - move back on target and wavelength calibrate - take exposure of target at new wavelength - etc. This approach assure precise wavelengths in all channel maps and real time sky observations, but is a very time consuming procedure. Alternatively one could do 2 or 3 channel maps on target before moving to sky. Then if the next calibration shows a big shift one would throw the last channel maps away. Depending on the stability of the FP this may be a better option.

Chapter 3

Continuum emission from the VLT/NACO-FP

The origin of continuum emission at 2μm was discussed in Sect. 1.5.2. Here we compare our data for the continuum at 2.2μm, as extracted from the VLT/NACO-FP data (Sect. 2.5), with existing observations. We show the first detection of IRc2-C at wavelengths shorter than 3.8μm and find two new sources not previously detected in JHK or L band (Hillenbrand & Carpenter 2000; Muench et al. 2002; Lada et al. 2004) or in X-ray emission (Grosso et al. 2005).

Figure 3.1 shows the continuum at 2.2μm close to the H_2 v=1-0 S(0) line. Many stars are detected, however as flux calibration have not yet been attempted for these data no absolute flux values will be given. In order to compare with stars previously detected in the region we have plotted the position of sources detected in IR, JHKL bands, by Muench et al. (2002) (MLLA from now on, triangles) as well as X-ray sources from COUP (diamonds, Grosso et al. 2005) where these do not correlate with MLLA sources. We detect compact continuum emission corresponding to point sources in most locations corresponding to a MLLA source. However, in 8 regions there is only diffuse emission at 2.2μm at the position of a MLLA source. The positions of these 8 regions are listed in Table 3.1. 6 of the positions, excluding MLLA 578 and 615 (IRc2-B), are associated with zones of high H_2 emission possibly tracing shocks from outflows from embedded objects (see Chapter 4). Four MLLA sources are undetected.

We detect compact point-like emission from four sources previously undetected at IR wavelengths. These are indicated in Fig. 3.1 by squares and labeled 1-4. The four sources are present in all channel maps obtained of the area. That is, the detected emission is not line emission but continuum and is not due to bad pixels. The coordinates are listed in Table 3.2. Two of the four sources are also detected in the COUP survey which suggests that

Source	RA	DEC	MLLA
1	18.47	-5.99	553
2	15.77	-2.16	561
3	1.73	4.97	594
4	-3.89	0.54	572-a
5	-6.26	9.72	615
6	-14.42	1.84	578
7	-18.74	27.43	686
8	-20.68	-6.05	552

Table 3.1: Position in arcseconds relative to TCC0016 of eight regions of extended diffuse continuum emission at the position a MLLA source (Muench et al. 2002). The MLLA designation is stated.

Source	RA (J2000) (5^h35^m)	DEC (J2000) ($-5°22'$)	COUP
1	15.35	26.5	
2	15.18	29.6	681
3	15.09	31.5	678
4	13.58	09.8	

Table 3.2: Coordinates of four compact sources previously undetected at IR wavelengths and the number designation for the two sources detected in COUP. Positions relative to TCC0016 are indicated in Fig. 3.1.

they are embedded young stellar objects. One the of new sources (number 4) is associated with H_2 emission extending from the source in a fan-like shape. This could be produced by a bipolar outflow with a large opening angle, which again suggests an early evolutionary state of the central object (Sect. 1.1.5). The H_2 outflow structure will be shown in Chapter 4 (Fig. 4.8).

A large region of diffuse emission is seen in the eastern part of the field centered on 13″E, 10″N, just north of Peak 2. This is most likely scattered light from dust as described in Sect. 1.5.2. Very little H_2 emission is seen in this region where the continuum emission is strong as a comparison with Fig. 2.16 will reveal. This suggests that the H_2 emission in the northern part of Peak 2 is partly obscured by dust.

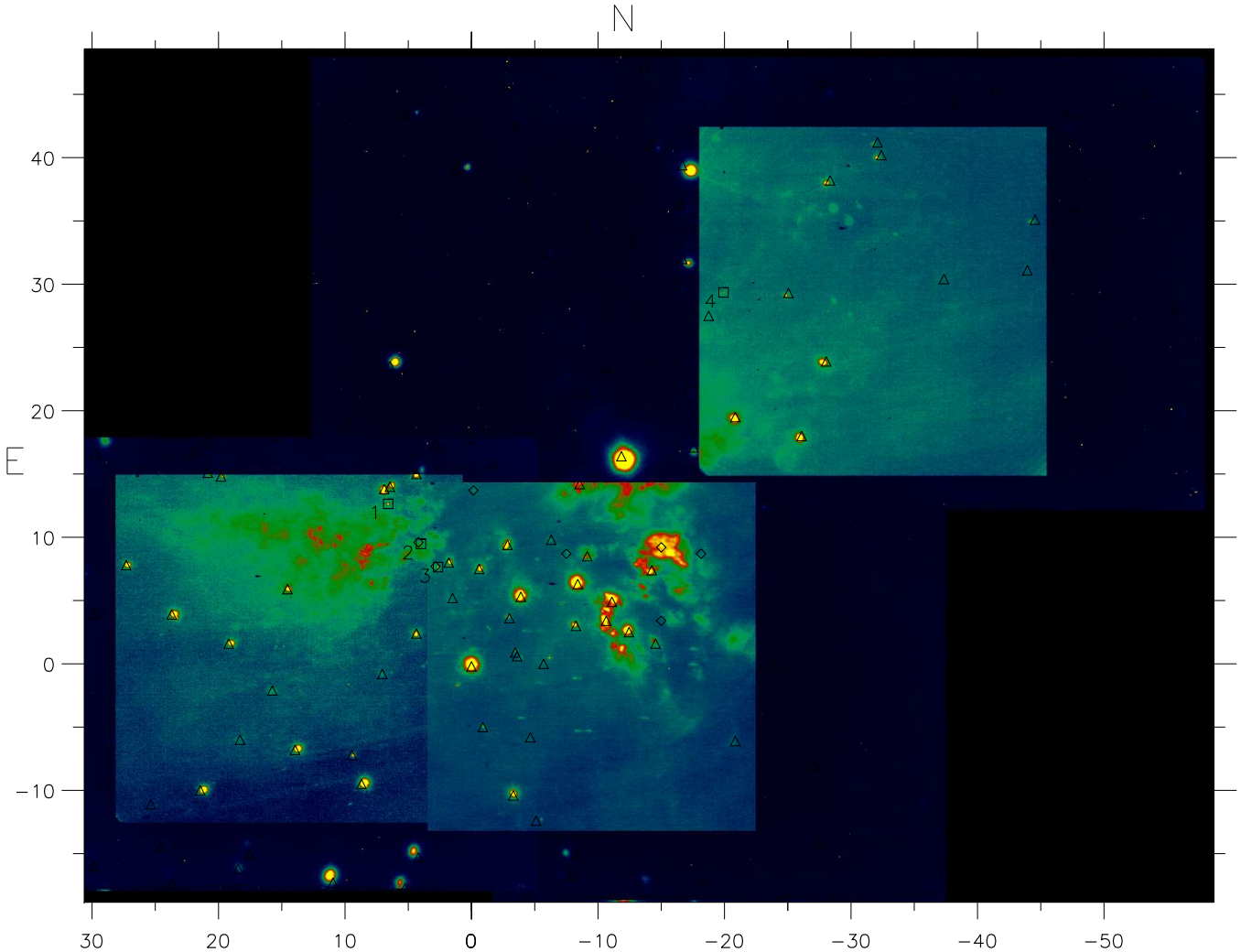

Figure 3.1: Continuum emission at 2.22μm extracted from the VLT/NACO-FP data. △: point sources at 3.8μm from Muench et al. (2002). ◇: X-ray sources from Grosso et al. (2005). □: New sources.

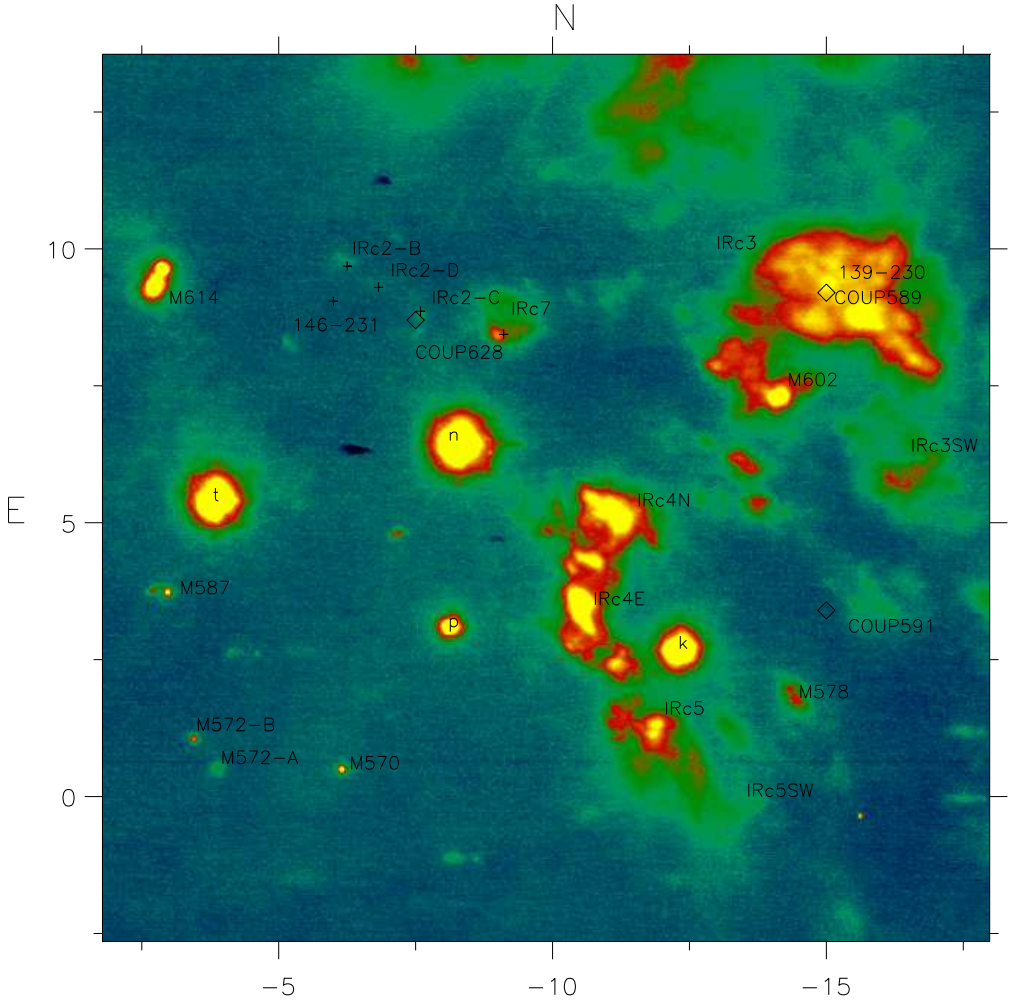

Figure 3.2: Continuum emission at 2.22μm extracted from the VLT/NACO-FP data. COUPXXX refer to COUP sources, MXXX refer to MLLA sources, 139-230 and 146-231 are found in Simpson et al. (2006). The positions of IRc2 (A-D) are from Dougados et al. (1993).

The region around IRc2

South of BN at 11″W, 16″N and west of TCC0016 at (0,0) we see the strong IR sources, IRc2, IRc3, IRc4, IRc5, IRc7 (Gezari et al. 1998; Shuping et al. 2004). A close-up of the region is shown in Fig. 3.2 with MLLA and COUP sources indicated. The figure uses the standard nomenclature for the IR sources n,p,k, IRc2 etc. (Rieke et al. 1973; Lonsdale et al. 1982; Gezari et al. 1998). COUPXXX refers to sources from COUP, MXXX refer to MLLA sources. The positions of the four knots of IRc2 resolved at 3.8μm (Dougados

et al. 1993) are also plotted in Fig. 3.2. We find diffuse emission at 2.2μm at the position of IRc2-B and IRc2-C. IRc2-B was first detected by Stolovy et al. (1998) at 2.15μm and IRc2-D by Simpson et al. (2006). However, this is the first detection of emission from IRc2-C short-wards of 3.8μm. IRc2-C has also been seen in X-ray (source 628, Grosso et al. 2005), giving a strong indication that the source is a young protostar. As described in Sect. 1.5.2 Simpson et al. (2006) found that IRc2-B and D are deeply embedded objects. Thus evidence is accumulating for all the IRc2 knots to be protostellar candidates.

We also find diffuse emission at the positions of protostellar candidates identified in Simpson et al. (2006), namely 146-231 and 139-230 using the naming convention for the Orion Nebula from O'Dell & Wen (1994). Object 139-230 is also detected by COUP (source 589).
In Fig. 3.3 we show the continuum emission overlaid with H_2 contours from the v=1-0 S(0) line from which the continuum was extracted. Generally there is very little spatial overlap between continuum emission and H_2 (shocked) emission. One exception is around source k (Lonsdale et al. 1982) where strong H_2 emission is seen overlapping with IRc5. H_2 emission seems to extend from source k in four lobes (Fig. 3.3). Since the H_2 emission is not obscured by the dust it indicates that the exciting source lies in front of the obscuring material, that is, in front of the Orion "hot core" (Sect. 1.4.1).
There seems to be shocked H_2 emission in an arc west of and very close to source n. This could be due to an outflow from that source.
The data presented here together with work by e.g. Muench et al. (2002); Grosso et al. (2005); Simpson et al. (2006) show evidence of many protostellar objects surrounding BN-KL. Many of the protostellar objects detected by Muench et al. (2002) and Grosso et al. (2005) are undoubtedly foreground objects, but some of the sources are intrinsic to BN-KL. These will contribute to the shock-excitation of H_2 in addition to the large scale outflow creating Peaks 1 and 2 (Sect. 1.4.1). In the next chapter we analyse the origin of the H_2 emission in detail.

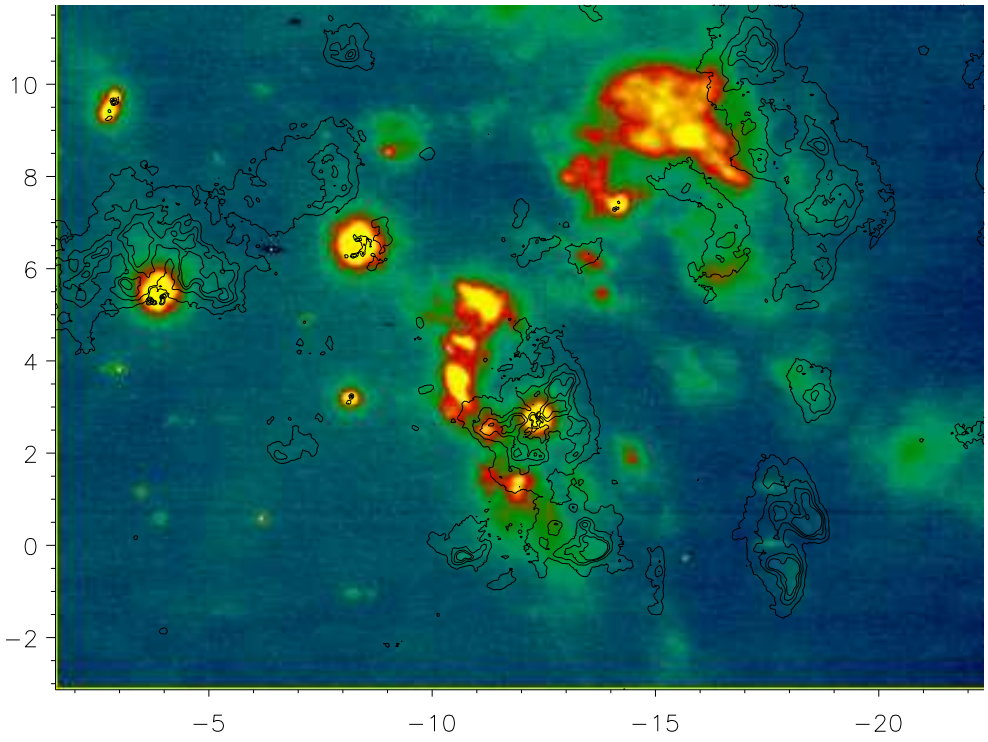

Figure 3.3: Continuum emission at 2.22μm overlaid with contours of H_2 v=1-0 S(0) emission. See Fig. 3.2 for naming.

Chapter 4

Spatial and velocity structure

Here we present the Fabry-Perot data from CFHT/GriF (Sect. 2.4). We exploit the strength of these data, that is, combining velocity and brightness in a 2D region in the plane of the sky, and use it to obtain a detailed view of the relation between velocity and brightness in regions dominated by shocks and outflows. By looking at the motions in the outflow in detail we can obtain a better model for the origin of the H_2 emission than previous data. We develop a simple model of a shock based on geometrical arguments which allows us to determine the direction of the shock in the plane of the sky. This analysis suggests that some regions in OMC1 are excited through local, internal shocks from developed protostars in contrast to being excited by the general outflow.
The results presented here are mainly based on the CFHT/GriF data. Due to the problems associated with the derived velocity maps from VLT/NACO-FP (see Sect. 2.5.3) these data have not been used in a full scale analysis. A few examples from the VLT/NACO-FP data will however be shown in order to illustrate some interesting features.

4.1 General appearance of the OMC1 region

The presence of large scale velocity differences in OMC1 has been known for many years. Sugai et al. (1995); Chrysostomou et al. (1997) and Salas et al. (1999) have all used FP interferometry in OMC1 in the NIR and studied the large scale velocity structure of the hot H_2 component. These earlier studies involved higher spectral resolution, of respectively 14kms^{-1}(Chrysostomou et al. 1997) and 24kms^{-1}(Sugai et al. 1995; Salas et al. 1999), than our data, but all three studies suffered from a lack of spatial resolution, which was 1.″5, 8.″0 and 2.″0 respectively. The image of peak brightness (Fig. 2.8) illustrates that the gas in OMC1 is highly structured with many bright knots. The

results in Fig. 2.11 illustrate the velocity difference between the NW region, so-called Peak 1 (Beckwith et al. 1978) and the SE region, Peak 2. Emission in Peak 1 is found on average to be $\sim$10kms^{-1} more blueshifted than emission in Peak 2. This is in agreement with results in Chrysostomou et al. (1997). This velocity difference has generally been viewed in the context of an outflow mechanism from the IRc2-complex and has previously been explained by an expanding shell (Scoville et al. 1982; Sugai et al. 1995), a bipolar outflow (Chrysostomou et al. 1997) or a spherical wind (Salas et al. 1999).
Comparison between our data and those of specific regions in Chrysostomou et al. (1997) may also be made, bearing in mind the different spatial resolution in the latter work. For example, the blueshifted clumps, cited in Chrysostomou et al. (1997), SW of IRc2, may be seen very clearly in our data, in a region bounded by -15″to -25″E, -5″to 15″N relative to TCC0016. Chrysostomou et al. (1997) also draw attention to redshifted clumps in Peak 2. These are among the most prominent features of our data in Fig. 2.11. Salas et al. (1999) mention that the region around BN-IRc2 appears blueshifted, while the emission is redshifted in Peak 2 and in the direction of Peak 1. The redshifted emission in Peak 1 is not as redshifted as in Peak 2 though, and it appears further from BN-IRc2 than in Peak 2. This area lies to the north of our field, see Fig. 3 in Salas et al. (1999).

4.2 Dynamics of the fast flowing gas

In an initial attempt to extract the wealth of information contained within the CFHT/GriF data we identify 19 distinct emitting regions and analyse these regions with respect to the morphology and velocity of the flow causing the emission. The selection of regions was based on the criteria that the regions should be bright to ensure a high accuracy for the peak velocities in each pixel group (see Sect. 2.4).
In each region the position and value of the maximum velocity and the maximum brightness were determined as well as the spatial displacement between the two. The maximum velocity of the flow was determined as the difference between the maximum velocity in the region and the velocity of the ambient gas estimated from the average velocity of weakly emitting material in the vicinity of the flow. On this basis we are ignoring the overall velocity gradient of the area and are only discussing local flows of shocked gas superimposed on the large-scale velocity field. The nature of the velocity gradient is discussed in detail in Chapter 5. During the analysis it became apparent that some of the regions contained more than one distinct flow. These are named after the region first selected. For example region 1 was found to consist of two flows, 1a and 1b. The results are summarized in Table 4.1.

Object	Location of max brigthness		Location of max velocity		Max bright. counts s^{-1}	Max vel. kms^{-1}	Displacement /arcsec	Pos. angle
1a	25.″8W	36.″2N	25.″6W	36.″5N	2.52	-27	0.4	315°
1b	28.″2W	35.″0 N	28.″3 W	34.″3N	2.75	15	0.7	125°
2	20.″6W	29.″0 N	20.″4W	28.″8N	1.97	-29	0.4	220°
3	4.″6E	11.″0 N	4.″4E	11.″0N	2.91	-21	0.2	60°
4	17.″4W	10.″1 N	17.″3W	10.″1N	1.99	-17	0.1	260°
5	24.″0W	6.″3 N	24.″1W	6.″3N	1.75	-15	0.1	240°
6	15.″9E	1.″6 S	15.″7E	1.″5S	3.43	11	0.3	60°
7	3.″6W	6.″2 N	3.″8W	6.″8N	2.28	-31	0.6	30°
8	8.″7W	14.″7 N	8.″8W	14.″6N	2.37	-20	0.2	150°
9a	6.″3E	0.″5 S	6.″3E	0.″4S	2.36	15	0.2	40°
9b	6.″4E	1.″1 N	6.″7E	1.″5N	1.73	22	0.5	340°
9c	7.″0E	2.″9 N	6.″8E	2.″8N	1.62	27	0.3	120°
10	17.″3W	45.″9 N	18.″3W	45.″1N	2.88	-20	1.3	140°
11	31.″0W	10.″1 S	–	–	1.75	0	–	–
12a	27.″6W	16.″9 N	27.″1W	17.″6N	2.04	-25	0.7	330°
12b	25.″3W	16.″8 N	25.″0W	17.″1N	2.33	-25	0.5	320°
13	36.″4W	33.″4 N	34.″9W	33.″4N	1.19	-16	1.4	270°
14	18.″9W	35.″8 N	18.″5W	35.″0N	2.28	-10	0.9	210°
15	13.″8W	22.″8 N	13.″8W	22.″5N	0.98	-17	0.3	175°
16	18.″0W	24.″0 N	17.″9W	24.″1N	1.23	-20	0.2	290°
17	18.″1W	1.″2 S	17.″8W	1.″8S	1.99	-25	0.7	200°
18	7.″9W	22.″9 N	7.″9W	22.″9N	1.94	-13	0.1	210°
19	16.″3E	6.″4 S	16.″2E	6.″4S	1.67	15	0.1	55°

Table 4.1: Location, peak brightness, peak velocity, spatial displacement between maximum brightness and velocity and position angle of the 19 objects analysed. The location is measured in arcseconds relative to TCC0016 and the peak brightness is given in counts s^{-1} (see Sect. 2.4). The peak velocity is the peak radial velocity with respect to the velocity of the ambient gas. The position angle is measured clockwise from north.

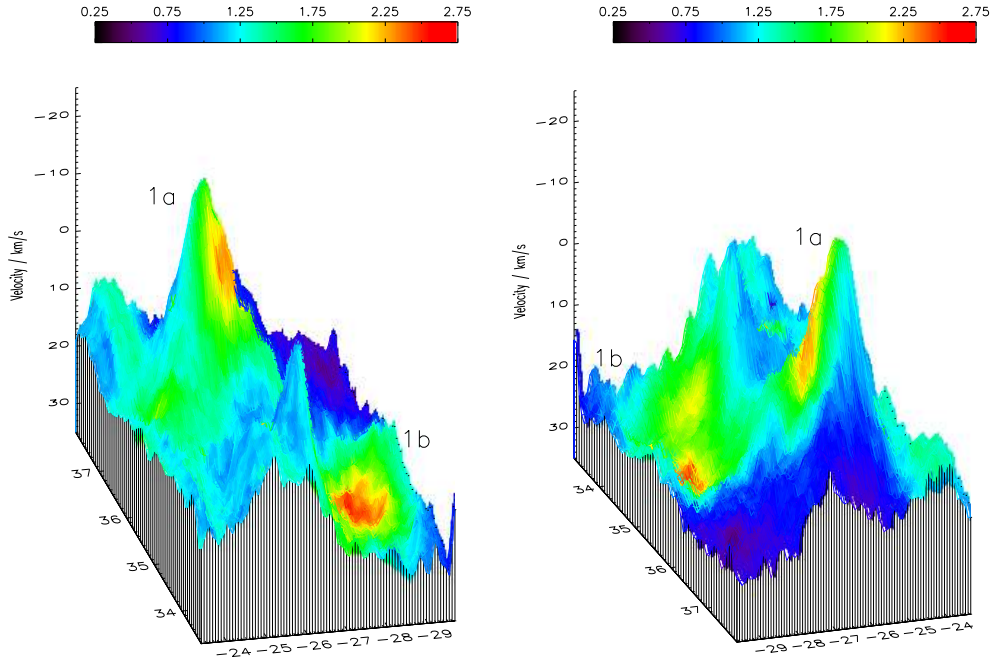

Figure 4.1: Two views of the brightly emitting zones labeled 1a and 1b in Table 4.1. The vertical axis shows the radial velocity relative to the local standard of rest (v_{lsr}). The horizontal plane is the plane of the sky and the centre of this image lies 26.″9W and 35.″6N relative to TCC0016. Colours represent brightness, with the scale shown by the colour bar, in counts per pixel per second. The viewing angle in the lhs image is as seen from the south-east. The rhs image presents a view from the north-west. Taken from Gustafsson et al. (2003).

Representative examples of specific regions are given in Figs. 4.1 to 4.4 in which are shown velocity on the vertical axis, with contours to guide the eye, and the position of the zone in the xy-plane in arcseconds, relative to TCC0016. The colour scale superimposed on the velocity profiles shows the brightness of emission. For purposes of visualization, the brightness scale is different from figure to figure.

The principal features illustrated by data in Table 4.1 and in Figs. 4.1 to 4.4 may be summarized as follows.

(i) There exists strong spatial correlation between flows and emission brightness. However, bright emission may also be found in the absence of detectable velocity shift (object 11, Table 4.1 and Fig. 4.4).

(ii) Velocity maxima are not precisely spatially coincident with brightness maxima. Spatial displacements between velocity and brightness maxima are shown in Table 4.1, where values are seen to range from close to zero, e.g. 0.″1 to 0.″2 in regions 3,4,5,8,9a,16,18,19 to more than 1.″0 in regions 10 and

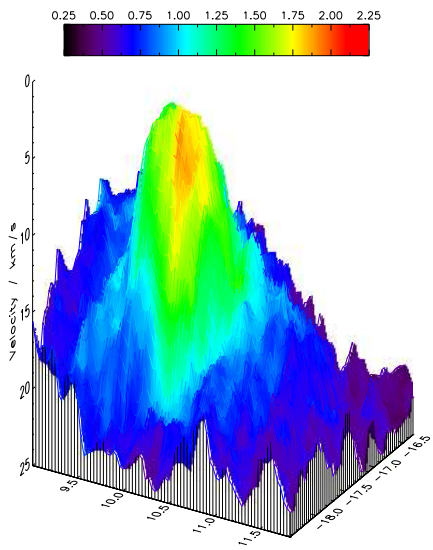

Figure 4.2: The brightly emitting zone labeled 4 in Table 4.1. The centre of this image lies 17.″6W and 10.″1N relative to TCC0016. Otherwise as for Fig. 4.1, but with a viewing angle from the north-west. From Gustafsson et al. (2003).

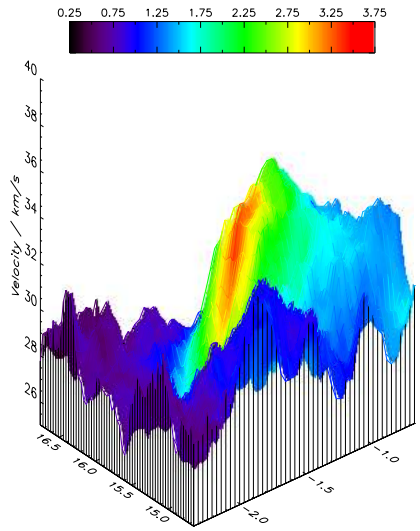

Figure 4.3: The brightly emitting zone labeled 6 in Table 4.1. The centre of this image lies 15.″7 E and 1.″8 S relative to TCC0016. Otherwise as for Fig. 4.1, but with a viewing angle from the south-west. Note that this flow is redshifted relative to the ambient gas. From Gustafsson et al. (2003).

13.
(iii) Brightly emitting regions may lie in close proximity. In Table 4.1, it may be seen that the objects 1a,1b appear very close, as do 9a,b,c and 12a,12b. This is illustrated in Fig. 4.1, where the two bright regions, 1a and 1b (see Fig. 4.6 and Table 4.1), lie $\sim$ 2500 AU apart.
In addition, bright features tend to be superimposed on a relatively weak background emission which pervades large areas of OMC1. The background emission is due to PDRs from θ^1 Ori C and BN (Kristensen et al. 2006), as described in Sect. 1.5.1.
The difference in velocity between the ambient gas and the velocity extrema in the 19 objects shown in Table 4.1 are consistent with the line widths recorded in Chrysostomou et al. (1997). The latter lie between 18 and 45 kms^{-1} with a spatial resolution of 1.″5, where the present values of peak velocity lie between $\sim$ 10 and $\sim$ 30 kms^{-1} in regions of spatial extent of $\sim$ 2.″0 $\times$ 2.″0 (typically). This suggests that the broad line widths observed

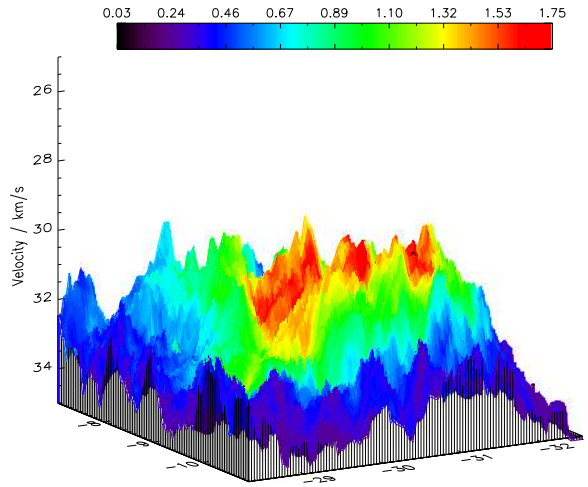

Figure 4.4: The brightly emitting zone labeled 11 in Table 4.1. The centre of this image lies 30.″4 W and 9.″1S relative to TCC0016. Otherwise as for Fig. 4.1, but with a viewing angle from the south-east. From Gustafsson et al. (2003).

in low spatial resolution studies are composed of narrower lines from the constituent gas parcels moving at different velocities. We do not however resolve the narrower lines at the high spatial resolution obtained here but approximate it by the peak velocity. We cannot of course rule out that some features in our data may represent chance superposition in the line-of-sight, rather than spatially coherent structures.

Data in Table 4.1 illustrate the effect of preferentially observing material emerging from the cloud, with the large majority of flows showing locally blueshifted emission. Region 6, in Fig. 4.3 and objects 9a,b,c and 19 are exceptions to this, where objects 9 may be clearly seen as the redshifted group east of TCC0016 in the velocity field illustrated in Fig. 2.11.

4.2.1 Simple model of bow shock

Data are analysed below to show that some of the flows in OMC1, such as those in Figs. 4.1 to 4.4, are local to the regions observed and do not represent components of a large-scale flow. This is in contrast to data for high velocity Herbig-Haro objects whose motion is represented by a general outflow with an origin close to BN-IRc2 (Lee & Burton 2000; Doi et al. 2002; Rosado et al. 2001). Implicit in our subsequent discussion is the assumption that shocks are responsible for the major part of the emission observed in these bright regions, as discussed in Sect. 1.5.1.

A simple model of a bow shock has been developed to interpret the data

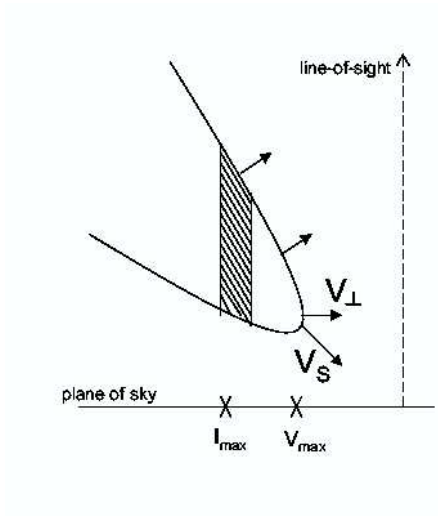

Figure 4.5: Illustration of the shock model. The shocked gas moves with $V_{S\perp}$ of the shock velocity V_S. The radial velocity depends on the orientation relative to line-of-sight. Maximum intensity depends on column density in the shock gas. A vector from maximum intensity to maximum velocity defines the direction of the flow in the plane of the sky.

purely on geometrical grounds. In the reference frame of the shock, the ambient gas is incident at the shock velocity $-\boldsymbol{V_S}$. The parallel component $-\boldsymbol{V_{S\|}}$ is continuous across the shock front and the perpendicular component $-\boldsymbol{V_{S\perp}}$ diminishes immediately behind the shock according to the shock jump conditions (Hartigan et al. 1987). The shocked gas thus moves with $-\boldsymbol{V_{S\|}}$ and in a frame where the ambient medium is at rest the post-shock gas flows with the velocity $\boldsymbol{V_S} - \boldsymbol{V_{S\|}} = \boldsymbol{V_{S\perp}}$. The velocity perpendicular to the shock surface decreases moving from the head down the flanks, see Fig. 4.5. Seen from any angle the post-shock velocity at the projected edge of the shock will be in the plane of the sky, thus displaying no radial velocity. Gas from further down the flanks in the near part will contribute to negative velocities and gas in the far part to positive velocities. If the shock is tilted so that the velocity of the shock has a component towards the observer, the highest radial velocity will be present near the head of the shock and the highest radial velocity will be negative. If the shock is tilted away from the observer the highest radial velocity will be positive (Hartigan et al. 1987; Chrysostomou et al. 1997).

The location of maximum brightness depends on the combined effects of local excitation efficiency and the column density of gas observed. Making the assumption that column density is the dominating effect leads to the following model, which is called the column density model. If the region is of uniform density, and of homogeneous magnetic field, a flow travelling in

the line-of-sight (l.o.s.) would show maximum brightness spatially coincident with maximum velocity. Conversely, the tip of a bow-shaped shock travelling at some arbitrary angle to the l.o.s. may yield weak emission, because of low column density of excited H_2. Progressing further down the flanks of the shock in projection, a combination of column density and optimum shock excitation conditions can be expected to yield a maximum in brightness behind the tip of the shock in the plane of the sky.

We thus interpret the displacement of maxima in velocity and brightness in terms of viewing angle effects in flows travelling at an angle to the l.o.s.. The shock is travelling in a direction from maximum brightness to maximum velocity and the orientation of the shock in the plane of the sky, that is, the position angle, is given by the vector through the two maxima. The geometry of this model is shown in Fig. 4.5. Position angles are determined accordingly and are listed in Table 4.1. One region, object 11, shows no observable radial velocity (Fig. 4.4), which we interpret as a flow in the plane of the sky and thus it is not possible to determine the position angle from radial velocities. Spatial uncertainties in the position of the maximum velocity, and the presence of more than one maximum in either or both velocity and brightness, result in an uncertainty in the derived position angle of typically $\pm 10^o$. Flows with small displacements between maximum velocity and maximum brightness will, however, have a larger uncertainty. Displacements of $< 0\farcs2$ are close to the resolution limit, and small variations in displacement would have a large influence on the derived position angles. Figure 4.6 shows estimated position angles of each of the 19 features (save feature 11), through arrows attached to each zone, where the direction of the arrow gives the position angle of the flow. The length of the arrow gives the maximum radial component of the shock velocity.

4.2.2 An alternative model

The model described above assumes that the brightness distribution depends solely on the column density. This is however far from certain as the excitation conditions may vary greatly throughout the shocked region. Nissen et al. (2006) discussed this in detail and we recapitulate to some extent their discussion here.

Let us illustrate the changing excitation conditions by a simplified description of the evolution a shock. Envisage a jet of material being ejected from a protostar and colliding at a super-Alfvenic velocity with a dense clump of gas in the surrounding medium. For simplicity we consider a continuous jet. As the jet collide with the clump of gas the jet slows and energy is converted into heat. Hereby H_2 is sufficiently excited that subsequent cooling can take place through radiation in the IR rovibrational bands. Simulations of C-type

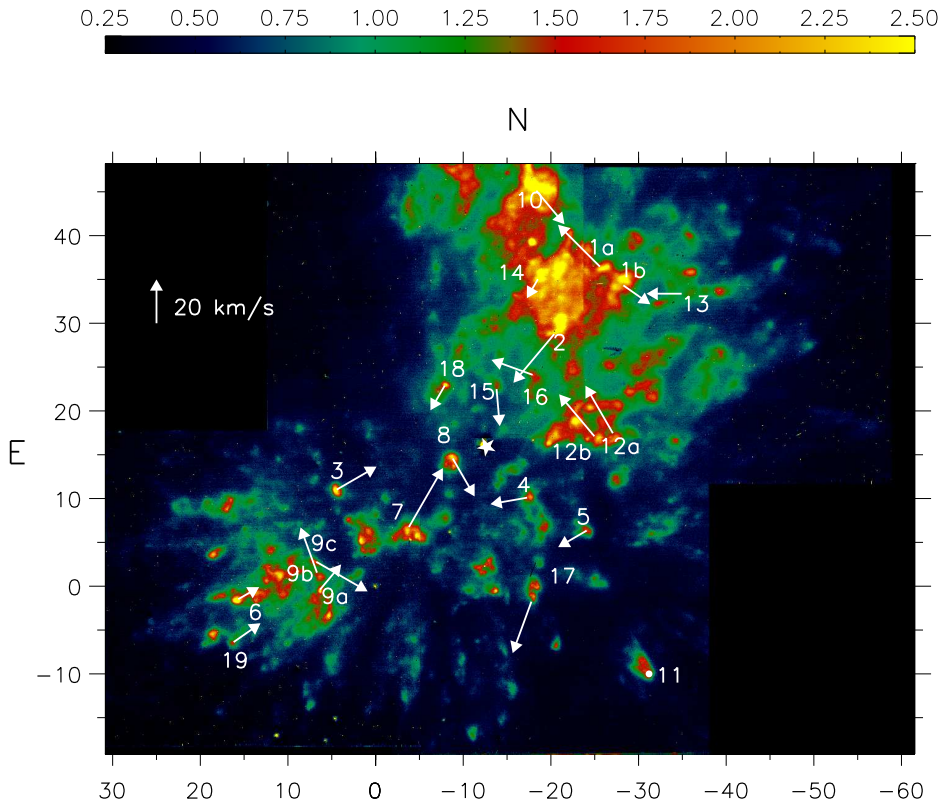

Figure 4.6: Peak emission of the H_2 v=1-0 S(1) line from CFHT/GriF. Numbers refer to regions listed in Table 4.1. Arrows show the position angle of the flows analysed. The lengths of the arrows represent maximum radial velocity relative to the ambient gas. Region 11 shows no measurable radial velocity. Regions 1b,6,9a,9b,9c,19 are redshifted, the rest are blueshifted. BN is marked by a star, (0,0) is the position of TCC0016. The colourbar indicates counts per second per pixel.

shocks show that the most strongly emitting gas is moving at velocities of about 10kms^{-1} less than that of the original jet (Wilgenbus et al. 2000; Le Bourlot et al. 2002; Flower et al. 2003, Lars Kristensen, private comm.). As the gas slows down more gas from the continuous jet is entering the system. Where this newly arrived gas and the slower gas meet a structure called the "Mach disk" is formed, which is itself a shock, given that the relative speeds are super-Alfvenic. Thus there are effectively two shocks, one at the Mach disk, and one around the apex of the system where the gas is impacting the ambient medium (Raga & Cabrit 1993). The gas flows in front of and around the outside of the Mach disk, forming a bow structure with so-called "working surfaces" at which weaker shocks form in 3D around the Mach disk

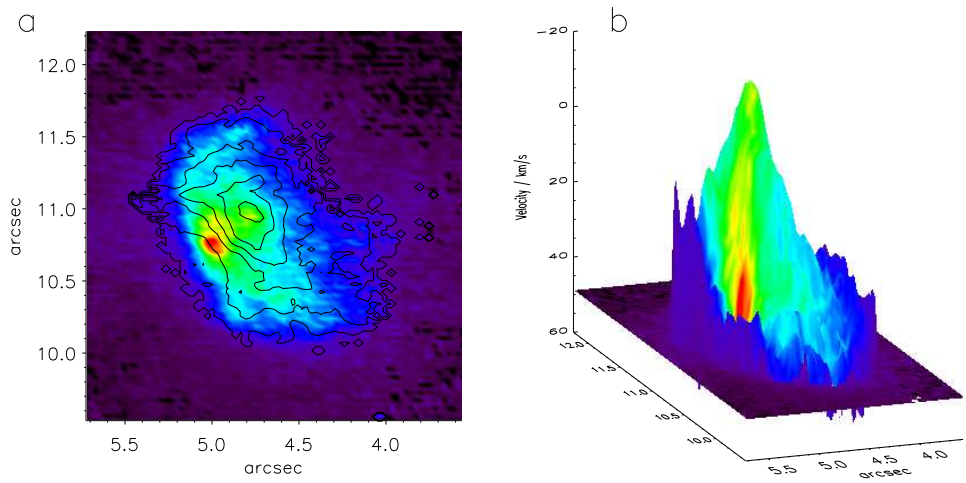

Figure 4.7: The brightly emitting zone labeled 3 in Table 4.1 from VLT/NACO-FP data. **a)** v=1-0 S(0) emission with contours of velocity. Contour levels are 0, 10, 20, 30, 40 and 50kms^{-1}. **b)** The velocity structure is shown on the vertical axis and colours represent brightness as in Fig. 4.1. The viewing angle is from the south-east. The velocities have been smoothed using a 3 by 3 moving average.

(see Fig.1 in Raga & Cabrit 1993). In all parts of this flow the gas cools and emits.

In this picture the Mach disk is in general the point of highest velocity relative to the surrounding gas. Moreover one might suppose that the brightest emission tend to lie in front of the Mach disk, since it is in front of the disk that bulk energy is being turned into heat.

Zone 3, shown in Fig. 4.7, might be an example of such a shock. The data shown in Fig. 4.7 are from VLT/NACO-FP which show substantially more detail than the CFHT/GriF data (see Sect. 2.5.2). The geometry of zone 3 appears to be like that of a bowshock moving towards the south-east. It is clear that there exist two local maxima of brightness. The brightest of these two is situated near what appears to be the apex of the shock while the lesser of the two local maxima is located somewhat behind that. The maximum of velocity is coincident with the lesser maximum, that is, behind the tip of the bowshock. The same structure is found in the v=2-1 S(1) data from VLT/NACO-FP, so although velocities from the VLT/NACO-FP data should be regarded with some caution this particular structure seems genuine.

Using this alternative model, called the velocity to brightness model, the shock would be travelling in a direction from maximum velocity to maximum brightness. That is, in the opposite direction as inferred from the column density model. The velocity to brightness model was used in Nissen et al.

(2006) who analysed 193 regions of emission (see Sect. 4.4).
The velocity-brightness structure of shocks is complex and not well understood. In the picture above it is not trivial to know if the Mach disk is brighter or less bright than the slower moving gas in front of it. In C-type shocks, as in OMC1 (Vannier et al. 2001; Kristensen et al. 2003, and as described in Sect. 1.3.1), the extended shocked zones may well cause the Mach disk to merge with the bow region. Further complexity arise from the fact that the shocks in OMC1 might be caused by different mechanisms. Some are caused by outflows from young stars, but others may simply be caused by supersonic turbulent motions which do not involve impacts of a continuous amount of material over a long period of time. A quantitative understanding of the velocity-brightness structure requires full 2D or 3D shock models including chemistry and hydrodynamics. Without such models we can only guess which processes and models might be relevant in any particular case.

It is important to notice that the common feature of both models is that the orientation of the shock in the plane of the sky is defined by a vector between the maximum brightness and maximum velocity. The direction of the vector depends however on the model and thus position angles given in Table 4.1 could be off by 180° in some or all regions. This does however not alter the conclusion drawn below.

4.3 Discussion

There is no general direction or common origin for the shocks illustrated in Fig. 4.6. Arrows appear to point in random directions, that is, shocks do not propagate preferentially in the direction outlined by the large-scale outflow from the BN-IRc2 region creating Peaks 1 and 2 as described in Sect. 1.4.1. This remains true even when the 180° uncertainty in the flow direction is taken into account. Some of the shocked regions, however, clearly resemble bowshocks, most likely formed from the general outflow. Examples are region 3 which seems to be moving directly away from BN (taking the 180° uncertainty into account), region 11 and the bowshock at (-21″,-6″) relative to TCC0016 shown in Fig. 2.20. Some of the shocks analysed here which do not constitute a part of the general outflow may be an expression of the turbulent motions inherent in the gas as a result of energy cascading from larger scales or as created in the wakes of the massive outflows from the young massive stars in the central region. These turbulent shocks may arise in random directions. However, some of the shocks in OMC1 may be intrinsic to the clumps of gas studied. We propose that at least some of the clumps reported here contain low mass protostars, where characteristic outflow (André et al. 1993; Evans 1999; Eisloffel et al. 2000) creates strongly

emitting shocked regions. Outflows from local low mass protostars would be expected to show no preferential direction of motion within the plane of the sky, with each site acting independently of any other.

To develop this model for protostellar outflows creating the strongly emitting zones, reference may be made to objects 1a and b (Figs. 4.6 and 4.1). As noted, 1a and b lie $\sim$ 2500 AU apart in projection. If the bright zones are the Mach disks of a bipolar outflow, a protostar would be found roughly midway in velocity and position between the regions of bright emission, with each outflow having a radial velocity component of $\sim$ 25 kms^{-1}. Other regions also show closely-lying bright zones. For example region 8 (details not shown here) is nearly as striking as region 1 in this respect, with the two zones lying only $\sim$ 450 AU apart in projection. Other objects listed in Table 4.1 show however only one region of very bright emission, as in objects 4 (Fig. 4.2) and 6 (Fig. 4.3). This may arise if one side of the bipolar flow is obscured by dust. In this connection it should be mentioned that L-band data from VLT/NACO show that region 6 contains a compact object of diameter of no more than 140 AU (D. Rouan & J.-L. Lemaire, private communication). This is a good diagnostic of a partly unveiled solar system size disk. A source at this location has also been detected in H and K band by Muench et al. (2002) (source 561).

Reference may also be made to features noted in the VLT/NACO-FP data. In Chapter 3 we identified four previously undetected IR continuum sources. The region around the source located (-20″,29.4″) relative to TCC0016 (labeled 4 in Fig. 3.1) is shown in Fig. 4.8. South-east of the continuum source there are two fan-shaped features with the heads pointing towards the source. The velocity data show that the southern tails are highly blue-shifted with radial velocities of -30kms^{-1} while the northern tails are red-shifted with velocities of 15-30kms^{-1}. This could be caused by an outflow with a large opening angle in the line-of-sight. To the north of the continuum source there is another fan-shaped feature. Here the head is pointing away from the source, but it might also be connected to the outflow. The same morphology and velocity structure are found in the v=1-0 S(1) and v=2-1 S(1) data and are therefore believed to be real.

In Fig. 4.9 a similar region is shown, namely the region around source 594 from Muench et al. (2002). This source was not detected in continuum here, but was identified as a possible protostar in Nissen et al. (2006). South-east of the position of the source at (1.″4, 5.″2) relative to TCC0016 there is a red-shifted arc of H_2 emission curving around the source. This could resemble an outflow with a wide opening angle ploughing into the molecular cloud. Again we find the same structure in the v=2-1 S(1) data.

In this picture there are two types of gas flows within OMC1, large scale

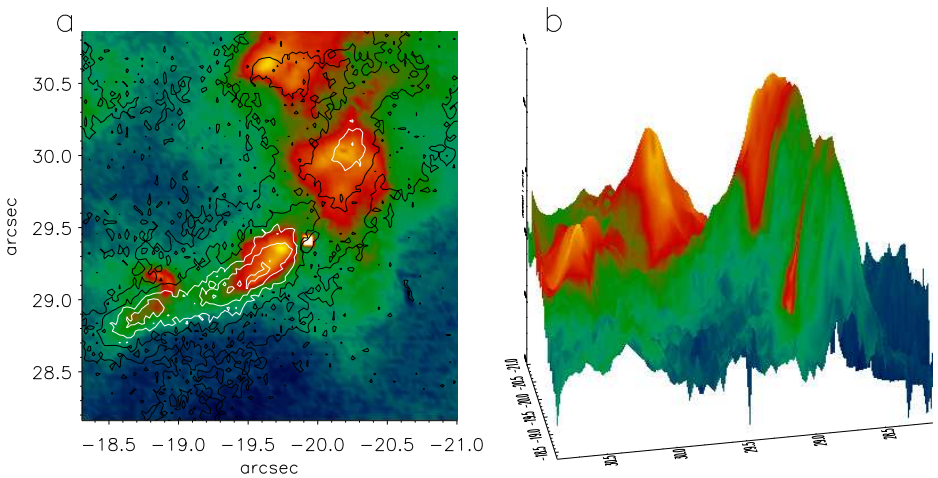

Figure 4.8: H_2 emitting zone around unknown continuum source labeled 4 in Fig. 3.1 from VLT/NACO-FP data. **a)** v=1-0 S(0) emission with contours of velocity. White contour levels are -30, -15, 0kms^{-1}and black contour levels are 15 and 30kms^{-1}. Coordinates are relative to TCC0016. The continuum source is located at (-20″,29.4″) **b)** The velocity structure is shown on the vertical axis and colours represent brightness as in Fig. 4.1. The viewing angle is from the north-east. The velocities have been smoothed using a 3 by 3 moving average.

flows and small scale flows. The high velocity HH-objects seen in the fingers and bullets north of Peak 1 and SE of Peak 2 (Lee & Burton 2000; Doi et al. 2002) and probably most of the bright emission in Peaks 1 and 2 arise from a large scale outburst from one or more massive stars which causes the overall structure of OMC1. We refer to Sect. 1.4.1 and Axon & Taylor (1984); Allen & Burton (1993); Stone et al. (1995); McCaughrean & Mac Low (1997); O'Dell et al. (1997a); Lee & Burton (2000); O'Dell (2001); Doi et al. (2002) for models and discussions of the formation mechanism of the fingers and bullets. Blended in with the excitation caused by the large scale flow, are small scale flows not directly associated with the general outflow. Small scale flows are associated with shocks arising from turbulent motions and with local low mass star formation, both perhaps triggered by the large scale flows. Candidates for newly formed protostars can be found in the continuum data of Chapter 3 together with X-ray data (e.g. Grosso et al. 2005) and IR photometry (e.g. Muench et al. 2002).

4.4 Summary of recent developments

The analysis presented above was greatly expanded by Henrik Nissen in Nissen et al. (2006) where the analysis was extended to 193 regions. They

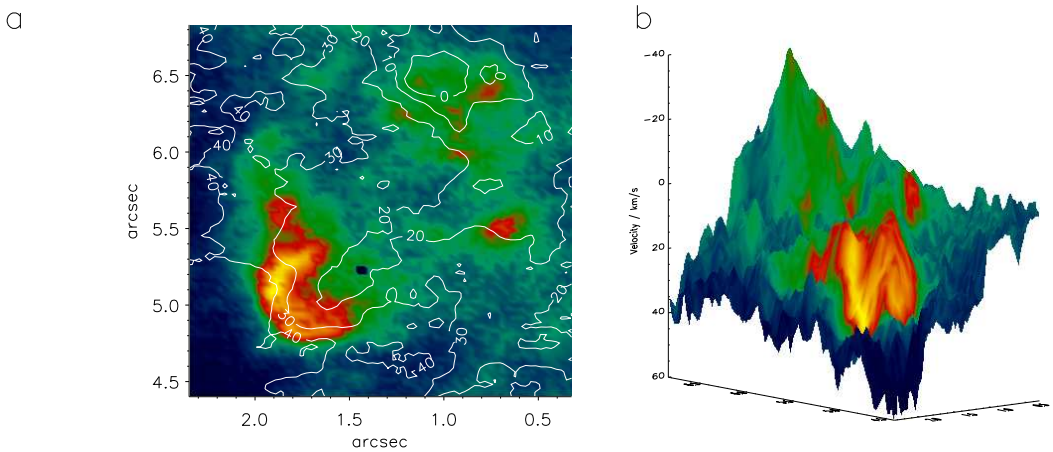

Figure 4.9: H_2 emitting zone around unknown continuum source (594 from MLLA) from VLT/NACO-FP data. **a)** v=1-0 S(0) emission with contours of velocity. Contour levels are 0, 10, 20, 30 and 40kms^{-1}. Coordinates are relative to TCC0016. The position of the source is marked by a black square at (1.4″,5.2″). **b)** The velocity structure is shown on the vertical axis and colours represent brightness as in Fig. 4.1. The viewing angle is from the south-east. The velocities have been smoothed using a 3 by 3 moving average.

found that the distribution of position angles of flows in Peak 2 is nearly isotropic, whereas the flows in Peak 1 show a small degree of anisotropy. This suggests that the emission in Peak 1 is partly described by an outflow motion. In contrast the flows in Peak 2 are only weakly affected by such motions and the emission tend to arise from individual flows. Peak 2 also have a larger concentration of flows suggesting that this region is particularly active.

Nissen et al. (2006) also identified a region south-west of BN (Region B in Nissen et al. 2006) where only blue-shifted emission is found with highly preferentially flow directions in the SW direction. This indicates that the motions are dominated by an overall outflow motion in the NE-SW direction consistent with the outflow from radio source I traced by SiO masers (Greenhill et al. 2004b, see Sect. 1.4.1).

Based on K-L and H-K magnitudes from Muench et al. (2002) and Lada et al. (2004) Nissen identified 32 protostellar candidates within our field showing that low mass protostars are present in the region. Some of these protostellar candidates are most likely foreground stars and thus have no influence on the H_2 emission we observe while other candidates may very well be located in the outskirts of the molecular cloud. Note that, as we are considering the earliest stages of protostellar evolution the sources may be highly obscured and deeper observations may yield different results, revealing protostars not

yet detected.

4.5 Comparison with conventional protostellar regions

If some of the H_2 emission in OMC1 arises from local protostellar outflows and if some of the zones recorded in Table 4.1 represent sites of star formation, how do they compare with more conventional protostellar regions and is it possible to place such objects within the standard classification of protostellar zones as described in Sect. 1.1 (André et al. 1993; Evans 1999, Sect. 1.1)?
The properties of isolated protostellar zones, to some degree as characterized through H_2 emission, may be summarized as follows:
(i) The density in the circumstellar envelope is typically 10^4 to 10^5 cm^{-3} at distances of a few hundred to a few thousand AU or more from the protostars (Evans 1999).
(ii) Regions containing shocked H_2 tend to be highly localised (Eisloffel et al. 2000) and the emission brightness is at least a factor 5 and typically an order of magnitude or more below that seen here (Buckle et al. 1999; Davis et al. 2001, 2002), ignoring any differences in NIR opacity.
(iii) With regard to values of velocity, in a set of 9 protostellar zones, Davis et al. (2001) reports projected H_2 flow velocities ranging from 5 to 40 kms^{-1} for low velocity components.
(iv) H_2 emission has been observed to start as close as a few hundred AU from the protostar and outflows have projected lengths which vary between 500 AU to more than 10^4 AU (Richer et al. 2000; Davis et al. 2001, 2002).
(v) Class 0 objects are invisible at NIR wavelengths in the direction of the objects themselves, have a sub-mm (λ>350μm) to bolometric luminosity ratio of $\geq$0.5%, possess a spectral energy distribution characterised by a modified black-body with a bolometric temperature <70K (André et al. 1993) and show molecular outflows, which may often be visible in H_2 NIR emission far from the highly obscured core. Class 0 protostars also possess a circumstellar envelope more massive than the protostar itself (Bachiller 1996; Ciardi et al. 2003).
For the present for the Orion objects we unfortunately lack standard ingredients for a description of the nature of protostellar zones, namely spectral energy distributions (SEDs) and bolometric luminosities. With regard to density, shock models (Vannier et al. 2001; Le Bourlot et al. 2002; Kristensen et al. 2006) show that in order to reproduce the high H_2 emission brightness recorded in Table 4.1, magnetic C-type shocks are required of velocity 10 to 40 kms^{-1} impinging on preshock gas of density in the range

$10^5 - 10^7 \mathrm{cm}^{-3}$. Thus the densities of gas in the 19 regions in Table 4.1 are more than an order of magnitude higher than in conventional isolated sources (see (i) above). However the density is consistent with densities of prestellar cores ($10^6 - 10^7 \mathrm{cm}^{-3}$) found in cluster forming regions (Ward-Thompson et al. 2006).

Bright emission is seen here from zones extended over a greater range of angle than in conventional regions (see (ii) above), that is, the outflows are not well collimated, but maintain a significant isotropic component. Shock velocities, recorded (in projection) as peak velocities in Table 4.1, cover the range encountered in protostellar zones (see (iii) above). The energy flux in the shocks is however more than an order of magnitude greater, given the higher densities involved.

In connection with item (iv) above, H_2 emission is observed in projection all around the possible position of a protostar. This might suggest that the extinction is weak even very close to the protostar, in marked contrast to isolated protostellar zones. In Orion however, as mentioned above, many different mechanisms contribute to the total emission. Apart from the emission caused by the proposed protostars, H_2 excitation arises primarily in shocks from the massive outflow from the BN-IRc2 complex, which shapes Peak 1 and 2. Shocks may also arise from supersonic turbulence and furthermore some of the weaker emission arises from photon-induced processes from θ^1Ori C (Störzer & Hollenbach 1999; Kristensen et al. 2003, 2006). Thus the morphology of the H_2 emission may be regarded as a superposition of all these contributions. This indicates that low extinction is not necessarily implied when emission is observed close to a protostellar candidate.

Using the density estimates from shock models we show in Chapter 8 that the amount of circumstellar material in the clumps observed here is not more than $0.4 \mathrm{M}_\odot$ (see also Vannier et al. 2001). Thus a Class 0 characteristic would imply protostars of this mass or less. However, material may have been removed both by the wind from BN-IRc2 (O'Dell 2001) and, by analogy with the later "proplyds" in ONC (see Sect. 1.4), by photoevaporation due to the Trapezium stars (Störzer & Hollenbach 1999; Henney & O'Dell 1999; O'Dell 2001). This suggests that the mass of the circumstellar material may originally have been greater than estimates of the current mass in Vannier et al. (2001). At all events, these removal processes will limit the accretion that can take place.

4.6 Conclusion

We have shown that there exists strong spatial correlation between flows and emission brightness and we have used this correlation to infer the direction

of motion for the shocks involved. The absolute direction in the plane of the sky is uncertain by 180° depending on the shock model, but even with this ambiguity it is clear that all the shocks causing the H_2 emission in OMC1 cannot have a common origin. Some of the shocks are most likely due to supersonic turbulence and some may be caused by local, internal outflows from embedded low-mass protostars. Candidate protostars were identified in Chapter 3.

However, the comparison in Sect. 4.5 between the general properties of objects in Table 4.1 and the known general characteristics of early stages of star formation, the latter for isolated protostars in the absence of perturbations from nearby massive stars, reveals both similarities and differences. The high brightness of the Orion objects requires high densities and high energy flux in the associated flows, whereas flow velocities and the physical scale of shocked regions seem typical of early stages of star formation. The properties of the present regions suggest that the subset of objects in Orion which can be associated with protostellar zones may represent a more energetic and less structured stage of star formation than has previously been recorded, but which may be characteristic of cluster forming regions. If this is so, objects may settle down to less unruly behaviour or they may represent a different stellar lineage, eaten away on one side by the powerful radiation field of the Trapezium stars to the south and blasted continuously on the other face by the fast wind from BN-IRc2.

Chapter 5

Characterizing turbulence

Turbulence plays a central role in star forming molecular clouds as described in detail in Sect. 1.1. However it is vigorously debated how exactly turbulence contribute to the regulating processes. In order to settle this question we need detailed observations of motions in star forming regions and to use these observations to characterise in detail the nature of the turbulent, weakly ionized and magnetised plasma in which stars form. The velocity and brightness data from CFHT/GriF provide the first opportunity to study the physical properties of a star forming region both in terms of its morphology and bulk gas motion at scales associated with individual star formation. The aim of this chapter is to characterise the turbulent velocity field in OMC1 for the subset of gas represented through highly excited H_2. Our results should help to provide a benchmark for comparison with numerical models of star formation and in Chapter 7 the statistical results of the present chapter will be directly compared with such hydrodynamical simulations.

Several techniques, such as the size-line width relation (Larson 1981; Goodman et al. 1998; Ossenkopf & Mac Low 2002), probability distribution functions (Falgarone & Phillips 1990, 1991; Falgarone et al. 1994; Miesch & Scalo 1995; Lis et al. 1998; Miesch et al. 1999; Ossenkopf & Mac Low 2002; Pety & Falgarone 2003), structure functions (Falgarone & Phillips 1990; Miesch & Bally 1994; Ossenkopf & Mac Low 2002) and Δ-variance (Bensch et al. 2001; Ossenkopf & Mac Low 2002), have previously been used to characterize the structure of brightness or velocity in molecular clouds. Comparisons between observations and models have earlier been made by Falgarone et al. (1994, 1995); Lis et al. (1998); Joulain et al. (1998); Padoan et al. (1998, 1999); Pety & Falgarone (2000); Klessen (2000); Ossenkopf & Mac Low (2002); Padoan et al. (2003); see also the review by Elmegreen & Scalo (2004). These earlier comparisons are all based on CO observations, tracing relatively cool and low density gas. These radio data are limited in spatial resolution and can only be used to address the physics at scales larger than roughly 0.03 pc

(6000 AU).
When dealing with turbulence it is usually assumed that most features are scale-free between the driving and dissipation scale, as described in Sect. 1.2, and that the behaviour for example of the structure functions (see Sect. 5.4) can be extrapolated to the very much smaller scales of individual star formation. This is true for the "Kolmogorov" type of turbulence (Kolmogorov 1941) in an incompressible, non-dissipative medium, but as mentioned in Sect. 1.2 it is far from certain that features observed in incompressible media can be extrapolated to turbulence in the interstellar medium, which is highly compressible (Elmegreen & Scalo 2004). The high spatial resolution infrared data from CFHT/GriF give the opportunity to discover how structure functions develop at scales of two orders of magnitude smaller than have hitherto been probed.
Here we use three standard statistical measures to provide observational constraints on theories and simulations concerning gravitational collapse and star formation in a turbulent ISM. First, we test whether the observed scaling behaviour of the velocity structure, encapsulated in the size-line width relation (Larson 1981) holds for the smaller scales involved here (Sect. 5.2). Second, we use probability distribution functions (PDFs) of velocities (Sect. 5.3) and compare with other observations. Third, we calculate the low order moments of the velocity difference PDF as a function of lag (Sect. 5.4), that is, the structure functions or functions directly related to structure functions. In Sect. 5.5 we investigate the structure functions further and test how the scaling behaviour compare with theories of turbulence. Only data from CFHT/GriF (Sect. 2.4) are used in this chapter. Here we use the full data set. Individual regions of emission are considered in Chapter 6.

5.1 Filtering of data

As mentioned in Sect. 4.1 the presence of large scale velocity differences in OMC1 has been known for many years. This velocity difference has generally been viewed in the context of an outflow mechanism from the BN-IRc2 complex (Scoville et al. 1982; Sugai et al. 1995; Chrysostomou et al. 1997; Salas et al. 1999) and thus as a local phenomenon. The velocity difference could however be a manifestation of turbulent energy cascading down from very large scales, stirring of the gas in large scale vortices. Thus the origin of the velocity difference remains uncertain and in the following we will explore this question further.
As discussed in Miesch & Bally (1994), Miesch & Scalo (1995) and Miesch et al. (1999), large scale trends - such as a general velocity gradient - could dominate any statistical quantifier and give misleading results. This is due

to the fact that the statistical methods generally lose spatial information and therefore rely on the assumption that systematic trends within the data are not present. It may therefore be argued that any large scale trends should be removed and only local velocity fluctuations studied. Ossenkopf & Mac Low (2002) however point out that large scale systematic motions may be part of the turbulent cascade if they inject energy into the system and should therefore only be removed if the turbulence studied is exclusively driven on scales smaller than the size of the map.

Turbulent motions in OMC1 could, as mentioned in Chapter 1, be driven on large scales by supernovae explosions (Mac Low & Klessen 2004) or locally by the massive outflow from the BN-IRc2 complex, which contains a number of possible candidate sources such as source I, source n, BN itself (Menten & Reid 1995; Gezari et al. 1998; Doeleman et al. 1999; Greenhill et al. 2004a; Shuping et al. 2004, see Sect. 1.5.2). Turbulence may also be driven on smaller scales by outflows from low mass protostars (e.g. Mac Low & Klessen 2004). Evidence of such low mass protostellar candidates in the vicinity of BN-KL was discussed in Chapters 3 and 4.

Since the driving mechanism and thus the driving scale is unknown we test the statistical quantifiers explored in this chapter with the full velocity field and also the residual velocity fluctuations resulting from removing the large scale velocity trends.

5.1.1 Removal of large scale trends

The procedure of removal of large scale gradients, or filtering, follows Miesch & Bally (1994). The removal is performed by convolving the data with a smoothing function and then subtracting the smoothed image from the original to obtain the residual image of the small scale velocity fluctuations. The residual image should then reveal any small scale structures that were superposed on the large scale trends in the original. The filtering or smoothing function used here is a two-dimensional equally weighted moving average in the form of a square box. The optimal size of the filter is the broadest possible that removes the large scale gradient but leaves all other features (Miesch & Bally 1994). The 2D autocorrelation function of a velocity map can be used for detecting velocity gradients. These show up as anticorrelations in the direction of the gradient and recorrelations in the direction at right angles (Spicker & Feitzinger 1988). Thus the widest filter where no anticorrelated sidelobes are discernible in the autocorrelation function of the residual image is the optimal.

Following Spicker & Feitzinger (1988) we calculate the unbiased estimate of the two-dimensional spatial autocorrelation function (ACF) of the velocity

field as

$$ACF(\boldsymbol{\tau}) = \frac{1}{\sigma^2(N_x - |\tau_x|)(N_y - |\tau_y|)} \sum_{m_x}^{M_x} \sum_{m_y}^{M_y} (v(\boldsymbol{r}) - \mu)(v(\boldsymbol{r} + \boldsymbol{\tau}) - \mu) \quad (5.1)$$

where v is the radial velocity. The lag, $\boldsymbol{\tau}$, and the position, $\boldsymbol{r}$ are two-dimensional vectors in the plane of the sky. N_x and N_y are the numbers of pixels in the data in the x- and y-direction, respectively. The limits of the sums are defined by

$$m_x = max(1, 1 - \tau_x) \qquad m_y = max(1, 1 - \tau_y)$$
$$M_x = min(N_x, N_x - \tau_x) \qquad M_y = min(N_y, N_y - \tau_y).$$

Furthermore, the mean and the variance of the velocity are given as

$$\mu = \frac{1}{N_x N_y} \sum_{1}^{N_x} \sum_{1}^{N_y} v(\boldsymbol{r}) \quad (5.2)$$

$$\sigma^2 = \frac{1}{N_x N_y} \sum_{1}^{N_x} \sum_{1}^{N_y} (v(\boldsymbol{r}) - \mu).^2 \quad (5.3)$$

Using this definition the maximum value of the ACF is unity which is obtained at $\boldsymbol{\tau}$=0. Note that ACF($\boldsymbol{\tau}$) = ACF($-\boldsymbol{\tau}$). Positive values of the ACF imply correlated motions while anti-correlations, that is, correlated motions with opposite directions, result in negative values. In a completely random velocity field, no correlations would exist, and the ACF would be essentially zero everywhere except at $\boldsymbol{\tau}$=0. The value of the ACF can decrease (decorrelate) and increase again (recorrelate) for increasing lags. Recorrelations emerging at specific lags are signs of systematic velocity components connected with energy sources and sinks acting at the scale and orientation associated with the lag (Spicker & Feitzinger 1988).

ACFs have been calculated in the spatial domain directly from Eq. (5.1) although working in the spatial domain is less efficient than working in the frequency domain using Fourier transformations. It has, however, been preferred here because it enables us to ignore pixels where data are missing, treating them as nulls instead of zeros.

The two-dimensional ACF of the original velocity map from CFHT/GriF is shown in the left-hand-side of Fig. 5.1 in a coordinate system defined by the lag. Positive values of the ACF, that is, correlation, persist for a distance of nearly 20″ and furthermore recorrelations are seen at $\boldsymbol{\tau}$=(35″,40″) and at $\boldsymbol{\tau}$=(40″,-45″). The elongation in the NE-SW direction of the correlation

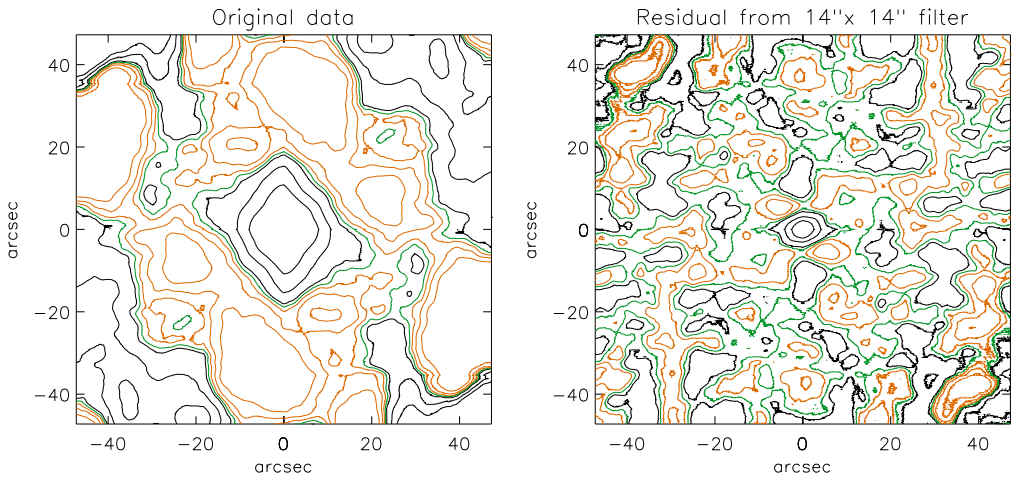

Figure 5.1: Autocorrelation function of the original velocity image from CFHT/GriF (left) and of the residual image obtained from filtering with a filter size of 14″× 14″. Coordinates are shown in the lag system. The green contour represent an ACF level of 0, positive levels of 0.02, 0.1 and 0.2 are shown in black and negative levels (anti-correlations) of -0.02, -0.05 and -0.1 are shown in red.

feature in the centre of the ACF map in Fig. 5.1 is a hint of the velocity gradient of OMC1 in the NW-SE direction. The recorrelation in the NW corner of the map is also connected to the velocity difference between Peak 1 and 2 and shows that the difference is more complicated than a velocity gradient. Whatever the nature of the velocity difference, Fig. 5.1 clearly shows that large correlations exist in the motion of the gas, which could potentially disturb the statistical results.

In order to remove the large scale motions, the ACF has also been calculated for residual images using filters of varying size as described above. The widest filter where no strong sidelobes are present, that is, the optimal filter, has been found to be of size 14″× 14″(6400 AU × 6400 AU). The ACF of the optimal filtered image is displayed in the right-hand-side of Fig. 5.1. The residual image of this filter contains no large scale trends, only small scale velocity fluctuations.

All further analysis has been carried out on both the original full velocity field and on the residual image obtained from filtering with the optimal filter. The latter will be referred to as the filtered velocity image or field. We find that it is certainly unwise to remove apparent large scale velocity trends, which are found to be an integrated part of the dynamics in OMC1. Thus the filtered image is not representative of the motions in OMC1, as discussed immediately below in Sect. 5.2.

5.2 Relation between size and velocity dispersion

Larson (1981) identified an empirical relation between line width (or velocity dispersion) and size for molecular clouds and clumps within clouds over scales of $\sim$ 0.1-100 pc. He obtained a power-law

$$\Delta v_{obs} \propto R^{\alpha} \qquad \alpha \simeq 0.38 \tag{5.4}$$

where Δv_{obs} is the observed line width and R is the radius of the object. Eq. (5.4) is also known as "the Larson relation". As mentioned in Sect. 1.1.1 this relationship essentially supports a model in which larger motions are associated with larger scales. More recent studies give a range of values for α over dimensions of 0.02-100 pc (e.g. Caselli & Myers 1995; Peng et al. 1998) showing α varying between 0.2 and 0.7. Some studies indicate that massive star forming regions tend toward the lower values. For example Caselli & Myers (1995) found $\alpha = 0.53$ in low mass cores and $\alpha = 0.21$ in massive cores in Orion. There are also indications that the relation in Eq. (5.4) breaks down in the most massive star forming regions (Plume et al. 1997) and in dense cores of low mass star formation in Taurus and L1251A (Barranco & Goodman 1998). A comprehensive overview was given in Goodman et al. (1998). Size-line width measurements require that objects are well defined within a map and that a line width and size can be objectively assigned to objects within the field of observation. The definition of objects is obvious for isolated clouds, but encounters a certain degree of arbitrariness when dealing with clumps in a cloud.

5.2.1 Method

The structure of OMC1, measured in vibrationally excited H_2, reveals a very clumpy environment where the regions of bright emission are in many circumstances imposed on extended weaker emission (Figs. 2.5, 2.8, 2.16). OMC1 is thus a case study in the difficulty of determining the physical extent of individual clumps in a turbulent environment. In order to circumvent this problem in computing a size-line width relation we follow the method developed by Ossenkopf & Mac Low (2002) and described below. We remind the reader at this stage that our observations of line width are indirect. That is, we obtain the radial velocity associated with any pixel from the peak of the line profile observed with the low resolution Fabry-Perot, as described in Sect. 2.4. Thus the line width associated with any chosen assembly of pixels is given by the velocity dispersion of these peak velocities. This is in contrast to the standard technique in radio observations in which the velocity

resolution of observations is a fraction of the line width, and the line width may then be obtained directly from the measured lineshape (e.g. Larson 1981; Falgarone & Phillips 1990; Ossenkopf & Mac Low 2002). For this reason we refer to the Larson relationship as a size-velocity dispersion relation, rather than the more familiar size-line width. The technique which we use here, that of taking the dispersion of peak velocities, was also used by Ossenkopf & Mac Low (2002) on CO data. They argue that this method is less sensitive to the cloud depth than the method of finding line widths directly from line profiles. Note that Ossenkopf & Mac Low (2002) use centroid velocities and that the peak velocities used here are essentially equal to centroids (Sect. 2.4.3).

The average brightness weighted velocity dispersion, Δv_{obs}, within regions of varying size, is estimated following the prescription of Ossenkopf & Mac Low (2002). For any particular radius, R, we compute the brightness weighted probability distribution function of the peak velocities (see Sect. 5.3) in a circular region of that radius and estimate the corresponding velocity dispersion from a fit to a gaussian profile. This is repeated for a number of circles centered on pixels distributed uniformly throughout the map with a mesh size of 50 pixels. The average velocity dispersion of that particular radius is then calculated using intensity weighting. That is, each velocity dispersion is weighted by the total intensity in the corresponding circular region. The statistical standard error of the average value of the velocity dispersion is used as an error estimate. This procedure is repeated for a number of different radii ranging from the spatial resolution limit of 70 AU to 14000 AU approaching the size of the map. The number of circles used to calculate the average velocity dispersion decreases with increasing radius.

5.2.2 Results for OMC1

The relation between average velocity dispersion and size is shown in Fig. 5.2a for the full velocity image (that is, without filtering of the data - see Sect. 5.1). Within the errors the relation for the full velocity field is consistent with a single power law over more than two orders of magnitude in R with an exponent $\alpha = 0.205 \pm 0.002$, although there also appears to be some deviation above 8000 AU. The value of the exponent agrees with the average value of 0.21 ± 0.03 that Caselli & Myers (1995) found for massive cores in the Orion A and B clouds at scales 0.03 - 1pc. That study did not in fact include OMC1. It is striking that the Larson relationship appears both to hold in these very smaller scales and to have a very similar exponent as for massive cores, although we are dealing here with highly excited material.

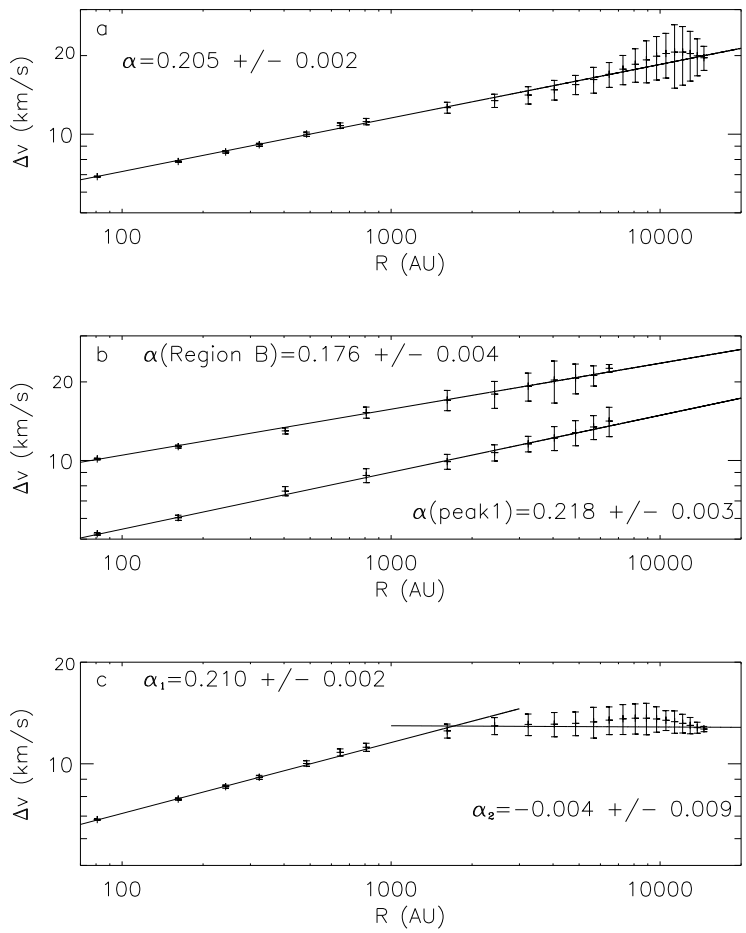

Figure 5.2: Larson size-line width relations, Eq. (5.4). **a)**: Velocity dispersion as a function of size for the full velocity field. A power law fit of index 0.205 is overlaid. **d)**: Velocity dispersion for Region B (upper line) and Peak 1 (lower line) with power law fits overlaid. **c)**: Velocity dispersion for the filtered velocity image. Power laws of index 0.210 and -0.004 are overlaid.

Separate analysis of Peaks 1 and 2 and outflow region

We have also computed the size-velocity dispersion relation for the region south-west of BN and Peaks 1 and 2 separately, in each case for the full velocity field. We do this in order to test if smaller regions adhere to the same relation as the composite region. The appearance of the region south-west of BN, bounded by -2″ to the east and 15″ to the north, with fewer and more isolated clumps of emission, suggests that the dominating physical processes in this region are different from those in Peak 1 and 2. In Peaks 1 and 2 the emission is more homogeneous and more spatially concentrated. In the

south-west zone all clumps with measurable radial velocities are blue-shifted and Nissen et al. (2006) provides clear evidence that these objects form the IR counterpart of an outflow detected in radio observations of SiO masers associated with a buried O-star within OMC1 (Menten & Reid 1995; Doeleman et al. 1999; Greenhill et al. 2004a,b; Shuping et al. 2004, Sect. 1.4.1). Following Nissen et al. (2006) we refer to this zone as Region B.

The resulting size-velocity relationships, shown for Region B and Peak 1, with Peak 2 omitted for clarity, are shown in Fig. 5.2b. The velocity dispersions of all three regions adhere to the size-velocity dispersion relation. The figure, however, illustrates that the structure in Region B south-west of BN has a significantly lower slope (α=0.176) and a somewhat higher proportionality parameter κ in $\Delta v_{obs} = \kappa R^{\alpha}$ than Peaks 1 (α=0.218) and 2 (α=0.213). In the latter two regions κ's and the exponents α are the same within observational error. The lower value of α associated with Region B supports the conclusion of Caselli & Myers (1995) that lower exponents are characteristic of massive star-forming regions.

The nature of the large scale trends

We now return to analysis of the whole observed region. The relation based on the filtered velocity image (Sect. 5.1), displayed in Fig. 5.2c, shows that the velocity dispersion is not well represented by a single power law. At radii smaller than $\sim$ 1600 AU the relation follows a power law of index 0.210, essentially the same as for the full velocity field. This similarity of behaviour is expected since the filter applied to remove the velocity gradient has a width of 14″$\sim$ 6400 AU (Sect. 5.1), and an equivalent radius of 3200AU, and thus should not affect smaller scales. In contrast to the full velocity field, the velocity dispersion for the filtered data at scales larger scales than 1600 AU is constant within observational error as a function of size with an index of -0.004 $\pm$ 0.009. This is in marked contradiction to the accepted form of the Larson relationship and seems unnatural. If this behaviour were correct it would imply that motions in the region were uniform on scales larger than 1600 AU while showing features related to a turbulent energy cascade at smaller scales. This is difficult to explain physically. Since the break in power law occurs at clump diameters of exactly half the size of the filter it is natural to conclude that the low exponent is due to the filtering.

We conclude that by removing the large scale gradient we have artificially removed some of the turbulent velocities at large scales. It follows therefore that the large scale motions in OMC1, reported both here and by a number of other authors (Scoville et al. 1982; Sugai et al. 1995; Chrysostomou et al. 1997; Salas et al. 1999) should be seen as representing real scales of a tur-

bulent cascade. By implication the turbulence is driven at large scales and this suggests that turbulence on the scale of the map ($\sim 0.15\,\mathrm{pc}$) could be either the result of an energy cascade from still greater scales or injection of turbulent energy by the large scale outflows associated with massive star formation in the BN-IRc2 region.

This in turn implies that the turbulence in the OMC1 region does not have a strong injection of energy at scales of less than 0.1 pc and is thus not primarily driven on small scales, for example by low mass protostellar outflows. In support of this, the energy injected by a high mass stellar outflow considerably exceeds that of low mass outflows. Nissen et al. (2006) has estimated that the mass outflow rate is of the order of $> 10^{-3}$ $\mathrm{M_\odot/yr}$ in the blue-shifted outflow, south-west of BN, with an average velocity of 18 $\mathrm{kms^{-1}}$, the so-called "low velocity outflow" (Sect. 1.4.1). Low mass protostellar outflow rates are typically three orders of magnitude lower (Arce et al. 2006), with a similar velocity. This simple argument on the basis of energetics supports our conclusion that the injection of energy at the 0.1 pc scale of massive stars outweighs on the global scale the energy input from low mass stars. However, as we find in Chapter 6, locally as opposed to globally, the character of the turbulence is generally more affected by low mass protostellar outflows. This is also suggested by the results shown in Chapter 4.

The velocity gradient, as identified in Sect. 5.1, should consequently not be removed prior to analysis. In the following we thus mainly focus on the full velocity field containing velocities on all scales, but for completeness we also include analysis of the filtered velocity image.

5.3 Probability Distribution Function of velocities

The probability distribution function (PDF) of velocities is defined in terms of 3D velocity components as the number of pixels at a certain velocity vs. velocity. Here we are restricted to a set of radial velocities and we estimate the PDF of these velocities sampled over the spatial region in the plane of the sky shown in Fig. 2.11. This corresponds to the PDF of centroid velocities used in Miesch & Scalo (1995); Miesch et al. (1999); Ossenkopf & Mac Low (2002); Klessen (2000). An alternative procedure is to use the line profile of an optically thin line as an estimate of the PDF along the line-of-sight (Falgarone & Phillips 1990, 1991; Falgarone et al. 1994; Ossenkopf & Mac Low 2002), taking advantage of the high velocity resolution of radio-observations. Note that the spectral resolution of our data is too low to make this approach useful here. Ossenkopf & Mac Low (2002) provides

a comparison of the two methods based on CO observations showing that PDFs from centroid velocities provide the correct distribution when the map is larger than or comparable to the depth of the cloud. Our map (Fig. 2.11) covers nearly the full extent of the molecular outflow in OMC1 indicating that the size is comparable to the depth of the outflow assuming that the radial dimension is similar to the spatial extent on the sky.

Even though the PDF contains no information on spatial correlations, for example experimental and theoretical work suggest that the PDF velocity is sensitive to dynamical processes. These studies include velocities for the large scale structure of galaxies (Bernardeau 1994; Kofman et al. 1994; Catelan & Moscardini 1994) and distinguishing nonlinear chaotic processes from stochastic processes (Wright & Schult 1993). The shape of the wings of the PDF is thought to be diagnostic of intermittency (Miesch et al. 1999; Ossenkopf & Mac Low 2002), in which, at random scales and/or time intervals, energy is dissipated as heat in the turbulent medium. Increasing degrees of intermittency create a transition from gaussian ($\propto \exp(-x^2)$) to exponential ($\propto \exp(-x)$) wings in a PDF. Note however that the relation between non-gaussian PDFs and intermittency is heavily debated. Klessen (2000) for example show that exponential PDFs can occur in numerical simulations without intermittency.

Although the PDF of the velocity field itself is in general nearly gaussian in incompressible turbulence, nonzero skewness (third order moment, see Eq. (5.7)) must exist in order to provide energy transfer among different scales (Davidson 2004). That is, the PDF must be asymmetric. Non-gaussian behaviour is well-established for PDFs of velocity differences in incompressible turbulence (Sect. 5.4). Often the PDF of velocity differences displays a near-exponential form at small lags (Davidson 2004).

PDFs of centroid velocities with gaussian shapes may be found in studies of decaying supersonic turbulence (Chappell & Scalo 2001; Ossenkopf & Mac Low 2002) and incompressible turbulence (e.g. Batchelor 1956; Jayesh & Warhaft 1991). Exponential PDFs can also be found in the literature of simulations, e.g. from inelastic collisions of clouds (Ricotti & Ferrara 2002) and interactions of shells in models driven by strong stellar winds (Chappell & Scalo 2001). Further relevant theoretical studies involve the stretched exponential form ($\propto \exp(-a|x|^\beta)$) where β is fractional (e.g. Frisch & Sornette 1997; Eggers & Wang 1998). $\beta = 2$ reproduces the gaussian PDF and $\beta = 1$ the exponential form. Fractional β values can arise from random processes of energy transfer whose overall effect accumulate in a multiplicative manner (Eggers & Wang 1998, see Sect. 5.4.4).

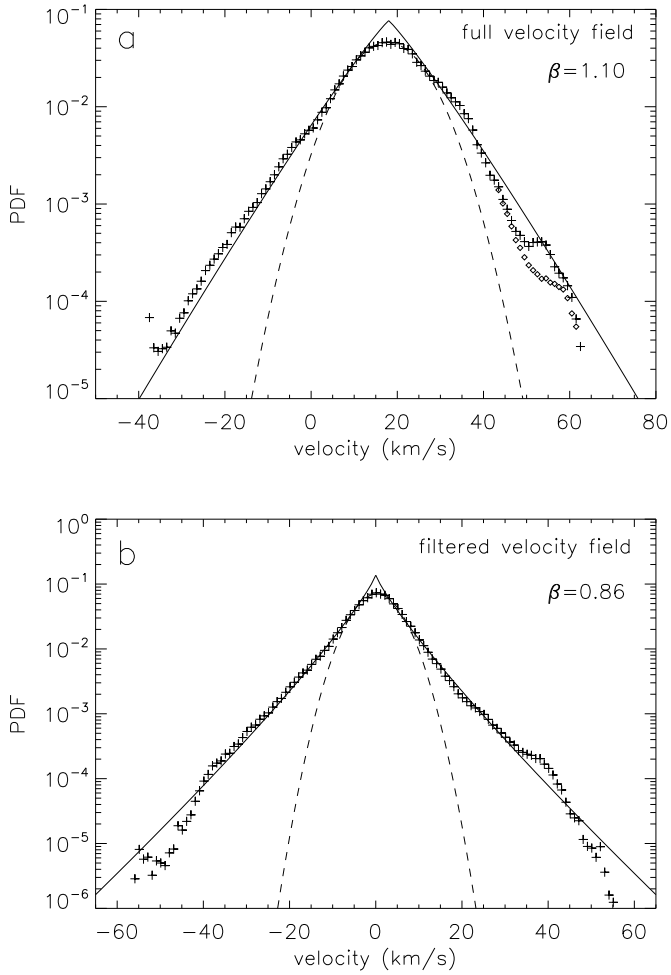

Figure 5.3: Probability distribution functions of peak velocities. **a)**: (+) PDF for the full velocity field. (◇) PDF with velocities associated with the clump in fig. 5.4 removed. **b)**: PDF for the filtered data (see Sect. 5.1). Stretched exponentials with $\beta = 1.10$ and $\beta = 0.86$ respectively are shown for comparison. The dashed lines are gaussian fits to the core.

5.3.1 PDFs of OMC1

We have calculated the normalized PDF of velocities by binning the velocities in intervals of 1kms^{-1}. The PDF can be estimated by assigning the same weight to every pixel or by weighting every velocity with the corresponding brightness in that pixel. By testing both methods we found that the chosen method of weighting does not influence the shape of the PDF significantly. However, brightness weighting is less influenced by observational noise and is therefore used in the following analysis.

Figure 5.3 shows the peak velocity PDF of the full velocity field and of the filtered velocity image. The PDF of the filtered velocity image is artificially centered around 0 kms^{-1} through the action of filtering. The PDFs are shown on a log-linear scale where a gaussian distribution would form a parabola and an exponential a straight line. The PDFs in Fig. 5.3 are clearly not well represented by gaussians except in the inner core, where gaussians are shown as dashed lines. The wings can be fitted best by stretched exponentials (full lines). These lines are derived for the full velocity field data by fitting between -32 and +12 kms^{-1} and yield β=1.10±0.06. A similar fit for the filtered data yields β=0.86±0.05.

5.3.2 Errors and uncertainties

To test the influence of uncertainties in the determination of velocities on the shape of the PDFs in Fig. 5.3, we have added to each velocity in the original dataset a random velocity. The random velocity was picked from a gaussian distribution with standard deviation corresponding to the uncertainty of the velocity in the pixel in question, as given by Eq. (2.8) ($\sigma = -9.37 + 3.05\exp(-I * 6.93) + 10.11\exp(-I * 0.026)$). We created a series of such velocity fields and calculated the PDF from each of them. The PDFs of velocity fields so generated are effectively indistinguishable from the PDF of the real data set, reflecting the fact that the large number of pixels used in the PDF, $\sim 3.2{\cdot}10^6$, reduces the effect of the observational noise to a negligible level. Again, since every bin of the histogram is populated by a large number of pixels, the relative error, $\sqrt{n}/n$, becomes very small. This include taking the effective 3x3 pixels resolution into account, which means that the number of independent pixels is 1/9 times the total number. Except for the very least populated bins the statistical error bars would be smaller than the symbols in Fig. 5.3 and have therefore been omitted.

5.3.3 Discussion

Using line profile data for CO from various isotopes Falgarone & Phillips (1990, 1991); Falgarone et al. (1994); Ossenkopf & Mac Low (2002) do not find simple gaussian behaviour for most observations. However, Falgarone & Phillips (1991) showed that most of the PDFs could be represented by two gaussians, with the wing component being about 3 times broader than the core component. The PDFs in Fig. 5.3 cannot be so represented. Thus our data - for hot dense gas - show a different result to the data reported for much larger scales in Falgarone & Phillips (1991) - for cool, diffuse gas. Other work uses centroid velocities, corresponding to the peak velocities used here. For example, Ossenkopf & Mac Low (2002) found that the PDFs of the

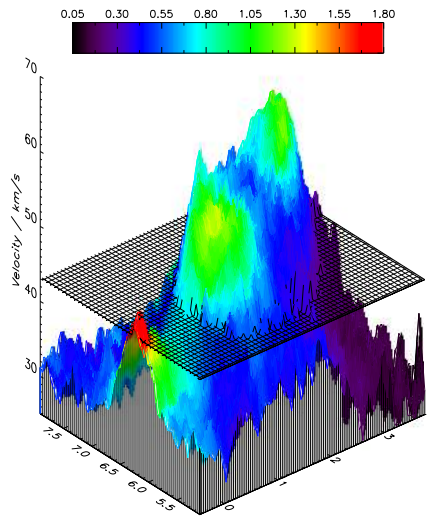

Figure 5.4: The brightly emitting clump that causes the hump in the red wing of the PDF (Fig. 5.3a, + symbols). The xy plane is the plane of the sky, the vertical axis shows the radial velocity v_{lsr}. The plane at (x,y,43) shows the boundary of the region of pixels ignored in the PDF shown as (◇) in Fig. 5.3. The centre of this clump is 6.″5 E, 1.″5 N of TCC0016. The colour scale refers to brightness in counts pixel^{-1}s^{-1}. This clump corresponds to region 9 in Table 4.1

Polaris Flare could be reproduced by two gaussians as in Falgarone & Phillips (1991), while Miesch & Scalo (1995); Miesch et al. (1999) found exponential tails in most of their PDFs, in agreement with our results.

5.3.4 Asymmetries in the PDF

It is clear from Fig. 5.3 that the PDFs are not symmetric and that the red wing displays large deviations from a smooth behaviour, especially at velocities of 50-60 kms^{-1}, where a hump is seen in the PDF. By inspection of the velocity data we found that the hump results from a single structure in the field corresponding to region 9 in Chapter 4 (see Table 4.1). This structure is the only clump of emission with velocities consistently larger than 50 kms^{-1} and is shown in Fig. 5.4 in xy-velocity space. If we ignore all pixels in this structure with velocities larger than 43 kms^{-1}, then the PDF for the full field no longer contains a secondary hump at 55 kms^{-1}(diamonds in Fig. 5.3a). This suggests that the structure involved is an independent entity which does not fit into the overall turbulent cascade. The nature of this dense fast moving object remains mysterious.

Field	std-dev / kms^{-1}	skewness	kurtosis	β
full	10.3	-0.20	4.4	1.10
filtered	7.8	-0.042	6.4	0.86

Table 5.1: Moments and stretching exponents of the peak velocity PDF for the full velocity field and the filtered velocity field

5.3.5 Statistical moments

The shape of the PDF(s) in Fig. 5.3 can be further quantified by the brightness weighted statistical moments, computed directly from the dataset as:

$$\text{mean} = \mu = \frac{\sum_{map} I(\boldsymbol{r}) v(\boldsymbol{r})}{\sum_{map} I(\boldsymbol{r})} \tag{5.5}$$

$$\text{std.dev.} = \sigma = \sqrt{\frac{\sum_{map} I(\boldsymbol{r})[v(\boldsymbol{r}) - \mu]^2}{\sum_{map} I(\boldsymbol{r})}} \tag{5.6}$$

$$\text{skewness} = \frac{\sum_{map} I(\boldsymbol{r})[v(\boldsymbol{r}) - \mu]^3}{\sigma^3 \sum_{map} I(\boldsymbol{r})} \tag{5.7}$$

$$\text{kurtosis} = \frac{\sum_{map} I(\boldsymbol{r})[v(\boldsymbol{r}) - \mu]^4}{\sigma^4 \sum_{map} I(\boldsymbol{r})} \tag{5.8}$$

where the summations represented by *map* encompass all pixels in the data set.

The standard deviation quantifies the spread of the PDF, the skewness is a measure of the asymmetry and the kurtosis characterizes the deviation from a gaussian profile. A gaussian distribution has a kurtosis of 3 and larger values imply that the PDF has relatively more prominent wings. For example, an exponential distribution has a kurtosis of 6. The calculated values for the PDF from our present data are listed in Table 5.1, showing a departure from gaussian and from pure exponential behaviour.

We conclude that the data show near exponential wings which are consistent with results of Miesch & Scalo (1995); Miesch et al. (1999). Exponential wings are for example seen in simulations of wind driven star formation (Chappell & Scalo 2001). There is also a skewness towards the blue. This may arise through preferential obscuration of red-shifted flows, compared to blue-shifted, in this dusty partly obscured region, as evidenced in Chapter 4.

5.4 Structure functions

The PDFs presented in Sect. 5.3 carry no spatial information. In order to retain some of the spatial characteristics of the velocity field and to quantify

how velocities are spatially related within the medium, we now construct the probability distribution function of velocity differences between points separated by a certain distance in the plane of the sky, the lag. The resulting distributions should provide a more searching test of theoretical models than PDFs of peak or centroid velocities.

Velocity differences, $\Delta v = v(\boldsymbol{r}) - v(\boldsymbol{r} - \boldsymbol{\tau})$, are used in this analysis. Here both $\boldsymbol{r}$ and $\boldsymbol{\tau}$, the lag, are two-dimensional space vectors. Previous authors, using both observational data, theoretical models and numerical simulations (with and without self-gravity) (Miesch & Scalo 1995; Lis et al. 1998; Miesch et al. 1999; Klessen 2000), have described how the shape of the PDF changes with different lags. Specifically, PDFs were found to exhibit strong non-gaussian forms at small lags.

It is assumed here that the turbulence is homogeneous and isotropic. This implies that the statistical properties, such as the average of velocity differences, are invariant under translation and rotation in space and only depend on the distance between regions. Using this assumption the evolution of the PDF of velocity differences with changing lags can be studied in a more compact form by investigating the structure functions as a function of lag magnitude, L=$|\boldsymbol{\tau}|$. Structure functions of order p of the velocity vector $\boldsymbol{u}$ are defined as (Frisch 1995):

$$S_p(L) = \langle |[\boldsymbol{u}(\boldsymbol{r}) - \boldsymbol{u}(\boldsymbol{r} - \boldsymbol{\tau})] \cdot \boldsymbol{e}|^p \rangle \propto L^{\zeta_p} \tag{5.9}$$

where $\boldsymbol{e}$ is a unit vector parallel (longitudinal structure function) or perpendicular (transversal structure function) to the vector $\boldsymbol{\tau}$ and $L = |\boldsymbol{\tau}|$. An average is taken over all spatial positions $\boldsymbol{r}$. The modulus sign in our definition (Eq. (5.9)) is adopted to improve the statistics for odd moments for which the structure functions would otherwise be essentially zero. Structure functions are measures of the spatial correlations of the velocity. A completely random distribution would result in a constant structure function as a function of L, whereas for example a gradient in the image would lead to a structure function increasing with L.

Structure functions are in fact the traditional manner in which to characterise turbulence, as Kolmogorov (1941) originally prescribed. The structure functions of fully developed turbulent fields are known to follow power laws in the inertial range, $\eta \ll r \ll l$, where η is the dissipation scale and l is the integral scale (Kolmogorov 1941; Davidson 2004), as described in Sect. 1.2. This simply conveys that in turbulent regions, the velocity field is spatially correlated in such a way that larger separations correspond to larger velocity differences on average. This is in fact a manifestation of the turbulent energy cascade originally proposed by Kolmogorov. The set of scaling exponents for different p, ζ_p in Eq. (5.10), can be determined (Frisch 1995) and are expected to be characteristic of the turbulence involved. That is, the degree of

intermittency or if the turbulence is subsonic or supersonic determines the scaling exponents (Frisch 1995; Boldyrev 2002). The scaling exponents are also expected to be universal for all scales and Reynolds numbers (She & Leveque 1994) where an inertial range can be found (see Sect. 1.2). Kolmogorov (1941) found from energy conservation in incompressible, isotropic and homogeneous turbulence that ζ_2=2/3 and ζ_3=1. Numerical and analytical studies of driven supersonic magnetohydrodynamic turbulence find ζ_2= 0.74, ζ_3= 1 (Boldyrev et al. 2002a).

5.4.1 Structure functions of observational data

In our case the observational data consist of projected radial velocities. We measure differences in radial velocity across the plane of the sky and we are therefore dealing with transversal structure functions. Thus, the relevant structure functions can be written as:

$$S_p(L) =<\mid v(\boldsymbol{r}) - v(\boldsymbol{r} - \boldsymbol{\tau}) \mid^p> \tag{5.10}$$

where v is the radial velocity. $\boldsymbol{r}$ and $\boldsymbol{\tau}$ are now 2-dimensional vectors in the plane-of-the-sky.
In order to emphasize the relationship between structure functions and PDFs of velocity differences we note that structure functions can be derived by first computing the PDF of velocity differences Δv, PDF($\Delta v, L$), and then obtaining the moments in Δv (Padoan et al. 2003). That is,

$$S_p(L) = \int_{\Delta v} \Delta v^p \cdot PDF(\Delta v, L) d(\Delta v) \tag{5.11}$$

For purposes of comparison with other work we focus in this section on the second order structure function, S_2(L), that is the variance of the velocity difference PDFs, and the kurtosis, $S_4(L)/S_2(L)^2$ as a function of lag magnitude, L. In Sect. 5.5 we study higher order structure functions. We have included here a brightness weighting, w, for the velocity differences, see Eqs. (5.12) and (5.13). This allows us to give more weight to bright pixels where the associated error on the velocity is smaller (Eq. (2.8)). To avoid confusion with the traditional definition of the structure functions (Eq. (5.10)), we refer to Eq. (5.12) as the variance function and to Eq. (5.13) as the kurtosis function. Both the variance and the kurtosis functions are powerful tools when comparing observations with different models of turbulence.
The variance and kurtosis functions are then

$$V(L) \quad = \quad \frac{\sum_{map} \sum_{|\boldsymbol{\tau}|=L} w(\boldsymbol{r}) w(\boldsymbol{r} - \boldsymbol{\tau}) (v(\boldsymbol{r}) - v(\boldsymbol{r} - \boldsymbol{\tau}))^2}{\sum_{map} \sum_{|\boldsymbol{\tau}|=L} w(\boldsymbol{r}) w(\boldsymbol{r} - \boldsymbol{\tau})} \tag{5.12}$$

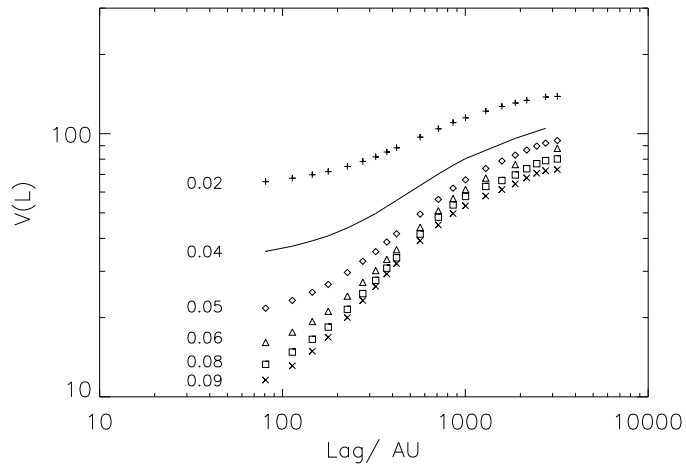

Figure 5.5: Variance functions calculated for different cut-off values in brightness. Figures beside the curves shown represent the intensity cut-off value as fractions of I_{max}.

$$K(L) = \frac{\sum_{map}\sum_{|\boldsymbol{\tau}|=L} w(\boldsymbol{r})w(\boldsymbol{r}-\boldsymbol{\tau})(v(\boldsymbol{r})-v(\boldsymbol{r}-\boldsymbol{\tau}))^4}{V^2(L)\sum_{map}\sum_{|\boldsymbol{\tau}|=L} w(\boldsymbol{r})w(\boldsymbol{r}-\boldsymbol{\tau})} \quad (5.13)$$

where the summations are performed over all pairs of pixels in the whole map that fulfill the requirement $|\boldsymbol{\tau}|$=L. We have not used L < 4 pixels (0.15 ″), since this coincides with the spatial resolution of the data.

5.4.2 The effect of errors in structure functions

An important issue is, however, whether the velocity data should be brightness weighted (w($\boldsymbol{r}$)=I($\boldsymbol{r}$) in counts per second, where I is the brightness) or equally weighted (w=1) in calculating the variance and kurtosis of the velocity difference PDFs. In order to address this problem, we need further to consider errors in the data. We have already removed data at the 2% level as described in Sect. 2.4.3. We now examine whether this cut-off is sufficiently low for the examination of variance and kurtosis functions. We find that a 2% cut-off is too low if we do not use brightness weighting but that it is acceptable if brightness weighting is included.

To investigate the effect of errors, we use equal weighting and calculate the variance function for a number of cut-off values in brightness. The resulting variance functions are shown in Fig. 5.5. Note that these were derived from the filtered image (Sect. 5.1) and not from the full velocity image. Due to the

filter the variance function tend to level off at scales greater than ~ 2000 AU. This effect is related to the constant value of velocity dispersion above this scale seen in the filtered image in Sect. 5.2 and has no effect on scales smaller than $\sim$2000 AU (see below). All the variance functions can be approximated by power laws, but we find that the scaling exponent, ζ_2 in $V(L) \propto L^{\zeta_2}$, increases with increasing cut-off value before converging to a constant value when the cut-off value reaches $\sim 9\%$ of I_{max}. This indicates that pixels with brightness lower than this value contribute significantly to the random noise and that they should be removed prior to analysis. This analysis emphasizes that caution should always be exercised when equal weighting is used since results may show dependence on the choice of cut-off.
The brightness weighted variance function is expected to be less influenced by noise. We find that the brightness weighted variance function including all pixels is essentially the same as the equally weighted variance function with a brightness cut-off of 9% of I_{max}. Due to the lesser influence from noise we use the brightness weighted variance and kurtosis functions in the following.

Errors in the brightness weighted variance function resulting from uncertainties in the velocities have been calculated by using the error propagation law and taking the 1σ uncertainty on the velocity in each pixel from Eq. (2.8). We neglect the uncertainty in the determination of the brightness as this is a second order effect entering from the weighting function w, and calculate the resulting error as the standard deviation, E:

$$\begin{aligned} E(V(L)) &= 2\frac{\sqrt{\sum_{map}\sum_{|\boldsymbol{\tau}|=L} w^2(\boldsymbol{r})w^2(\boldsymbol{r}-\boldsymbol{\tau})(v(\boldsymbol{r})-v(\boldsymbol{r}-\boldsymbol{\tau}))^2}}{\sum_{map}\sum_{|\boldsymbol{\tau}|=L} w(\boldsymbol{r})w(\boldsymbol{r}-\boldsymbol{\tau})} \\ &\quad \times\sqrt{\sigma^2(v(\boldsymbol{r}))+\sigma^2(v(\boldsymbol{r}-\boldsymbol{\tau}))} \end{aligned} \tag{5.14}$$

where the summation is performed over all pairs of pixels in the map that satisfy $|\boldsymbol{\tau}| = L$ and $\sigma^2(v(\boldsymbol{r}))$ is the uncertainty of $v(\boldsymbol{r})$ from Eq. (2.8). Due to the large number of pixel pairs that goes into the calculation of the variance function the relative error, $E(V(L))/V(L)$, is typically 10^{-3} and therefore negligible.

5.4.3 The variance function

The brightness weighted variance function is shown in Fig. 5.6 for the full velocity field in a log-log plot. The best fit of the variance function to a power-law is found to have ζ_2=0.53±0.01 and this is also shown in Fig. 5.6. For comparison, Miesch et al. (1999) obtained values of ζ_2 between 0.33 and 1.05 for several molecular clouds at scales larger than $1.4{\cdot}10^3$ AU while Ossenkopf & Mac Low (2002) obtained $\zeta_2 = 0.94$ for the Polaris Flare at

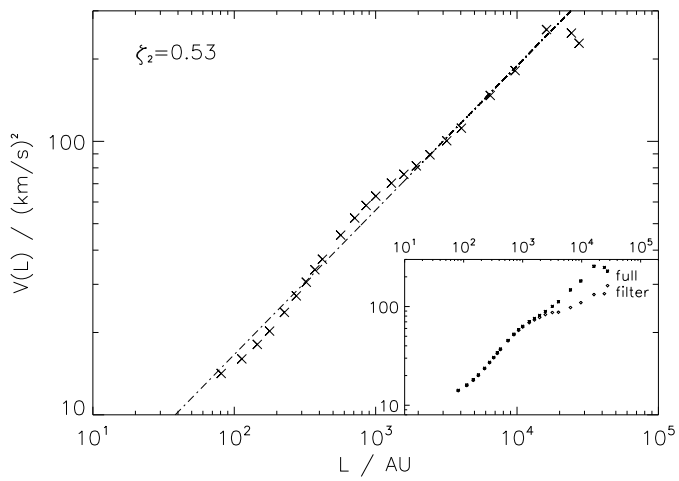

Figure 5.6: The variance function for the full velocity field. A power-law form with exponent 0.53 is overlaid. The inset displays the variance function of the filtered velocity image compared to the variance function of the full field.

scales larger than 2000 AU. It is noteworthy that our value of 0.53±0.01 is significantly lower than both the Kolmogorov value of 0.67 and the value of 0.74 from supersonic turbulence (Boldyrev et al. 2002a). We also note that the variance function is closely related to the Larson relationship such that the exponent of the variance function should be approximately two times the Larson exponent. In Sect. 5.2 the exponent of the Larson relation was found to 0.21 which is a little less than half the value of 0.53 found here.

The variance function in Fig. 5.6 in fact deviates significantly from a single power law, again underlining the non-Kolmogorov nature of the gas dynamics. This is particularly apparent through a positive deviation around 800 AU and a negative deviation around 100-200 AU. These deviations can be interpreted as the presence of preferred scale sizes. This interpretation is proved in Sect. 8.2. In principle, the curvature of the structure function may suggest the presence of more than one fractal distribution of scales, that is, a multi-fractal medium. At all events, several power laws operating in different ranges would appear necessary to fit the behaviour of the variance function. Irrespective of the process(es) behind such different power laws this again suggests the existence of a special scale where one power law distribution becomes dominant over another.

The physical meaning attached to V(L) in Fig. 5.6 is that it approximately represents all energies in eddies below the scale L (Davidson 2004). This is evident from the fact that V(L) in Eq. (5.12) is related to $\boldsymbol{u}^2$ where $\boldsymbol{u}$ is the velocity vector. The deviation from a power law in Fig. 5.6 below $\sim$ 2000AU

therefore represents more energy at lower scales and implies that there is an excess of material in motion at 2000 AU and below. This in turn implies that excess energy is being injected or that cascading energy accumulates at this scale due to insufficient dissipation or some sort of bottleneck effect in the energy cascade. The scale size of 2000 AU suggests that the excess arises from outflow events associated with low mass star formation injecting energy into a system dominated by a turbulent energy cascade from larger scales. Conversely the material appears to suffer less velocity dispersion at scales below 300AU. Thus material associated with these smaller scales appears to have dissipated some of its turbulent energy at larger scales.
The inset in Fig. 5.6 shows the effect of the removal of the large scale gradient on the variance function. The variance function of the filtered velocity image is identical to the variance function of the full field for scales smaller than half the size of the filter ($\sim$ 3000 AU) above which the function flattens. It is clear that the filter has no effect on very small scales and that the removal of the large scale velocity structure causes the variance function to be systematically smaller on larger scales. This effect of the filtering has also been noted by Miesch et al. (1999) and is most likely an artefact due to the finite size of the map (Ossenkopf & Mac Low 2002).

5.4.4 The kurtosis function

Turning now to the kurtosis function Eq. (5.13), the kurtosis is a measure of the degree of correlation in the internal motions at a certain scale. A velocity field with no spatial correlations would display a gaussian shape, which as mentioned above, has a kurtosis of 3. Thus values of kurtosis exceeding 3 indicate the strength of velocity correlation at specific lags. From simulations Ossenkopf & Mac Low (2002) found that kurtosis values above 3 can only be verified if the map contain motions on scales considerably larger than the lag. As the lag approaches the size of the map, the value of the kurtosis tends to approach the gaussian value of 3. This suggests that the kurtosis in fact measures correlations on a particular scale relative to the total motions in the map (Ossenkopf & Mac Low 2002). Thus the value of 3 for lags approaching the size of the map arises because the map cannot of course contain motion on larger scales than the size of the map itself. It follows that a kurtosis value around 3 is always expected at scales approaching the size of the map and provides no useful information on the velocity correlations at that scale.

Looking specifically at filamentary structure from both simulations and CO data of the ρ Ophiuchi molecular cloud, Lis et al. (1998) found non-gaussian wings of velocity difference PDFs at small scales evolving into gaussians at larger scales. Miesch et al. (1999) reported kurtosis values between 10 and

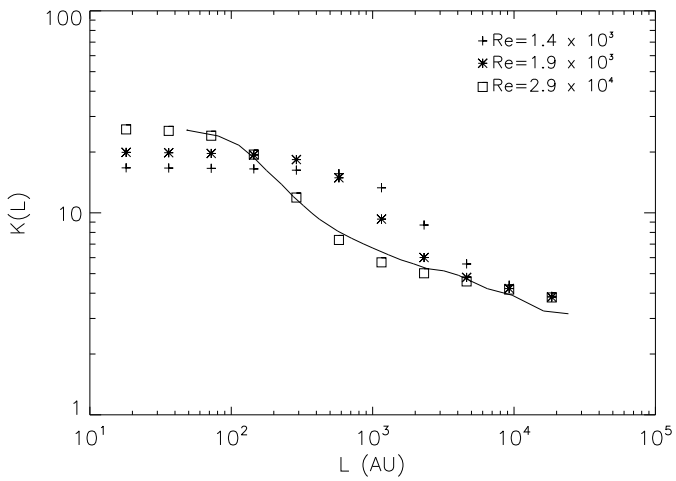

Figure 5.7: The kurtosis function, Eq. (5.13), for the full velocity field (solid line). Theoretical predictions for 3 different Reynolds numbers from Eggers & Wang (1998) are shown for comparison. Taken from Gustafsson et al. (2006b)

30 at the smallest lags (1.4×10^3 - 1.2×10^4 AU) for regions with active star formation in the Orion B and Monoceros clouds, with the required gaussian value of 3 at lags of the order of the map size (2×10^6 AU). Similar behaviour was found by Ossenkopf & Mac Low (2002). Klessen (2000) showed that numerical simulations including self-gravity achieve higher values of the kurtosis at small lags than simulations without self-gravity.

The kurtosis function derived from our present data is shown in Fig. 5.7 as a continuous line. The kurtosis values approach 30 at small lags (100 AU) and decrease gradually until reaching the gaussian value of 3 at lags of about the map size. This is consistent with the finding of Ossenkopf & Mac Low (2002) as described above. The shape of the kurtosis function shows some similarity to those presented in Miesch et al. (1999). This similarity suggests that the scaling of correlations of motions relative to the total motion in a map is universal and independent of the size of the scales involved. The details of how the correlations scale are most likely characteristic of the interstellar turbulence.

Comparison with a theoretical model

A very striking comparison may be found with semi-analytical results of a model of multiplicative processes (see below) in Eggers & Wang (1998). In Eggers & Wang (1998) the kurtosis, called flatness in that work, is constant out to some lag beyond which the kurtosis decreases with increasing lag. The

shape of the kurtosis was found by Eggers & Wang (1998) to depend on the Reynolds number, where R $>1.1\times10^4$ marks a transition from a convex shape to a concave shape (see Fig. 5.7). The shape remains essentially unchanged for higher Reynolds numbers.

In order to compare with results in Eggers & Wang (1998) we make an estimate of the Reynolds number, Re $= ul/\nu$ (Eq. (1.3)) , of the flows in OMC1. The dynamical viscosity, ν, can be approximated by $\nu \sim \lambda v_{th}$, where λ is the mean-free-path of the particles and $v_{th} = (k_B T/\mu m_H)^{1/2}$ is the rms thermal velocity (Frisch 1995). Since $\lambda = (n\sigma)^{-1}$, where σ is the cross section of H_2-H_2 collisions and n is the number density,

$$Re = \frac{ul}{\lambda v_{th}} = uln\sigma\sqrt{\frac{\mu m_H}{k_B T}}. \tag{5.15}$$

The cross section for H_2-H_2 collisions is 2.7×10^{-16} cm^2 (Atkins 1990). The shocked regions observed here have a typical temperature of 2000-3000K and gas densities are 10^6 to 10^7 cm^{-3} (Kristensen et al. 2003, 2006). The velocity u may be approximated by the velocity dispersion in our observed region and u is therefore given by twice the standard deviation of the PDF of peak velocities (Table 5.1), that is, $u \sim 20$kms^{-1}. The corresponding l is the size of the region $\sim 3\times10^4$ AU. Using these values, we obtain a Reynolds number of Re $\sim 3 \times 10^9$. The significance of this value is only that it is very large and greatly exceeds the critical value in Eggers & Wang (1998) for which convex behaviour of the kurtosis function versus lag becomes concave. If we were to include magnetic effects, the magnetic Reynolds number might be substantially higher.

The Eggers & Wang (1998) description of turbulent processes is ad hoc in the sense that it does not result from detailed high resolution three dimensional MHD simulations. Instead some reasonable assumptions, described below, are made concerning the cascade of turbulent energy, assuming it to be a stochastic process, isotropic and homogeneous in space, with certain additional properties which are briefly summarized below. Once one assumes that the turbulence is isotropic and homogeneous, the turbulence in the Fourier domain is represented by a spectrum which is a function of a single variable r, corresponding to a size of turbulent eddies. The approach of Eggers & Wang (1998) is to impose a recipe for the cascade of energy from larger to smaller scales. The recipe states that energy at a given scale r is transferred *only* to a scale $r/2$. The *amount* of energy transferred, or more precisely the ratio s of the velocity amplitudes between scale r and $r/2$ in equilibrium, is given by a probability distribution :

$$p(s) \;=\; p\delta(s - s_1) + (1 - p)\delta(s - s_2) \tag{5.16}$$

with

$$p = 0.688, \qquad s_1 = 0.699, \qquad s_2 = 0.947$$

where the probability p and parameters s_1 and s_2 were obtained by fitting to reproduce laboratory data of a low temperature helium experiment.

Eq. (5.16) states that the probability p is high ($\sim 2/3$) for the ratio of velocities to be relatively small ($s = s_1$), which corresponds to a low efficiency of energy cascade from one scale to the next. However there remains a probability of $\sim 1/3$ that there is efficient cascading, $s = s_2$. Starting from some chosen outer scale, this recipe allows for a very quick calculation of the energy at any given smaller scale by multiplying the probabilities for every cascade step lying between these two scales and producing the appropriate PDF semi-analytically. Hence the term multiplicative turbulence. The viscous cut-off of the turbulence is implemented through stopping the further cascading of energy if the Reynolds number at a given scale falls below a set value. The velocity fluctuation PDF is replaced below that scale by an exponentially decaying tail.

We show in Fig. 5.7 a comparison between our observed kurtosis and that presented in Eggers & Wang (1998) for Reynolds numbers between 1.4×10^3 and 2.9×10^4, the highest which Eggers & Wang (1998) show, noting once more that the form of the kurtosis function appears to be independent of Reynolds number above $\sim 10^4$. The lower Reynolds number cases are shown purely for comparison. The lag values in Eggers & Wang (1998) are scaled to 40000 AU in order to fit our range of lags. The similarity of the kurtosis function between that for our data and that of Eggers & Wang (1998) suggests that the model of a multifractal, multiplicative turbulent medium on which Eggers & Wang (1998) is based may capture some of the physics of the turbulence in the hot component of the gas in OMC1.

5.5 Scaling of exponents

We now extend the analysis of structure functions from the previous chapter. Here we concentrate on how structure functions (Eq. (5.9)) behave as a function of the order p. In particular we investigate how the exponents of the structure functions, that is, ζ_p in $S_p(L) \propto r^{\zeta_p}$, scale with p. As mentioned in Sect. 5.4 the scaling exponents are believed to be universal, however see below, and characteristic of the nature of the turbulence. Kolmogorov (1941) found that $\zeta_p = p/3$. Using corrections to the Kolmogorov theory, She & Leveque (1994) described the scaling of velocity structure functions in

incompressible turbulence by:

$$\zeta_p/\zeta_3 = \frac{p}{9} + 2\left[1 - \left(\frac{2}{3}\right)^{p/3}\right], \tag{5.17}$$

which is confirmed by simulations of nearly incompressible turbulence (Padoan et al. 2004; Haugen et al. 2004a) and by experiments (Anselmet et al. 1984; Benzi et al. 1993).

Dubrulle (1994) however suggested that ratios of scaling exponents, say ζ_p/ζ_3, are inherently universal, while the individual scaling exponents may not be universal themselves. In this connection Frick et al. (1995) showed in the context of cascade models that one may have $\zeta_3 \neq 1$ and yet recover scaling laws for the structure functions in good agreement with the She-Leveque model for the ratio ζ_p/ζ_3. Dubrulle (1994) generalized the She-Leveque formula to:

$$\zeta_p/\zeta_3 = (1-\Delta)\Theta p + (3-D)(1-\Sigma^{\Theta p}) \tag{5.18}$$

where $\Sigma = 1 - \Delta/(3-D)$ measures the degree of intermittency of energy dissipation and $\Sigma \in (0,1)$ (Boldyrev et al. 2002a). Eq. (5.18) is descriptive of both incompressible and compressible turbulence when the parameters, Θ, Δ and D, are adjusted accordingly. D is the dimension of the most dissipative structures, that is, representative of how dissipation occurs. In incompressible turbulence the dissipation is organized in filaments with dimension D=1 (Padoan et al. 2003). The two other parameters represent nonintermittent scalings of the velocity difference, $u_l \sim l^{\Theta}$, and of the characteristic time of energy transfer at this scale, that is, the turn-over time of an eddy of that size $t_l \sim l/u_l \sim l^{\Delta}$ (Boldyrev et al. 2002a; Kritsuk & Norman 2004). For the Kolmogorov cascade, described in Sect. 1.2, $\Theta = 1/3, \Delta = (1-\Theta) = 2/3$ and Eq. (5.17) is recovered.

For supersonic turbulence Boldyrev (2002) assumed that dissipation mainly occur in sheetlike shocks with D=2 and obtained, as an extension to the She-Leveque model, the scaling:

$$\zeta_p/\zeta_3 = \frac{p}{9} + 1 - \left(\frac{1}{3}\right)^{p/3}, \tag{5.19}$$

which is confirmed by observations in the Perseus and Taurus molecular clouds (Padoan et al. 2003) and simulations (Boldyrev et al. 2002a,b; Padoan et al. 2004; Joung & Mac Low 2006; de Avillez & Breitschwerdt 2006). This type of scaling was originally proposed by Politano & Pouquet (1995) for magnetohydrodynamic turbulence, where the dissipative structures are thought to be two-dimensional current sheets.

In the following we calculate the scaling exponents of the transversal structure functions and compare with the theoretical scalings of She-Leveque (Eq. (5.17)) and Boldyrev (Eq. (5.19))

5.5.1 Results for OMC1

The structure functions of radial velocities are calculated using brightness weighting as in Sect. 5.4:

$$S_p(L) = \langle I(\boldsymbol{r}) I(\boldsymbol{r} - \boldsymbol{\tau}) \, |v(\boldsymbol{r}) - v(\boldsymbol{r} - \boldsymbol{\tau})|^p \rangle. \tag{5.20}$$

I and v are the brightness and radial velocity, respectively. When $p = 2$ this reduces to Eq. (5.12) with $w(\boldsymbol{r}) = I(\boldsymbol{r})$.
The third order structure function of OMC1, $S_3(L)$, is displayed in Fig. 5.8a. It is not well represented by a single power law showing a clear deviation around 10^3AU, as has already been noticed for the second order structure function (Sect. 5.4). This is also evident from the large variations in the local logarithmic derivatives of $S_p(L)$, shown in Fig. 5.8b for $p = 1$–5.
However, Benzi et al. (1993) discovered that structure functions can be represented as functions of, say, the third order structure function, namely

$$S_p(L) \propto S_3(L)^{(\zeta_p/\zeta_3)_{\mathrm{ESS}}}. \tag{5.21}$$

This is now known as extended self-similarity (ESS). Even if the structure functions of Eq. (5.10) or Eq. (5.20) are not power laws over any given range, the functions represented by Eq. (5.21) nevertheless exhibit good power law behaviour. The scaling in Eq. (5.21) is generally found to extend over a much larger range than for the structure functions of Eq. (5.10). Self-similarity, as expressed by Eq. (5.21), is believed to be more fundamental than the self-similar scaling with respect to L (Benzi et al. 1993).
In Fig. 5.8c we have plotted the ratios of the logarithmic slopes of S_p and S_3, $d \ln S_p(L)/d \ln S_3(L)$, for $p = 1$–5. If a range in which good power law scaling is present is encountered in the various structure functions, the ratios of logarithmic slopes should display plateaus in that range at values of $(\zeta_p/\zeta_3)_{\mathrm{ESS}}$. From Fig. 5.8c we find that the structure functions for $p = 1$–5 exhibit a reasonably good scaling range from $L = 160\,\mathrm{AU}$ to $L = 7000\,\mathrm{AU}$. This range is marked by the dotted vertical lines in Fig. 5.8c. The scaling exponents are found by fits to Eq. (5.21) in this range. As an example we show in Fig. 5.8d the extended self-similarity plot of $S_5(L)$ vs. $S_3(L)$ together with the best fit yielding the slope $(\zeta_5/\zeta_3)_{\mathrm{ESS}} = 1.06$. The dotted lines mark the range of the fit. It is clear from Fig. 5.8c that the scaling gets poorer when the order p is increased. At $p = 5$ the plateau is rather ill-defined (see also Fig. 5.8d) and therefore we cannot determine a scaling at higher orders than $p = 5$. In Fig. 5.8e we show the scaling exponents $(\zeta_p/\zeta_3)_{\mathrm{ESS}}$ vs. p compared to the values predicted by the She-Leveque model of incompressible turbulence, Eq. (5.17) (dotted line) and the Boldyrev model of supersonic turbulence, Eq. (5.19) (dashed line). The scaling exponents derived from the velocity in

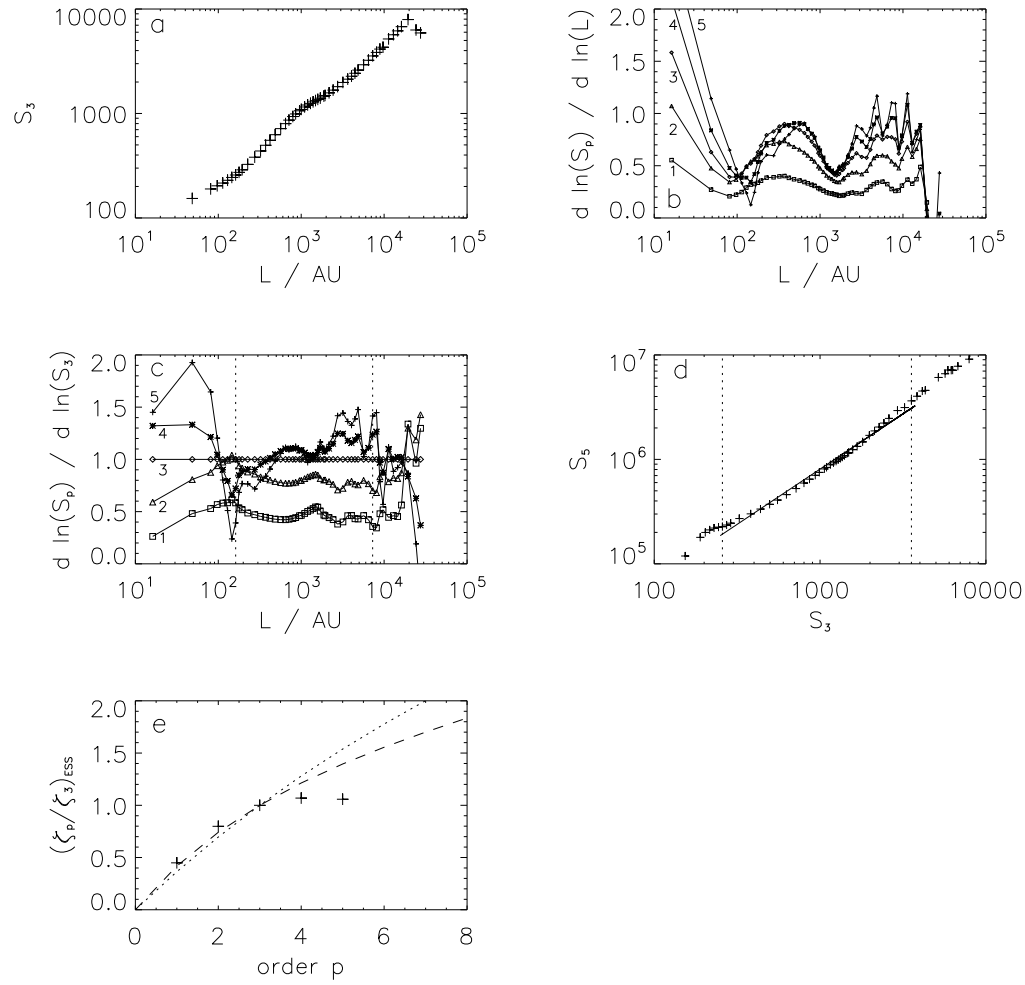

Figure 5.8: a) Third order structure function of the velocities in OMC1. b) Logarithmic derivatives of $S_p(L)$ for $p = 1$–5. c) Ratios of the differential slopes of $S_p(L)$ to the slope of the third order structure function for $p = 1$–5. The vertical dotted lines mark the interval in which the scaling exponents have been fitted. d) $S_5(L)$ vs. $S_3(L)$. The dotted lines mark the range of the fit and the solid line is the best fit within that range yielding the logarithmic slope, $(\zeta_p/\zeta_3)_{\rm ESS} = 1.06$. e) The ESS scaling exponents (+) OMC1, (dotted line) She-Leveque scaling, (dashed line) Boldyrev scaling.

OMC1 clearly deviate from both the She-Leveque and the Boldyrev scaling at $p \geq 4$. The OMC1 scaling exponents show signs of becoming constant at $(\zeta_p/\zeta_3)_{\rm ESS} \sim 1$ or even slightly decreasing for $p > 4$, in contrast to the theoretical scalings, which are monotonically increasing.

This result for velocities of hot, shocked gas in OMC1 at scales 70 AU –

3×10^4AU (3.4×10^{-4}pc to 0.15 pc) differs from the findings of Padoan et al. (2003). They found that the density fields in the Perseus and Taurus molecular clouds as observed in CO follow Boldyrev scaling at scales larger than 0.08 pc up to $p = 20$.

5.5.2 Generalized She-Leveque formalism

The generalized She-Leveque formula (Eq. (5.18)) is based on two assumptions (She et al. 2001). If the assumptions are valid in the region and for the turbulent motions involved the data can be described in the generalized She-Leveque formalism. The assumptions can be tested by the so-called β- and γ-tests which should also yield the values of the parameters in Eq. (5.18). Here we attempt to use these tests on the OMC1 data.
The generalized She-Leveque formula with $\Theta = 1/3$ (Eq. (5.18)) can be transformed into

$$\zeta_p/\zeta_3 = \gamma p + C(1 - \beta^p) \tag{5.22}$$

where $C = (1 - 3\gamma)/(1 - \beta^3)$ and $\beta^3 = \Sigma$ (She et al. 2001). Note that $D = 3 - C$.
Eq. (5.22) was derived based on two assumptions. The first assumes that there exists a universal scaling behaviour,

$$F_{p+1}(L) = A_p F_p(L)^\beta F_\infty(L)^{1-\beta} \tag{5.23}$$

where

$$F_p(L) = S_{p+1}(L)/S_p(L) \tag{5.24}$$

Here $0 \leq \beta \leq 1$ is a constant and A_p is independent of L. A_p has been observed to be independent of p (She et al. 2001; Padoan et al. 2003), but this is not a requirement. The assumption in Eq. (5.23) can be validated with a log-log plot of $F_{p+1}(L)/F_2(L)$ vs $F_p(L)/F_1(L)$. If the plot is a straight line the data pass the β-test and the value of β is the slope of the line.
In Fig. 5.9 we show $F_{p+1}(L)/F_2(L)$ vs $F_p(L)/F_1(L)$ for p=1-5. The points lie on a straight line with a slope of 0.76. Thus the data pass the β-test with β=0.76. We also verify that the constants A_p are independent of p, as found in She et al. (2001) and Padoan et al. (2003). β measures the degree of intermittency in a turbulent flow. If $\beta = 1$ there is no intermittency and if $\beta \to 0$ only the most intermittent structures persists (She et al. 2001). In supersonic turbulence $\beta = 0.69$ (Boldyrev 2002). In the Taurus and Perseus molecular clouds Padoan et al. (2003) found $\beta = 0.79$ and 0.79, respectively, very close to our value of 0.76. The value of 0.76 verify the finding in Sect. 5.3 that the energy dissipation in OMC1 is intermittent.

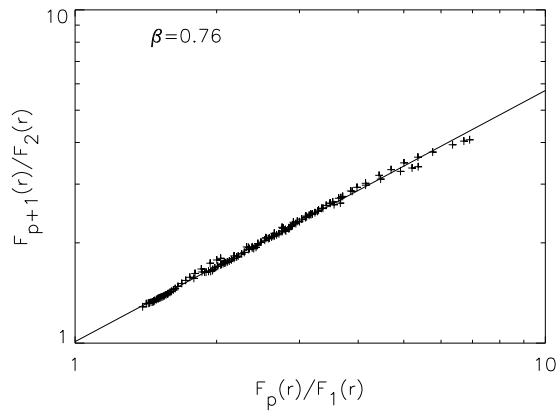

Figure 5.9: β-test: $F_{p+1}(L)/F_2(L)$ vs $F_p(L)/F_1(L)$ for p=1-5. A fit to a straight line yields $\beta = 0.76$.

The second assumption by She et al. (2001) is,

$$F_\infty \sim S_3^\gamma \tag{5.25}$$

If the data have passed the β-test the assumption in Eq. (5.25) can be tested by using the value of β and plotting $\zeta_p/\zeta_3 - \chi(p,\beta)$ vs $p - 3\chi(p,\beta)$ where $\chi(p,\beta) = (1-\beta^p)/(1-\beta^3)$. If the plot is a straight line the data pass the γ-test and the slope provides an estimate of γ. The test of this assumption involves high orders ($p \to \infty$), but as we saw in Sect. 5.5 the scaling is not well defined for moments much higher than p=5. Thus we are unable to test this.

5.6 Summary and conclusion

The fraction of gas studied here is highly excited and very dense and quite distinct from gas whose statistical properties have been studied in earlier work. The latter refers to CO data which involve much larger scales and much cooler, lower density and relatively quiescent gas. Nevertheless we have found that the hot dense gas in OMC1 nicely follows the general trends observed in earlier studies, down to the smallest, densest scales investigated here. However, significant differences are also found.

The major conclusions are:
(1) The size-line width relation of Larson (1981) is recovered at the small scales investigated here. The scaling exponent is $\alpha = 0.205 \pm 0.002$, which agrees with the average value of 0.21 ± 0.03 that Caselli & Myers (1995)

found in Orion at scales 0.03 - 1pc, using CO as an indicator (and which did not in fact include OMC1).
(2) If we use velocity filtered data, removing the largest scales which appear as an apparent gradient of velocity, the Larson relationship breaks down. We conclude that the large scale motions are an inherent part of the turbulent cascade and should therefore not be removed from the data. Large scale injection of turbulent energy is the dominant process and outflows from massive star(s) in the IRc2 complex contribute a substantial part of the driving of the turbulence at the scale of 0.1 pc.
(3) The probability distribution function (PDF) of velocities is best fitted by an exponential or a weakly stretched exponential and departs strongly from gaussian. This suggests that the turbulence in the region studied here is characterized by intermittency. Intermittency is also implied by the β-value of 0.76 which quantifies the deviation of the motions in OMC1 from Kolmogorov turbulence where $\beta = 1$.
(4) The variance function of the velocity differences or the second order structure function is not well represented by a single power law. A multifractal model is implied. The best fit scaling exponent is ζ_2 =0.53±0.01, significantly lower than the Kolmogorov value of 0.67, underlining the non-Kolmogorov nature of the turbulence. The behaviour of the variance function shows that there are preferred scale sizes in the medium below 2000 AU reflecting the presence of protostellar zones of this dimension and below.
(5) As further evidence of the multifractal nature of the medium, the kurtosis function of the velocity differences closely resembles that of the multifractal model of Eggers & Wang (1998) for high Reynolds numbers.
(6) The scaling exponents, ζ_p/ζ_3, of higher order structure functions exhibit unusual dependence of the order p. The scaling exponents are nearly constant for p $>$ 3 and smaller than predicted by both She & Leveque (1994) and Boldyrev (2002).
In Chapter 7 we will compare the structure functions obtained for the observation with numerical hydrodynamical simulations. From this comparison we find that the unusual scaling relation (Sect. 5.5) is caused because we observe preferentially shocked gas. However structure functions of shocked gas in the simulations do not show deviations from power laws as observed here.

Chapter 6

Analysis of individual clumps

The high spatial resolution of the CFHT/GriF data (Sect. 2.4) allows us to perform the analysis of individual clumps of shocked gas with the same statistical methods as in Chapter 5. This enables us to obtain a more detailed view of the turbulence in the OMC1 region. We will see that individual clumps show large variations with regards to the shape of the PDF and the slope of the second order structure function.

6.1 Definition of clumps

In order to separate individual clumps, the dimensions must be defined. The following algorithm is used to identify the extent of any clump. The data are smoothed by a 9 by 9 pixel boxcar, in order that random fluctuations become unimportant. A clump is defined as a region which encompasses all pixels surrounding a local brightness maximum where the emission is situated on a continuously decreasing slope from the maximum brightness. Thus when we move in any direction starting from the pixel of maximum brightness and encounter a pixel with higher brightness than the preceding pixel, we define this as the boundary of the clump in this direction. As a further constraint we only use pixels with a brightness larger than 20% of the local brightness maximum. This avoids clumps becoming unrealistically large in the outer regions of the outflow emission with low brightness and few brightness maxima (see Fig. 2.8). The 20% restriction has no effect in bright congested regions such as Peak 1 and 2. In passing, we note that we cannot rule out that some clumps so identified are the result of chance superpositions of two or more isolated clumps in the same line-of-sight. We have ignored this possibility.
With the above definition, we have delineated 170 clumps. These are in most part essentially the same features as analyzed in Nissen et al. (2006).

Coordinates of the clumps are listed in Table A.1 in Appendix A. The number of pixels in each clump ranges from 841 to 18026, which corresponds to sizes of clumps between approximately 500 and 2200 AU. Due to the small size of the clumps, the earlier discussion concerning the removal of the large scale gradient (Sect. 5.1) is irrelevant here, since filtering does not affect the velocity field over such restricted regions.

6.2 PDFs of clumps

The PDFs of peak velocities of the 170 individual clumps have been calculated as in Sect. 5.3 with a bin-size of $1\mathrm{kms}^{-1}$. The sensitivity of the shape of the PDF to uncertainties in the velocities has been investigated in the same way as in Sect. 5.3, that is, by creating a number of noisy velocity fields and comparing the resulting PDFs. Errors vary from clump to clump but do not influence the general shape of the PDF in any of the clumps. Eight representative PDFs with error estimates are shown in Fig. 6.1. Error bars shown represent the values spanned by the observed data and the simulated data. The PDFs for the clumps take on many different shapes. Here we catagorize the shapes in three basic forms, that is, gaussian, exponential and multi-modal. For most clumps the shapes are complex and appear bi- or multi-modal. Bi- or multi-modal PDFs, such as shown in Fig. 6.1a, b, c and d, can for example result from bipolar outflows from one or multiple protostellar objects. 39 clumps have clear stretched exponential wings. Two such clumps are shown in Fig. 6.1e,f. 27 clumps have PDFs that can be fitted by a single gaussian. Two examples are shown in Fig. 6.1g,h. Table A.1 list the PDF shape of all 170 clumps.

Note that, gaussian PDFs would of course arise if the velocity data had a significant random noise contribution. However it turns out that this is not the case save perhaps in 3 of the 27 clumps with gaussian PDFs mentioned above. For six of the 27 clumps with gaussian PDFs, the 1σ uncertainty on the velocities (Eq. (2.8)) exceeds the half-width (one standard deviation) of the gaussian PDF in 1% or more of the total number of pixels. The number of pixels is 1%, 4%, 5%, 28%, 32% and 54% of the totals. In the latter three of these six clumps the velocity distribution could be dominated by uncertainties in the velocities and these data may therefore be spurious, in the sense that the gaussian character may be over-emphasised by noise. The exact shape of the PDF of those three clumps has no influence on the conclusion drawn below.

The spatial distribution of clumps with gaussian PDFs, stretched exponential PDFs and bi- or multi-modal PDFs is shown in Fig. 6.2 on basis of Table A.1. Clumps with gaussian PDFs are found in all regions of the observed field, ex-

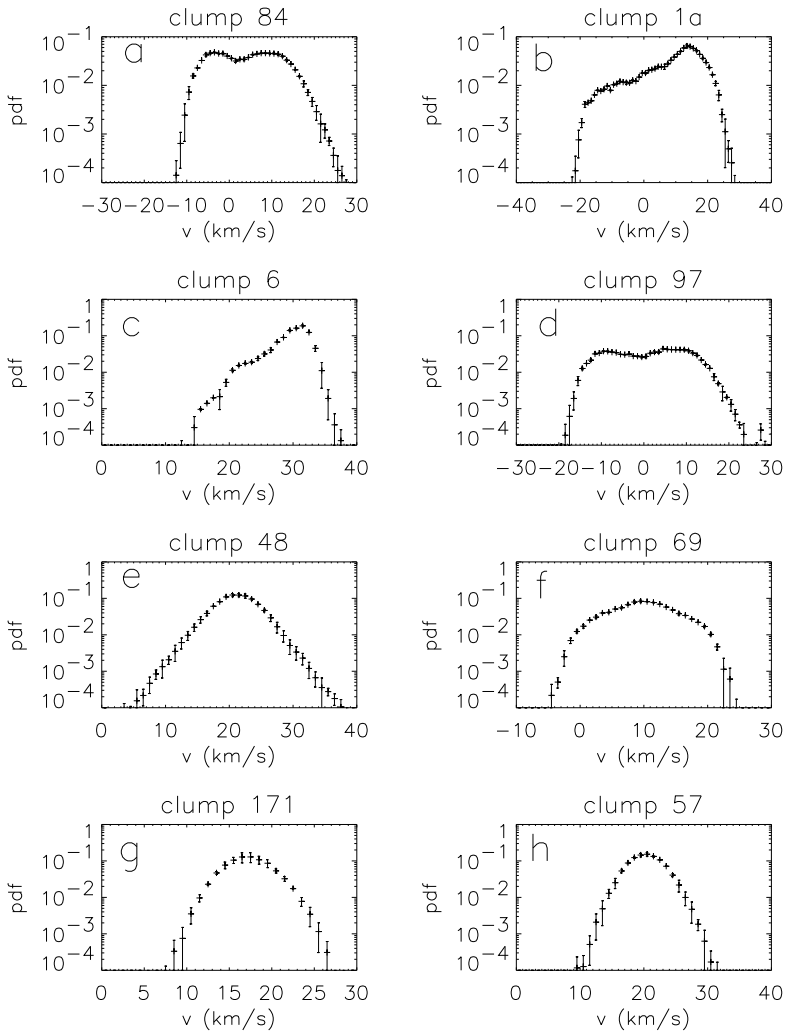

Figure 6.1: PDFs of eight representative clumps. a, b, c and d are multi-modal, e and f are stretched exponential, g and h are gaussian. The locations within OMC1 of the clumps are shown in Figs. 6.2, 6.5, 6.6. The number of the clumps refer to Table A.1 in Appendix A.

cept in the central region around BN-IRc2. Essentially the same distribution is found for clumps with non-gaussian PDFs. That is, there is no tendency for clumps with gaussian PDFs, for example, to group together in small areas. Thus it seems that the dynamical processes dominating the gas motions in the BN-KL nebula can simultaneously produce both gaussian and non-gaussian PDFs in clumps with sizes of $\sim 10^3$ AU, and that the clumps with gaussian and non-gaussian PDFs are intermingled. However there appears to be some mechanism that inhibits the formation of clumps with gaussian

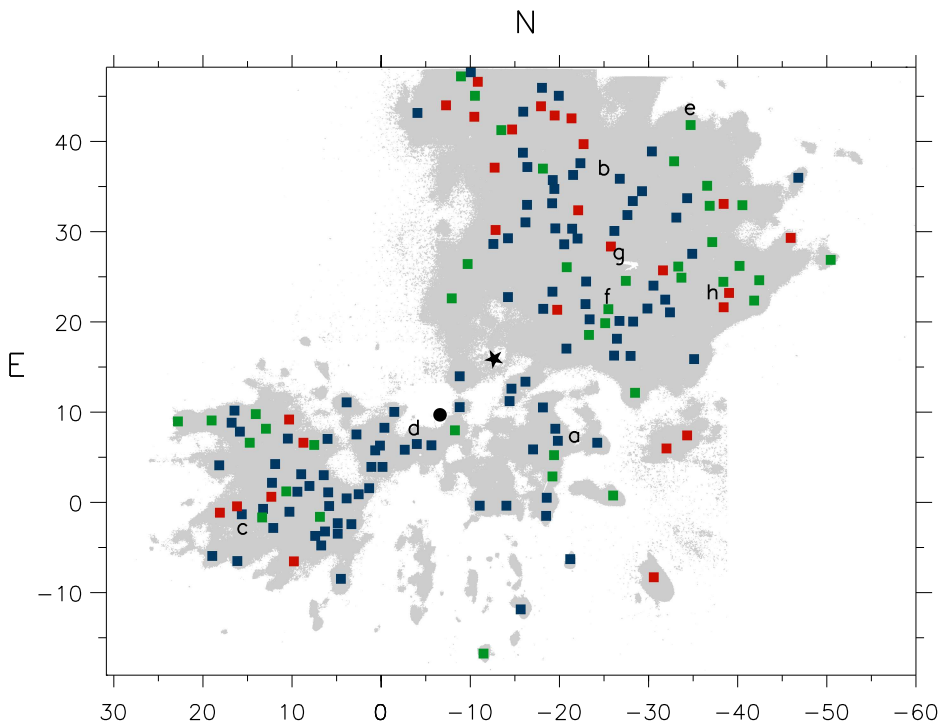

Figure 6.2: Position of clumps with bi- or multi-modal PDF (blue), stretched exponential PDF (green) and gaussian PDF (red). The underlying grey background represents the spatial extent of H_2 emission at 2.121 μm with brightness greater than $\sim$ 2.4 x 10^{-6}Wm^{-2}sr^{-1} (8% of the maximum). The position of BN is marked with a star, IRc2 with a circle. a,b,c,d,e,f,g,h marks clumps shown in Figs. 6.1, 6.3. From Gustafsson et al. (2006b).

PDFs in the outflow region around BN-IRc2.

6.3 Variance functions for clumps

The variance function or the second order structure function of the velocity field has also been calculated for each clump, using Eq. (5.12). Most of the variance functions appear to be well approximated by power laws with a few exceptions, but the value of the scaling exponent, ζ_2, varies between essentially zero, that is, a flat distribution, and 1.61. The variance functions are shown in Fig. 6.3 for the same eight representative clumps shown in Fig. 6.1. Values of ζ_2 are listed in Table A.1 for all analysed clumps.
The errors in the variance functions have been calculated in the same way as for the full region in Sect. 5.4 using the law of error propagation (Eq. (5.14)).

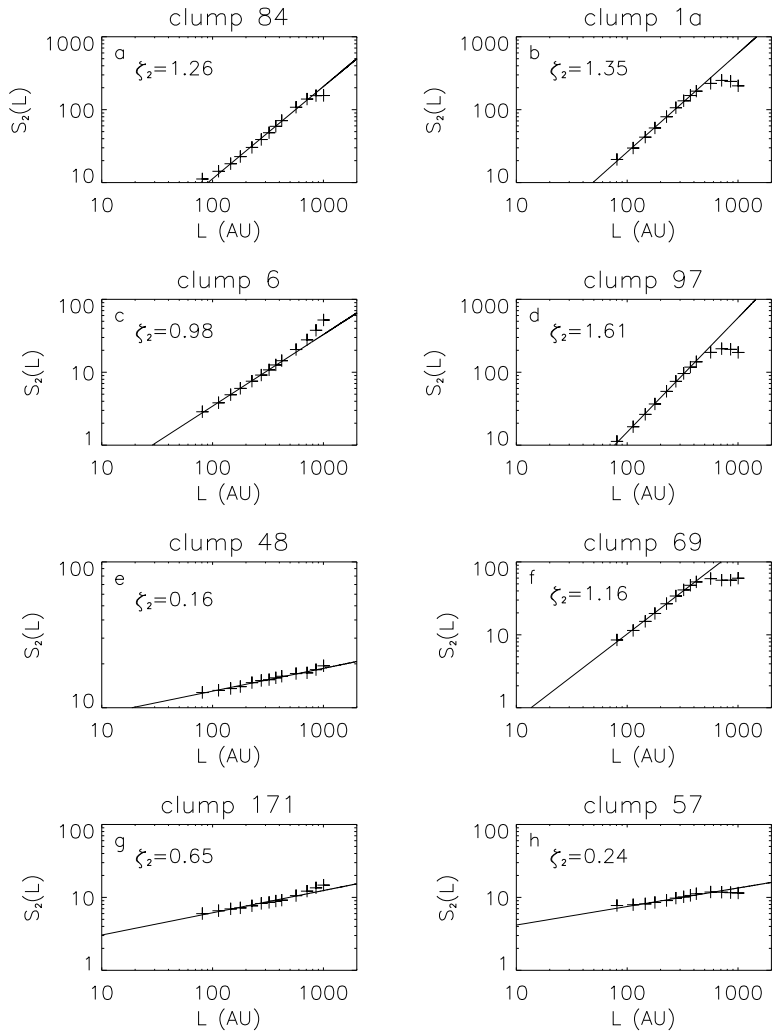

Figure 6.3: The variance function for the eight individual clumps shown in Fig. 6.1. Power-law fits are overlaid and the value of the exponent, ζ_2, is given.

The magnitude of the errors depend on the brightness (see Eq. (2.8)) and the physical size of the clump, where size is the dominating parameter. Thus the smaller clumps have the larger errors, but even the smallest clumps have variance functions with relative errors of no more than 10%. Relative errors of 10% are of the same order of magnitude as the size of the symbols in Fig. 6.3 and therefore the errors have been omitted in the figure. Errors in values of ζ_2 arise from lack of precision of the power law fit, rather than from random errors in the variance. Typical errors in ζ_2 are ± 0.01.

The distribution of values of ζ_2 is shown in a histogram in Fig. 6.4. ζ_2 values are nearly normal distributed around a mean of 0.75. Clumps with gaussian

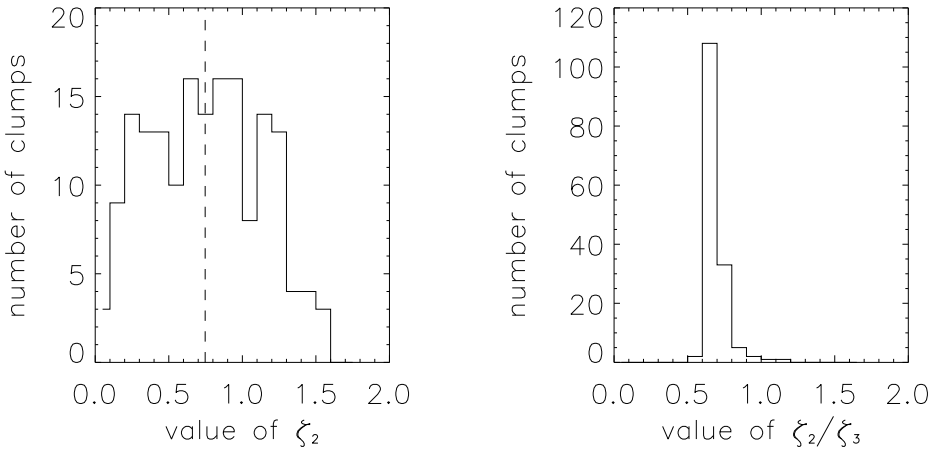

Figure 6.4: (left) Histogram of ζ_2. The mean value $\zeta_2 = 0.75$ is marked with the dashed line. (right) Histogram of ζ_2/ζ_3.

PDFs show $\zeta_2 = 0.0$ - 0.97 including or excluding the 3 clumps with significant noise contributions (see Sect. 6.2). Clumps with non-gaussian PDFs cover the whole range of $\zeta_2 = 0.0$ - 1.61. Thus it seems that gaussian PDFs are incompatible with high values of ζ_2, that is, steep structure functions. In the following we explore how clumps with high and low values of ζ_2 are spatially distributed.

6.3.1 Spatial distribution of clumps based on the ζ_2 value

A high value of ζ_2 represents more ordered structure in the velocity field and large velocity gradients within the clump. This suggests the presence of ordered shock structure. Fig. 6.5 shows the spatial distribution of clumps with $\zeta_2 > 1.0$, that is, clumps with the highest degree of order in the velocity field. The less ordered clumps with $\zeta_2 < 0.67$, the Kolmogorov value, are shown in Fig. 6.6. Examination of Figs. 6.5 and 6.6 shows that the value of ζ_2 does not correlate with brightness, that is, high ζ_2 for example can occur equally for strong and weak emission clumps. Furthermore, in Peaks 1 and 2 - but not in the central region around BN-IRc2, see below - clumps with high ζ_2 may be found mixed with clumps with low ζ_2 in the same spatial region. A theory of star formation including turbulence, self-gravity and bipolar outflows should thus be able to reproduce such a range of exponents of the variance function within a limited physical region.

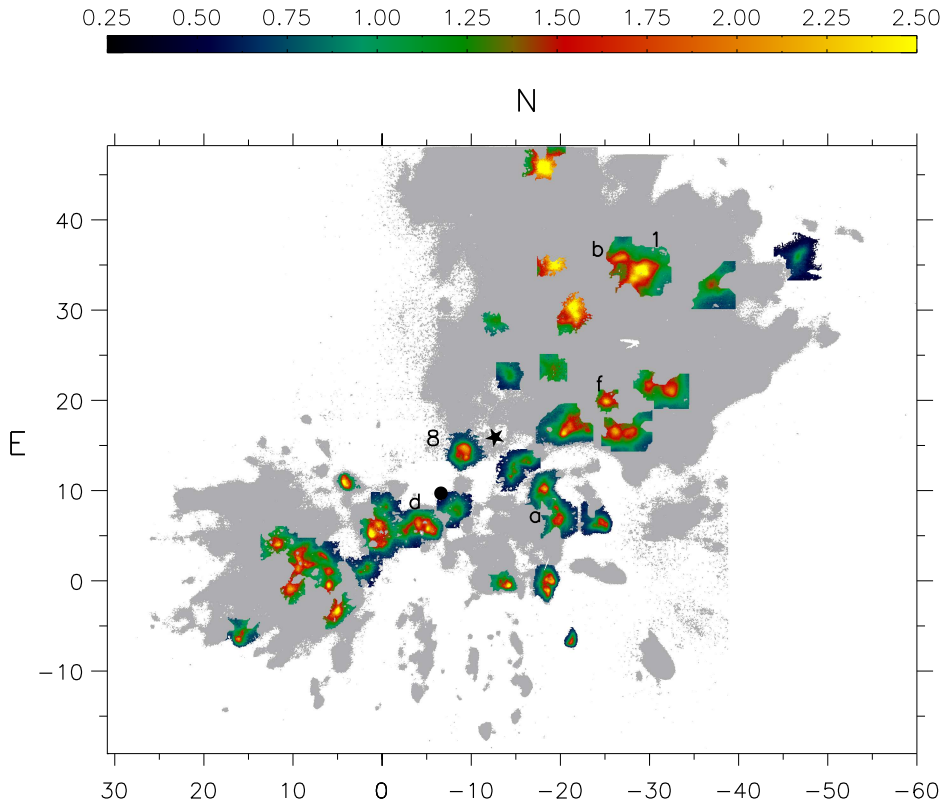

Figure 6.5: Clumps with the variance function scaling exponent $\zeta_2 > 1.0$. As in Fig. 6.2, the underlying grey background represents the spatial extent of H_2 emission at 2.121 μm with brightness greater than $\sim$ 2.4 x 10^{-6}Wm^{-2}sr^{-1} (8% of the maximum). The position of BN is marked with a star, IRc2 with a circle. Colours represent brightness in counts per pixel per second in the clumps analyzed in Chapter 6. 1 and 8 mark sites of protostellar candidates (Chapter 4). a,b,d,f mark clumps shown in Figs. 6.1, 6.3. From Gustafsson et al. (2006b).

Clumps with high ζ_2 values

Many clumps with high ζ_2 (Fig. 6.5) are situated in the vicinity of the BN-IRc2 complex in the central region. Moving away from BN-IRc2, their occurrence becomes progressively less. Some of the high ζ_2 clumps possess morphologies which resemble bow shocks (e.g. at (-18″, 0″) and (-21″,-7″), see Fig. 6.5) and are part of the blue-shifted lobe of a bipolar outflow from radio source I, itself associated with a massive O-star (Menten & Reid 1995; Doeleman et al. 1999; Greenhill et al. 2004a,b; Shuping et al. 2004; Nissen et al. 2006). Other high ζ_2 clumps correspond to protostellar candidates identified in Chapter 4 and Nissen et al. (2006) and may arise from out-

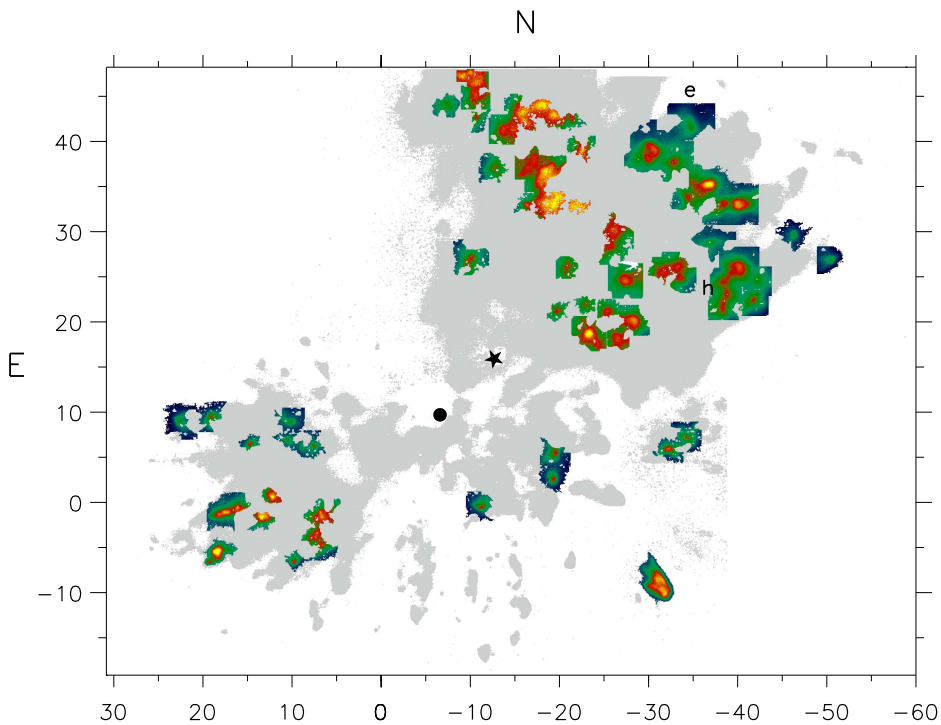

Figure 6.6: Clumps with the variance function scaling exponent $\zeta_2 < 0.67$. Grey background as in Fig. 6.5. The position of BN is marked with a star, IRc2 with a circle. Colours represent brightness in counts per pixel per second in the clumps analyzed in Chapter 6. e,h mark clumps shown in Figs. 6.1, 6.3. From Gustafsson et al. (2006b).

flows created internally in the clumps. Examples are found at (-30″,35″) and (-10″,15″). These correspond to zone 1 (Fig. 4.1) and 8 in Chapter 4, respectively, and are marked accordingly in Fig. 6.5.

The formation and evolution of protostellar objects involve periods where a high degree of order in the velocity field surrounding the protostar is expected (Arce et al. 2006, and references therein, see Sect. 1.1.6). A bipolar outflow hitting the circumstellar envelope would for example shock-excite the gas while creating an organized velocity field, with accompanying high ζ_2. The detection of clumps with high values of ζ_2 could therefore potentially allow an independent method of identifying early protostellar objects in the Class 0/I phase. This method may prove of value with the advent of very high spatial resolution radio maps with the Atacama Large Millimetre Array. This suggestion and the presence of clumps with high ζ_2 in Peaks 1 and 2 support the conclusion reached in Chapters 4 and 5 that that low mass protostars

have already formed in this region and reveal themselves through outflows injecting energy into the H_2.

Clumps with low ζ_2 values

The majority of clumps with ζ_2 less than the Kolmogorov value of 0.67 resides in Peaks 1 and 2 as seen in Figs. 6.5 and 6.6. The major part of these correspond to clumps with measured velocities which display no clear structure and whose relative velocities within any clump do not exceed 5 kms^{-1} (Nissen et al. 2006), accordingly giving low values of the exponent. We suggest that some of these regions may arise from photodissociation regions (PDRs) involving an irregular surface containing a variety of lines of sight, illuminated by θ^1Ori-C, in a model essentially as described in Field et al. (1994) for the PDR NGC2023. This would be consistent with a region lacking regular structure. However some low ζ_2 clumps are very bright and cannot be reconciled with a PDR excitation model. These are likely to be shocks travelling in the plane-of-the-sky. In such shocks the line-of-sight component of the velocity changes more gradually across the emission region compared to shocks moving at an angle to the plane-of-the-sky. This could explain the low ζ_2 values.

The BN-IRc2 region

The region around BN-IRc2 seems to be somewhat special. In contrast to regions of high ζ_2, regions of low ζ_2 are notably absent around BN-IRc2 and in the vicinity of source I close to IRc2 (Fig. 6.6). For precise location of source I we refer to Fig. 1.5. In Sect. 6.2 we also saw that no clumps with gaussian PDF are found in this region.
Our view of turbulent motion, based on models of turbulence, like that for example of Eggers & Wang (1998) described in Sect. 5.4.4, deals only with spatial scales and not directions. Thus we tend to consider only isotropic turbulence. However in the central region between Peaks 1 and 2, and also to the south-west of BN, the outflow from the IRc2-source I region in the NE-SW direction (Sect. 1.4.1) imposes a strong constraint on the radial motion of clumps in that region. Here the clumps show a strong blue-shift as mentioned in Sect. 5.2 (Nissen et al. 2006). Motion is evidently not isotropic here. We suggest that high values of ζ_2 may arise in this region because effects of turbulence in the radial direction are effectively swamped in the variance function by large blue-shifted motions and the turbulence tends to 2D rather than isotropic 3D. That is, the structure imposed on the clumps by the outflow causes strong correlated motions with relatively weak turbulent motions superposed. This lead to high ζ_2 values. As we move away from the

region of the blue-shifted outflow, low ζ_2 clumps are once more encountered (see Fig. 6.6). It is an interesting challenge to theory to test if imposition of a strong outflow has the effects that we observe here on values of ζ_2, as a check on our interpretation. Models should also demonstrate the absence of gaussian PDFs in the same central region.

6.4 Scaling of exponents

It was shown above that there is a large variation in the ζ_2 values associated with individual clumps of emission. We have also investigated if the structure functions, $S_p(L)$ (Eq. (5.20)), for the clumps can be represented by extended self-similarity (ESS, Benzi et al. 1993) and how the structure function exponents, ζ_p/ζ_3, scale with order p (see Sect. 5.5).
Using ESS, as in Sect. 5.5, we find that the structure functions of order 1-5 for most clumps display power law behaviour over a range in lag. Examples of the ratios of the logarithmic slopes of S_p and S_3, $d\ln S_p(L)/d\ln S_3(L)$, are shown in Fig. 6.7 for four clumps. A range of scales in which the curves are relatively constant or display plateaus, that is, show power law behaviour, can be distinguished in three of the clumps. The ranges are marked in Fig. 6.7. In the fourth clump no such power law range can be found. For the three clumps with power law behaviour the fitted exponents are shown in the right column of Fig. 6.7. In clump number 69 (Table A.1 in Appendix A) the power law exponents, ζ_p/ζ_3, follow the She-Leveque scaling of incompressible turbulence (Eq. (5.17)). The scaling in clump 60 follows close to the Boldyrev scaling (Eq. (5.19)) for supersonic turbulence. In clump 107 the scaling resembles that of the full data set of OMC1 (Sect. 5.5) with decreasing exponents for $p > 4$ (see Fig. 5.8).
The scaling of exponents has been analysed for all 170 clumps. The scaling relation associated with each clump can seen in Table A.1 in Appendix A. The scaling in the majority of clumps follow the She-Leveque scaling as clump number 69 in Fig. 6.7. However, in 18 clumps the scaling resembles that of Boldyrev (clump 60 in Fig. 6.7) and 27 clumps show an unusual scaling of the exponents resembling the scaling relation found in Sect. 5.5 for the full dataset (clump 107 in Fig. 6.7). The structure functions for 20 clumps cannot be described using ESS, since no interval of good power law behaviour is found for $p = 1 - 5$ (clump 109 in Fig. 6.7). $\zeta_2 < 0.5$ in all of these clumps (see Table A.1) indicating that they are among those clumps most dominated by chaotically distributed velocities.
There is no association between the scaling behaviour of a clump and the shape of the PDF nor is there any relation to the brightness of the clump. It is striking that although most of the individual clumps follow the She-Leveque

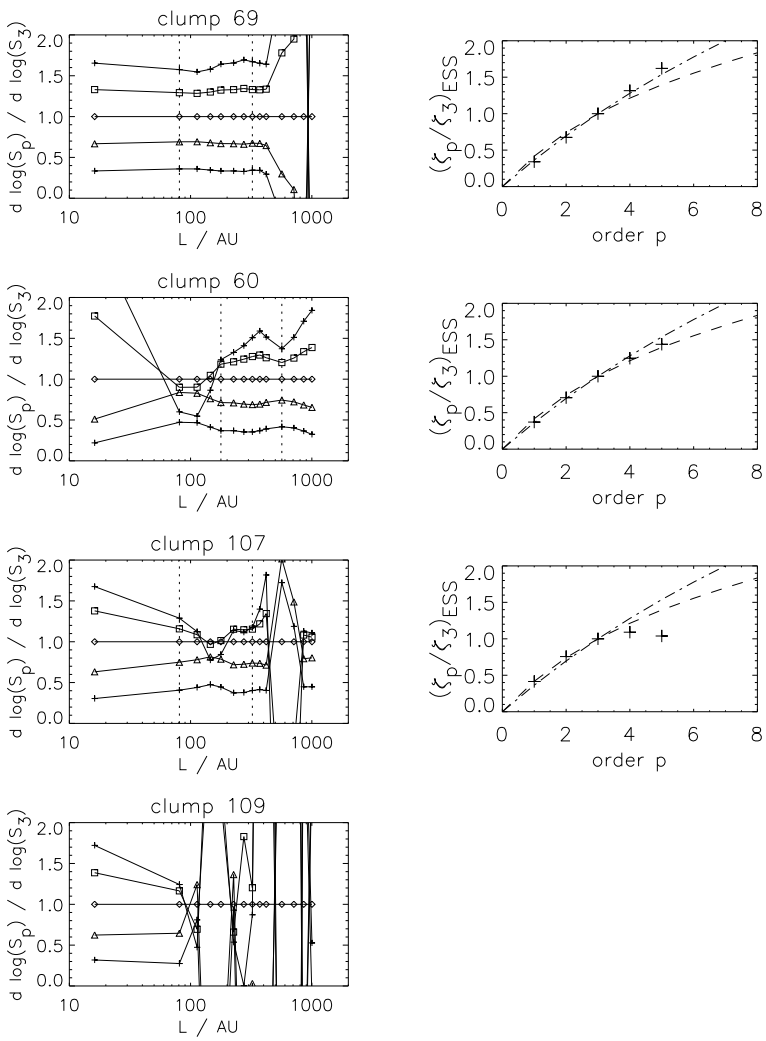

Figure 6.7: Examples of how structure function exponents scale in individual clumps for clump number 69, 60, 107, 109. **Left column:** ratios of differential slopes of $S_p(L)$ to the slope of $S_3(L)$ for $p = 1 - 5$. An interval of scales is marked by dotted lines. In this interval power law behaviour is found and the exponents have been fitted. **Right column:** The ESS scaling exponents compared with She-Leveque scaling (dash-dotted line) and Boldyrev (dashed line).

or Boldyrev scaling, the full data set show strong deviation (Sect. 5.5). However the unusual scaling of the full data set is related to larger scales ($\sim$ 1000 AU, see Fig. 5.8) than those associated with individual clumps ($\sim$ a few times 100 AU) and arises from the combined effect of all the individual clumps and how they are spatially distributed in the region.

Figure 6.4 (right) shows the distribution of ζ_2/ζ_3 for the 170 clumps where

this value can be evaluated. Nearly all clumps show $\zeta_2/\zeta_3 \in [0.6, 0.8]$ (see also Table A.1), which is a much narrower range than for ζ_2. This shows that clumps are found throughout the OMC1 region with very different values of ζ_2 and yet the ratios of ζ_p/ζ_3 are remarkably similar for all clumps. The median value of $\zeta_p/\zeta_3 = 0.69$ is very close to the Kolmogorov value of 0.67 (Kolmogorov 1941) and the value of supersonic turbulence of 0.74 (Boldyrev et al. 2002a).
This finding support the suggestion by Dubrulle (1994) mentioned in Sect. 5.5. That is, that the ratios ζ_p/ζ_3 should be regarded as universal and not the values of ζ_p's themselves. Thus when comparing observations, simulations and experiments we should compare the ratio ζ_p/ζ_3. Our results also suggest that different molecular clouds may have similar values of ζ_2/ζ_3 even though ζ_2 values show a large spread from cloud to cloud (Miesch et al. 1999; Ossenkopf & Mac Low 2002) as mentioned in Sect. 5.4.
By considering ESS and relating (say) the second order structure function to the third order structure function the individual characteristics of a clump or molecular cloud are smoothed out. This is the case for the individual values of the scaling exponents, ζ_p, as well as for possible deviations from power laws. If for example the second order structure function deviates from a power law, so does the third order structure function. However the effect is minimized by using ESS. Thus ζ_p/ζ_3 might be universal and characteristic of the turbulence involved, but variations in ζ_2 are most likely evidence of regional differences as discussed in Sect. 6.3.

6.5 Conclusion

The analysis of 170 individual clumps with sizes between 500 and 2200 AU presented above opens a window on a regime of scales that has never before been explored using statistical techniques. The main conclusions are summarized below:
(i) Studies at these scales reveal considerable diversity of velocity PDFs, with some gaussian, some with exponential wings showing evidence of intermittency and many with complex structure, reflecting multiple outflows. Variance functions are approximately power laws, with exponents varying between zero and 1.61. There is no spatial association between high and low exponent clumps nor is there any association between gaussian PDFs and high or low exponents.
(ii) To emphasize the last point, clumps with a variety of forms of the PDF and different values of the scaling exponent of the variance function are found in the same spatial region and in the whole region covered by the observations.
(iii) An outflow region associated with a deeply embedded O-star, e.g. source

I, between Peaks 1 and 2 shows markedly different statistical characteristics from Peaks 1 and 2. Clumps in the vicinity of the BN-IRc2 complex typically show high scaling exponents in the variance function. This may be due to the action of the energetic outflow from a high mass protostar imposed on intrinsic turbulent motion within individual clumps. At all events high and low exponent clumps are spatially segregated in this zone, with low exponent clumps found only at the edges.

(iv) Values of ζ_2/ζ_3 are found in a narrow range between 0.6 and 0.8 for nearly all clumps. This supports the notion that it is the ratios ζ_p/ζ_3 that are universal (Dubrulle 1994) and should be compared with theories of turbulence. However differences in the values of ζ_p are most likely evidence of regional differences in the physical parameters and their importance as such should not be neglected. Differences may for example arise if regions are dominated by different energy sources.

(v) Our results suggest that the slope of the variance function could be used as a indicator for the presence of early star forming regions.

The above results constitute a challenge for numerical simulations of turbulence in star forming regions. To our knowledge the resolution of any present numerical simulation is substantially lower than the resolution of these observations, but advances in computer technology will soon allow simulations to reach the scales encountered here. A self-consistent theory of star formation including self-gravity, MHD turbulence and energy feedback from protostars should be able to reproduce the features outlined above.

Chapter 7

Comparison with simulations

Numerical simulations of hydrodynamic and MHD turbulence are very important for our understanding of interstellar turbulence and its relation to star formation, as discussed in Sect. 1.2. Simulations solve directly the hydrodynamical equations and therefore we can use them to interpret the observations. However, in order to compare with simulations we need to be clear about what we actually observe. While simulations include both cold and hot gas and shocked and quiescent regions, observations are usually biased towards a specific temperature or density regime. Thus, not all of the simulated data may be represented in the observations. Furthermore, meaningful comparisons are only made if both observational and simulated data are treated alike.
Here we consider data from supersonic isothermal compressible turbulence simulations and compare with the observational data of OMC1 (Chapter 5). Such simulations have been performed by a number of different groups (Passot & Pouquet 1987; Vazquez-Semadeni et al. 1995; Padoan et al. 1998; Klessen 2000; Vázquez-Semadeni et al. 2003; Cho & Lazarian 2003; Kritsuk & Norman 2004). Since the observational data consist of preferentially shocked gas we also select the regions where shocks occur in the simulations. The simulated data are furthermore projected into the "plane-of-the-sky" as are the observations and structure functions are calculated. We will see that structure functions of subsets of shocked gas in the simulations are well approximated by power laws unlike the observations and that the exponents scale similarly to the relation observed in OMC1 (Sect. 5.5).

7.1 Simulations

The simulations considered here have been performed by Axel Brandenburg by use of the Pencil Code, which is a high-order finite-difference code

(sixth order in space and third order in time) for solving the compressible hydrodynamic equations.[1] The Horseshoe Cluster[2] in Odense, Denmark has been used for the computations.
The simulations are closely related to those of Haugen et al. (2004b), except that magnetic fields are neglected here. A shock-capturing viscosity is included, such that the viscosity is locally enhanced in a shock, allowing less diffusion between the shocks (Haugen et al. 2004b). The governing equations are the Navier-Stokes equations defined in Sect. 1.2

$$\frac{\partial \boldsymbol{u}}{\partial t} + \boldsymbol{u} \cdot \boldsymbol{\nabla} \boldsymbol{u} = -c_{\mathrm{s}}^2 \boldsymbol{\nabla} \ln \rho + \boldsymbol{f} + \frac{1}{\rho} \boldsymbol{\nabla} \cdot \boldsymbol{\tau} \tag{7.1}$$

$$\frac{\partial \ln \rho}{\partial t} + \boldsymbol{u} \cdot \boldsymbol{\nabla} \ln \rho = -\boldsymbol{\nabla} \cdot \boldsymbol{u} \tag{7.2}$$

Here $\tau_{ij} = 2\rho\nu \mathsf{S}_{ij} + \rho\mu\delta_{ij} \boldsymbol{\nabla} \cdot \boldsymbol{u}$ is the stress tensor and $\mathsf{S}_{ij} = \frac{1}{2}(u_{i,j} + u_{j,i}) - \frac{1}{3}\delta_{ij} u_{k,k}$ is the rate of strain matrix. Commas denote partial differentiation. Here ν is the viscosity and μ is the shock viscosity. Following Nordlund & Galsgaard (1995), we assume μ to be proportional to the positive maximum of the negative divergence of velocity smoothed over a zone of $3 \times 3 \times 3$ mesh widths (or "pixels"). The maximum value is found in a zone of $5 \times 5 \times 5$ mesh widths. That is,

$$\mu = c_{\mathrm{shock}} \left\langle \max_5 [(-\boldsymbol{\nabla} \boldsymbol{u})_+] \right\rangle, \tag{7.3}$$

where c_{shock} is an artificial viscosity parameter. Hereby the dissipation range in shocks are artificially broadened to approximately 5 mesh widths, but the effective viscosity is only enhanced in the neighbourhood of the shock. The dissipation scale associated with the viscosity ν is just 1–2 mesh widths. This is also the technique used by Padoan & Nordlund (2002) and Haugen et al. (2004b).
The function $\boldsymbol{f}$ denotes a forcing function that consists of plane waves injecting energy on random scales. $\boldsymbol{f}$ is normalized by a dimensionless amplitude factor f_0 that will be varied in the different simulations discussed below.

The equations are solved on a periodic mesh of size L^3, where $L = 2\pi/k_1$ is the length of the side of the box and k_1 is the smallest wave number in the domain. The flow is forced in a band of wavenumbers between 1 and 2 times k_1, that is, at large spatial scales. The average wavenumber is $k_f = 1.5k_1$.

We here consider runs with different forcing amplitudes, f_0, leading to different root mean square Mach numbers, $\mathrm{Ma}_{\mathrm{rms}} = u_{\mathrm{rms}}/c_{\mathrm{s}}$ where c_{s} is the speed of sound and u_{rms} is the root-mean-square velocity, see Table 7.1. The

[1] http://www.nordita.dk/software/pencil-code
[2] The Horseshoe Cluster is operated by the Danish Center for Scientific Computing

run	resolution	ν	$c_{\rm shock}$	f_0	$\mathrm{Ma}_{\rm rms}$	Re	$\Delta t_{\rm run}/\tau_{\rm turn}$
1	256^3	0.01	2	2	3	200	270
2	512^3	0.01	3	10	7–9	530	320
3	512^3	0.01	2	10	8–10	600	360

Table 7.1: Parameters of the numerical simulations: resolution, viscosity, shock viscosity, forcing amplitude, Mach number, Reynolds number, run time $\Delta t_{\rm run}$ in terms of turnover times $\tau_{\rm turn}$.

Reynolds number $Re = u_{\rm rms}/(\nu k_f)$ is approximately 200 in Run 1 and 500-600 in Runs 2 and 3, high enough for turbulence to develop (see Sect. 1.2). The high resolution runs, in rows 2 and 3 of Table 7.1, have been evolved for about 40 sound travel times, $\tau_{\rm sound} = (c_s k_1)^{-1}$, while the low resolution run has been conducted for about $90\,\tau_{\rm sound}$. The sound travel time can be associated with the turn-over time of an eddy, l/u, by noting that $\tau_{\rm turn} = (u_{\rm rms} k_1)^{-1} = \tau_{\rm sound}/\mathrm{Ma}_{\rm rms}$.

7.2 Results from full 3D simulation

First, we show that the structure functions of the full 3D simulation follow the theoretical scaling of Boldyrev (2002). For a snapshot of Run 1 at $t = 70\,\tau_{\rm sound}$ (corresponding to $t = 210\,\tau_{\rm turn}$) we have calculated the longitudinal and transversal structure functions of the 3D simulation using

$$S_{p,\rm long}(r) = \langle |u_x(x+r,y,z) - u_x(x,y,z)|^p \rangle, \tag{7.4}$$

$$S_{p,\rm trans}(r) = \langle |u_y(x+r,y,z) - u_y(x,y,z)|^p \rangle + \langle |u_z(x+r,y,z) - u_z(x,y,z)|^p \rangle, \tag{7.5}$$

as in Eq. (5.9). Here and throughout this chapter we use r to define the lag magnitude which was denoted by L in Chapter 5. The change in notation is chosen to distinguish between simulations and observations.
In Fig. 7.1a the third order transversal structure function is shown. The logarithmic derivatives of $S_{p,\rm trans}(r)$ (Fig. 7.1b) show no range of scales where plateaus, that is, good power law scaling, are present. In Fig. 7.1c we have plotted the logarithmic slope of $S_{p,\rm trans}(r)$ vs. $S_{3,\rm trans}(r)$ for $p = 1$–5, using the method of extended self-similarity (ESS), as described in Sect. 5.5. A range of good scaling is now seen to be present over most of the dynamical range from 10–80 mesh widths. The longitudinal structure functions are nearly identical to the transversal functions as expected for high Reynolds numbers (Kerr et al. 2001). The scaling exponents found from fits to the structure functions in the interval of 10–80 are plotted in Fig. 7.1d for both the transversal

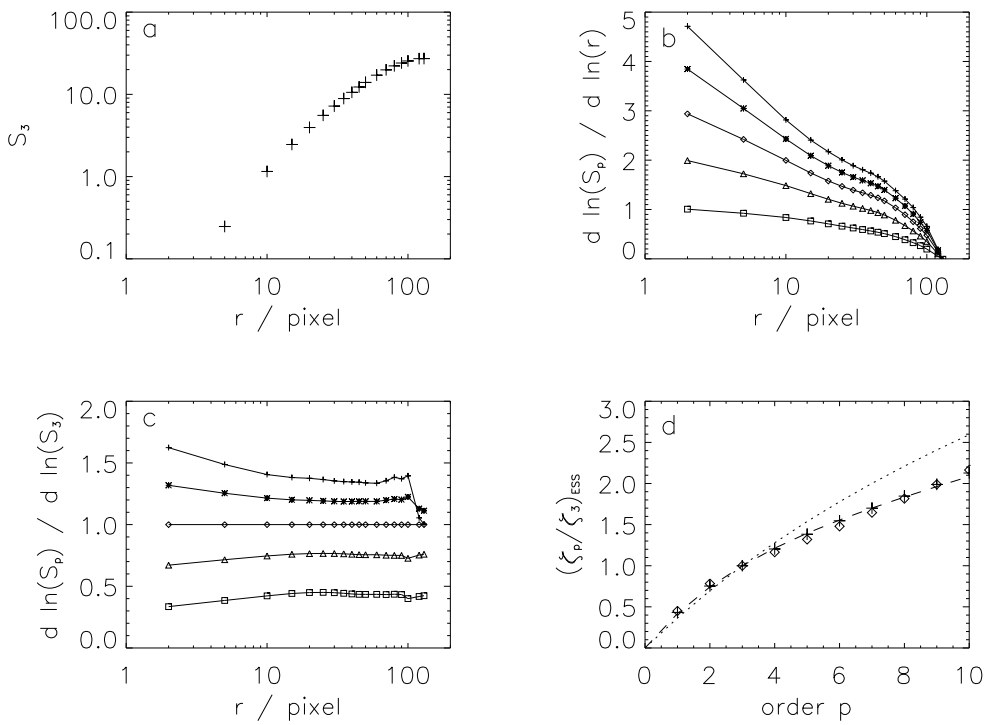

Figure 7.1: **a)** The third order transversal structure function of Run 1. **b)** logarithmic derivatives of $S_{p,\mathrm{trans}}(r)$ for $p = 1$–5 (in ascending order). **c)** Ratios of the differential slopes of the transversal structure functions of order 1-5 to the slope of the third order structure function. **d)** The ESS scaling exponents of the transversal structure function (+) and the longitudinal structure function ($\diamond$) compared to the She-Leveque scaling ($- - -$) and the Boldyrev scaling ($\cdots$).

structure functions (+) and the longitudinal structure functions ($\diamond$). Both the transversal and the longitudinal structure functions follow the velocity scaling for supersonic turbulence of Boldyrev (2002) as expected.

7.3 Scaling of subsets of the simulations

We now study structure functions of subsets of the simulations that resemble the physical properties of the observational data. That is, subsets being composed of preferentially shocked gas.

7.3.1 Projection of simulated data

First, in order to compare the simulations to the observations, we need to project the simulated 3D velocity components onto a 2D map of only radial velocity. The radial velocity in each spatial position is found by averaging the density weighed z-component (say) of the velocity over the z-range. That is,

$$\overline{u}_z(x,y) = \int_z \rho u_z \,\mathrm{d}z \Big/ \int_z \rho \,\mathrm{d}z. \tag{7.6}$$

We have checked that this expression yields the same values of velocities as the method adopted in the reduction of the observational data obtained with CFHT/GriF. In the observations, the true H_2 line profile is convolved with the very much broader instrumental lorentzian profile of the Fabry-Perot interferometer and the radial velocity is found from a lorentzian fit (see Sect. 2.4.3). The same procedure has been used on simulated velocity profiles through convolution and fitting and it has been found in numerous tests that the velocities derived are essentially the same as the centroid velocities obtained via Eq. (7.6). In Fig. 7.2 (top left, marked "all") the resulting 2D map is shown for Run 1 at $t = 50\,\tau_{\mathrm{sound}}$, corresponding to $t = 150\,\tau_{\mathrm{turn}}$.
If the turbulence is homogeneous and isotropic the projected map should be independent of the projection angle. However, since the simulations have limited spatial extent, they turn out to show residual anisotropy, in the sense that independence of projection angle is not assured. Thus the projection map and subsequently the structure functions could depend on the projection angle. Klessen (2000) also found dependence on viewing angle in simulations of both driven and decaying turbulence. To minimize such effects we have calculated projected velocity maps (Eq. (7.6)) from a number of different random projection angles and calculated structure functions (see below) for each angle. The number of angles used was limited by the available computer power. In Run 1 we used 50 different angles for all subsets. Tests performed on one set of data showed that using a larger number of angles did not change the result significantly. Due to computational limitations we only used 3 angles in Runs 2 and 3. However, the higher resolution of those runs should alleviate the problem of projection angle. There could also be projection effects in the observations, but we have no choice but to ignore these.
For each map of radial velocities the structure functions are calculated in the same way as for the observations in Sects. 5.4 and 5.5:

$$S_p(r) = \langle |\overline{u}_z(x,y) - \overline{u}_z(x-\tau_x, y-\tau_y)|^p \rangle. \tag{7.7}$$

Eq. (7.7) is the same as Eq. (5.20) with $I(x,y) = 1$. We use no brightness weighting since the velocities in the simulations are free of "observational"

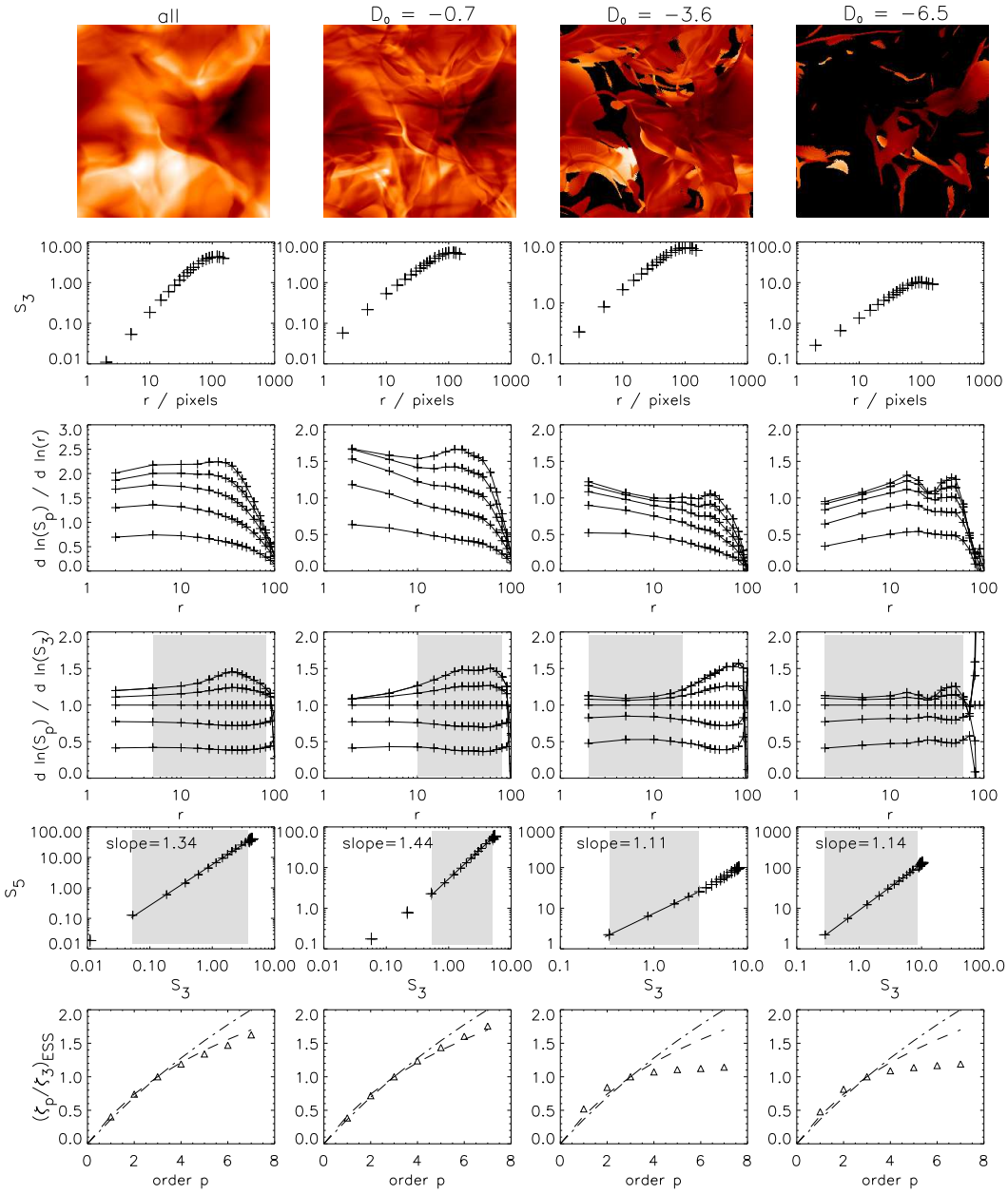

Figure 7.2: Run 1, $t = 50\,\tau_{\rm sound}$. Results for projected maps including all points (1st column) and for subsets with $D_0 = -0.7$, -3.6, and -6.5 (as marked), using $w = 0.7$. Top row: radial velocity maps projected in the z-direction. Second row: third order structure functions averaged over 50 projection angles (see text). Third row: logarithmic derivatives of $S_p(r)$ for $p = 1$–5 (in ascending order). Fourth row: ratios of differential slopes to ζ_3 for order $p = 1$–5. The grey shades indicate the ranges over which average values of $(\zeta_p/\zeta_3)_{\rm ESS}$ are determined. Caption continues on next page.

Figure 7.2: Continued from last page: Fifth row: $S_5(r)$ vs. $S_3(r)$. The ranges of grey shades correspond to those in the fourth row. Solid lines are best fits within the indicated ranges yielding the logarithmic slope, $(\zeta_5/\zeta_3)_{\mathrm{ESS}}$. Bottom row: the radial velocity scaling ($\triangle$) compared to the She-Leveque scaling ($- \cdot -$) and the Boldyrev scaling ($- - -$). From Gustafsson et al. (2006a).

error. The lag magnitude is $r = |\boldsymbol{\tau}| = |\tau_x \boldsymbol{e_x} + \tau_y \boldsymbol{e_y}|$, where $\boldsymbol{e_x}$ and $\boldsymbol{e_y}$ denote unit vectors in the x- and y-direction respectively. The structure functions for the different projection angles are subsequently averaged. In the following all structure functions of projected maps refer to such an average of structure functions.

The average third order structure function, Eq. (7.7) with $p = 3$, the logarithmic derivatives of $S_p(r)$ for $p = 1$–5, the ratio of the logarithmic slopes of $S_p(r)$ and $S_3(r)$, the extended self-similarity plot of $S_5(r)$ vs. $S_3(r)$, and the velocity scaling exponents are shown in Fig. 7.2, passing down the left column, for the projected simulation of Run 1. It is found that the scaling of the structure functions of the projected radial velocity follows that of Boldyrev, as did the transversal and longitudinal structure functions of the full 3D simulation (Fig. 7.1). This is in contrast to the scaling observed in OMC1. The observational data are not well reproduced by projection of the full simulation because the observations do not include the bulk of the gas. Below we select subsets of the simulations assumed to represent the observations.

7.3.2 Selection of shocks in simulations

The problem is to identify the subset of structures in the simulations which corresponds to the structures represented in our H_2 observations. As mentioned above we observe a subset of the gas in OMC1 consisting very largely of shocked gas. In order to make comparison between observations and simulations it is therefore necessary to extract regions in the simulations where shocks occur. Shocks are generated where fast material collide with slower moving material and material shows rapid deceleration. In such regions a negative velocity gradient is present. In simulations, shocked regions can thus be identified as regions with strong negative divergence of velocity ($\boldsymbol{\nabla} \cdot \boldsymbol{u} < 0$), that is, convergence.

Thus, in order to extract regions where shocks occur, we choose different subsets of the simulations consisting only of regions with negative divergence. We associate the value of the divergence with the strength of the shock. That is, low negative values of the divergence are associated with weak shocks and large negative values with strong shocks. We can then tune the strength

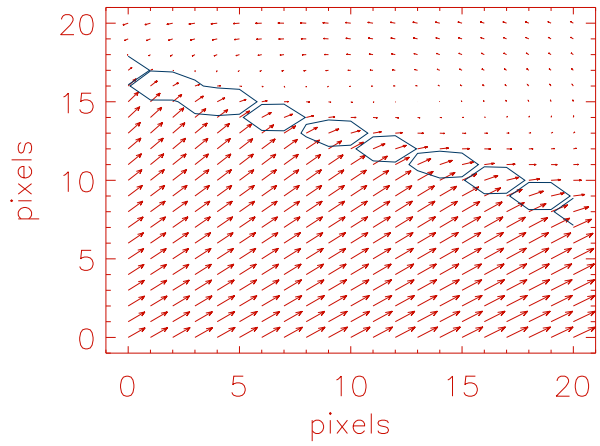

Figure 7.3: Vector plot of (u_x, u_y) in a section of an xy-plane in Run 1. Contours outline shocked regions where $s > 0$ for the cut-off value $D_0 = -6.5$, $w = 0.7$, that is, regions where $D < -5.8$. From Gustafsson et al. (2006a).

of the shocks, that we wish to include in a particular subset, by defining a cut-off value of divergence D_0. In the subsets considered below only pixels with values of divergence less than the cut-off value D_0 are included. Note that $D_0 < 0$. The selection is achieved by defining

$$D = \boldsymbol{\nabla} \cdot \boldsymbol{u} / \langle (\boldsymbol{\nabla} \cdot \boldsymbol{u})^2 \rangle^{1/2} \tag{7.8}$$

as the relative velocity divergence, and the selection function s:

$$s(x, y, z) = \begin{cases} 0 & \xi \leq -1 \\ \frac{1}{2} + \frac{1}{4}\xi(3 - \xi^2) & -1 < \xi < 1 \\ 1 & \xi \geq 1, \end{cases} \tag{7.9}$$

where $\xi = (D_0 - D)/w$, and w is the width of the selection function. All points with $D > D_0 + w$, which we seek to exclude, have $s = 0$. The selection function is chosen for its smooth variation between 0 and 1. We have used other somewhat different forms of the selection function and found that the results do not significantly depend on the specific form. Fig. 7.3 shows an example of a local velocity field where shocks are present. The figure shows velocity vectors (u_x, u_y) in an xy-plane and contours of shocked regions where $s > 0$ for $D_0 = -6.5$ and $w = 0.7$ in Run 1 (Table 7.1).

The shock structure in an xy-slice of Run 3 is shown in Fig. 7.4, where regions with large negative values of $\boldsymbol{\nabla} \cdot \boldsymbol{u}$ (red and green regions) represent shocks. It is seen that shocks occur in long filaments. The profiles of u_x, u_y, and u_z are shown along a horizontal cut on which the presence of a shock for

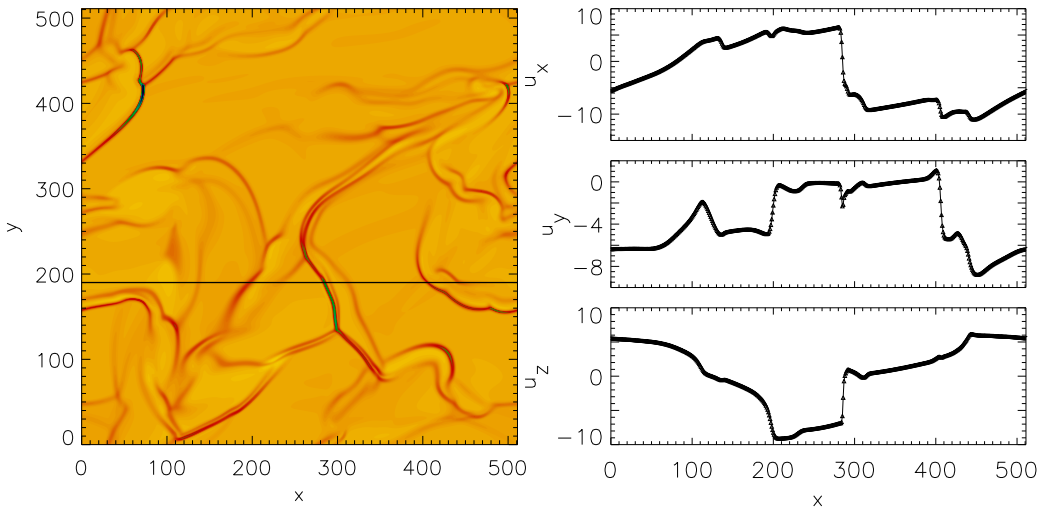

Figure 7.4: Left panel: xy-slice of $\boldsymbol{\nabla} \cdot \boldsymbol{u}$ through the box of Run 3 at some arbitrarily chosen value of z. Red and green colours represent regions with negative divergence. The horizontal line indicates the location along which the profiles of u_x, u_y, and u_z (in kms^{-1}) are shown in the three panels on the right hand side. A strong shock is seen at $x = 290$. From Gustafsson et al. (2006a).

example at $x = 290$ is evident through large velocity changes in u_x, u_y, and u_z over a range of only ~ 5 mesh widths. The higher Mach number of these simulations leads to larger velocity differences and stronger shocks compared to the simulations of Run 1.

7.3.3 Projected velocity of subsets of shocks

Using the function in Eq. (7.9) to select regions, the radial velocity in each spatial position (x, y) is now found by a modified form of Eq. (7.6):

$$\overline{u}_z(x, y) = \int_z s\rho u_z \, \mathrm{d}z \Big/ \int_z s\rho \, \mathrm{d}z. \tag{7.10}$$

It is evident that only regions with divergence of velocity less than $(D_0 + w)$ contribute to this projected velocity. Figure 7.2 (top row) shows examples of projected radial velocity maps of such subsets from a snapshot of Run 1 at $t = 50\,\tau_{\mathrm{sound}}$. The subsets correspond to $D_0 = -0.7$, -3.6, and -6.5 and $w = 0.7$.

The physical significance of the cut-off value D_0 in the subsets above is explained as follows. The value of D in a region depends on how the velocity changes in the vicinity. Large differences in velocity over a limited region lead to high values of D. Thus the restrictions on D in the subsets can be

associated with typical minimum values of the velocity change that must occur in a shocked region for that region to be included in the structure function analysis. For example in the subsets of Run 1 above the physical interpretation of the restriction $D_0 = -3.6$ is, that in order for a pixel to be included there must be a velocity gradient in the immediate vicinity of that pixel, such that $|\Delta \boldsymbol{u}| \sim 3\text{kms}^{-1}$ over $\Delta r = 10$ pixels. This is measured in the simulated data where it can also be observed that the size of shocks is typically 5 pixels (Fig. 7.4).
An estimate of the value of the gradient in physical units can be given by assuming a physical shock width of C-shocks of 50 AU (Lacombe et al. 2004, and see Sect. 1.5.1). Then 10 pixels in the simulations correspond to 100 AU and the value of the velocity gradient above corresponds to $\sim 0.03\text{kms}^{-1}\,\text{AU}^{-1}$. When $D_0 = -6.5$, typical values are $|\Delta \boldsymbol{u}| \sim 5\text{kms}^{-1}$ over $\Delta r = 10$ pixels. These values are estimated for Run 1 and are found to be higher in Run 2 and 3 with stronger forcing and higher Mach numbers for the same value of D.
The size of velocity gradients in the simulations estimated above has the same order of magnitude as the velocity gradients we observe in local regions of shocks in the observational data. In Chapter 4 we analysed local regions of shocked gas and found typical values of velocity differences to be $\sim 20\text{kms}^{-1}$ over distances of 1000 AU, that is, $0.02\text{kms}^{-1}\,\text{AU}^{-1}$.

7.3.4 Results of subsets of Run 1

Turning to Fig. 7.2(top row) we start with a comparison of the projected velocity maps of the chosen subsets. The map of $D_0 = -0.7$, that is, excluding all non-shocked regions, displays sharp filamentary structure, compared with the map of all points in the simulation, which has smoother contours. Excluding the weakest shocks, that is, for $D_0 = -3.6$, leads to a more broken up appearance, and the filaments are clearly visible. When only the strongest shocks are considered, $D_0 = -6.5$, the radial velocity map consists mostly of sheets and filaments.
Figure 7.2 also displays the third order structure functions for the three subsets as defined by values of D_0, as well as the logarithmic derivatives of $S_p(r)$, the ratio of the logarithmic slopes of $S_p(r)$ and $S_3(r)$, the extended self-similarity plot of $S_5(r)$ and $S_3(r)$, and the scaling exponents of the structure functions of the radial velocity. The structure functions are averages of 50 projected maps as described in Sect. 7.3.1. The third order structure function for the full simulation and the three subsets all display good power laws. This confirms that the subset of the gas associated with shocks retain the turbulent characteristics of the bulk gas, that is, the power law distribution. The leveling off of the power laws at lags around 100 mesh widths is an

artifact due to the finite size of the simulation of 256 mesh widths. This effect was also noted in the observations (Sect. 5.4). No bumps in the structure functions are seen. This is in marked contrast to the structure functions of the observations where clear bumps are present (see the first panel of Fig. 5.8).

The logarithmic slopes in the 3rd row of Fig. 7.2 indicate that the slopes of the structure functions related to the shocked gas (e.g. at $D_0 = -3.6$ or -6.5) have smaller values compared to those of the projected bulk motion including all points in the simulation (left column). If this is a general characteristic of the turbulence in OMC1 our measured value of $\zeta_2 = 0.53$, which stems from observations of shocked gas (Sect. 5.4), is only a lower limit to the slope associated with bulk motions. To our knowledge this effect has however not been shown directly in other simulations by other authors and thus remains tentative. However the ζ_2/ζ_3 values from both bulk gas and shocks remain similar (see 4th row in Fig. 7.2) and thus provide a more unbiased comparison between features in the shocked emission and bulk gas.

The ratios of logarithmic slopes in the 4th row of Fig. 7.2 show plateaus over about an order of magnitude in scale, especially in the lower order structure functions, $p = 1$, 2. The scaling exponents ζ_p/ζ_3 are found by fits to Eq. (5.21), that is, $S_p(r) \propto S_3(r)^{(\zeta_p/\zeta_3)}$, in the interval of r where $d \ln S_p(r)/d \ln S_3(r)$ shows the best plateau. The plateau is found at $r = 5$ to 80 mesh widths for the full simulation, at $r = 10$ to 80 mesh widths for $D_0 = -0.7$, at $r = 2$ to 20 for $D_0 = -3.6$ and at $r = 2$ to 60 for $D_0 = -6.5$. The ranges used for fitting are indicated in Fig. 7.2 with grey shading. The best power law fits to $S_5(r)$ vs. $S_3(r)$ in the indicated ranges are shown in the fifth row of Fig. 7.2. The value of the slope is indicated.

In the last row of Fig. 7.2 one can see that the velocity scaling is close to following that of Boldyrev when all points in the simulation are included and when only shocked regions with $D < 0$ ($D_0 = -0.7$) are included. There is, however, a dramatic change in the scaling when the restrictions on the strength of the shocks are made tighter. For both $D_0 = -3.6$ and $D_0 = -6.5$ the scaling deviates strongly from both She-Leveque and Boldyrev scalings. The scaling in these two subsets is seen to remain nearly constant for $p \geq 3$, resembling the scaling found in the observations of OMC1 in Sect. 5.5 (Fig. 5.8). This shows that the unusual scaling observed in OMC1 can be the effect of observing only the hot, shocked gas, and that hydrodynamical turbulence simulations without self-gravity or magnetic fields are able to reproduce this. However, as argued below, the artificial viscosity may simulate the effect of magnetic fields by broadening the shocks turning them from J-shocks into C-shocks (Sect. 1.3.1).

The scaling in shocked regions shown above is qualitatively similar to results

of Kritsuk & Norman (2004), who found systematically smaller scaling exponents for $p > 3$ when only high density regions were considered. These can also be associated with regions of shocks.
The change in the behaviour of the scaling in the last row of Fig. 7.2 is associated with a shift in the range for which a plateau can be seen, see above. Especially in the last column of Fig. 7.2 the scaling is seen to extend all the way from the resolution limit (2 mesh widths) to 60 mesh widths. We interpret the apparent shift of the ranges as an effect of the artificial viscosity. As described in Sect. 7.1 the artificial viscosity is only important in regions with high convergence (Eq. (7.3)) and these regions become more strongly dominant as the cut-off value, D_0, is moved to more negative values. The artificial viscosity broadens the dissipation scale (Sect. 7.1) and seems to merge the dissipation range with the inertial range at large values of D_0. This may explain why the scaling extends down to 2 mesh widths at the highest value of D_0 in Fig. 7.2. The artificially smoothed shocks may resemble C-type shocks that occur in the magnetized interstellar medium and are known to be a common feature in OMC1 (Vannier et al. 2001; Kristensen et al. 2003; Nissen et al. 2006).

7.3.5 Results of subsets of Run 3

Figure 7.5 shows similar results to Fig. 7.2 but for a snapshot of Run 3 (Table 7.1) with high Mach number at $t = 39\,\tau_{\rm sound}$. The subsets corresponding to $D_0 = -0.20$, -2.0, -7.5, and -9.0 show the same trends as seen in Fig. 7.2. The tighter the restrictions on the strength of the shocks, that is, the higher value of D_0, the sharper and more broken up the filamentary structures become. The radial velocity scaling flattens strongly when $D_0 = -7.5$ and -9.0 (bottom row in Fig. 7.5).
The grey-shaded areas in the fourth row of Fig. 7.5 indicate two different regions where scaling can tentatively be noted, in contrast to the single regions identified in Fig. 7.2. The two different scales identified in Fig. 7.5 (rows 4 and 5) cover lags of 2 to >10 mesh widths and 30 to >100 mesh widths. The smaller of these ranges covers the scale of ~ 5 mesh widths associated with artificial viscosity acting in large velocity gradients (see Sect. 7.1). The scaling at the lower range will thus likely be more affected by the presence of shocks than the scaling at larger scales.
We now consider the scaling associated with these two different regions separately. In the last row of Fig. 7.5, open triangles refer to the smaller lags and open squares to the larger lags. For the data in the left column for $D_0 = -0.20$, where all regions with a positive value of the convergence are included, that is, all shocks, it is seen that both scaling regions (small scales, 2–15 mesh widths, and large scales, 20–170 mesh widths) show scaling be-

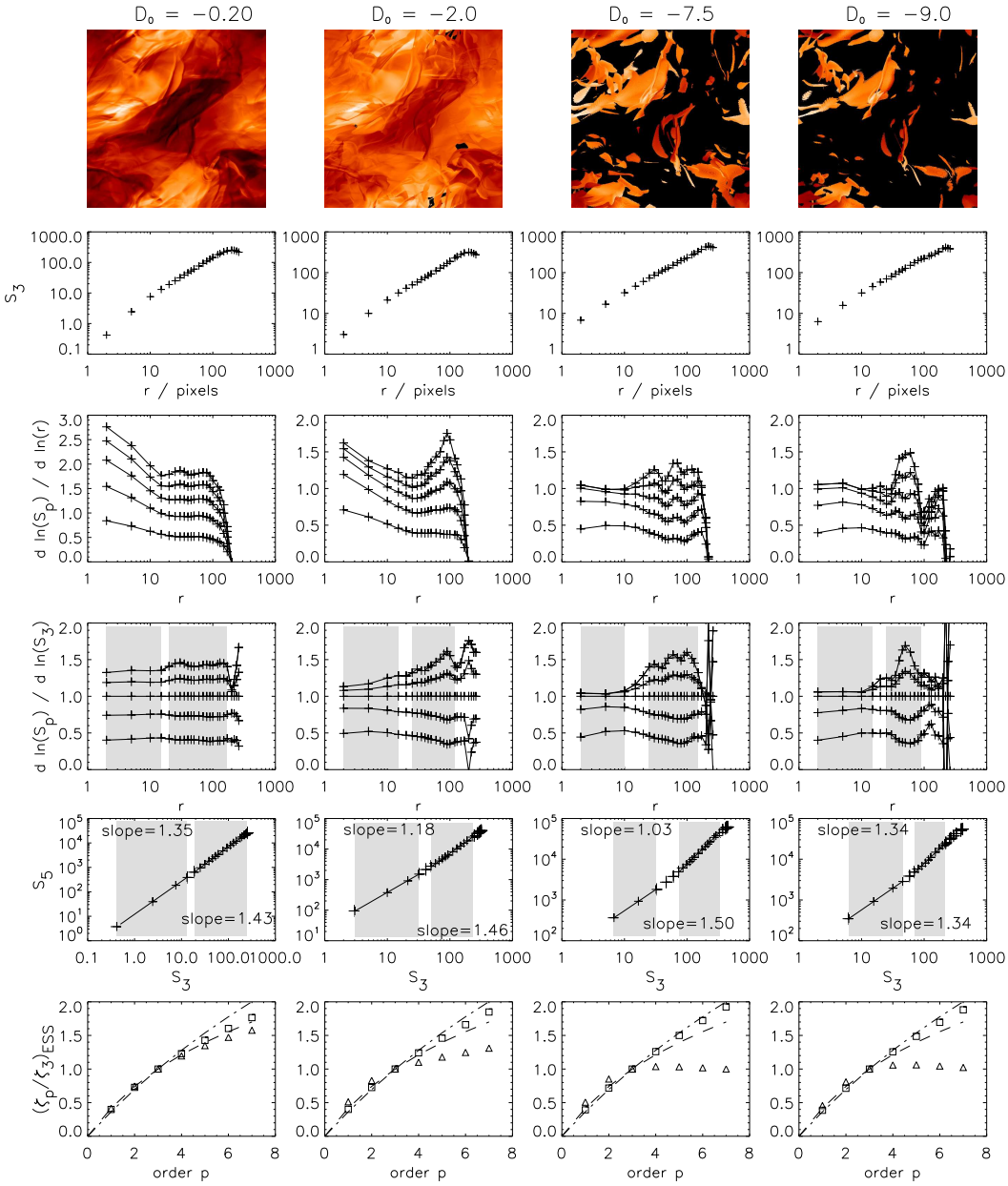

Figure 7.5: Run 3, $t = 39\,\tau_{\rm sound}$. Results for projected maps for subsets with $w = 0.20$ and $D_0 = -0.20$, -2.0, -7.5 and -9.0. Top row: radial velocity maps projected in the z-direction. Second row: third order structure functions averaged over 3 projection angles (see text). Third row: logarithmic derivatives of $S_p(r)$ for $p = 1$–5 (in ascending order). Fourth row: ratios of differential slopes to ζ_3 for order $p = 1$–5. The grey shades indicate the ranges over which average values of $(\zeta_p/\zeta_3)_{\rm ESS}$ are determined. Caption continues on next page

Figure 7.5: Continued from last page: Fifth row: $S_5(r)$ vs. $S_3(r)$. The ranges of grey shades correspond to those in the fourth row. Solid lines are best fits within the indicated ranges yielding the logarithmic slope $(\zeta_5/\zeta_3)_{\rm ESS}$. Bottom row: the radial velocity scaling compared to the She-Leveque scaling (dash-dotted line) and the Boldyrev scaling (dashed line). $\triangle$: small scales, $\square$: large scales. From Gustafsson et al. (2006a).

haviour roughly compatible with Boldyrev scaling. When we introduce more restrictive thresholds for D_0 different behaviour is found. The large scales then begin to follow more closely the standard She-Leveque scaling. At the same time, the small scales, associated with shocks, show the levelling off discussed in connection with Fig. 7.2 for strongly shocked regions, and as seen in the observations, Fig. 5.8e. We therefore are able to explain the unexpected scaling found in the observations through an inherent selection of shocked regions.

7.3.6 Non-power law behaviour in structure functions

The structure functions of Run 1 and Run 3 (second row in Figs. 7.2 and 7.5) are all well represented by power laws in contrast to the behaviour found in the structure functions of OMC1 (Fig. 5.8). In one snapshot of Run 2, however, similar bumps to those in the observations are detected. This is shown in Fig. 7.6. The deviations from power laws of the structure functions in Run 2 are found in subsets with high values of the threshold, D_0, in the snapshot at $t = 37\,\tau_{\rm sound}$. Examples are shown for $D_0 = -5.1$ and $D_0 = -7.5$ where it is clear that the third order structure functions display bumps around 20 and 60 mesh widths. Other snapshots of Run 2 however do not show this feature.

The bumps in the structure functions indicate the presence of preferred scale sizes in the simulation. This means that even if the starting point is a fully isotropic hydrodynamic solution of supersonic turbulence, then preferred scales can be encountered by selecting shocked regions that have a typical filamentary length of some hundred mesh widths (see Fig. 7.4). Run 2 has a higher value of shock viscosity than Run 1 and 3 (Table 7.1) which leads to higher energy dissipation. This may be the cause of the preferred scales. However, as the bumps are only observed in one snapshot it is most likely an artifact.

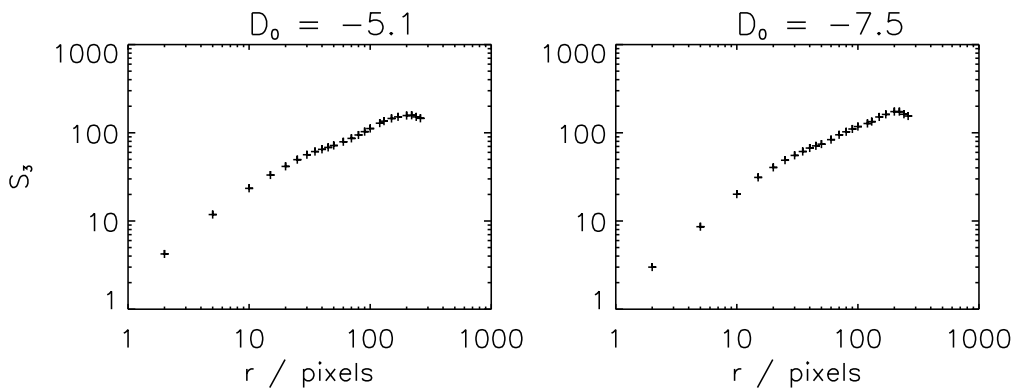

Figure 7.6: Run 2, $t = 37\,\tau_{\rm sound}$. Third order structure functions of projected maps with $w = 0.2$ and $D_0 = -5.1$ and $D_0 = -7.5$. From Gustafsson et al. (2006a).

7.4 Discussion & Conclusion

In three simulations we have selected shocked regions by imposing requirements on the value of the velocity divergence, $\boldsymbol{\nabla} \cdot \boldsymbol{u}$. In certain important respects the simulations presented here are then remarkably successful in reproducing the statistical behaviour observed in OMC1 in Chapter 5. In other equally important areas, they fail. Let us first reiterate the success.

We have found that by only including shocks that are relatively strong ($D_0 < -1.5$), the unusual scaling exponents of the observations (Sect. 5.5) are reproduced in the simulations. By contrast, a scaling following that of She & Leveque (1994) or Boldyrev (2002) is found when all points in the simulations are included in the data. An explanation for this behaviour is as follows. Enhanced energy content at small scales, relative to larger scales, implies smaller slopes, that is, smaller values of ζ_p. Both the observational data of OMC1, and some of those subsets of the simulations selected only to include shocks, show that the values of ζ_p are reduced for $p \geq 4$. Since structure functions of high order p are dominated by regions of strong velocity differences, it follows that the observed excess of small scale energy is associated with regions of large velocity differences. These are likely to be the regions of strong shocks, as is evidenced by the fact that reduced values of ζ_p are most clearly seen in subsets of the simulations that select the most strongly convergent high density regions.

The present work does not however furnish any explanation of why departure from the She-Leveque or Boldyrev scaling occurs at the specific value of $p \geq 4$. It is possible that the critical value of p is in some way connected with the physical nature of the shocks, for example the fact that they are smoothed in the simulations, mimicking the structure of continuous (C-) type shocks,

rather than jump (J-) type shocks (see Sect. 1.3.1).
We now turn to the failure of the simulations. The structure functions of the observations in OMC1 all deviate from power laws and exhibit clear bumps around 10^3AU (Figs. 5.6 and 5.8). This cannot be reproduced by the simulations. There appears to be two possible explanations for this observed behaviour. The first is that the deviation from power laws is due to protostar formation and associated outflows at a preferred scale as suggested in connection with the observations (Sect. 5.4). The second is that the behaviour is in some way inherent in the nature of the turbulence as opposed to the presence of protostars.
Turning to the first suggestion, as described in Sect. 1.2 the process of star formation pulls structure of a certain size out of the cascade and creates outflows, injecting energy into a turbulent background. Gravitational energy and angular momentum is spewed out of the star via such outflows and turned into local turbulence, hence increasing the overall turbulent content of the gas – and restarting the whole cascade process. Such outflows are of course not present in the simulations.
The second suggestion, that the deviation from power law is somehow inherent in the nature of the turbulence, requires that there is some special scale in this medium which is otherwise governed by self-similar scaling. This may be related to the details of energy dissipation and arise through our selection of strong shocks as a subset of the whole. We have seen in Fig.7.6 that traces of bumps in the structure functions are found in one snapshot of Run 2 when highly shocked material is selected. The deviations of the structure functions from power laws are not as pronounced in the simulation as in the observations of OMC1. However this finding provides some evidence that part of the explanation for the deviations from power laws of the structure functions in OMC1 arises from the fact that we observe preferentially shocked gas. As departures from power law behaviour are only evident in a single snapshot and not throughout the simulation at other times, this suggestion remains tentative.
In order to explore the reasons for the departure from power law behaviour, more advanced simulations are necessary. These should include self-gravity and energy feedback from protostellar zones through outflows and should ultimately incorporate ionization and magnetic fields.

Chapter 8

Identifying characteristic scale

Characteristic scales may be imposed on an otherwise turbulent medium, as described in Sect. 1.2, by processes such as energy injection and self-gravity. Energy injection from different sources may act on very different scales. In order to improve both theories of star formation and turbulence we need to identify the presence of these preferred scales, the scale sizes at which they occur and ultimately the processes which give rise to them.

The non-fractal nature of molecular clouds at the star-forming scale of $\sim$ 500-1000 AU was first detected in Vannier et al. (2001) for OMC1. Non-fractal nature has also been reported at larger scales in Blitz & Williams (1997) who found a preferred scale of 0.25-0.5 pc (5-10$\times 10^4$ AU) in Taurus. Material may however be self-similar down to a few x 10^{-4}pc (<100 AU) in diffuse material, with clumps of mass $\sim 10^{-7}$M$_\odot$, as found in the photodissociation region around the B-star HD37903 in NGC2023 (Rouan et al. 1997).

Experience has proven that it is non-trivial to establish the scale(s) at which self-similarity begins to break down and as broad array of techniques as possible should be made available. For example, four different methods were used in Vannier et al. (2001) in order to demonstrate that the size distribution of hot H_2 clumps in Orion is not fractal at star-forming scales. In Sect. 5.4 deviations from a power law of the second order structure function of velocities were also interpreted as evidence of preferred scale sizes in OMC1. In this chapter we analyse the spatial structure in OMC1 in detail with three methods, see below, and show that the H_2 emitting clumps are associated with a number of characteristic scale sizes.

The methods currently available are those of (i) Blitz & Williams (1997), who introduced a method of degrading the spatial resolution and establishing the presence of preferred scales from histograms of the degraded images (the brightness histogram method), a method used for example in Vannier et al. (2001). (ii) Fourier transform power spectra, used to pick out frequencies and hence scales in images (e.g. Vannier et al. 2001), (iii) clump

decomposition (Stutzki & Guesten 1990), (iv) Δ-variance analysis (Stutzki et al. 1998; Bensch et al. 2001), (v) wavelet transformation (e.g. Farge 1992; Rouan et al. 1997).
Here we use three different methods to detect preferred scale sizes. First we use the brightness histogram method of Blitz & Williams (1997) to detect preferred sizes in OMC1 from the VLT/NACO (Sect. 2.2) data and compare with Vannier et al. (2001) (Sect. 8.1). In Sect. 8.2 we introduce a new technique, based on structure functions (SFs), to identify characteristic scales in a medium. This technique was inspired by the results in Sect. 5.4 showing that the SFs in OMC1 deviate from power laws. We show that structure functions or local derivatives of SFs provide a powerful way to detect such scales and that the technique appears more sensitive to preferred scales than methods presently used . In Sect. 8.3 the SF method is tested on observations from VLT/NACO (Sect. 2.2), CFHT/GriF (Sect. 2.4) and the intensity maps from VLT/NACO-FP (Sect. 2.5). In Sect. 8.4 we compare the SF method to the method of Fourier transformation and in Sect. 8.5 we summarize the results from the different methods.

8.1 The brightness histogram method

In this section we use the method introduced by Blitz & Williams (1997) of degrading images and calculating histograms to detect preferred sizes. This method involves counting in the original image the number of pixels $N(B_n)$ at a certain brightness, binned into small brightness intervals, as a function of the pixel normalized brightness, B_n. B_n is defined as brightness divided by the value in the brightest pixel in the image. The resolution of the image is then degraded by boxcar averaging over some chosen number of pixels on a square and a new set of $N(B_n)$ calculated. This process is repeated, successively degrading the resolution of the image. Plots of $N(B_n)/N_{tot}$ vs. B_n yield a set of curves which remain unchanged for an image with no preferred scale, that is, a fractal image, as the resolution of the image is degraded. N_{tot} is the total number of pixels which remain constant. By contrast, for an image with a preferred scale, such plots should change in form as the resolution is degraded to the point at which any preferred scale has been washed out. Beyond this critical smoothing, the form of such plots should remain constant, mimicking a fractal. The amplitude of the critical smoothing is a direct measure of the preferred range of scale in the image.
The method has been tested with a 2-dimensional fractal image produced from fractional Brownian motion (fBm) structures which is characterized by a power law power spectrum, $P(k) \propto k^{\beta}$ (e.g. Peitgen & Saupe 1988), and randomly distributed phases (Frank P. Pijpers, private com.). The fractal

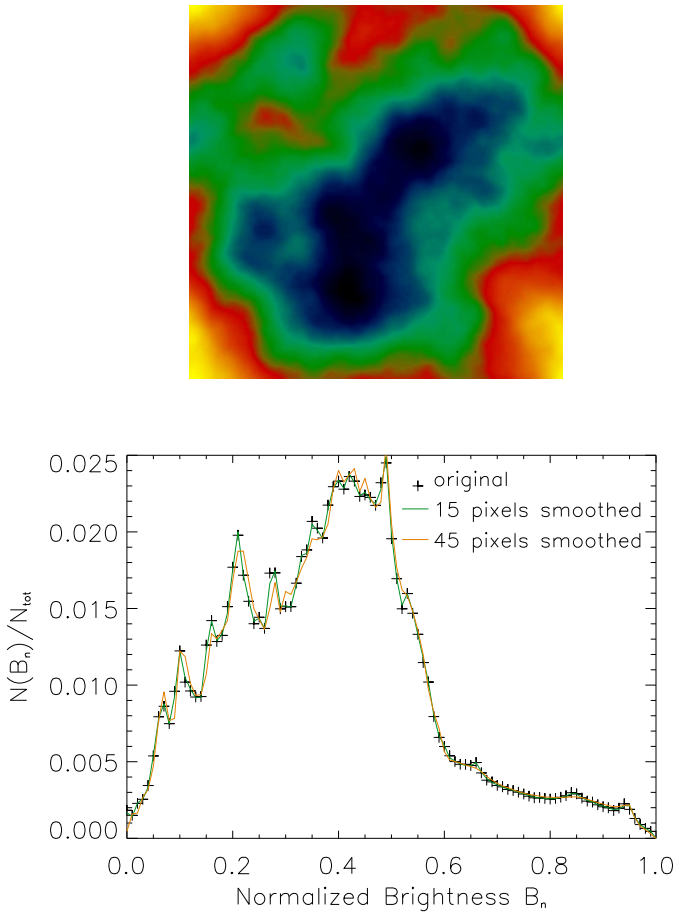

Figure 8.1: **Top:** Fractal Brownian Motion image with $\beta = 5.0$. **Bottom:** Brightness histogram of the fractal image. Histogram of the original image is displayed with plus-signs. The resolution of the image has been degraded using boxcar smoothing with box sizes of 15 and 45 pixels. Histograms of the degraded images are shown with colored lines.

image with $\beta = 5.0$ is displayed in Fig. 8.1 along with brightness histograms of the original image and of two images with degraded resolution. The degrading of the resolution has been performed by boxcar smoothing using boxsizes of 15 and 45 pixels. The resulting set of curves of $\mathrm{N(B}_n)/\mathrm{N}_{tot}$ vs. B_n for the original and smoothed images are seen to display exactly the same shape as expected for a fractal image.

8.1.1 Results from OMC1

The histogram method has been used on brightness data from VLT/NACO (Sect. 2.2). The two fields observed (ESE and SE, see Figs. 2.1 and 2.5) were analysed independently. In both fields, images of the H_2 v=1-0 S(1) emission were analysed as well as the images of continuum emission. In all cases stars were masked out in the images before the analysis.

The results of the analysis of the H_2 brightness data are displayed in Fig. 8.2. The top panel shows the brightness histograms evaluated for the ESE field. Each curve correspond to a degraded resolution version of the ESE image and the box sizes used for the boxcar smoothing are stated beside the curves. It can be seen that the form of the histogram changes when the resolution is degraded. This is the behaviour of a non-fractal image. However, for box sizes greater than ∼90 pixels the form remains constant, indicating that the preferred scale has been washed out. We estimate the preferred scale to be $\sim 90 \pm 5$ pixels, that is, at a scale of $2\farcs4 \pm 0\farcs14$ or 1075 AU.

In the SE region, Fig. 8.2b, the histograms at 40–60 pixels are seen to change very little. However at box sizes greater than 60 the form of the histogram changes and breaks off from those at 40-60. At a box size of 145 pixels the form of the histograms converges again. We interpret this behaviour as a manifestation of two distinct scales present in the region. One scale at $\sim 40 \pm 5$ pixels, that is $1\farcs1 \pm 0\farcs14$ or 500 AU, and a larger scale at $\sim 145 \pm 5$ pixels ($3\farcs9 \pm 0\farcs14$ or 1800 AU). In Lacombe et al. (2004) only the smaller scale size was mentioned, however the more detailed analysis presented here clearly shows the presence of the larger scale as well.

If we choose a region which samples approximately equally both the ESE and SE regions and perform a brightness histogram analysis, we encounter two scales present together, of 40 pixels / 1.1" /500 AU and 100 pixels/ 2.7" /1250 AU (Fig. 8.3). The large scale at $3\farcs9$ seen in the SE region does not show up indicating that it consists of a less dominant population. We conclude therefore that the ESE and SE region contains clumps of material from two different and distinct distributions. The clumps in the ESE region are of about twice the scale of the material in the small clumps in the SE region and there is a well-defined demarcation between the two distributions of clump sizes.

In a region roughly corresponding to the ESE, Vannier et al. (2001) identified a scale size of $2\farcs0$ (900 AU) using the brightness histogram technique. This was from data from the ESO 3.6 m telescope of spatial resolution of $0\farcs38$. This is in substantial agreement with the present work.

The analysis has also been applied to the images of the continuum emission. For the ESE region shown in Fig. 2.6 this yields a scale of $\sim 70 \pm 5$ pixels, that is $1\farcs9 \pm 0\farcs14$ (870 AU, Fig. 8.4a). Since the continuum emission in OMC1

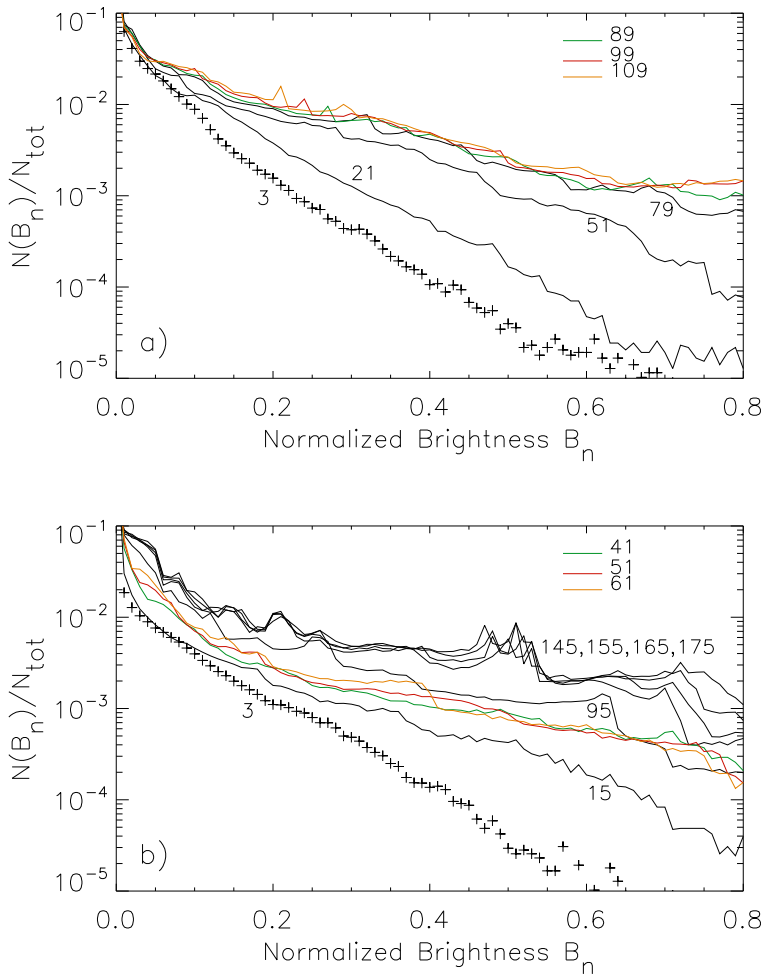

Figure 8.2: **a)** Brightness histogram analysis of the H_2 v=1-0 S(1) emission in the ESE region from VLT/NACO data. The numbers beside the curves represent the box sizes used for degrading the resolution. A preferred scale is found around 90 pixels $\sim$ 1075 AU. **b)** Same as above but for the SE region. Two preferred scales are detected at 40 and 150 pixels (500 and 1800 AU).

is mostly reflected light from dust (Sect. 1.5.2 and Chapter 3), this indicates that dust, and also by implication, cold unexcited gas in the northern part of this region is clumped on the same or somewhat smaller scale as the shocked gas in the southern region of the ESE field. In Fig. 8.4b histograms of the continuum emission in the SE field are shown. The shape of the histogram curve changes persistently when the resolution is degraded and the curves do not converge at any resolution. We therefore conclude that the scale size, if one is present, of the continuum emission in the SE region cannot be

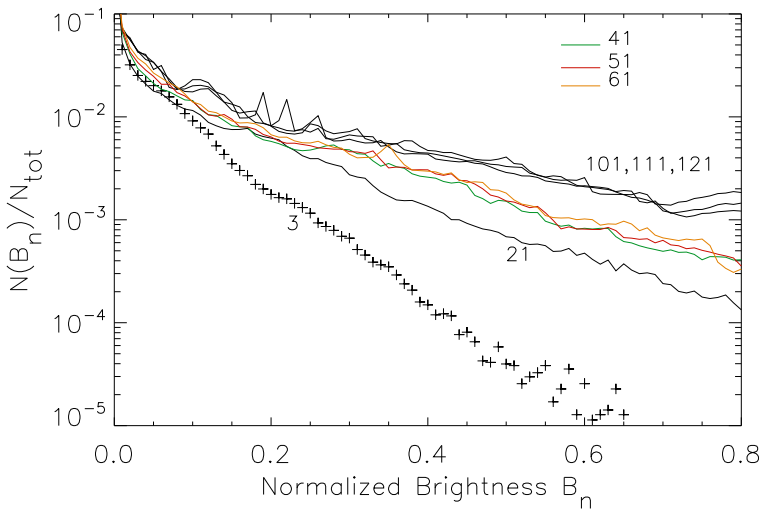

Figure 8.3: Brightness histogram analysis of the H_2 emission in a region from VLT/NACO data which samples equally both the ESE and the SE field. The numbers beside the curves represent the box sizes used for degrading the resolution. Two preferred scale are found around 40 and 100 pixels (500 and 1250 AU).

determined using the brightness histogram technique. In any case it is larger than 5.″4 (2500 AU).

8.2 Structure function technique

Here we introduce a new technique for identifying structures based on structure functions (SFs) or derivatives of SFs. In Chapter 5 we saw that SFs in OMC1 deviate from power laws, and interpreted the deviations as the presence of preferred scales. No formal proof of this assumption was however given in Chapter 5. Here we show by use of synthetic data that preferred scales in the medium do indeed give rise to deviations from power laws of SFs. Thus the interpretation in Chapter 5 was justified and deviations from power laws in SFs can be used to detect preferred scales. SFs are subsequently used in a more detailed analysis of the data in order to determine the scale sizes precisely.

As throughout this thesis the SFs of order p of a spatially resolved parameter A are defined as

$$S_p(L) = \langle |A(\boldsymbol{r}) - A(\boldsymbol{r} - \boldsymbol{\tau})|^p \rangle = \langle |\Delta A|^p \rangle \tag{8.1}$$

where the average is taken over all map positions $\boldsymbol{r}$ and all lags $\boldsymbol{\tau}$ such that $|\boldsymbol{\tau}| = L$. The structure functions were previously calculated for the

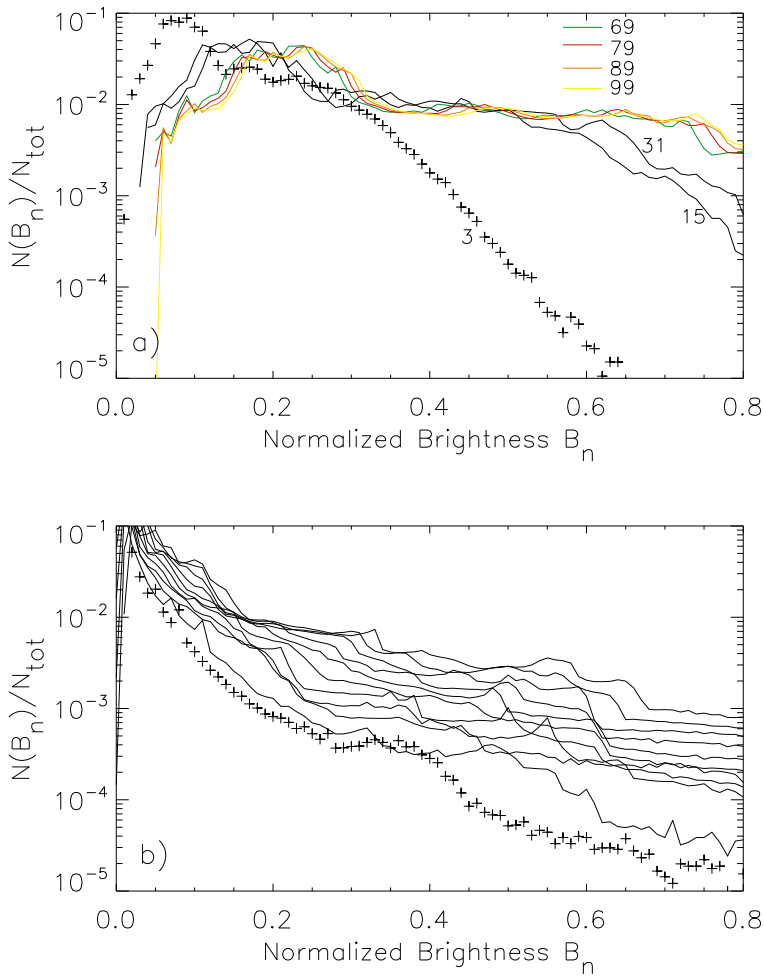

Figure 8.4: **a)** Brightness histogram analysis of the continuum emission in the ESE region from VLT/NACO data (Fig. 2.6). The numbers beside the curves represent the box sizes used for degrading the resolution. A preferred scale is found around 70 pixels (870 AU). **b)** Same as above but for the SE region. Curves correspond to images degraded by a box size of 3,15,35,55,75,95,115,135,155,175,195. The form of the curves keep changing and a preferred scale can therefore not be identified

velocity field ($A = v$) in Chapters 5- 7. However, the parameter A can be any parameter, such as for example brightness or velocity divergence.

As seen in Sect. 5.4 the SFs are measures of the spatial correlations of the parameter A. In a predominantly turbulent medium the SFs are well described by power laws, $S_p(L) \propto L^{\zeta(p)}$. On the other hand, if the region in question is not self-similar, but contains structure with a preferred scale, the SFs will deviate from power laws, as described below. In this section we show that

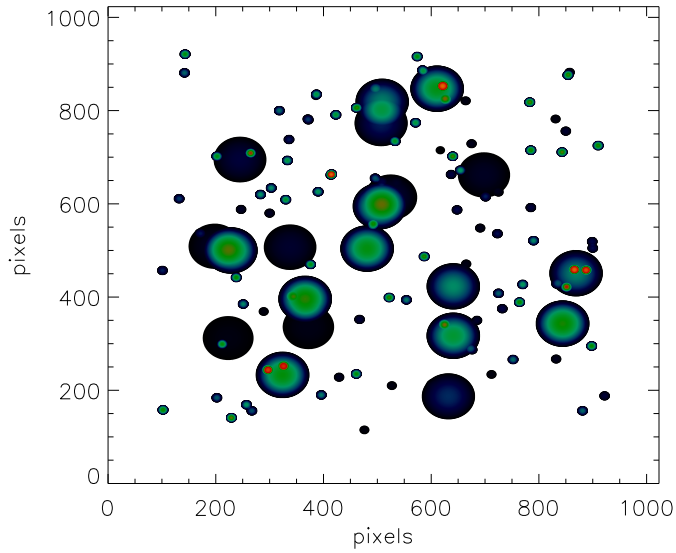

Figure 8.5: Map of randomly placed clumps. The map contains 100 clumps with a diameter of 20 pixels and 20 clumps with a diameter of 100 pixels corresponding to case iii). The intensity of the clumps varies randomly.

these deviations provide a very sensitive test of the size of such structure.

8.2.1 Results from model systems

If the region contains only a single structure in the map of parameter A of a certain size, R, it is evident that correlations will only persist up to scale R. In the structure function this will show up as an increase of $S_p(L)$ at scales $<$ R and a constant value at scales $>$ R. The same behaviour will be found if there is a large number of structures with the same size randomly distributed in the map. When clumps with two or more distinct preferred sizes are present, which is most likely the case in star forming regions, the structure function will show this effect for all sizes involved. The effect on the SFs will become successively less pronounced at any specific size as more scales are identified. In a real system, structures will most likely tend to group around a preferred scale with some characteristic deviation from a mean value. This aspect turns out to be more of a gloss on the present description than a fundamental point but can lead to systematic errors in structure size determination. This is described in Sect. 8.2.3.

To test the ideas set out above, three maps have been constructed with

i) a single circular clump with a diameter of 40 pixels and an intensity dis-

tribution given by the paraboloid function

$$f(x,y) = C\left(1 - \frac{(x-x_0)^2 + (y-y_0)^2}{r^2}\right) \tag{8.2}$$

where r is the radius of the clump, (x_0, y_0) is the centre position and C is the peak intensity,
ii) 100 randomly distributed clumps with the same characteristics as in i) and
iii) 100 clumps with a diameter of 20 pixels and 20 clumps with a diameter of 100 pixels where again all clumps are randomly distributed and of paraboloid shape. An example of such a map is shown in Fig. 8.5.
In all cases the clumps have been distributed on a square 1024 by 1024 grid and the peak intensity of any clump is allowed to vary randomly.
Similar maps were also constructed using conic shapes,

$$f(x,y) = C\left(1 - \frac{\sqrt{(x-x_0)^2 + (y-y_0)^2}}{r}\right) \tag{8.3}$$

of the intensity distribution in the clumps.

Cases (i) and (ii)

The SFs of order 1-5 for case (i) are shown in Fig. 8.6a. The SFs become roughly constant at $L \geq 30$ pixels close to the expected value of 40, that is, the diameter. The SFs for case (ii) are essentially the same and are therefore not shown. The effects on the SFs caused by the presence of clumps are more clearly seen at higher orders, p.
Preferred scale sizes in a map or an image result in changes in the logarithmic slope of SFs. Therefore the local logarithmic derivatives, $d\log S_p(L)/d\log L$, highlight the deviations from fractality and we can use these derivatives to detect such scales. As seen above the presence of preferred scales causes a decrease in the slope of the SFs making it roughly constant near the relevant size. This results in a plateau in the logarithmic derivatives if larger scales are not present, or a minimum if such scales are present. The former case is demonstrated in Fig. 8.6b for case (i) above, that is, for a single clump, and in Fig. 8.6c for case (ii), that is, for 100 such clumps. A minimum is seen at ~ 35 pixels in both Figs. 8.6b and c, very close to the imposed structure size of 40 pixels (see above). The inset to Fig. 8.6b displays the derivatives around $L \sim 35$ in detail and shows that the position of the minimum moves towards a lower value of L when p is increased. This occurs because higher orders of the structure function give more weight to higher values of ΔA (see Eq. (8.1)), thus depressing the outer regions of clumps in which low values

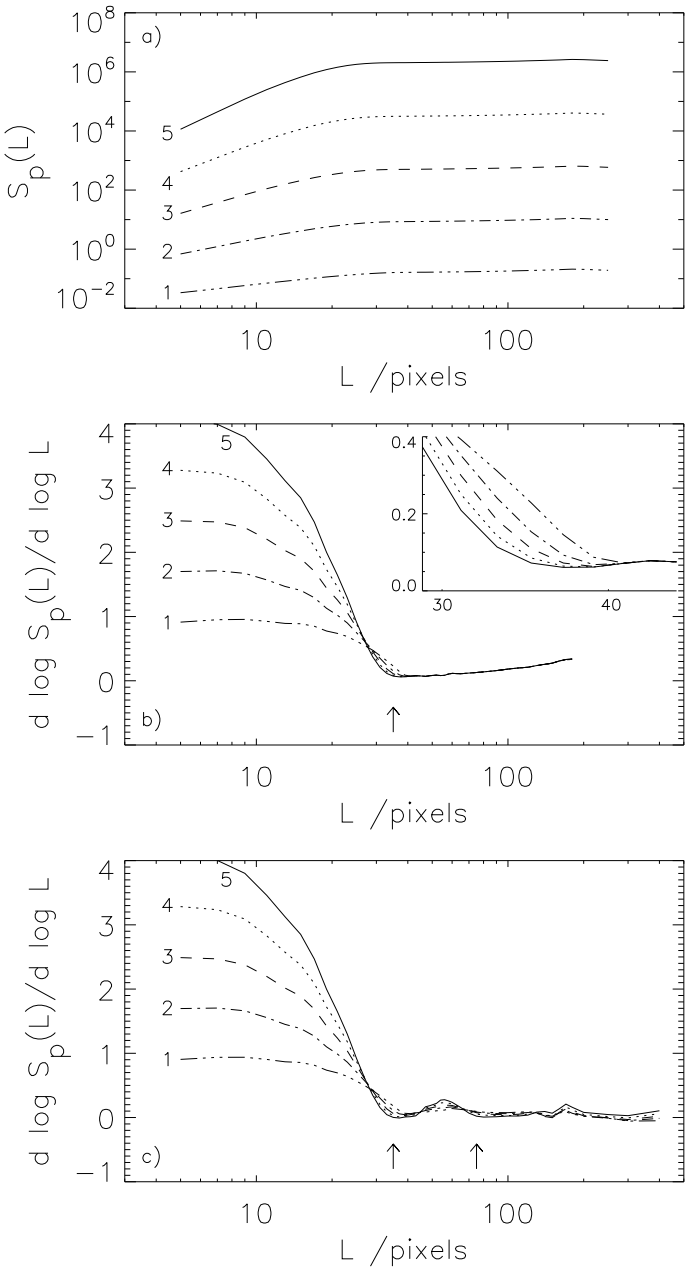

Figure 8.6: a) Structure functions of order 1-5 (labelled accordingly) for a simulated map, case (i) (see text). b) Local logarithmic derivatives of the SFs shown in a) Inset: Blow-up of r=29-45 pixels. c) Local logarithmic derivatives of SFs of order 1-5 derived from the simulated map of case (ii).

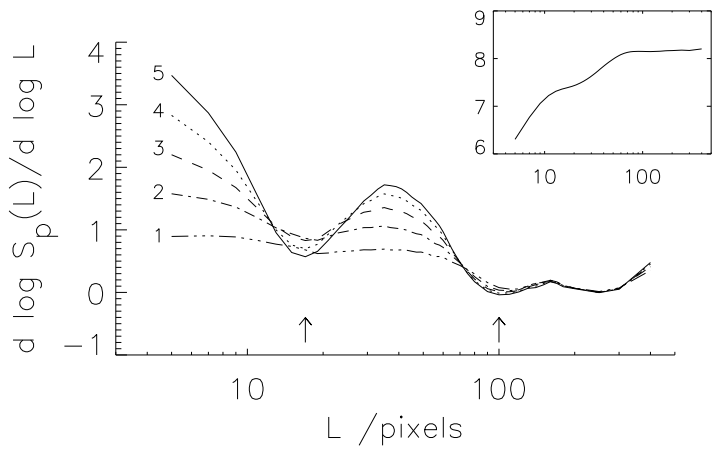

Figure 8.7: Local logarithmic derivatives of SFs of order 1-5 from the simulated map of case (iii) (see text). Inset: the logarithm of the 5th order structure function of case (iii).

of ΔA are found. Thus estimates of scale sizes from high order SFs represent lower bounds to the scale sizes and the estimated values can be 10-20% too low. In Fig. 8.6c, in addition to the first plateau or weak minimum at ~ 35 pixels, there is a secondary plateau at ~ 75 pixels, indicating the presence of a scale size approximately twice as large as the clumps in the simulation. This is most likely due to overlapping of the randomly placed individual clumps. By implication this method cannot distinguish between one large clump or several smaller clumps nearly coinciding in the same line-of-sight.

Case (iii)

The local logarithmic derivatives for p=1-5 are shown in Fig. 8.7 for case (iii) involving 100 clumps of diameter 20 pixels and 20 clumps of diameter 100 pixels. Here a local minimum is seen at ~ 17 pixels and ~ 100 pixels, representing the scales of 20 and 100 pixels included in this test image. Note that two scale sizes will only show clearly if the scales are well separated. If they are too close the larger scale will dominate and suppress the smaller. In real data this means that a detected scale size might conceal other smaller scales (see also Sect. 8.2.3). The inset to Fig. 8.7 shows the corresponding structure function for 5th order, showing plateaus at ~ 15 pixels and at $>\sim 80$ pixels.

An additional property evident in Figs. 8.6 and 8.7 is that in the presence of structure the derivatives of structure functions of all orders tend to congregate around the same value at a local minimum or plateau. This provides a further characteristic which aids the detection of structure. In numerical simulations

of fully developed turbulence, Biferale et al. (2004) noted a similar tendency for the local derivatives to accumulate at a certain value. The reason remains unclear.

Other tests

Structure functions were also calculated on the maps of clumps with conical shaped intensity distribution (Eq. (8.3)) and yielded similar results as above. This suggests that effects seen in the structure functions are independent of the shape of the clumps. This is of course only valid for clump geometries which can at least crudely be characterised by a single dimension.
Tests were also carried out on clumps with an ellipsoid shape with randomly oriented axes. These are characterized by two sizes, that is, those of the major and minor axes and the results are very similar to those of clumps with two different sets of diameters, that is case iii) above. Thus, in a medium with several scale sizes, it is not possible to distinguish between distributions consisting of circular clumps with different sizes and non-circular clumps with the same size characterized by two or more dimensions.

8.2.2 Edge-effects

A further point in assigning the presence of structure is the question of how large a structure may be detected for a given size of image, so called "edge-effects". In case (iii), in Fig. 8.7, there is already evidence for apparent structure at ~ 250 pixels which is not in the data. Edge-effects have been studied here using fractional Brownian motion structures (fBm-fractals), an example of which was shown in Fig. 8.1. We have calculated SFs and logarithmic derivatives for a number of such fractal images. For these, the SFs are expected to be pure power laws and the derivatives should be independent of L. The value of the logarithmic derivative depends on the choice of power spectral index and the order of the structure function involved. The slope is proportional to the order and fractal systems cannot therefore yield logarithmic derivatives of SFs of different orders which congregate at a particular value, as seen in the models above (e.g. Fig. 8.7).
An example of these test calculations is seen in Fig. 8.8 where SFs of order 1-5 and logarithmic derivatives for a fractal image of size 2048×2048 pixels are shown. The SFs may be approximated by power laws save at the largest scales. The logarithmic derivatives are nearly constant up to $L \sim 700$ pixels, any deviations from constancy below this value being due to the imperfect fractal nature of the simulations arising from pixelation. At around 700 pixels, a local minimum is found and the derivatives for p=3-5 congregate around the value of 0.4, apparently indicating a preferred structure size.

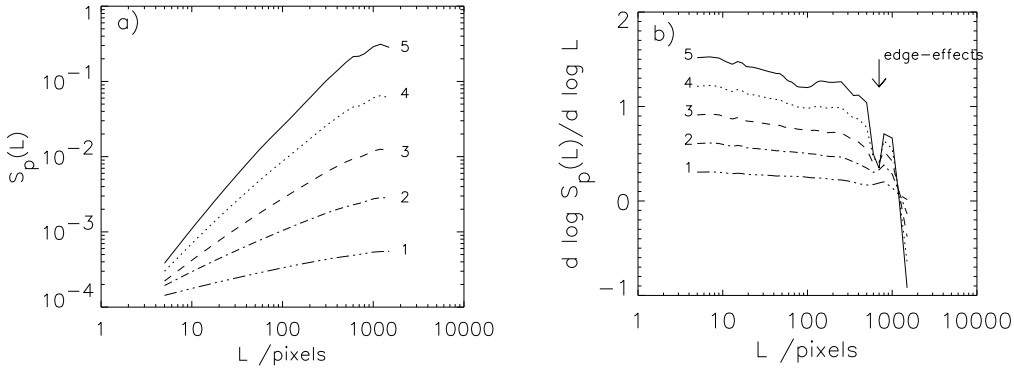

Figure 8.8: a) Structure functions of order 1-5 (labelled) of fractal image. b) Corresponding local logarithmic derivatives of structure functions of order 1-5.

The same analysis has been carried out on fractal images of size 1024×1024, 512×512 and 256×256 pixels. In all images apparent structure at scales of ∼ 1/5 - 1/3 of the size of the map were found. Hence increasing the size of the map also increased the absolute value of the apparent structure size. Thus we conclude that the apparent structure in the fractal images is an edge-effect and that detection of scale sizes much greater than 1/5 of the size of the map should not be attempted as such scales cannot be reliably identified.

8.2.3 Systematic errors associated with estimates of structure scale

There are systematic errors inherent in the present method. As already noted, derivatives of higher order SFs tend to pick out scales which are too small by as much as 10-20%. It turns out that when we consider a distribution of clump sizes about some mean value, this causes an overestimation of the mean clump size as we discuss below. These two effects tend to cancel but to an extent which cannot be quantified.

In a real molecular cloud the detection of a preferred scale size would imply that there exists a range of sizes around the derived value. The extent of such a range is difficult to assess and in common with other methods, the SF method does not give any direct measure of the extent of such a range. However, with the artificial data, described above, we can test the effect of introducing a distribution of clump sizes about some mean preferred scale. In order to illustrate the behaviour of such systems, we assume that the sizes of clumps are gaussian distributed about the mean. Using synthetic maps similar to those in Sect. 8.2.1 we have created a number of maps with 200 randomly positioned circular clumps. Three mean sizes of 40, 60 and

80 pixels were used in different maps. We have found that when the half-width of the gaussian distribution is smaller than ∼5% of the mean value the SFs are indistinguishable from the original of only one clump size and the minimum of the SF derivatives are found at the mean value. Increasing the half-width beyond ∼5% causes the minimum to move towards larger scales. That is, the larger scales start dominating the smaller. If the half-width of the distribution is 10% of the mean value the minimum is found at 1.07 times the mean value. For 20% the factor is 1.25 and for 25% the factor is 1.50. This analysis only conveys the sensitivity of the systematic error to the width of the distribution but does not allow an estimation of the width from observations. The distribution of clump sizes about some preferred scale is presumably directly linked to the IMF as discussed in Sect. 1.1 and it would be useful to develop methods which were capable of making a reliable width estimate.

8.3 Preferred scales in OMC1 from SF method

We now use the structure function technique on our data for OMC1. First we use the brightness information from the CFHT/GriF data (Sect. 2.4) and show that the molecular gas in OMC1 contains a number of preferred scales. Then we use the radial velocity of the same data set. It has already been shown in Sect. 5.4 that the velocities contain characteristic scales around 200 AU and 2000 AU but the analysis is presented here for completeness.
We also use the technique on the VLT/NACO data (Sect. 2.2) and the brightness data from VLT/NACO-FP (Sect. 2.5).

8.3.1 Use of the method with CFHT/GriF H_2 brightness data

Here we use the CFHT/GriF data (Sect. 2.4) and calculate SFs and logarithmic derivatives using the brightness information in these data. Note that brightness is roughly representative of the density structure in the excited H_2, assuming that differential obscuration from dust (Rosenthal et al. 2000) is negligible (but see Sect.1.4.1). In Fig. 8.9a and b the structure function of order 5 for the brightness and the corresponding derivatives are shown. Relative errors on values in the SFs are found using the law of propagation of errors for uncorrelated variables as in Sect. 5.4. Using the notation of Eq. (8.1), the variance is calculated as:

$$\begin{aligned} \sigma^2(S_p(L)) = \quad & (p^2/N^2) \quad \sum \left(\sigma^2(A(\boldsymbol{r})) + \sigma^2(A(\boldsymbol{r}-\boldsymbol{\tau}))\right) \\ & \times \qquad |A(\boldsymbol{r}) - A(\boldsymbol{r}-\boldsymbol{\tau})|^{2(p-1)} \end{aligned} \tag{8.4}$$

where the summation is performed over all pairs of pixels in the map that satisfy $|\tau| = L$, N is the total number of such pairs and $\sigma^2(A(\boldsymbol{r}))$ is the variance of $A(\boldsymbol{r})$. For $p = 2$ this is the same as Eq. (5.14) with $w = 1$. Due to the large number of pixel pairs in our data ($2 \cdot 10^7$-$4 \cdot 10^9$) the variances are very small. Typical values of the relative errors, $\sigma(S_p(L))/S_p(L)$, are 10^{-5} in the 2nd order SF, 10^{-4} in the 5th order SF and 10^{-3} in the 10th order SF. Thus the errors are negligible in SFs of order up to 10, as well as in the logarithmic derivatives of these functions.

In Fig. 8.9b local minima in the derivatives as a function of L are present at L $\sim$ 110AU and L $\sim$ 1700AU, providing clear evidence that the brightness structure, and by implication the density distribution, in OMC1 shows preferred scales. The positions of the minima indicate that the (largely) shocked regions in the field have two preferred sizes close to 110 and 1700AU. Two less pronounced minima or points of inflection are present at L $\sim$ 550AU and L $\sim$ 2700AU, which suggests that clumping at these scales is also present in the field, but to a lesser degree. As noted earlier these sizes may be representations of diameters in near-circular clumps or major and minor axes in elliptical shaped clumps.

In Fig. 8.9c the logarithmic derivatives of SFs of order 4,6,8,10 are displayed for the same data. This illustrates the tendency for the derivatives of higher order SFs to congregate at the same value, a property mentioned in Sect. 8.2.1. In Fig. 8.9d the same derivatives are displaced on the ordinate to give a clearer view of the evolution with regard to the order of the SF. As the order of the structure function increases, the derivatives show more detail. High order SFs accentuate the presence of weaker structure hidden in lower order SFs, resulting in more minima in the derivatives. Thus in the limit of very high order, derivatives will essentially pick out the size of every clump in the region. This property is useful since the order of the structure function at which a structure becomes apparent is a measure of the prevalence of that structure. A structure that is clearly seen in the 2nd order SF is more dominant in the region than a structure which is first seen in the 6th order SF, say. Examples are the scale sizes at L$\sim$ 550AU and 2700AU which are barely visible in the derivatives of the 4th order SF, but are clearly seen in the derivative of the 6th order SF. These are less dominant than the scale sizes at L$\sim$ 110AU, 1700AU, which are clearly apparent in the derivative of the 4th order SF. Note, however, that in observational data in general, random errors in the calculated values will increase when higher orders are computed, thus limiting the maximum value of p that may be used. This means that uncertainties in observational data may generally be a limiting factor in this form of data analysis.

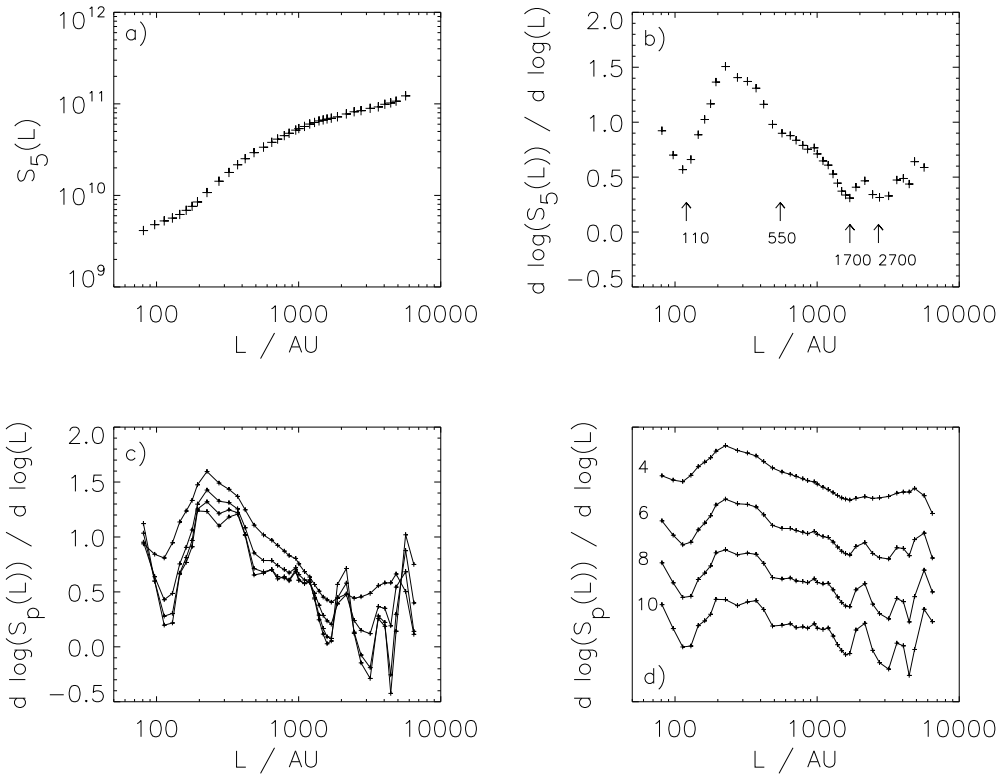

Figure 8.9: **a)** The 5th order structure function of velocity integrated brightness in OMC1 from CFHT/GriF data. **b)** Corresponding local logarithmic derivatives of the structure function of order 5. **c)** Local logarithmic derivatives of structure functions of order 4,6,8,10. **d)** Same as in c) but with the graphs displaced to get a better view of the evolution.

8.3.2 Use of the SF method with CFHT/GriF H_2 velocity data

We now analyse the velocity information obtained by the CFHT/GriF observations, as described in Sect. 2.4. The 5th order structure function of the velocity data from GriF and the corresponding derivatives are shown in Fig. 8.10. Because the accuracy of the velocity in each pixel depends on the brightness in the pixel (Sect. 2.4) each velocity difference in Eq. (8.1) has been weighted by the product of the brightness in the two pixels in question, thus giving more weight to pixels with high brightness. This is the same procedure used in Sects. 5.4 and 5.5, see Eq. (5.20). Relative errors on the calculated values in the weighted SFs are typically 10^{-3} for fifth order (p=5) and therefore negligible. An analysis of the velocity data has also been performed without brightness weighting with essentially the same result as

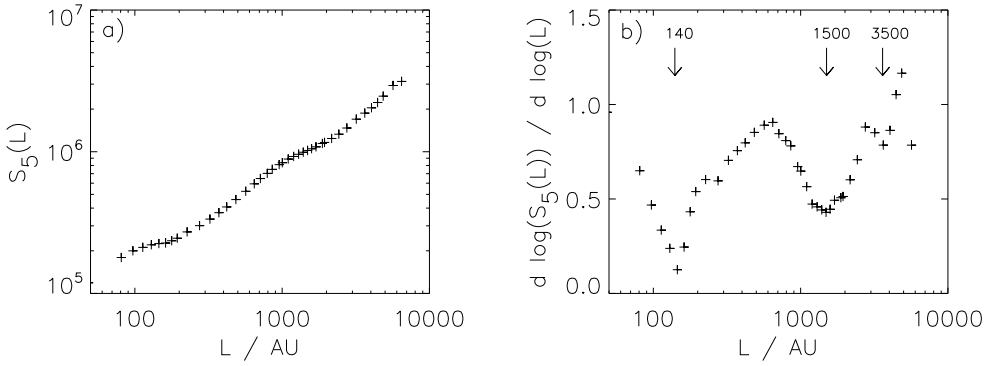

Figure 8.10: a) The 5th order structure function of velocities in OMC1 from CFHT/GriF. b) Corresponding local logarithmic derivatives of the 5th order structure function.

described below for the weighted SFs.

Figure 8.10 shows that local minima in the derivatives as a function of L are present at L $\sim$ 140AU, 1500AU and 3500AU. The two smaller scales were already noted in Sect. 5.4 from deviations in the second order SF, but by using the present method we are able to pin-point the position of these scales with much higher precision. We also detect the largest scale at 3500 AU, which was not evident before. Scale sizes in velocity indicate the sizes of regions moving like coherent entities. The scales detected here are approximately the same as those identified in the brightness data, which were found to be at 110 and 1700 AU, although there appears to be an additional larger scale at 3500 AU in velocity. Thus there seems to be a correlation of sizes of structures and the length of coherent velocities. This may be inherent in the physical processes of shocks. The weak structure in the brightness at L$\sim$ 550AU and 2700AU (Sect. 8.3.1) is however not seen in the velocity.

8.3.3 Use of the SF method with VLT/NACO data

We now turn to the VLT/NACO data (Sect. 2.2). In Sect. 8.1 the ESE and SE region were analysed independently using the brightness histogram technique. Here we present a structure analysis of the two regions based on the SF method and compare with the results from the histogram technique in Sect. 8.1.

In Fig. 8.11 we show the local logarithmic derivatives of the 3rd and 4th order SF corresponding to the ESE and SE regions. In the ESE region (Fig. 8.11a) two clear scale sizes of $L \sim$500 AU and 2000 AU are evident and a weaker minimum at 1000 AU. Using the brightness histogram technique we found

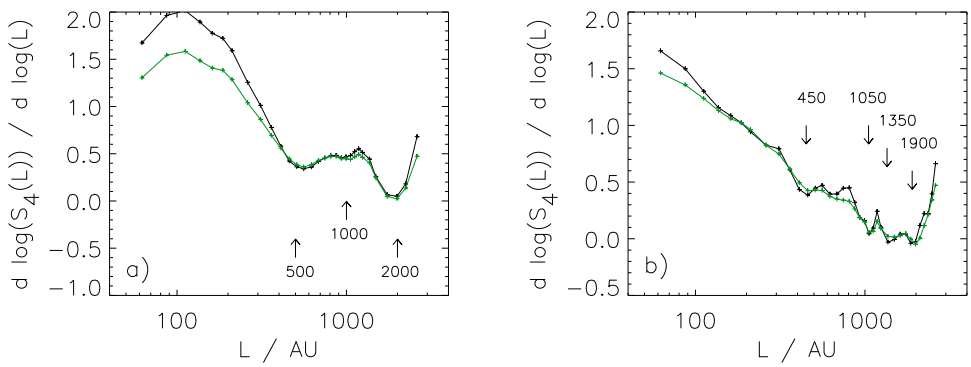

Figure 8.11: a) Local logarithmic derivatives of the 3rd (green) and 4th (black) order structure function of the VLT/NACO data in the ESE region. b) Same as a) but for the SE region.

only one scale size of $\sim$ 1075 AU and with the same technique Vannier et al. (2001) found a scale size of $\sim$ 900 AU. Thus there seems to be some discrepancy between the two methods. The nature of the results suggests that the three sizes detected with the SF method are present but mixed to a degree that the histogram method is unable to isolate them.
The SE region (Fig. 8.11b) displays a number of scale sizes at $\sim$ 450 AU, 1050 AU, 1350 AU and 1900 AU. The scales at 450 AU and 1900 AU are consistent with the result from the histogram technique (Sect. 8.1).

8.3.4 Use of the method with VLT/NACO-FP data

We have also performed the analysis using the brightness information from the VLT/NACO-FP data (Sect. 2.5). SFs have been calculated for the combined brightness images for the three H_2 lines observed (Figs. 2.14, 2.16, 2.18). The results for the three lines are very similar and show essentially the same characteristic scale sizes. This is expected since the three lines are all tracers of shock excitation. The results for these data have a close resemblance to those of the CFHT/GriF data in Fig. 8.9 as they should have and are not shown here. Preferred scale sizes are found at 600, 1000, 2000 and 3700 AU in these data. This is to be compared with the scales of 110, 550, 1700 and 2700 AU found in the CFHT/GriF data. The smallest scale of 110 AU in the CFHT/GriF data does not seem to have a counterpart in the VLT/NACO-FP data of the v=1-0 S(1) and v=2-1 S(1) lines. However, there is an indication of a scale size of $\sim$80 AU in the v=1-0 S(0) line data, which is the data set of highest resolution (see Table 2.3).
The data of continuum emission obtained from the VLT/NACO-FP data and

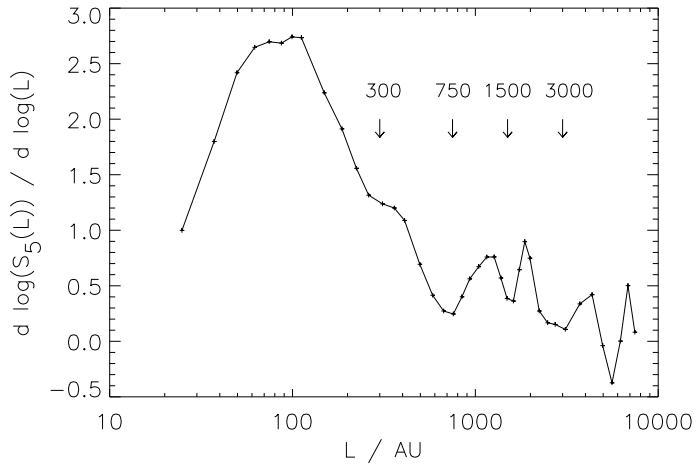

Figure 8.12: Local logarithmic derivatives of the 5th order SF for the continuum data from VLT/NACO-FP. Preferred scales are indicated.

presented in Chapter 3 have also been analysed and the results are shown in Fig. 8.12. Clear preferred scales have been identified at 300, 750, 1500 and 3000 AU. The scale at 750 AU is consistent with the size estimate of 870 AU for the ESE image of the VLT/NACO data found using the histogram method (Fig. 8.4a).

The scale sizes found in the continuum and H_2 emission, respectively, suggest that the continuum emitting dust is clumped in a similar fashion to the hot, shock excited H_2 although with somewhat smaller scale sizes. This conclusion was also reached from the histogram technique in Sect. 8.1, but based on only one scale size. Assuming that the dust-to-gas ratio is constant as have been observed elsewhere (e.g. Predehl & Schmitt 1995) this implies that the cold unexcited gas is distributed in a manner similar to the hot component and that observations of excited gas are good tracers of the cold gas. This is very important, since stars are formed in the densest regions of the cold gas.

8.4 Fourier Transform technique

We briefly describe the standard two-dimensional Fourier transform technique commonly employed to identify scale size in images in order to make a detailed comparison with the SF method for detection of structures (Sect. 8.2). We then calculate the Fourier transform for a few test images and compare the results with the SF method.

From a two-dimensional Fourier transform of an image, a power spectrum

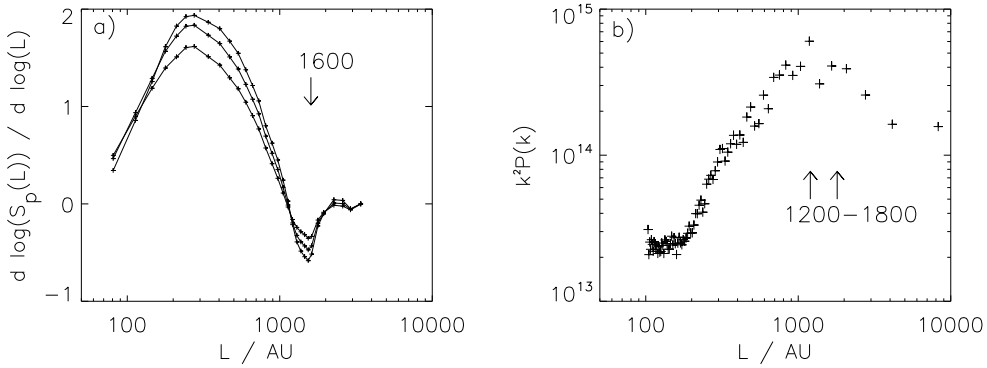

Figure 8.13: a) Local logarithmic derivatives of structure functions of order 4,5,6 of a region south-west of BN in OMC1 calculated from data from Kristensen et al. (2006). b) Fourier transform of the same set of data: the power spectrum multiplied by k^2 vs. the scale size, L ($\propto k^{-1}$).

$P(k)$ can be calculated from the complex modulus. That is, $P(k) = \hat{v}(k)\hat{v}(k)^*$ where $\hat{v}$ is the two-dimensional Fourier transform of the velocity $\hat{v} = \int e^{ikr} v(r) dr$ and $\hat{v}^*$ is the complex conjugate. In the case of self-similar of fractal structure the power spectrum would be a power law in k ($P(k) \propto k^{-\beta}$), where $k \propto \mathrm{r}^{-1}$. Departures from a power law in k signify an over-population at some scale compared to a fractal. Deviations from a power law are nicely illustrated by showing $k^2P(k)$ vs k, as described in Vannier et al. (2001).

To constitute a simple test case, we now use an image where only one characteristic size has been detected using the SF method. For this purpose we have to look outside the data sets mainly analysed in this thesis since they all show several scale sizes. It turns out that data from Kristensen et al. (2006) contains only one scale size, see below, and thus we use this for comparison.

Data from Kristensen et al. (2006) were obtained at the CFHT with the PUEO adaptive optics and the KIR infrared detector. The data are of H_2 v=1-0 S(1) line emission and cover the same region in OMC1 as the field named SW in the CFHT/GriF observations (Fig. 2.2). The field is $36'' \times 36''$, the pixel scale is $0\farcs035$ and the resolution is $0\farcs45$ or 200 AU.

Figure 8.13a shows the derivatives of the SFs of order 4,5,6 of this region indicating a single preferred scale of 1600 AU. Figure 8.13b displays $k^2\mathrm{P}(k)$ vs. scale size (k^{-1}) of the same region and shows that there is a range of scales which are over-populated. This over-population peaks at $\sim$ 1200-1800 AU. The above results show good agreement between the scales obtained from the power spectrum and the SF derivatives, at any rate in this simple case in which only a single scale, or a single range of scales, is present in the

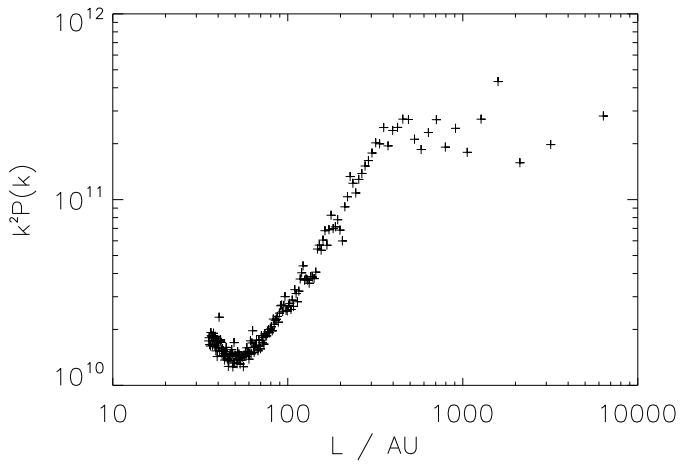

Figure 8.14: a) Fourier transform of the ESE region in the VLT/NACO data: the power spectrum multiplied by k^2 vs. the scale size, L ($\propto k^{-1}$).

region.

Note that this region is known from the CFHT/GriF data (Sect. 8.3.1) as well as the VLT/NACO data (Sects. 8.1.1 and 8.3.3) to be composed of clumps with several scale sizes at $\sim$ 450, 1050, 1350 and 1900 AU. However the poor spatial resolution of the data from Kristensen et al. (2006) of 200 AU not only affects the small scales of $<$ 200AU, but also blends the different scales at larger lags. Thus the presence of several preferred scales may not be detected in low resolution observations. This emphasizes the demand for high spatial resolution in this kind of analysis.

For a more complicated example we re-analyse the ESE region from the VLT/NACO data. The SF method showed this region to have three distinct scale sizes of 500, 1000 and 2000 AU (Fig. 8.11). We created a two-dimensional Fourier transform to yield the power spectrum, $P(k)$, shown in Fig. 8.14. The power spectrum is - as it should be - very similar to that reported in Vannier et al. (2001) showing marked departure from a power law. There is a range of scales excessively populated. This range has a broad and rather poorly determined maximum around the value of 600 AU. This value agrees with the lower value detected using the SF method of 500 AU, but a comparison between Fig. 8.14 and Fig. 8.11a shows that the SF method is capable of much more precision in the identification of structure scale than a simple Fourier transform.

Region	Method	sizes / AU
OMC1 (CFHT/GriF)	SF	110, 550, 1700, 2700
OMC1 (VLT/NACO-FP)	SF	80[a], 600, 1000, 2000, 3700
ESE (VLT/NACO)	histo	1075
ESE (VLT/NACO)	SF	500, 1000, 2000
ESE (VLT/NACO)	FT	600
SE(VLT/NACO)	histo	500, 1800
SE (VLT/NACO)	SF	450, 1050, 1350, 1900
Kristensen et al. (2006)	SF	1600
Kristensen et al. (2006)	FT	1200-1800
continuum (VLT/NACO-FP)	SF	300, 750, 1500, 3000
continuum ESE (VLT/NACO)	histo	870
continuum SE (VLT/NACO)	histo	> 2500
velocity (CFHT/GriF)	SF	140, 1500, 3500

Table 8.1: Summary of the preferred scale sizes detected in OMC1 with different method using different data sets. The methods used are: the brightness histogram technique (histo), the structure function method (SF) and Fourier transforms (FT). [a]: only detected in the v=1-0 S(0) line.

8.5 Concluding remarks on scale size identification

The presence of preferred scale sizes in molecular clouds is very important for theories of turbulence and star formation. It was already shown in Chapter 5 that the gas in OMC1 is not fractal and that preferred scale sizes are present in the hot component of the gas in OMC1 as observed through H_2. In order to estimate the sizes of structures in OMC1 more accurately we have implemented three different methods. There is however some ambiguity in the determination of the exact value of the preferred scale size among the methods. The results are summarized in Table 8.1.

There is reasonably good correspondence between the standard technique of 2D Fourier transform and the SF method, so far as comparison can be made. Both show clear departure from self-similarity and a similar scale size, where this can be identified, as in the data of Kristensen et al. (2006), see Table 8.1. The histogram technique is also in reasonable agreement with the SF methods as evidenced in the SE region of the VLT/NACO data (Table 8.1). There may be some discrepancy between the histogram technique and the Fourier transform. In the ESE region of the VLT/NACO data these methods pick out two different scales, which are, however, shown both to be present from the SF method. It is clear that the SF method is much more sensitive to

the presence of more than one scale size than both the Fourier transform and the histogram technique. This is evident in the ESE and SE regions of the VLT/NACO data (Table 8.1). Here the SF method detects several scale sizes while both the Fourier transform and the histogram technique reveal only one (or two) scale(s).

The SF technique developed here, whilst suffering from some degree of uncertainty and imprecision to an extent common to all methods, has proved valuable for detection of scale sizes. It is easy to implement and appears to be very sensitive.

Note that the spatial resolution has a large effect on the scales sizes found. This is evident in Figs. 8.11b and 8.13a which display the derivatives of the SFs for essentially the same region but for two different data sets. The spatial resolution of the VLT/NACO data in Fig. 8.11b is ∼40 AU while it is ∼200 AU in the data of Fig. 8.13a. The poor spatial resolution of the latter data set does not only affect the smaller scales but also blurs the presence of more than one characteristic scale size.

Based on the analysis presented here we conclude that the hot, excited H_2 gas in OMC1 exhibit a number of mean characteristic scale sizes around 100, 550, 1000, 1900 and 3000 AU. The cold component of the gas, as traced by dust emission, is distributed in a similar way.

Are the clumps gravitationally unstable?

Using the scale sizes of clumps found above together with estimates of the mean density we can determine if the clumps contain enough mass to be gravitationally unstable. The stability criterion can be expressed through the Jeans length, which is the size of a region in which the thermal pressure exactly balances the gravity. In the absence of other support mechanisms, such as magnetic fields or turbulent motions (see Chapter 1), all scales larger than the Jeans length are unstable while smaller scales are stable against gravitational collapse.

The Jeans length depends on temperature and density of the gas and can be expressed as $R_J \sim 3.7(T/n)^{1/2}$ pc where T is the kinetic temperature and n is the number density, $n(H) + 2n(H_2)\,\mathrm{cm}^{-3}$ (Blitz & Williams 1997). The number density in the field observed was estimated by Vannier et al. (2001); Kristensen et al. (2003, 2006) (see also Chapter 4). They found that in zones of bright emission shocks impinge on gas with pre-shock densities of $10^5 - 10^7\,\mathrm{cm}^{-3}$. The gas swept up by the shock will achieve post-shock densities of $10^6 - 10^8\,\mathrm{cm}^{-3}$ as the shocked gas cools to 10K (Kristensen et al. 2006). Assuming a typical post-shock density of $10^7\,\mathrm{cm}^{-3}$ the Jeans length is 760 AU. Thus the largest characteristic scale sizes identified here exceed the Jeans length. This means that sufficient gas may have accumulated through

shock induced compression to form gravitationally unstable clumps which are potential sites of star formation.
Given the density of $10^7\,\mathrm{cm}^{-3}$ the mass contained in clumps of size 3000 AU is only $\sim 0.4 M_\odot$. Some of these clumps may thus be candidates of low mass star formation triggered by the shocks formed by the energetic outflow from the BN-IRc2 region. This supports the conclusion reached throughout this thesis from different aspects of analysis, namely that low mass protostars are present in the OMC1 region.

Chapter 9

Summary and outlook

The work presented in this thesis revolves around using data of radial velocity and brightness to describe the environment in a highly active star forming region. For this purpose we have used both detailed analysis of observational data and comparisons with numerical hydrodynamical simulations.

We have presented high spatial resolution infrared observations of rovibrationally excited H_2 emission in OMC1, yielding both the brightness of the gas and the associated radial velocity. The spatial resolution of these velocity data surpasses that of similar data previously published by an order of magnitude and has enabled us to study in detail the motions of gas at very small scales.

We have shown very graphic views of interstellar shocks with strong velocity shifts over small local regions of bright H_2 emission. The H_2 emission in OMC1 is dominated by one or two outflows from high mass sources in the BN-IRc2 region. However, based on a model of shock directions, we present evidence that not all flows in this region move in the outflow direction. Some of the shocks that cannot be associated with the general outflow may arise from supersonic turbulence, while others may be caused by local, small scale outflows from embedded low-mass protostars.

Analysis of the morphology of the H_2 emission as well as continuum emission reveals that the region consists of clumps of gas with a number of preferred scale sizes. That is, the distribution of clumps is not self-similar. Some clump forming mechanism produces clumps preferentially with sizes of 100, 550, 1000, 1900 and 3000 AU. The largest of these clumps contain $0.4 M_\odot$ (Sect. 8.5) and may be gravitationally unstable.

We have also performed a statistical analysis of the radial velocities. This type of analysis has previously only been used to analyse characteristics of the cold gas at large scales as traced by CO. The work presented here extends this kind of analysis by two orders of magnitude in scale and show that the size-line width relation observed in the cold gas, and associated with self-

similar structures, is recovered at these smaller scales. However, preferred scales in the velocity field, related to the preferred scale sizes of clumps, are evident from structure functions. It is found that an excess of energy is in motion at $\sim 1500\,\mathrm{AU}$ which is interpreted as evidence of outflows from low-mass stars re-injecting energy into the system at this scale.

The preferred scales found in the velocity field of OMC1 cannot be reproduced by simulations of supersonic turbulence driven at large scales. The simulations are based on the assumption of energy injection at the largest scale only. It may be that the emergence of preferred scales in the data arises because of the injection of energy at much smaller scales associated with outflows from protostellar objects. However, this suggestion remains to be confirmed by simulations that do contain small scale energy injection.

In conclusion, various aspects of the analysis shown in this thesis suggest that some low-mass protostars are present in OMC1. Outflow from these causes shocks and inject energy into the region at scales of $\sim 1500\,\mathrm{AU}$. Candidates for such protostars can be seen from X-ray emission and infrared photometry to be present throughout the region. Infrared continuum emission from VLT/NACO-FP shown here also reveals several compact sources of which at least one source, located at (-20″,29.4″) relative to TCC0016 and shown in Fig. 4.8, may be associated with an H_2 outflow.

In addition to the statistical analysis of the velocity field of the whole region, we have conducted a similar analysis on 170 individual clumps. The analysis reveal large differences between clumps concerning the shape of the velocity probability distribution function and the scaling exponents of the structure functions. That is, clumps exist with gaussian, exponential and multi-modal probability distribution functions and with scaling exponent ranging from zero to 1.6. A self-consistent theory of star formation should be able to reproduce such differences.

The results presented in this thesis indicates that motions are governed by turbulence even at the small scales analysed here. This supports the turbulent picture of star formation, discussed in the introduction, in which clumps of dense gas are formed by shock compression caused by the supersonic turbulence. The densest clumps will be gravitationally unstable and form protostars. It is most likely the aftermath of such star formation that we observe, where newly formed stars inject energy into an otherwise turbulent medium.

The analysis presented here leaves many open questions. The most important question is whether the preferred scales we observe are really associated with protostars. With the present data we cannot entirely exclude the possibility that the observed features are direct consequences of supersonic turbulence

and the nature of shocks. This is an equally interesting conclusion, but would tell us more about turbulence and shock physics than about star formation directly. In order to settle this question we need more detailed numerical simulations of supersonic turbulence including local energy injection at small scales representing protostellar outflows. With some simplifying assumptions this can be achieved within the existing computer codes. Comparisons of the observational data with such simulations are the subject of proposed future work. In the more distant future simulations of turbulence should include all the relevant physics of the interstellar medium. This include magnetic fields, shock physics and self-gravity.

Another future prospect is to test how statistical results obtained from observations of hot H_2 compare to data of the cold bulk gas observed in radio transitions of CO for example. Our results indicate that the cold gas, as traced by light reflected from dust, is distributed much like the hot H_2 gas. Furthermore, results show that the exponents found in OMC1 of the size-line width relation and for example the second order structure function are similar to those found from CO observations at scales larger than 0.02 pc. All this suggests that results from hot H_2 and cold CO (say) should show the same characteristics. However, a direct comparison of CO and H_2 data in the same region and on the same scales has not yet been made. This could for example be done by mapping H_2 in a large region and smoothing the infrared data to the resolution of the radio data.

With the advent of ALMA, high spatial resolution mapping of molecular transitions in the radio regime with $\leq 0\farcs1$ resolution will become feasible. Thus the distribution and the velocities of the cold gas can be traced down to the same small scales that are observed in the infrared. Furthermore velocity fields of different molecules tracing different density regimes and excitation conditions may also be used to yield a much more detailed description of the structures and velocities in star forming regions. This offers a unique opportunity for extending the analysis presented here to the cold gas at small spatial scales.

Appendix A

Table of clump parameters

Table A.1: Position relative to TCC0016 of clumps analysed in Chap. 6, values of structure function exponents ζ_2 and ζ_2/ζ_3, the scaling relation of exponents (SL: The scaling relation is best resembled by the She-Leveque formula, B: The scaling relation is best resembled by the Boldyrev formula, OMC1: The scaling relation resembles that of the full dataset (Fig. 5.8)) and the shape of the PDF (1: gaussian, 2: Exponential, 3: Multi-modal). Clumps 1-19 are also analysed in Chap. 4. ^{a,b,c,d,e,f,g,h} mark the eight clumps displayed in Figs. 6.1 and 6.3.

No	RA (arcsec)	DEC (arcsec)	ζ_2	ζ_2/ζ_3	scaling	PDF shape
1a^b	-25.95	35.68	1.16	0.72	SL	3
1b	-28.36	34.30	1.29	0.66	SL	3
2	-20.69	30.19	1.19	0.75	B	3
3	4.15	11.06	1.08	0.69	SL	3
4	-17.47	10.50	1.12	0.70	SL	3
5	-23.47	6.63	1.25	0.67	SL	3
6^c	15.72	-1.26	0.98	0.65	SL	3
8	-8.30	13.95	1.33	0.68	SL	3
10	-17.38	45.69	1.03	0.98	OMC1	3
11	-29.68	-8.19	0.43	0.78	OMC1	1
12a	-27.13	16.17	1.25	0.71	SL	3
12b	-25.32	16.21	1.20	0.69	SL	3
13	-35.84	32.69	0.63	0.76	OMC1	2
14	-18.57	35.54	0.92	0.69	SL	3
15	-13.62	22.65	1.32	0.69	SL	3
16	-18.53	23.26	1.26	0.66	SL	3
17	-17.82	-1.44	1.47	0.68	SL	3
18	-7.44	22.51	0.81	0.66	SL	2
19	16.21	-6.39	1.13	0.73	OMC1	3
20	18.97	-5.85	0.66	0.69	SL	3

Table A.1: continued

No	RA (arcsec)	DEC (arcsec)	ζ_2	ζ_2/ζ_3	scaling	PDF shape
21	-25.20	0.81	0.93	0.68	SL	2
22	18.20	4.13	0.97	0.68	SL	3
23	4.80	-8.35	0.46	–	–	3
24	-20.48	-6.18	1.23	0.68	SL	3
25	-13.44	-0.30	1.14	0.71	SL	3
26	-20.07	16.98	1.15	0.69	SL	3
27	18.11	-1.07	0.39	0.72	B	1
28	1.02	5.78	1.11	0.69	SL	3
29	0.49	6.32	0.80	0.68	SL	3
30	-22.56	18.50	0.36	0.65	SL	2
31	-26.62	24.43	0.37	1.14	OMC1	2
32	-29.66	23.92	0.75	0.70	SL	3
33	-31.47	20.98	1.10	0.76	OMC1	3
34	-15.28	38.55	0.55	0.68	SL	3
35	-15.77	36.96	0.43	0.69	SL	3
36	-17.48	36.79	0.87	0.73	B	2
37	-12.88	41.02	0.76	0.69	SL	2
38	-14.09	41.09	0.30	0.70	SL	1
39	-9.98	44.82	0.28	0.65	SL	2
40	-10.31	46.34	0.26	0.69	SL	1
41	-9.52	47.41	0.69	0.87	OMC1	3
42	-8.44	46.95	0.60	0.69	SL	2
43	-29.49	38.68	0.51	0.72	OMC1	3
44	-31.94	37.59	0.27	–	–	2
45	-35.56	34.90	0.72	0.70	OMC1	2
46	-39.45	32.78	0.11	–	–	2
47	-45.61	35.79	1.16	0.68	SL	3
48[e]	-33.76	41.58	0.16	0.75	OMC1	2
49	-32.18	31.41	0.91	0.78	OMC1	3
50	-36.14	28.70	0.34	0.72	B	2
51	-33.93	27.41	0.78	0.79	OMC1	3
52	-44.78	29.17	0.28	0.67	SL	1
53	-49.19	26.74	0.34	0.76	B	2
54	-39.15	26.09	0.12	–	–	2
55	-37.35	24.33	0.11	–	–	2
56	-41.32	24.50	0.16	–	–	2
57[h]	-37.99	23.10	0.21	0.67	SL	1
58	-37.40	21.53	0.19	0.68	SL	1

Table A.1: continued

No	RA (arcsec)	DEC (arcsec)	ζ_2	ζ_2/ζ_3	scaling	PDF shape
59	-40.76	22.26	0.11	–	–	2
60	-34.14	15.84	0.96	0.71	B	3
61	-30.71	25.60	0.56	0.67	SL	1
62	-32.39	26.02	0.38	–	–	2
63	-32.73	24.78	0.20	–	–	2
64	-30.96	22.38	0.65	0.69	SL	3
65	-28.98	21.40	1.26	0.67	SL	3
66	-27.41	19.95	0.54	0.78	OMC1	3
67	-25.92	20.04	0.82	0.71	OMC1	3
68	-24.69	21.32	0.48	0.66	SL	2
69[f]	-24.33	19.79	1.16	0.67	SL	2
70	-25.64	18.06	0.54	0.69	SL	3
71	-22.63	20.20	0.73	0.69	SL	3
72	-22.17	21.88	0.64	0.68	SL	3
73	-19.06	21.26	0.48	0.81	OMC1	1
74	-17.50	21.35	0.74	0.70	SL	3
75	-9.17	26.30	0.45	0.70	B	2
76	-20.09	25.95	0.43	0.53	–	2
77	-22.24	24.38	0.80	0.69	SL	3
78	-27.63	12.13	0.92	0.68	SL	2
79	-10.92	-16.57	0.60	0.68	SL	2
80	-15.02	-11.71	0.83	0.67	SL	3
81	-17.90	0.56	1.26	0.76	OMC1	3
82	-18.53	2.91	0.38	0.80	B	2
83	-18.71	5.25	0.50	0.69	SL	2
84[a]	-19.11	6.83	1.07	0.68	SL	3
85	-18.85	8.17	0.89	0.71	SL	3
86	-16.40	5.90	0.75	0.69	SL	3
87	-10.50	-0.32	0.53	0.89	OMC1	3
88	-31.10	6.00	0.50	0.70	B	1
89	-33.37	7.42	0.17	–	–	1
90	-13.79	11.22	1.28	0.71	SL	3
91	-14.00	12.57	1.29	0.70	SL	3
92	-15.56	13.34	1.24	0.74	B	3
93	-8.30	10.54	1.00	0.74	B	3
94	-7.77	7.98	1.07	0.69	SL	2
96	-5.20	6.34	1.57	0.69	SL	3
97[d]	-3.59	6.48	1.57	0.68	SL	3

Table A.1: continued

No	RA (arcsec)	DEC (arcsec)	ζ_2	ζ_2/ζ_3	scaling	PDF shape
98	-2.26	5.86	1.30	0.69	SL	3
99	-1.09	10.01	0.84	0.82	OMC1	3
100	3.06	7.53	0.82	0.73	B	3
101	0.00	8.28	1.00	0.85	OMC1	3
102	1.44	3.96	0.56	1.10	OMC1	3
103	0.21	3.96	1.40	0.72	SL	3
104	2.82	0.96	0.91	0.75	OMC1	3
105	1.66	1.63	1.09	0.74	SL	3
106	4.15	0.51	0.90	0.71	B	3
107	3.62	-2.35	0.81	0.76	OMC1	3
108	6.27	7.05	0.80	0.94	OMC1	3
109	7.74	6.37	0.24	–		2
110	10.64	7.09	0.65	0.69	SL	3
111	10.48	9.19	0.53	0.69	SL	1
112	8.93	6.62	0.38	0.71	SL	1
113	13.06	8.17	0.68	0.68	SL	2
114	14.18	9.78	0.64	0.69	SL	2
115	15.91	7.86	0.77	0.68	SL	3
116	16.50	10.15	0.76	0.72	B	3
117	16.84	8.82	0.68	0.68	SL	3
118	19.04	9.08	0.49	–	–	2
119	22.75	8.98	0.23	0.70	SL	2
120	14.82	6.62	0.05	–	–	2
121	12.02	4.27	0.95	0.66	SL	3
122	6.67	3.06	1.57	0.71	SL	3
123	6.20	1.16	1.45	0.75	B	3
124	6.09	-0.33	1.17	0.68	SL	3
125	9.17	3.15	1.04	0.69	SL	3
126	8.24	1.86	1.24	0.69	SL	3
127	9.59	1.24	1.10	0.67	SL	3
128	10.47	-0.98	1.10	0.73	OMC1	3
129	12.37	2.21	0.69	0.65	SL	3
130	12.46	0.67	0.48	0.73	B	1
131	10.80	1.28	0.81	0.66	SL	2
132	16.22	-0.39	0.56	0.69	SL	1
133	13.35	-0.67	0.91	0.67	SL	3
134	13.46	-1.61	0.34	0.68	SL	2
135	12.25	-2.77	0.12	–	–	3

Table A.1: continued

No	RA (arcsec)	DEC (arcsec)	ζ_2	ζ_2/ζ_3	scaling	PDF shape
136	9.98	-6.42	0.27	0.78	OMC1	1
137	6.95	-4.67	0.20	–	–	3
138	7.61	-3.62	0.46	0.68	SL	3
139	7.11	-1.54	0.61	0.66	SL	2
140	6.53	-3.13	0.78	0.68	SL	3
141	5.15	-3.40	1.13	0.66	SL	3
142	5.15	-2.22	0.74	0.70	SL	3
143	-3.64	42.93	0.96	0.67	SL	3
144	-6.81	43.75	0.38	0.68	SL	1
145	-9.91	42.51	0	–	–	1
146	-12.15	36.89	0.07	–	–	1
147	-19.23	44.82	0.81	0.65	SL	3
148	-15.30	43.07	0.68	0.79	OMC1	3
149	-17.27	43.65	0.29	0.66	SL	1
150	-18.78	42.63	0.65	0.68	SL	1
151	-20.63	42.33	0.38	0.74	B	1
152	-33.37	33.55	0.55	0.69	SL	3
153	-37.40	32.90	0.25	0.69	B	1
154	-12.01	28.51	1.04	0.70	SL	3
155	-13.62	29.14	0.81	0.67	SL	3
156	-12.25	30.05	0.97	0.68		SL1
157	-15.56	30.89	0.77	0.62	SL	3
158	-15.72	32.80	0.67	0.71		SL3
159	-21.95	39.48	0.38	0.55	–	1
160	-21.60	37.38	0.75	0.70	SL	3
161	-20.81	36.09	0.75	0.70	SL	3
162	-18.73	34.56	1.07	0.70	SL	3
163	-18.50	32.99	0.91	0.83	OMC1	3
164	-18.83	30.21	0.88	0.81	OMC1	3
165	-21.28	29.10	1.43	0.68	SL	3
166	-19.83	28.47	1.42	0.69	SL	3
167	-21.35	32.22	0.21	–	–	1
168	-27.39	33.22	1.32	0.65	SL	3
169	-26.78	31.69	0.92	0.64	SL	3
170	-25.36	29.93	0.49	0.67	SL	3
171[g]	-24.96	28.21	0.25	0.68	SL	1

Bibliography

Aitken, D. K., Bailey, J. A., Roche, P. F., & Hough, J. M. 1985, *MNRAS*, 215, 815

Alfven, H. 1950, Cosmical Electrodynamics (Oxford: Clarendon Press)

Allen, D. A. & Burton, M. G. 1993, *Nature*, 363, 54

Alves, J. F., Lada, C. J., & Lada, E. A. 2001, *Nature*, 409, 159

Amiaud, L., Fillion, J., Baouche, S., et al. 2006, Journal of Chemical Physics, 124, 094702

André, P., Ward-Thompson, D., & Barsony, M. 1993, *ApJ*, 406, 122

André, P., Ward-Thompson, D., & Barsony, M. 2000, Protostars and Planets IV, 59

Anselmet, F., Gagne, Y., Hopfinger, E. J., & Antonia, R. A. 1984, J. Fluid Mech., 140, 63

Arce, H. G. & Sargent, A. I. 2004, *ApJ*, 612, 342

Arce, H. G. & Sargent, A. I. 2005, *ApJ*, 624, 232

Arce, H. G., Shepherd, D., Gueth, F., et al. 2006, Protostars and Planets V, astro-ph/0603071

Atkins, P. 1990, Physical Chemistry (Oxford University Press, 1990)

Axon, D. J. & Taylor, K. 1984, *MNRAS*, 207, 241

Bachiller, R. 1996, *ARA&A*, 34, 111

Bailey, J., Chrysostomou, A., Hough, J. H., et al. 1998, Science, 281, 672

Ballesteros-Paredes, J., Hartmann, L., & Vázquez-Semadeni, E. 1999a, *ApJ*, 527, 285

Ballesteros-Paredes, J., Klessen, R. S., Mac Low, M. ., & Vazquez-Semadeni, E. 2006, Protostars and Planets V, astro-ph/0603357

Ballesteros-Paredes, J., Klessen, R. S., & Vázquez-Semadeni, E. 2003, *ApJ*, 592, 188

Ballesteros-Paredes, J., Vázquez-Semadeni, E., & Scalo, J. 1999b, *ApJ*, 515, 286

Bally, J., O'Dell, C. R., & McCaughrean, M. J. 2000, *AJ*, 119, 2919

Bally, J., Stark, A. A., Wilson, R. W., & Langer, W. D. 1987, *ApJ*, 312, L45

Bally, J. & Zinnecker, H. 2005, *AJ*, 129, 2281

Barranco, J. A. & Goodman, A. A. 1998, *ApJ*, 504, 207

Batchelor, G. 1956, The Theory of Homogeneous Turbulence (Cambridge: Cambridge University Press)

Bate, M. R., Bonnell, I. A., & Bromm, V. 2003, *MNRAS*, 339, 577

Beckers, J. M. 1993, *ARA&A*, 31, 13

Becklin, E. E. & Neugebauer, G. 1967, *ApJ*, 147, 799

Beckwith, S., Evans, N. J., Gatley, I., Gull, G., & Russell, R. W. 1983, *ApJ*, 264, 152

Beckwith, S., Persson, S. E., Neugebauer, G., & Becklin, E. E. 1978, *ApJ*, 223, 464

Belloche, A., André, P., Despois, D., & Blinder, S. 2002, *A&A*, 393, 927

Bensch, F., Stutzki, J., & Ossenkopf, V. 2001, *A&A*, 366, 636

Benzi, R., Ciliberto, S., Tripiccione, R., et al. 1993, *Phys. Rev. E*, 48, 29

Bernardeau, F. 1994, *ApJ*, 433, 1

Beuther, H., Zhang, Q., Greenhill, L. J., et al. 2004, *ApJ*, 616, L31

Biferale, L., Boffetta, G., Celani, A., et al. 2004, *Phys. Rev. Lett.*, 93, 064502

Blaauw, A. 1964, *ARA&A*, 2, 213

Black, J. H. & Dalgarno, A. 1976, *ApJ*, 203, 132

Black, J. H. & van Dishoeck, E. F. 1987, *ApJ*, 322, 412

Blitz, L. & Williams, J. P. 1997, *ApJ*, 488, L145

Boldyrev, S. 2002, *ApJ*, 569, 841

Boldyrev, S., Nordlund, Å., & Padoan, P. 2002a, *ApJ*, 573, 678

Boldyrev, S., Nordlund, Å., & Padoan, P. 2002b, *Phys. Rev. Lett.*, 89, 031102

Bonnell, I. A., Bate, M. R., & Vine, S. G. 2003, *MNRAS*, 343, 413

Bonnor, W. B. 1956, *MNRAS*, 116, 351

Born, M. & Wolf, E. 1999, Principles of optics, seventh ed. (Cambridge University Press)

Bourke, T. L., Garay, G., Lehtinen, K. K., et al. 1997, *ApJ*, 476, 781

Bragg, S. L., Smith, W. H., & Brault, J. W. 1982, *ApJ*, 263, 999

Briceno, C., Preibisch, T., Sherry, W., et al. 2006, Protostars and Planets V, astro-ph/0602446

Buckle, J. V., Hatchell, J., & Fuller, G. A. 1999, *A&A*, 348, 584

Cabrit, S., Raga, A., & Gueth, F. 1997, in IAU Symp. 182: Herbig-Haro Flows and the Birth of Stars, ed. B. Reipurth & C. Bertout, 163–180

Caselli, P., Benson, P. J., Myers, P. C., & Tafalla, M. 2002, *ApJ*, 572, 238

Caselli, P. & Myers, P. C. 1995, *ApJ*, 446, 665

Catelan, P. & Moscardini, L. 1994, *ApJ*, 436, 5

Ceccarelli, C., Castets, A., Caux, E., et al. 2000, *A&A*, 355, 1129

Chappell, D. & Scalo, J. 2001, *MNRAS*, 325, 1

Cho, J. & Lazarian, A. 2003, *MNRAS*, 345, 325

Chrysostomou, A., Burton, M. G., Axon, D. J., et al. 1997, *MNRAS*, 289, 605

Chrysostomou, A., Gledhill, T. M., Ménard, F., et al. 2000, *MNRAS*, 312, 103

Churchwell, E., Wood, D. O. S., Felli, M., & Massi, M. 1987, *ApJ*, 321, 516

Ciardi, D. R., Telesco, C. M., Williams, J. P., et al. 2003, *ApJ*, 585, 392

Clénet, Y., Le Coarer, E., Joncas, G., et al. 2002, *PASP*, 114, 563

Coulman, C. E. 1985, *ARA&A*, 23, 19

Crutcher, R. M., Troland, T. H., Lazareff, B., Paubert, G., & Kazès, I. 1999, *ApJ*, 514, L121

Davidson, P. 2004, Turbulence. An introduction for scientist and engineers (Oxford University Press, 2004)

Davis, C. J., Ray, T. P., Desroches, L., & Aspin, C. 2001, *MNRAS*, 326, 524

Davis, C. J., Stern, L., Ray, T. P., & Chrysostomou, A. 2002, *A&A*, 382, 1021

de Avillez, M. A. & Breitschwerdt, D. 2006, Protostars and Planets V, astro-ph/0601228

Di Francesco, J., Evans, II, N. J., Caselli, P., et al. 2006, Protostars and Planets V, astro-ph/0602379

Di Francesco, J., Myers, P. C., Wilner, D. J., Ohashi, N., & Mardones, D. 2001, *ApJ*, 562, 770

Doeleman, S. S., Lonsdale, C. J., & Pelkey, S. 1999, *ApJ*, 510, L55

Doi, T., O'Dell, C. R., & Hartigan, P. 2002, *AJ*, 124, 445

Doi, T., O'Dell, C. R., & Hartigan, P. 2004, *AJ*, 127, 3456

Dougados, C., Lena, P., Ridgway, S. T., Christou, J. C., & Probst, R. G. 1993, *ApJ*, 406, 112

Draine, B. T. 1980, *ApJ*, 241, 1021

Draine, B. T., Roberge, W. G., & Dalgarno, A. 1983, *ApJ*, 264, 485

Dubrulle, B. 1994, *Phys. Rev. Lett.*, 73, 959

Ebert, R. 1955, Zeitschrift fur Astrophysik, 37, 217

Eggers, J. & Wang, Z. 1998, Phys. Rev. E, 57, 4281

Eisloffel, J., Mundt, R., Ray, T. P., & Rodriguez, L. F. 2000, Protostars and Planets IV, 815

Elmegreen, B. G. 2000, *ApJ*, 530, 277

Elmegreen, B. G. & Lada, C. J. 1977, *ApJ*, 214, 725

Elmegreen, B. G. & Scalo, J. 2004, *ARA&A*, 42, 211

Evans, N. J. 1999, *ARA&A*, 37, 311

Fabry, C. & Perot, A. 1901, *ApJ*, 13, 265

Falgarone, E., Lis, D. C., Phillips, T. G., et al. 1994, *ApJ*, 436, 728

Falgarone, E. & Phillips, T. G. 1990, *ApJ*, 359, 344

Falgarone, E. & Phillips, T. G. 1991, in IAU Symp. 147: Fragmentation of Molecular Clouds and Star Formation, 119

Falgarone, E., Pineau des Forêts, G., & Roueff, E. 1995, *A&A*, 300, 870

Falgarone, E., Puget, J.-L., & Perault, M. 1992, *A&A*, 257, 715

Falgarone, E., Verstraete, L., Pineau Des Forêts, G., & Hily-Blant, P. 2005, *A&A*, 433, 997

Farge, M. 1992, Annual Review of Fluid Mechanics, 24, 395

Field, D., Gerin, M., Leach, S., et al. 1994, *A&A*, 286, 909

Flower, D. R., Le Bourlot, J., Pineau des Forêts, G., & Cabrit, S. 2003, *MNRAS*, 341, 70

Flower, D. R., Pineau des Forêts, G., Field, D., & May, P. W. 1996, *MNRAS*, 280, 447

Frick, P., Dubrulle, B., & Babiano, A. 1995, *Phys. Rev. E*, 51, 5582

Frisch, U. 1995, Turbulence. The legacy of A.N. Kolmogorov (Cambridge: Cambridge University Press)

Frisch, U. & Sornette, D. 1997, Journal de Physique I, 7, 1155

Garmire, G., Feigelson, E. D., Broos, P., et al. 2000, *AJ*, 120, 1426

Gaume, R. A., Wilson, T. L., Vrba, F. J., Johnston, K. J., & Schmid-Burgk, J. 1998, *ApJ*, 493, 940

Gautier, T. N., Fink, U., Larson, H. P., & Treffers, R. R. 1976, *ApJ*, 207, L129

Genzel, R., Reid, M. J., Moran, J. M., & Downes, D. 1981, *ApJ*, 244, 884

Genzel, R. & Stutzki, J. 1989, *ARA&A*, 27, 41

Gezari, D. Y., Backman, D. E., & Werner, M. W. 1998, *ApJ*, 509, 283

Goldreich, P. & Kwan, J. 1974, *ApJ*, 189, 441

Goodman, A. A., Barranco, J. A., Wilner, D. J., & Heyer, M. H. 1998, *ApJ*, 504, 223

Grasdalen, G. L. 1976, *ApJ*, 205, L83

Greenhill, L. J., Gezari, D. Y., Danchi, W. C., et al. 2004a, *ApJ*, 605, L57

Greenhill, L. J., Reid, M. J., Chandler, C. J., Diamond, P. J., & Elitzur, M. 2004b, in IAU Symposium, 155

Grosso, N., Feigelson, E. D., Getman, K. V., et al. 2005, *ApJS*, 160, 530

Gustafsson, M., Brandenburg, A., Lemaire, J. L., & Field, D. 2006a, *A&A*, 454, 815

Gustafsson, M., Field, D., Lemaire, J. L., & Pijpers, F. P. 2006b, *A&A*, 445, 601

Gustafsson, M., Kristensen, L. E., Clénet, Y., et al. 2003, *A&A*, 411, 437

Habing, H. J. 1968, *Bull. Astron. Inst. Netherlands*, 19, 421

Hartigan, P., Raymond, J., & Hartmann, L. 1987, *ApJ*, 316, 323

Hartmann, L. 2003, *ApJ*, 585, 398

Hartung, M., Lidman, C., Ageorges, N., et al. 2004, in Ground-based Instrumentation for Astronomy. Edited by Alan F. M. Moorwood and Iye Masanori. Proceedings of the SPIE, Volume 5492, pp. 1531-1541 (2004)., ed. A. F. M. Moorwood & M. Iye, 1531–1541

Haugen, N. E., Brandenburg, A., & Dobler, W. 2004a, *Phys. Rev. E*, 70, 016308

Haugen, N. E. L., Brandenburg, A., & Mee, A. J. 2004b, *MNRAS*, 353, 947

Hecht, E. 1998, Optics, third ed. (Addison Wesley Longman, Inc)

Henney, W. J. & O'Dell, C. R. 1999, *AJ*, 118, 2350

Henriksen, R., Andre, P., & Bontemps, S. 1997, *A&A*, 323, 549

Herbig, G. H. & Terndrup, D. M. 1986, *ApJ*, 307, 609

Herschel, W. 1785, Philosophical Transactions Series I, 75, 213

Hillenbrand, L. A. & Carpenter, J. M. 2000, *ApJ*, 540, 236

Hillenbrand, L. A. & Hartmann, L. W. 1998, *ApJ*, 492, 540

Hollenbach, D. J. & Tielens, A. G. G. M. 1997, *ARA&A*, 35, 179

Hollenbach, D. J. & Tielens, A. G. G. M. 1999, Reviews of Modern Physics, 71, 173

Hornekær, L., Baurichter, A., Petrunin, V. V., Field, D., & Luntz, A. C. 2003, Science, 302, 1943

Houde, M., Dowell, C. D., Hildebrand, R. H., et al. 2004, *ApJ*, 604, 717

Howell, S. B. 2000, Handbook of CCD Astronomy (Cambridge University Press)

Jayesh & Warhaft, Z. 1991, *Phys. Rev. Lett.*, 67, 3503

Jeans, J. H. 1928, Astronomy and Cosmogony (Cambridge, U.K.: Cambridge Univ. Press)

Jefferts, K. B., Penzias, A. A., & Wilson, R. W. 1970, *ApJ*, 161, L87

Jijina, J., Myers, P. C., & Adams, F. C. 1999, *ApJS*, 125, 161

Johnston, K. J., Migenes, V., & Norris, R. P. 1989, *ApJ*, 341, 847

Johnstone, D., Wilson, C. D., Moriarty-Schieven, G., et al. 2000, *ApJ*, 545, 327

Joulain, K., Falgarone, E., Pineau des Forêts, G., & Flower, D. 1998, *A&A*, 340, 241

Joung, M. K. R. & Mac Low, M.-M. 2006, astro-ph/0601005

Kaufman, M. J. & Neufeld, D. A. 1996a, *ApJ*, 456, 611

Kaufman, M. J. & Neufeld, D. A. 1996b, *ApJ*, 456, 250

Kerr, R. M., Meneguzzi, M., & Gotoh, T. 2001, Physics of Fluids, 13, 1985

Kleiner, S. C. & Dickman, R. L. 1987, *ApJ*, 312, 837

Kleinmann, D. E. & Low, F. J. 1967, *ApJ*, 149, L1

Klessen, R. S. 2000, *ApJ*, 535, 869

Kofman, L., Bertschinger, E., Gelb, J. M., Nusser, A., & Dekel, A. 1994, *ApJ*, 420, 44

Kolmogorov, A. N. 1941, Dokl. Akad. Nauk, 30, 301

Königl, A. & Pudritz, R. E. 2000, Protostars and Planets IV, 759

Kristensen, L. E., Gustafsson, M., Field, D., et al. 2003, *A&A*, 512, 727

Kristensen, L. E., Ravkilde, T., Field, D., Lemaire, J. L., & Pineau des Forêts. 2006, *submitted to A&A*

Kritsuk, A. G. & Norman, M. L. 2004, *ApJ*, 601, L55

Kwan, J. 1977, *ApJ*, 216, 713

Lacombe, F., Gendron, E., Rouan, D., et al. 2004, *A&A*, 417, L5

Lada, C. J. 1987, in IAU Symp. 115: Star Forming Regions, ed. M. Peimbert & J. Jugaku, 1–17

Lada, C. J., Alves, J. F., & Lombardi, M. 2006, Protostars and Planets V

Lada, C. J., Muench, A. A., Lada, E. A., & Alves, J. F. 2004, *AJ*, 128, 1254

Larson, R. B. 1981, *MNRAS*, 194, 809

Le Bourlot, J., Pineau des Forêts, G., Flower, D. R., & Cabrit, S. 2002, *MNRAS*, 332, 985

Lee, C.-F., Mundy, L. G., Stone, J. M., & Ostriker, E. C. 2002, *ApJ*, 576, 294

Lee, C. W., Myers, P. C., & Plume, R. 2004, *ApJS*, 153, 523

Lee, C. W., Myers, P. C., & Tafalla, M. 1999, *ApJ*, 526, 788

Lee, J.-K. & Burton, M. G. 2000, *MNRAS*, 315, 11

Lemaire, J. L., Field, D., Gerin, M., et al. 1996, *A&A*, 308, 895

Lemaire, J. L., Field, D., Maillard, J. P., et al. 1999, *A&A*, 349, 253

Lis, D. C., Keene, J., Li, Y., Phillips, T. G., & Pety, J. 1998, *ApJ*, 504, 889

Livingston, W. & Wallace, L. 1991, An Atlas of the Solar Spectrum in the Infrared from 1850 to 9000 cm^{-1}, N. S. O. Technical Report No. 91-001, Tech. rep., National Optical Astronomy Observatories

Lonsdale, C. J., Becklin, E. E., Lee, T. J., & Stewart, J. M. 1982, *AJ*, 87, 1819

Loren, R. B. 1989, *ApJ*, 338, 902

Mac Low, M. & Klessen, R. S. 2004, Reviews of Modern Physics, 76, 125

Mac Low, M.-M., Klessen, R. S., Burkert, A., & Smith, M. D. 1998, Physical Review Letters, 80, 2754

Maddalena, R. J., Moscowitz, J., Thaddeus, P., & Morris, M. 1986, *ApJ*, 303, 375

Matzner, C. D. 2002, *ApJ*, 566, 302

McCaughrean, M. J. & Mac Low, M. 1997, *AJ*, 113, 391

McCaughrean, M. J. & O'Dell, C. R. 1996, *AJ*, 111, 1977

McKee, C. F. 1989, *ApJ*, 345, 782

Meinel, I. A. B. 1950, *ApJ*, 111, 555

Menten, K. M. & Reid, M. J. 1995, *ApJ*, 445, L157

Miesch, M. S. & Bally, J. 1994, *ApJ*, 429, 645

Miesch, M. S., Scalo, J., & Bally, J. 1999, *ApJ*, 524, 895

Miesch, M. S. & Scalo, J. M. 1995, *ApJ*, 450, L27

Morris, M., Palmer, P., & Zuckerman, B. 1980, *ApJ*, 237, 1

Motte, F. & André, P. 2001, *A&A*, 365, 440

Motte, F., André, P., & Neri, R. 1998, *A&A*, 336, 150

Mouschovias, T. C. 1991, *ApJ*, 373, 169

Muench, A. A., Lada, E. A., Lada, C. J., & Alves, J. 2002, *ApJ*, 573, 366

Müller, W.-C., Biskamp, D., & Grappin, R. 2003, *Phys. Rev. E*, 67, 066302

Mundy, L. G., Scoville, N. Z., Baath, L. B., Masson, C. R., & Woody, D. P. 1986, *ApJ*, 304, L51

Myers, P. C. 1998, *ApJ*, 496, L109

Nakamura, F. & Li, Z.-Y. 2005, *ApJ*, 631, 411

Nakano, T. 1998, *ApJ*, 494, 587

Nissen, H., Gustafsson, M., Lemaire, J., et al. 2006, *accepted by* A&A

Nordlund, Å. & Galsgaard, K. 1995, a 3D MHD code for Parallel Computers; `http://www.astro.ku.dk/~aake/NumericalAstro/papers/kg/mhd.ps.gz`

Nordlund, Å. & Padoan, P. 2003, Lecture Notes in Physics, Berlin Springer Verlag, 614, 271

Norman, C. & Silk, J. 1980, *ApJ*, 238, 158

Norris, R. P. 1984, *MNRAS*, 207, 127

Nyquist, H. 1928, Trans. AIEE, 47, 617

O'Dell, C. R. 2001, *ARA&A*, 39, 99

O'Dell, C. R. & Doi, T. 2003, *AJ*, 125, 277

O'Dell, C. R., Hartigan, P., Bally, J., & Morse, J. A. 1997a, *AJ*, 114, 2016

O'Dell, C. R., Hartigan, P., Lane, W. M., et al. 1997b, *AJ*, 114, 730

O'Dell, C. R. & Wen, Z. 1994, *ApJ*, 436, 194

O'Dell, C. R., Wen, Z., & Hu, X. 1993, *ApJ*, 410, 696

Onishi, T., Mizuno, A., Kawamura, A., Tachihara, K., & Fukui, Y. 2002, *ApJ*, 575, 950

Ossenkopf, V. & Mac Low, M.-M. 2002, *A&A*, 390, 307

Padoan, P., Bally, J., Billawala, Y., Juvela, M., & Nordlund, Å. 1999, *ApJ*, 525, 318

Padoan, P., Boldyrev, S., Langer, W., & Nordlund, Å. 2003, *ApJ*, 583, 308

Padoan, P., Jimenez, R., Nordlund, Å., & Boldyrev, S. 2004, *Phys. Rev. Lett.*, 92, 191102

Padoan, P., Juvela, M., Bally, J., & Nordlund, A. 1998, *ApJ*, 504, 300

Padoan, P. & Nordlund, Å. 1999, *ApJ*, 526, 279

Padoan, P. & Nordlund, Å. 2002, *ApJ*, 576, 870

Passot, T. & Pouquet, A. 1987, J. Fluid Mech., 181, 441

Peitgen, H. & Saupe, D. 1988, The Science of Fractal Images (Springer, New York)

Peng, R., Langer, W. D., Velusamy, T., Kuiper, T. B. H., & Levin, S. 1998, *ApJ*, 497, 842

Pety, J. & Falgarone, É. 2000, *A&A*, 356, 279

Pety, J. & Falgarone, E. 2003, *A&A*, 412, 417

Pineau des Forêts, G., Flower, D. R., & Dalgarno, A. 1988, *MNRAS*, 235, 621

Plambeck, R. L., Wright, M. C. H., Mundy, L. G., & Looney, L. W. 1995, *ApJ*, 455, L189

Plume, R., Bensch, F., Howe, J. E., et al. 2000, *ApJ*, 539, L133

Plume, R., Jaffe, D. T., Evans, N. J., Martin-Pintado, J., & Gomez-Gonzalez, J. 1997, *ApJ*, 476, 730

Politano, H. & Pouquet, A. 1995, *Phys. Rev. E*, 52, 636

Predehl, P. & Schmitt, J. H. M. M. 1995, *A&A*, 293, 889

Pudritz, R. E., Ouyed, R., Fendt, C., & Brandenburg, A. 2006, Protostars and Planets V, astro-ph/0603592

Raga, A. & Cabrit, S. 1993, *A&A*, 278, 267

Richer, J. S., Shepherd, D. S., Cabrit, S., Bachiller, R., & Churchwell, E. 2000, Protostars and Planets IV, 867

Ricotti, M. & Ferrara, A. 2002, *MNRAS*, 334, 684

Rieke, G. H., Low, F. J., & Kleinmann, D. E. 1973, *ApJ*, 186, L7

Rosado, M., de la Fuente, E., Arias, L., Raga, A., & Le Coarer, E. 2001, *AJ*, 122, 1928

Rosenthal, D., Bertoldi, F., & Drapatz, S. 2000, *A&A*, 356, 705

Rouan, D., Field, D., Lemaire, J.-L., et al. 1997, *MNRAS*, 284, 395

Rousselot, P., Lidman, C., Cuby, J.-G., Moreels, G., & Monnet, G. 2000, *A&A*, 354, 1134

Salas, L., Rosado, M., Cruz-González, I., et al. 1999, *ApJ*, 511, 822

Scalo, J. M. 1984, *ApJ*, 277, 556

Scalo, J. M. 1986, Fundamentals of Cosmic Physics, 11, 1

Schild, H., Miller, S., & Tennyson, J. 1997, *A&A*, 318, 608

Schleuning, D. A. 1998, *ApJ*, 493, 811

Schmeja, S. & Klessen, R. S. 2004, *A&A*, 419, 405

Schultz, A. S. B., Colgan, S. W. J., Erickson, E. F., et al. 1999, *ApJ*, 511, 282

Scoville, N. Z., Hall, D. N. B., Ridgway, S. T., & Kleinmann, S. G. 1982, *ApJ*, 253, 136

She, Z. & Leveque, E. 1994, *Phys. Rev. Lett.*, 72, 336

She, Z.-S., Ren, K., Lewis, G. S., & Swinney, H. L. 2001, *Phys. Rev. E*, 64, 016308

Shu, F. H., Adams, F. C., & Lizano, S. 1987, *ARA&A*, 25, 23

Shuping, R. Y., Morris, M., & Bally, J. 2004, *AJ*, 128, 363

Simpson, J. P., Colgan, S. W. J., Erickson, E. F., Burton, M. G., & Schultz, A. S. B. 2006, *ApJ*, 642, 339

Smith, M. D. & Brand, P. W. J. L. 1990, *MNRAS*, 242, 495

Smith, M. D., Mac Low, M.-M., & Heitsch, F. 2000a, *A&A*, 362, 333

Smith, M. D., Mac Low, M.-M., & Zuev, J. M. 2000b, *A&A*, 356, 287

Spicker, J. & Feitzinger, J. V. 1988, *A&A*, 191, 186

Störzer, H. & Hollenbach, D. 1999, *ApJ*, 515, 669

Sternberg, A. & Dalgarno, A. 1989, *ApJ*, 338, 197

Stolovy, S. R., Burton, M. G., Erickson, E. F., et al. 1998, *ApJ*, 492, L151

Stone, J. M., Ostriker, E. C., & Gammie, C. F. 1998, *ApJ*, 508, L99

Stone, J. M., Xu, J., & Mundy, L. G. 1995, *Nature*, 377, 315

Stutzki, J., Bensch, F., Heithausen, A., Ossenkopf, V., & Zielinsky, M. 1998, *A&A*, 336, 697

Stutzki, J. & Guesten, R. 1990, *ApJ*, 356, 513

Sugai, H., Kawabata, H., Usuda, T., et al. 1995, *ApJ*, 442, 674

Tafalla, M., Mardones, D., Myers, P. C., et al. 1998, *ApJ*, 504, 900

Tafalla, M. & Myers, P. C. 1997, *ApJ*, 491, 653

Tan, J. C. 2004, *ApJ*, 607, L47

Testi, L. & Sargent, A. I. 1998, *ApJ*, 508, L91

Timmermann, R. 1998, *ApJ*, 498, 246

van Dishoeck, E. F. & Blake, G. A. 1998, *ARA&A*, 36, 317

Vannier, L., Lemaire, J. L., Field, D., et al. 2001, *A&A*, 366, 651

Vázquez-Semadeni, E., Ballesteros-Paredes, J., & Klessen, R. S. 2003, *ApJ*, 585, L131

Vázquez-Semadeni, E., Kim, J., & Ballesteros-Paredes, J. 2005, *ApJ*, 630, L49

Vazquez-Semadeni, E., Passot, T., & Pouquet, A. 1995, *ApJ*, 441, 702

Velusamy, T. & Langer, W. D. 1998, *Nature*, 392, 685

von Weizsäcker, C. F. 1951, *ApJ*, 114, 165

Ward-Thompson, D., Andre, P., Crutcher, R., et al. 2006, Protostars and Planets V, astro-ph/0603474

Wen, Z. & O'Dell, C. R. 1995, *ApJ*, 438, 784

White, G. J., Araki, M., Greaves, J. S., Ohishi, M., & Higginbottom, N. S. 2003, *A&A*, 407, 589

White, R. J., Greene, T. P., Doppmann, G. W., Covey, K. R., & Hillenbrand, L. A. 2006, Protostars and Planets V, astro-ph/0604081

Wilgenbus, D., Cabrit, S., Pineau des Forêts, G., & Flower, D. R. 2000, *A&A*, 356, 1010

Wilson, R. W., Jefferts, K. B., & Penzias, A. A. 1970, *ApJ*, 161, L43

Wilson, T. L., Gaume, R. A., Gensheimer, P., & Johnston, K. J. 2000, *ApJ*, 538, 665

Wolf, M. 1923, Astronomische Nachrichten, 219, 109

Wolniewicz, L., Simbotin, I., & Dalgarno, A. 1998, *ApJS*, 115, 293

Wright, J. & Schult, R. L. 1993, Chaos, 3, 295

Wright, M. C. H. & Plambeck, R. L. 1983, *ApJ*, 267, L115

Wright, M. C. H., Plambeck, R. L., & Wilner, D. J. 1996, *ApJ*, 469, 216

Zhang, Q., Hunter, T. R., Brand, J., et al. 2005, *ApJ*, 625, 864

Ziurys, L. M., Martin, R. N., Pauls, T. A., & Wilson, T. L. 1981, *A&A*, 104, 288

Zuckerman, B. 1973, *ApJ*, 183, 863

Zuckerman, B. & Evans, II, N. J. 1974, *ApJ*, 192, L149

List of Figures

List of Tables